CRANFIELD UNIVERSITY
School of Industrial and Manufacturing Science

PhD THESIS

HYDROGEN RE-EMBRITTLEMENT SUSCEPTIBILITY OF ULTRA HIGH STRENGTH STEELS

Douglas J. Figueroa Gordon

CRANFIELD UNIVERSITY
School of Industrial and Manufacturing Science

PhD THESIS

Academic Years 2002-2005

Douglas J. Figueroa Gordon

HYDROGEN RE-EMBRITTLEMENT SUSCEPTIBILITY OF ULTRA HIGH STRENGTH STEELS

Supervisor: Dr. M. J. Robinson

September 2005

ABSTRACT

300M ultra high strength steel has been widely used for over forty years as a structural material in aerospace applications where a high strength is required. These parts are generally protected from corrosion by electroplated cadmium sacrificial coatings. However, there are concerns over this coating material due to its high toxicity and alternative coatings including Zinc-14%Nickel and SermeTel®1140/962 have been considered.

It is known that applying electrodeposited coatings causes atomic hydrogen to be absorbed by the steel substrate producing delayed failure by direct hydrogen embrittlement. Hydrogen is also absorbed when a sacrificial coating undergoes corrosion in service and this process is known as re-embrittlement. The effect of electroplated Zinc-14%Nickel and aluminium based SermeTel®1140/962 sacrificial coatings in causing hydrogen embrittlement and re-embrittlement of 300M steel have been compared to that of conventional electroplated cadmium.

AerMet®100 ultra high strength steel has been also considered as alternative replacement for the conventional 300M. Hence, the hydrogen embrittlement and re-embrittlement susceptibilities of AerMet®100 were studied when coated with cadmium, Zinc-14%Nickel and SermeTel®1140/962. In addition, two alternative alloys GifloM2000 and CSS-42L™ were also taken into consideration and only the extent of hydrogen re-embrittlement was assessed when coated with cadmium and SermeTel®1140/962, respectively.

Slow strain rate tests, *SSRT*, were carried out for plated, plated and baked as well as plated, baked and corroded tensile specimens. The time to failure values were compared using a Weibull distribution, statistical *t*-tests and embrittlement indices. Differences in hydrogen susceptibility of the high strength steels considered might depend upon their intrinsic hydrogen transport characteristics. These properties were studied and compared in terms of hydrogen diffusivity and solubility.

ACKNOWLEDGEMENTS

I would like to express my gratitude to Dr. M. J. Robinson for his guidance and support during this research project. His expertise and contribution have been invaluable for my doctoral studies.

Moreover, I would like to thanks Dr. Steve Preston, Dave Light and David Collins from Airbus U.K, for their constant interest and financial support for this project. In addition, I would like to mention Andrew Dyer, Colin Matthews, Christine Kimpton, Rukhsana Ormesher and Tony Parker in the School of Industrial and Manufacturing Science at Cranfield University for their assistance and technical support in numerous occasions.

I would like to specially thank my mother, my father and my lovely wife Esmeralda for their unconditional support and I would like to mention my son Douglas Gabriel who was born during my postgraduate studies and has brought more happiness and joy into my life. I dedicate this work to them.

LIST OF CONTENT

LIST OF FIGURES

LIST OF TABLES

INTRODUCTION

High strength alloys are commonly used for a wide range of structural applications in many industry sectors including construction, oil and energy, automotive and aerospace. Specifically within the aerospace industry, structural components require the use of high strength alloys due to high loads as well as residual stresses due to manufacturing process such as forging or heat treatments.

Most of modern aerospace structural components are designed from low alloy high strength steels; materials strong and tough enough to meet or exceed minimum application requirements. These alloys generally have exceptional mechanical properties including yield and ultimate tensile strengths around 1800 and 2000 MPa, respectively.[1-3] The strength levels of these low alloyed steels are higher than virtually any other structural alloy, with approximately 40% strength to weight advantage over 7000 aluminium series, and superior mechanical properties compared to most titanium alloys.

For decades, the most commonly used low alloyed high strength steels had been AISI-4340 and 300M. AISI-4340 is a nickel-chromium-molybdenum low alloy steel, heat treated to reach tensile strength levels of approximately 1800 MPa. 300M is a modified version of AISI-4340 steel with silicon, vanadium and slightly greater carbon and molybdenum content. Both alloys have a good combination of tensile strength (1700 to 2000 MPa), toughness and fatigue resistance for structural applications. [4,5]

However, the main drawback of high strength steels is their intrinsic susceptibility to delayed failure, caused by hydrogen embrittlement, *HE*, stress corrosion cracking, *SCC*, or fatigue. Moreover, it has been estimated that approximately 20% of all mishaps, not caused by pilot errors, are related to failure of landing gear components.[1]

Hydrogen embrittlement is a process in which atomic hydrogen generated on the surface of the steel due to cathodic reactions, diffuses within the microstructure causing a deleterious effect on its mechanical properties. Thereafter, a sudden and unpredictable failure of the component will take place. Atomic hydrogen could be generated during electroplating processes or when the steel components are exposed in service to any aqueous fluid; mostly to corrosive environments such as marine atmospheres.[6,7]

On the other hand, a stress corrosion cracking process, *SCC*, usually involves the anodic polarisation of the steel surface, leading to a partial dissolution of the steel component in the electrolyte together with the simultaneous effect of mechanical stresses. *SCC* is normally associated with three different mechanisms: active path dissolution, film induced cracking and hydrogen embrittlement.[6,7] The latter mechanism of *SCC* is the most likely for high strength steels. In addition, hydrogen embrittlement has been considered particularly applicable to martensitic stainless steels.[8]

To assess the susceptibility of high strength steels to hydrogen embrittlement, *HE*, or stress corrosion cracking, *SCC*, mechanical tests are commonly performed using tensile specimens, as **Figure 1** shows. Alloys which are susceptible to embrittlement typically display brittle failure with relatively little reduction in area, *RA%*.[1]

Regarding corrosion fatigue failures, they are associated with the presence of corrosive environments and cyclic stresses. The propagation of a fatigue crack is related to the application of load cycles of sufficient magnitude to create an incremental advance of the crack front.[1,2,6] Nevertheless, the scope of the present research had been mainly focussed on *HE* related failures and *SCC* associated with high strength martensitic steels.

High strength steel components can easily undergo corrosion due to direct exposure to environmental conditions such as a marine atmosphere.

Therefore, high strength steel components are mostly protected with sacrificial electroplated cadmium coatings in order to prevent this deleterious process.

Cadmium has been used for decades as a sacrificial metallic coating within the aerospace industry. These coatings have been widely used to protect fasteners and other components, particularly for exposure in chloride containing environments, following British Standard BS 1706:1990.[9]

Figure 1. Tensile specimens showing brittle fracture due to hydrogen embrittlement, *HE*.[1]

Moreover, other alloys used in landing gear applications such as 2000 and 7000 series aluminium have similar free corrosion potentials to cadmium, lowering the risk of deleterious galvanic corrosion. All these advantages, together with the self lubrication properties of cadmium which aids uniformly tightening threaded fasteners, make this metal the primary protective coating for aerospace applications.[10, 11]

Cadmium is particularly sacrificial to steel due to its more negative free corrosion potential, -0.69 Volts (SCE), than that of steel, -0.60 Volts (SCE), related to hydrogen scale in flowing sea-water solutions. Therefore, cadmium becomes preferentially corroded, making the steel cathodically

protected. In addition, corrosion products resulting from cadmium coating dissolution do not remain on the surface.[10, 11]

Cadmium electroplating is commonly carried out from cyanide or sulphate solutions. Unfortunately, the current efficiency of this process is less than 100%, hence inevitable hydrogen evolution on the steel surface takes place during this process.[11] Part of this hydrogen diffuses into the steel producing hydrogen embrittlement as is shown is **Figure 2**.

Although hydrogen uptake by the steel represents a potential problem, baking the electroplated specimens for 24 hours at approximately 200°C, allows removal of the absorbed hydrogen from the steel and consequently a recovery of its original mechanical properties takes place.[6,11]

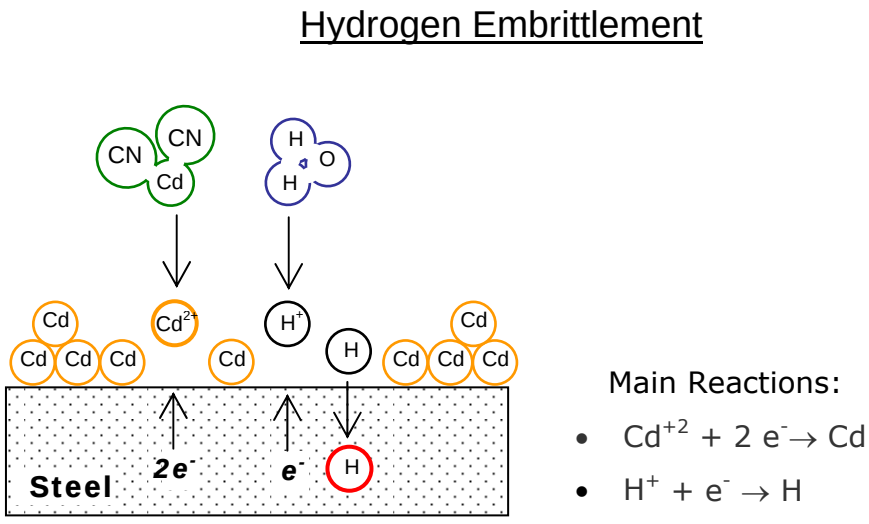

Figure 2. Schematic representation of hydrogen embrittlement during electroplating of cadmium coatings.

However, health and environmental concerns have been associated with the use of cadmium for engineering applications. It is well known that cadmium is a carcinogenic agent that could produce long terms damage to humans, animals and micro-organisms. Some of its adverse health effects on humans are lung cancer and kidney damage. Despite these serious implications, it has been reported that some employees in the aircraft servicing, repairing and maintenance industry have been exposed to 85

times the maximum limit (0.5 mg/m^3) resulting from exposure to cadmium dust.[13,14]

Since 1995 cadmium electroplating has been banned in the European Union for all purposes except aerospace, mining, offshore and nuclear activities according to the directive EU 91/338/EEC,[14] and continuous efforts have been made worldwide to replace electroplated cadmium in the aerospace industry.

Based on the principles of sacrificial coatings, properties of the alternative materials have to include: sacrificial behaviour stability to steels, galvanic compatibility with other alloys such as 2000 and 7000 series aluminium, good barrier properties. Among several alternative coatings, the present research work has been focussed on electroplated Zinc-14%Nickel alloys and aluminium-based coating SermeTel®1140/962, which represented strong candidates for the replacement of electroplated cadmium due to their promising characteristics.

Zinc-Nickel electroplated alloys display optimum corrosion behaviour at 14% nickel composition and a free corrosion potential in marine environments between -0.6 to -0.9 mV (SCE), depending on plating conditions. Therefore, this coating is gavanically compatible to aerospace aluminium alloys while remaining sacrificial to steel. Furthermore, it has been reported that the application of baking treatments to AISI-4340 high strength steel following Zinc-14%Nickel electroplating process, effectively removed hydrogen absorbed within the metal exhibiting thereafter 100% recovery of the mechanical properties.[12,15,16]

The second alternative coating under consideration was SermeTel®1140/962 which belongs to a different category of sacrificial coatings and consists of densely packed aluminium particles dispersed in a chromate/phosphate inorganic binder. Moreover, further application of a polymer silicon modified topcoat system enhances its corrosion and barrier properties.[17]

This coating is subjected to a curing process between 232 and 343°C and is recommended for use on high strength steels that can tolerate 274°C cure, such as 300M, with no effect on their mechanical properties. In addition, it has been claimed by the manufacturer that the application of this coating system does not cause hydrogen embrittlement.[17] However, recent studies carried out at Cranfield University on a similar aluminium based coating, specifically SermeTel®CR984/LT, concluded that significant levels of hydrogen re-embrittlement on AISI-4340 high strength steels were found when this coating became corroded in service.[18]

The latter observation indicates that special attention must be taken during corrosion of the sacrificial coatings in service. Pores or flaws in the sacrificial coating, could directly expose the steel component to corrosive fluids, generating localised galvanic cells between the steel and the coating itself. As a result, hydrogen evolution and its partial absorption take place on the steel surface when simultaneous anodic dissolution of the coating proceeds. This phenomenon has been defined as hydrogen re-embrittlement and unlike hydrogen embrittlement following electroplating processes, arises during operating conditions. **Figure 3** schematically shows this phenomenon including the main reactions involved.

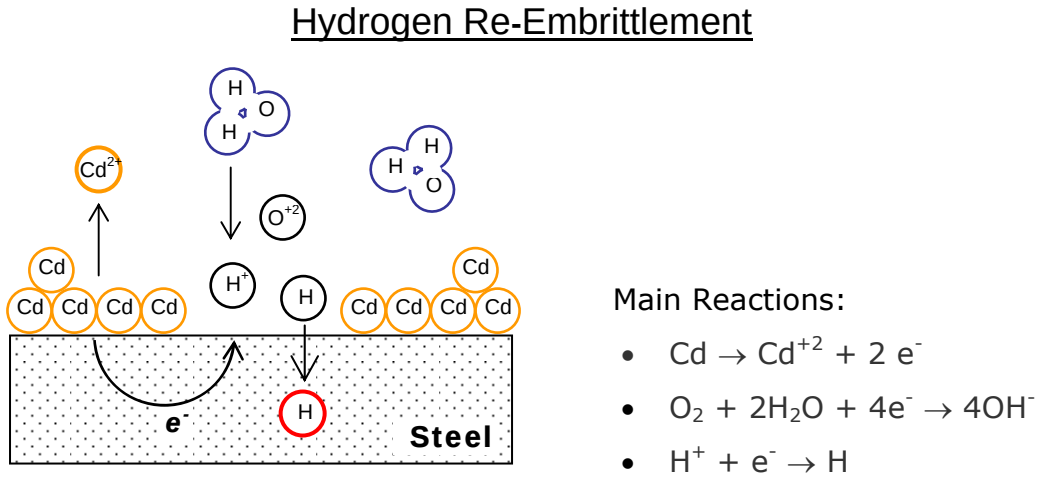

Figure 3. Schematic representation of hydrogen re-embrittlement due to corrosion of cadmium sacrificial coating during service.

For the development of the present research project, it was important to consider that in the two phenomena, embrittlement and re-embrittlement, hydrogen was generated in different conditions: A) hydrogen embrittlement which could take place during electroplating of the sacrificial coating and, B) re-embrittlement associated to the direct exposure of the steel substrate to corrosive environments during service.

Before Zinc-14%Nickel and SermeTel®1140/962 coatings could be considered suitable for aerospace applications, it is imperative to assess the effect of hydrogen embrittlement and re-embrittlement on high strength steels.

Furthermore, in recent years a new generation of materials have been developed as alternatives to the conventional AISI-4340 and 300M high strength steels to improve its properties by enhancing mechanical performance as well as resistance to corrosion related failures.

Within the extent of the present research programme, there were considered three alternative new ultra high strength steels as possible replacements for the conventional 300M alloy. The first of these new materials was AerMet®100; a revolutionary high strength steel developed by the American corporation Carpenter Technology. This alloy contains 11.1% nickel and 3% chromium with exceptional resistance to fatigue and *SCC*. AerMet®100 production-scale forgings have been previously used in undercarriage components for a variety of aircrafts.[19, 20]

The second material into consideration was GifloM2000 microalloyed steel developed by the Hungarian GifloSteels Company.[21] This alloy is basically a copper-manganese-nickel microalloyed steel, described as wear and atmospheric corrosion resistant. Finally, the last material taken under consideration was CSS-42L™ a high strength martensitic stainless steel originally developed for bearing applications and intended to operate at temperatures up to 427°C with excellent corrosion and wear resistant properties.[22]

Taking into account the alternative coatings to substitute cadmium as well as these high strength steels considered to replace 300M alloy, the main goals of the present research could be summarised as:

I. Evaluate the corrosion behaviour of SermeTel®1140/962 coating and Zinc-14%Nickel electroplating as possible alternatives to electroplated cadmium sacrificial coatings,

II. Compare the performance of AerMet®100, GifloM2000 and CSS-42L™ high strength steels to the conventional 300M, by assessing the risk of hydrogen embrittlement and re-embrittlement of the coated alloys,

III. Establish the best steel-coating system, which ideally might display the lowest susceptibility to hydrogen related failure during service of the structural component.

LITERATURE REVIEW

1. High Strength Steels for Aerospace Applications

To achieve the strength levels required for aerospace structural applications, several factors are involved in the development of ultra high strength steels. Among these, the alloy composition and heat treatment, which have an influence on phase transformations and hardening mechanisms, are used to control the microstructure and hence the mechanical properties.[23]

High strength steels are commonly obtained by quenching to form martensite, which is subsequently tempered at an intermediate temperature. As martensite has low ductility, tempering allows the carbon atoms to diffuse out and form precipitates like Fe_3C between fine martensite grains. For optimum development of strength, the steel first has to be fully transformed to martensite. This ability to form martensite by quenching is referred as *hardenability*, and the effectiveness of this process will depend mainly on the shape of the component and steel composition. The smaller the component diameter the more likely to become fully transformed to martensite due to uniform cooling rate within the cross section area of the specimen.[23]

On the other hand, alloying elements can affect the stability of the austenite phase (γ), changing the kinetics of its transformation or promoting the precipitation of carbides which are associated with the strengthening mechanism. Elements that tend to retard ferrite, (α), and pearlite transformations, ($\gamma \rightarrow \alpha + Fe_3C$), such as Ni and Mn enable Time-Temperature-Transformation curves, *TTT*, to move progressively to longer times by increasing the alloy content as is shown in **Figure 4**. By increasing manganese content of 1060-carbon steel (0.6%wt C, 0.9%wt Mn) this effect can be easily noticed. Moreover, additions of Ni, Cr and Mo to produce AISI-4340 high strength steel considerably increased the stability of austenite by moving the '*nose*' of the *TTT* diagram to longer times.

Overall, those elements tend to stabilise austenite and depress the position of the *TTT* curve relative to the temperature axis. Therefore, slowing down pearlite and ferrite formation reactions assists in obtaining much stronger low temperature phases such as martensite which increases the alloy strength.[23]

Alternatively, alloying elements such as Si, Cr, Mo, V, Nb and Ti form carbides thermodynamically more stable than cementite. The tendency of some of these elements is to form fine carbide dispersion in the temperature range from 500 to 600 °C, and this is accompanied by a marked increase of strength in excess of that of the as-quench martensite. This *secondary hardening* phenomenon has been associated with steels containing Mo, V, W, Ti and also in chromium steels at higher alloy concentrations like AerMet®100 and CSS-42L™.[23, 25, 26]

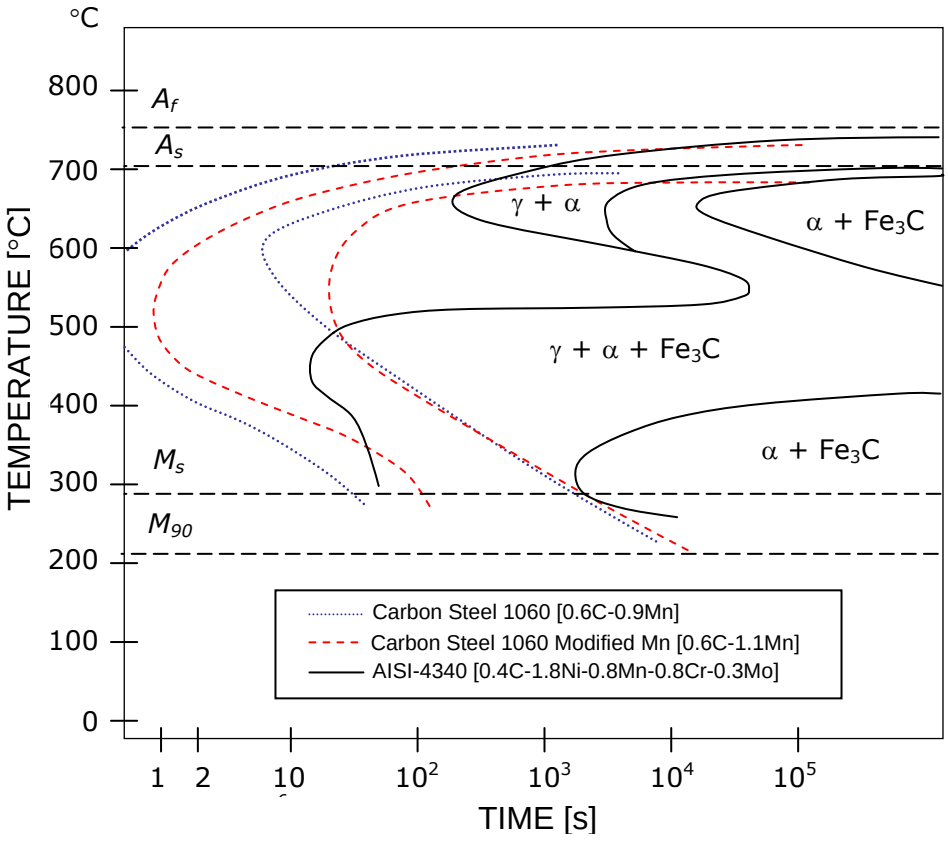

Figure 4. Effect of alloy elements on the *TTT* diagrams and hardenability of some steels, modified from *U.S.S.*[24]

Bearing in mind differences in composition and heat treatment recommended by their corresponding manufacturers, the strength levels

achieved by the high strength steels studied in this project are illustrated in **Figure 5**. The yield and tensile strengths of these alloys were compared in a bar chart. It can be seen that the yield strength of 300M is similar to AerMet®100 and GifloM2000, and significantly higher than CSS-42L™ stainless steel. The same trend is found in terms of ultimate tensile strength.

In addition to high strength levels to resist failure by plastic deformation, structural aerospace applications also require high toughness to resist failure by crack propagation. However, these objectives are contradictory since these alloys intrinsically have lower ductility, making the trade-off between strength and toughness a recurrent problem in the development of high strength steels.[23]

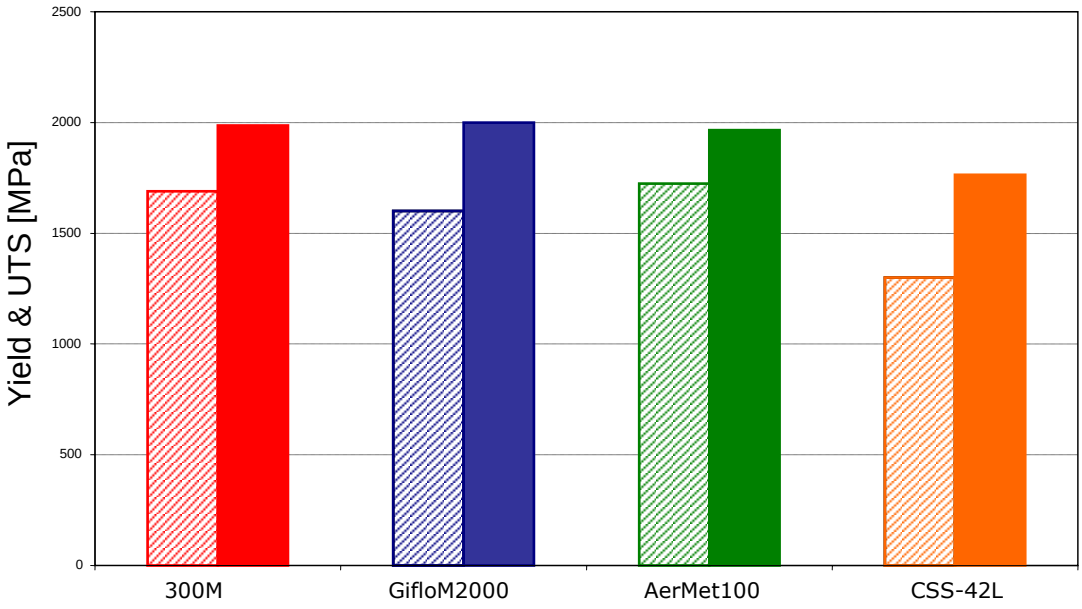

Figure 5. Comparison of yield strength, *YS*, and ultimate tensile strength, *UTS*, for 300M, GifloM2000, AerMet®100 and CSS-42L™ high strength steels.[4, 5, 19-22, 27]

To achieved high fracture toughness the fracture mode must be ductile and the ductile crack propagation must be difficult. The use of thermal mechanisms of grain refinement to achieve high toughness in martensitic steels is the most common solution to overcome this situation.[28] The most common way to refine the martensite grain size is by decreasing the prior austenite grain size using heat treatments that accomplished

austenitising treatments.[29] Moreover, additions of certain alloying elements such as vanadium to 300M steel restrict austenite grain growth during this process.[30]

AerMet®100 displays higher values of fracture toughness, K_{IC}, of approximately 120 MPa√m, than 300M and CSS-42L™ steels with 77 and 112 MPa√m, respectively. However, the susceptibility to *SCC* and hydrogen embrittlement remains a subject of study. [4, 5, 19-22, 27] These susceptibilities would be intrinsically determined mainly by the microstructures of each alloy. In order to describe these particular differences, high strength steels under study were classified in connection with their main alloying elements apart from carbon. Steels containing, up to approximately 1% of various alloying elements were considered as *low alloy steels* and 300M as well as GifloM2000 belong to this group, whereas, AerMet®100 was considered to be a *high alloy steel* due to its high levels of nickel and cobalt. CSS-42L™ stainless steel was an example of the *precipitation and transformation hardening stainless steels* group.[31]

1.1. Low Alloy Steels

Low alloy high strength steels are commonly austenitised at relatively low temperatures (typically 870 °C) to produce a fine prior austenite grain size before quenching, *Q*, and tempering, *T*. This conventional heat treatment cycle is referred as *QT* treatment. For example, the recommended treatment for vacuum induction melted, *VIM*, and vacuum arc re-melted, *VAR*, 300M steel include austenitising at 870 °C and oil quenching to room temperature, followed by a double tempering at approximately 315°C.[4, 29, 30, 32]

The resulting microstructure consists of a martensitic matrix with a variety of carbides distributed within or at the martensite boundaries.[33] Two major morphologies of martensitic grains can be present; laths and plates. The first is associated with steels with less than 0.5%wt carbon, and the latter is found in medium carbon martensite for steels with approximate 0.5%wt carbon.[23, 34]

Martensite laths are grouped together in packets with low angle boundaries as is shown in **Figure 6**, although a minority of laths are separated by highly disoriented boundaries. Whereas, plate morphology consists on lenticular plates that can be concurrent with lath martensite in the range 0.5-1.0% carbon and unlike the laths, the lenticular plates form in isolation rather than in packets. Moreover, **Figure 7** showed that the presence of laths or plates is highly dependent on the carbon content, %C, for unalloyed steels. The presence of both martensite morphologies in the microstructure determines the strengthening and properties of the alloy.[23, 34]

It has been reported that *QT* treated 300M steels display a mixture of predominantly twinned plate martensite and dislocated lath martensite with a mean lath width of 0.3μm approximately. Moreover, it contains 5 %Vol. of retained austenite as inter-lath film with thickness between 100 to 200 Å. The prior austenite grain boundaries also are typical sites for these films to arise. Retained austenite is formed when at the martensitic final transformation temperature, M_f, a small proportion of remaining austenite does not transform to martensite.[33, 35]

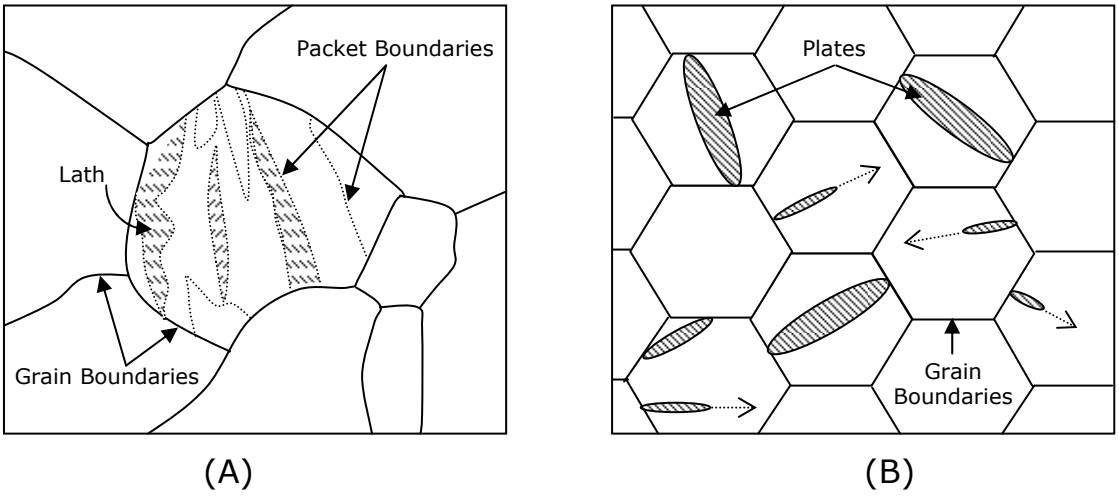

Figure 6. A) Microstructure of lath martensitic steels;[28] and B) Martensitic transformation where martensite plates nucleates at grain boundaries.

In addition, the strengthening effect of microalloying elements could be produced by dispersion of very fine precipitate particles and by inhibition of grain growth. The elements C and N are commonly in solid solution in

the austenite and the nucleation of carbides or nitrides mainly depends on their solubility and thermodynamic stability.[35-37]

During tempering of as-quenched martensite, precipitation of ε-carbide takes places due to the instability of martensite leading to a partial loss of tetragonality. This carbide has a close packed hexagonal structure, and precipitates as narrow laths or rodlets within martensite laths or plates.[23]

A second source of precipitates in low alloy steels are carbides, borides or nitrides thermodynamically more stable than cementite. Alloying elements like Cr, Mo, V, W and Ti tend to form stable carbides while Ni, Co and Cu do not form precipitates. It has been reported that 300M steels in addition to ε-carbides also could contain M_7C_3, $M_{23}C_6$ as well as Mo_2C carbides. In addition, alternative low alloy high strength steels such as AISI-4340 usually contains MnS inclusions randomly distributed through its microstructure.[23, 35, 38]

1.2. High Alloy Steels

AerMet®100 is considered a high alloy steel due to its high content of nickel (11.1%) and chromium (3.10%). Previous heat treatment, AerMet®100 is subjected to VIM/VAR processes like 300M in order to keep inclusions and impurities to a minimum concentration level. High alloyed high strength steels can receive a variety of heat treatments including intercritical annealing, *L*, quenching, Q, and tempering, T, or a combination of them like QT, LQT or QTL.[28, 29, 31]

The conventional and recommended heat treatment cycle for AerMet®100 steel involves austenitising at approximately 843°C and quenching in oil to room temperature, following by immediate transference to a cryogenic bath held at -73°C for 1 hour to transform retained austenite, and finally tempered at 485°C for 5 hours.[19]

Although martensite formation depends on the carbon content as is shown in **Figure 7**, it has been reported that by adding manganese and nickel to iron carbon alloys, Winchell *et al*. depressed the M_s temperature to -35°C, promoting the formation of a mixed and plate martensite morphology at temperatures below 25°C. By the use of this method the amount of martensite is increased by transforming the otherwise untransformed austenite.[23, 39]

AerMet®100 final microstructure after this heat treatment consists in a lath martensitic matrix with secondary hardening M_2C carbides and a thin film of *reverted* austenite precipitated at the plates or laths boundaries, which forms during tempering.[40, 41]

It has been proposed that reversion in AerMet®100 takes place because tempering at 482°C is close to the A_{c1} temperature (two phase region: $\alpha + \gamma \rightarrow \alpha$) which is approximately 485°C.[41] Morris *et al*. has referred this treatment as intercritical tempering which involved the precipitation of thin film austenite (γ) along lath boundaries while the residual fresh martensite (α') loses solute and tempers to form tempered martensite (α_t). The reaction involved is: $\alpha' \rightarrow \gamma + \alpha_t$.[28, 29]

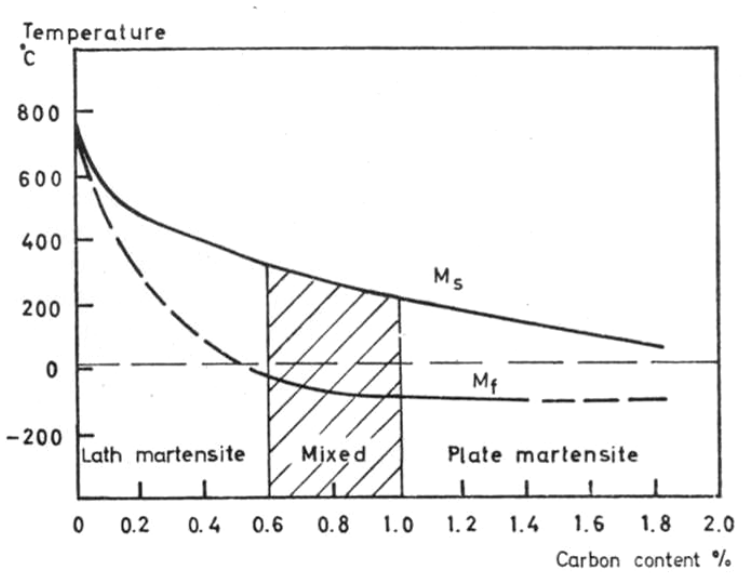

Figure 7. Influence of the austenitic carbon content on the M_s and M_f temperatures and the type of martensite formed in unalloyed steel.[39]

H. Smith *et al*.[42] showed for certain stainless steels that regions of reverted austenite contained a high density of tangled dislocations, numerous small twins and stacking faults. Therefore, increases in strength of austenite achieved by reversion are associated with the high dislocation density of the reverted regions. Moreover, similar observations have been made for reverted austenite transformations on 18Ni(350) maraging steels and Fe-24Mn as well as Fe-24Mn-6Si alloys.[43, 44]

Secondary hardening precipitates in high alloyed steels that are capable of high coherency with the matrix are MC (M= Nb, Ta, Ti and V) and M_2C (M= Fe, Cr, Mo and W) carbides. In contrast, less coherent but more stable carbides such as M_6C, M_7C_3 and $M_{23}C_6$ precipitate in coarse form with less strength.

C. H. Yoo *et al*.[40] as well as R. Ayer *et al.*[42] had shown that after tempering AerMet®100 at 482°C, M_2C carbides were needle-shaped and some still kept coherency with the matrix. The carbides average length and diameters were reported between 4 to 8 and 1.5 to 2.5 nm, respectively.

1.3. Precipitation and Transformation Hardening Stainless Steels

Precipitation hardened stainless steels are low carbon steels containing Cr and Ni together with some substitutional elements such as Mo, Co, Ti and Al. This group of steels differs from the martensitic stainless steel grades in the copper and aluminium additions to promote age hardening. Generally the high strength and good toughness is achieved by the dispersion of fine intermetallic precipitates in a martensitic matrix.[45] Heat treatments are designed to temper the martensite and several of these steels are hardened further by the precipitation of copper, aluminium or titanium, depending on composition.[31]

In this category is found CSS-42L™ stainless steel, which is a highly alloyed 14%Wt. chromium steel with austenite stabilizing elements such

as nickel and cobalt as well as carbide forming elements like Mo, Cr, V, and Nb. Additions of nickel in this alloy increases fracture toughness but decreases the M_s temperature and may suppress martensite formation. Conversely, addition of cobalt raises the M_s temperature thereby inhibiting the presence of retained austenite, which is detrimental for optimum mechanical properties.[26, 46]

The hardening cycle for VIM/VAR CSS-42L™ steels initially consists of austenitising at 1093°C following by oil quenching to room temperature and subsequent subzero cooling at -79°C to diminish retained austenite in the final microstructure. Thereafter, two tempering cycles at 496°C separated by a cryogenic bath for 1 hour are performed. [22, 26] It is known that in high alloyed chrome steels the retained austenite is transformed to martensite on cooling from a tempering temperature around 500°C, and such steels have to be re-tempered to produce further toughness of the newly formed martensite.[39]

Although this alloy can be additionally case carburized by either gas or vacuum carburizing techniques to improve fatigue resistance, these conditions were not considered in this research programme. The resulting microstructure displays a martensitic matrix with secondary hardening precipitation of alloys carbides containing V, Mo, Cr and Nb. While chromium carbides tend to precipitate at the grain boundaries, the formation of dispersed niobium carbides is the preferred structure to achieve best mechanical properties.[26, 46]

Likewise, precipitation hardening carbides such as $(Cr, Mo)_{23}C_6$ and $(Cr, Mo)_2C$ have been found within the martensitic matrix of 13Cr-8Ni-2.5Mo-2Al precipitation-hardened stainless steels.[45] Nonetheless, favourable thermodynamic stability of carbides like (Nb, V)C and $(Nb, V)_xC_y$, not only with respect to cementite but also to the several chromium and molybdenum carbides, compels their formation.[23]

2. General Aspects of Corrosion

Steel components can undergo corrosion during service particularly when they are directly exposed to marine conditions. This phenomenon is an electrochemical process that involves electron transfer through the metal from the oxidised species in the anodic region to the reduced species in the solution at the cathodic region.[6,10]

For iron or steel corroding in aqueous solutions at room temperature at least two reactions must take place. The first reaction (reaction 1) is anodic and is associated with the production of metal ions in solution with a net positive charge, as is depicted in **Figure 8**. This reaction is known as oxidation and generates electrons. Simultaneously, a second reaction takes place at the cathodic region which involves a reduction of the species gaining the electrons from the oxidation process.[6,10]

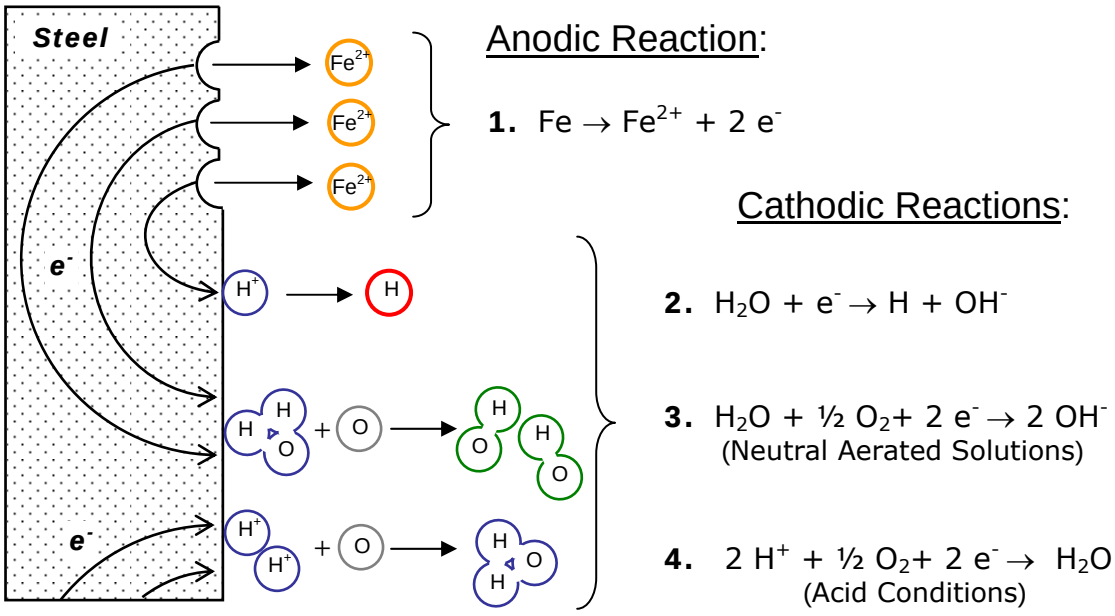

Figure 8. Electrochemical cell between anodic and cathodic regions on the steel surface undergoing corrosion.

There are two possible cathodic reactions, hydrogen evolution and the reduction of dissolved oxygen gas (in neutral or alkaline solutions) depending on the reducible species present in the electrolyte (reactions 2

and 3). However, in acid conditions the oxygen reduction could involve a third reduction reaction, (reaction 4), graphically depicted in **Figure 8**.

The thermodynamic tendency for these electrochemical reactions depends upon changes in the Gibbs free energy, ΔG, which can be associated to the electromotive force, ΔE, of the corrosion cell as follows:

$$\Delta G = -n\,F\,\Delta E \qquad [I]$$

In equation [I], *n* represents the numbers of electrons involved in the reaction and *F* is the Faraday constant. For $\Delta G<0$ the electrochemical reaction will spontaneously take place, whereas for $\Delta G>0$, the reaction will occurs in the opposite direction and the equilibrium condition is reached when the $\Delta G=0$.

To determine the standard electromotive force, ΔE, of an electrochemical system where the activities of the species are not equal to one, the *Nernst* equation is use:

$$E_{redox} = E_o + \frac{2.3\,RT}{nF} Log\,\frac{a}{b} \qquad [II]$$

Where E_o is the standard electrode potential that is calculated when the activities of the species involved are equal to unity; *a* and *b* represent the activity of products and reactants, respectively; *R* is the gas constant and *T* the temperature (K). The equilibrium potentials of the two cathodic reactions, hydrogen evolution and oxygen reduction, can be graphically represented as a function of *pH* ($-Log_{10}[H^+]$) by using the *Nernst* equation. This potential-*pH* graphs are known as *Pourbaix* diagrams.[6, 10, 47, 48]

For iron and steels in water at 25 °C the Pourbaix diagram is shown in **Figure 9**. The oxygen reduction and hydrogen evolution equilibrium reactions are represented by the dotted lines A and B, respectively. Therefore, the water stability region lies between the two lines.

Similarly, stability regions for different iron compounds are depicted in the same figure. In general, regions where corrosion is favoured are shown as dotted filled areas while the rest represent immunity or passivity conditions. Steel undergoing free corrosion due to direct exposure to marine atmosphere could be represented by the point (X) in the Pourbaix diagram below. This particular condition corresponds to the steel directly exposed to 1g/l NaCl solutions at a *pH* value of 6.9 and a potential of *E*~-0.445 (SHE).[47, 48] Nevertheless, *pH* values as well as NaCl concentrations can vary depending on environmental conditions.

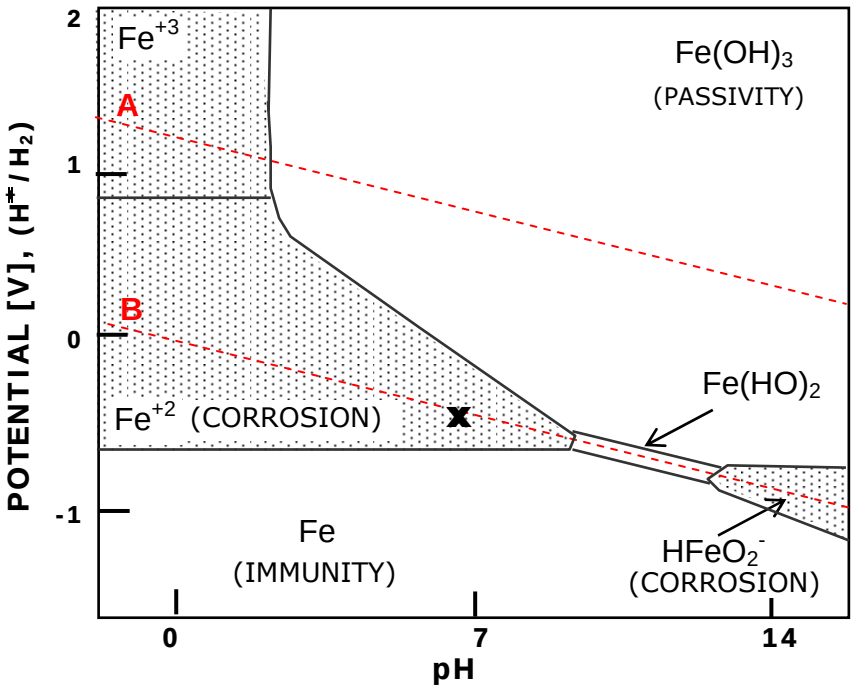

Figure 9. Simplified potential-*pH* diagram for the Fe-H_2O system.[46, 47]

In addition to the thermodynamic information given by the potential-*pH* diagrams, the kinetic information regarding corrosion reactions involved in the system is given by the *Evans* diagrams. This polarization curves shows changes in the electrode potential when the electric charge passes through the steel or working electrode. The typical polarization diagram for the corrosion of a metal in a reducing acid solution is illustrated in **Figure 10**.

The overall corrosion reaction converges where the cathodic hydrogen evolution and the anodic metal dissolution reactions intersect. This point is defined by the corrosion potential, $E_{corr,}$ and the corrosion current, I_{corr}. The electron flux between the anodic and the cathodic areas quantifies the rates of the oxidation and reduction reactions. Weight loss measurements and corrosion rates can be easily obtained if the corrosion current density, I_{corr}, is known. The corrosion rate displays units in *mpy* (mils per year) or *mdd* (milligrams per square decimetre per day) and can be established using the following equation:

$$CR = \frac{I_{corr}\, M\, t}{F\, z\, \rho} \qquad \text{[III]}$$

Where M is the atomic mass (gr/mol), t corresponds to the time (31536 x10^6 seconds/year), z is the number of electrons in oxidation reaction, F the Faraday constant, and ρ density (gr/cm^3).

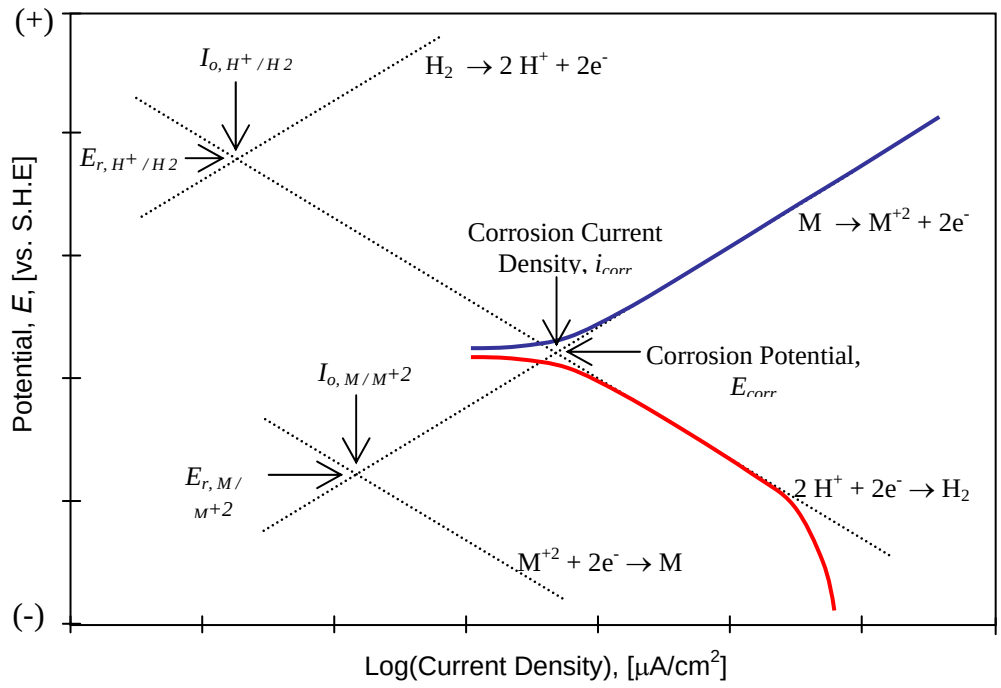

Figure 10. Polarization curve, (Potential, *E* vs. *Log(Current Density)*), for the corrosion of a metal in a reducing acid solution.[6]

In an illustrative comparison, Lee *et. al*.[49] have shown that the immersion corrosion rate for AerMet®100 in 3.5% NaCl solution was between 33-40% slower than that for 300M high strength steel, as is shown in **Figure 11**.

This results indicated that the AerMet®100 has relatively better resistance to immersion corrosion that 300M steel. These corrosion rates decreased with exposure time for both alloys.

Furthermore, salt spray corrosion rate of the AerMet ®100 has been shown to be 13-20% of that for 300M steel and like immersion corrosion tests, the corrosion rate decreases with time for both steels. AerMet®100 steel is not affected in humidity chamber (100% relative humidity at 120 °F) for 110 days of testing, whereas 300M is susceptible to corrosion with a rate of approximately 2.041 *mpy* (mils per year) or 0.045 *mdd* (milligrams per square decimetre per day).[49]

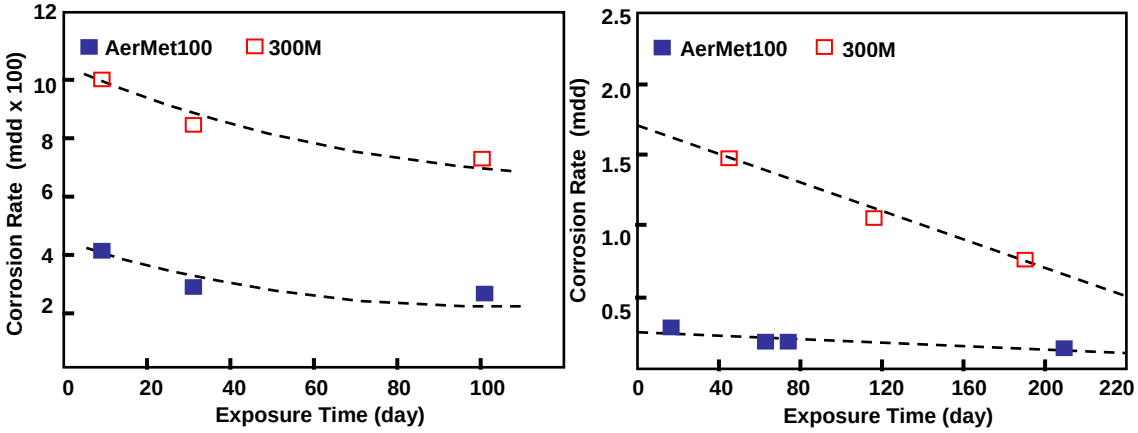

Figure 11. A) Immersion and B) Salt spray corrosion rates for AerMet®100 and 300M steels in terms of weight reduction in milligrams per square decimetre per day, *mdd*.[49]

Similar studies have been reported for carburised CSS-42L™ stainless steel and a similar precipitation hardening stainless high strength steel known as 440C. The potentiodynamic curve shown in **Figure 12** was produced following standard practice for calculation of corrosion rates and related information from electrochemical measurements (ASTM-G102).[22]

It can be seen that the passive current of the CSS-42L™ case is higher than the 440C steel, whereas the core current density was significantly lower. The performance of the core of carburised CSS-42L™ stainless steel might be similar to that of the studied condition in the present project.

This observation revealed that the corrosion rate for the case is slightly higher than 400C, whereas the core corrosion rate was significantly higher than the 440C steel.[22]

Moreover, additional research has concluded that CSS-42L™ was more susceptible to corrosion problems than similar precipitate hardening stainless steels like Cronidur-30 and XD15NW used for aerospace bearing applications.[50]

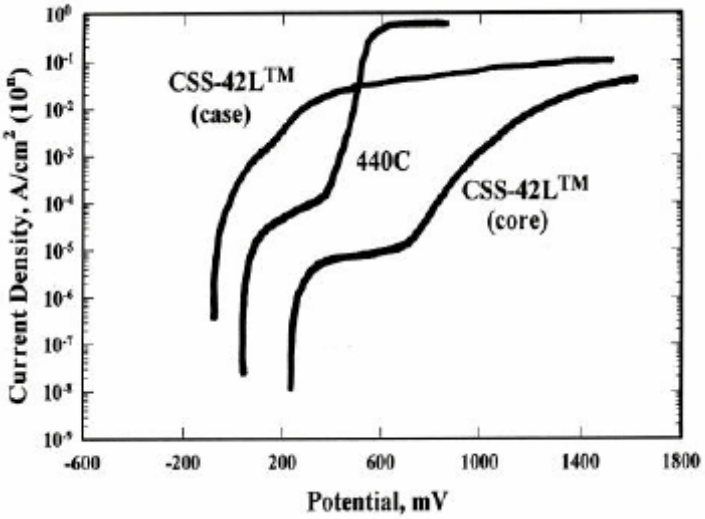

Figure 12. Current density – Potential curves for CSS-42L™ case and core and 440C steels in 3.5% NaCl solution using Ag/AgCl Reference Electrode.[22]

2.1. Marine Atmosphere Conditions

Sea water is approximately 3.5%Wt of sodium chloride with additions of magnesium, calcium, potassium, sulphate and bicarbonate ions. Oxygen concentrations are close to equilibrium with the atmosphere and *pH* values between 8 and 8.3. Hence, sea water can cause more corrosion problems for iron and steel than fresh water due to its higher electrical conductivity.[51]

Additional sources of water to sustain electrochemical corrosion include precipitation, wind or wave driven spray and atmospheric humidity, particularly in marine locations. Corrosion of structural components due to direct exposure to humidity and marine conditions produce continuous

accumulation of salts scales on the structure. Corrosion from intermittent wetting from rain, snow and condensation and its subsequent drying depends on a variety of factors such as temperature, humidity, wind speed, sunlight and in general climate conditions. Similarly, the presence of pollutants like certain ionic salts and sulphur dioxide might accelerate the formation of rust on steel structures if the relative humidity exceeds a threshold value of 70% approximately.[51]

2.2. Corrosion Control

The corrosion of steel components in service can be controlled by reducing the anodic dissolution of iron, previously referred as *reaction 1*. Galvanic coupling the steel to a more active metal in the galvanic series produces a reduction of the steel corrosion current, I_{Fe}, and therefore reduces its dissolution process. This phenomenon is commonly described by the mixed potential theory, which allows predicting the corrosion rate of the coupling system.[6, 10, 11]

Considering two metals with similar areas, the galvanic corrosion rate is determined through the polarization diagrams as is shown in **Figure 13**. The more active metal originally with more negative potential, E_{Anode}, corrodes at a higher rate, $I_{CoupledAnode}$, than its original condition, I_{Anode}. Simultaneously, the current density and corrosion rate of the steel component decreased from its original value, I_{Fe}, to $I_{CoupledFe}$.

This reduction in iron corrosion rates is known as cathodic protection, as the steel becomes cathodically protected while the more active metal undergoes preferential anodic dissolution. Finally, the resultant mixed potential, E_{Couple}, is the interception where the total oxidation and reduction rates are equal.[6, 10, 11]

By means of the previous analysis, metallic sacrificial coatings on structural steel components are the common corrosion protection system used in the aerospace industry. Although cathodic protection of steels also can be performed with separate sacrificial anodes or by making the

structures electrically negative using power impressed current, these two methods are irrelevant to the purpose of the present project.

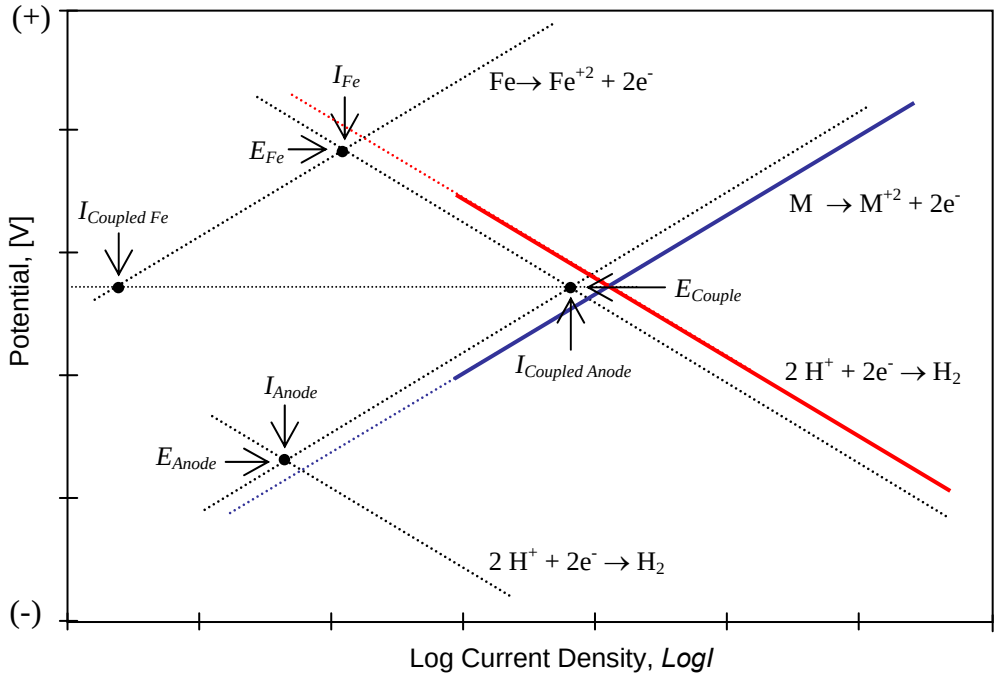

Figure 13. Polarization diagram for iron galvanically coupled to a sacrificial metal or alloy.[11]

2.3. Sacrificial Coatings in the Aerospace Industry

Based on the mixed potential theory, metals and alloys more electronegative or active than the steel, with -0.60 to -0.72 Volts SCE in the galvanic series, will corrode in preference. Cadmium, aluminium and zinc are some of these sacrificial metals, as is shown in **Figure 14**.

Galvanic potentials for cadmium and aluminium alloys coatings are -0.70 and -0.70 to -0.85 Volts (SCE), respectively. Both coating systems are galvanically compatible while remaining sacrificial to steel and stainless steel components. Although zinc coating displays a more electronegative potential of -1.0 Volts (SCE) approximately, it is considered to belong to the same galvanic compatibility group as aluminium and cadmium. Moreover, it has been possible to enhance its protective performance by alloying zinc coatings with more noble metals like nickel.[10-12 ,15, 51]

The galvanic compatibility of these metals and alloys indicate for example that cadmium-plated, zinc-plated as well as aluminium-plated components like fasteners are suitable to use in aerospace structures in contact with aluminium alloys, but some stainless steel parts could promote corrosion of adjacent aluminium parts. Nevertheless, the predictability of the performance for compatibility groups is sometimes inaccurate due to different factors such as cathode/anode area ratio, electrolyte conductivity and passivation phenomenon.[51]

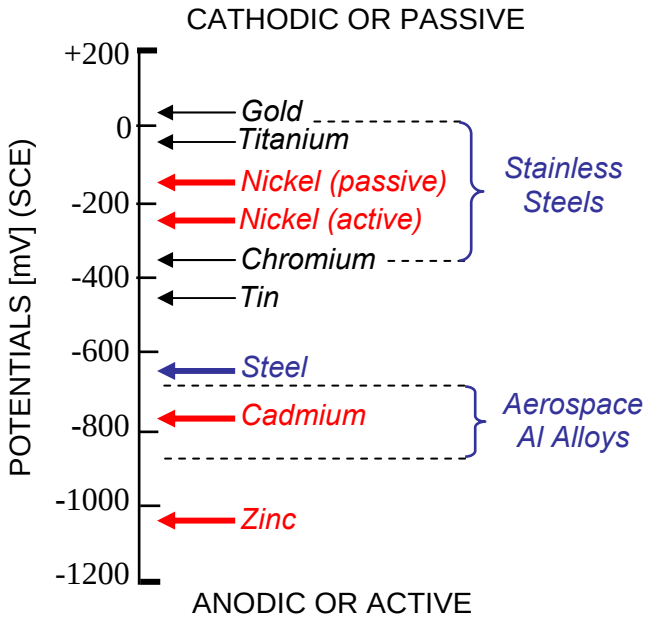

Figure 14.Galvanic series in sea water, modified from L.L. Sherir.[11]

In addition to the sacrificial behaviour of these metallic coatings a barrier mechanism can also provide further protection to the steel substrate in some coating systems. In this particular situation, the coating also isolates the substrate from the corrosive environment. However, this is only effective as long as the coating remains continuous.[10] Conversely, the presence of flaws or discontinuities in the coating lead to the formation of localised galvanic cells where atomic hydrogen might evolve and diffuse into the substrate.

2.3.1. Steel Surface Preparation

Cleaning and surface preparation of steel components is performed before electroplating or deposition of sacrificial coatings in order to achieve a good physical or chemical bond between the coating and adjacent steel substrate. It has been considered that the main factor that governs the durability of the coating is the adhesion. If the coating or the substrate are directly exposed to corrosive environments, any tendency for the coating to peel from the substrate might be aggravated.[11, 51, 52]

Manual methods such as shot peening and grit blasting are commonly applied to remove scale and roughen the steel surface providing better mechanical adhesion. In addition, oxide scales on hot rolled steel components are commonly removed by acid pickling in sulphuric acid. Scale formed below 575°C has an inner layer of magnetite, Fe_3O_4, adjacent to the steel covered by a layer of hematite, Fe_2O_3. The dissolution of the inner magnetite layer (reaction 5) takes place when the acid penetrates through-thickness cracks in the scale.[11, 51, 52]

$$Fe_3O_4 + 2\ e^{-2} + 8\ H^{+} \rightarrow 3\ Fe^{+2} + 4\ H_2O \qquad (5)$$

On the other hand, scales formed at temperatures above 575°C comprise a third oxide layer of wustite, FeO, between the magnetite and the steel. This layer is rapidly decomposed when the acid penetrates due to localised galvanic cells between fine anodic iron particles and the magnetite layer. Following this reaction, the release of the insoluble magnetite and hematite layer takes place. [11, 51, 52]

Steel components are commonly immersed in 0.1-0.5 M sulphuric acid at 60 to 80°C, with additions of organic inhibitors to avoid dissolution of the de-scaled metal. Nonetheless, the main drawback of the pickling process is the evolution of hydrogen on the de-scaled metal. Part of this hydrogen diffuses into the substrate producing embrittlement of the steel component. But high strength steel components for aerospace applications are not acid cleaned.

2.3.2. Cadmium Coatings

Cadmium sacrificial coatings are deposited by electroplating processes commonly from cyanide solutions. Although acid baths of sulphate or fluoborate can be also used, such conditions usually produce coarsely crystalline coatings unless effective additional agents are used. It has been widely discussed whether in the cadmium bath the main complex cyanide is $NaCd(CN)_3$ or $Na_2Cd(CN)_4$. Recent researches have confirmed the presence of the second compound in the electroplating bath.[53-56] Assuming this situation in the electroplating bath, the complex cyanide compound is produced as the following equation shows:

$$CdO + 4\ NaCN + H_2O \rightarrow\ Na_2Cd(CN)_4 + 2\ NaOH \qquad (6)$$

In addition, the possible cathodic reaction depositing cadmium could be represented as:

$$[Cd(CN)_4]^{-2} + 2\ e^- \rightarrow Cd + 4\ CN^- \qquad (7)$$

The potential of deposition for cadmium, $E_{\phi,Cd}$, in some cyanide solutions is close to the potential of hydrogen evolution reaction (Reaction 8), which could be between $-0.29 < E_{\phi,H} < -0.59$ Volts, in acid and alkaline conditions, respectively. Hence, the deposition of cadmium also involves the hydrogen evolution reaction:[53, 56]

$$2\ H^+ + 2\ e^- \rightarrow H_2 \qquad (8)$$

Two main problems are produced following the hydrogen evolution reaction: A) nucleation of pits at the cathode and B) hydrogen embrittlement produced when a small proportion of atomic hydrogen diffuses in the substrate. Both problems can be overcome by additions of wetting agents and secondly by baking the electroplated cadmium components at 200°C for 24 to 48 hours. This process allows hydrogen to diffuse from the steel after the electroplating.[53, 56] Alternatively, the hydrogen evolution reaction can be suppressed by either altering bath conditions and composition. For example, hydrogen embrittlement has

been reduced by enhancing the current efficiency through higher plating rates due to the high solubility of cadmium in fluoboric acid baths.[55]

Cadmium itself is highly toxic and can produce serious effects on living organisms, similar to those caused by arsenic and mercury. There has been a tendency worldwide to minimise the use of cadmium compounds for engineering applications. Furthermore, continuous efforts have been made to replace this material particularly in the aerospace applications. [12-16, 18, 54, 56]

2.3.3. Zinc-14%Nickel Based Coatings

Pure zinc coatings have been widely used for corrosion protection of steel. However, its high corrosion rates in marine conditions (2 to 5 μm/year) due to its very active potential, compared to cadmium (1 to 3 μm/year),[11] together with the tendency to form voluminous corrosion products are the main drawbacks for aerospace applications.

Nonetheless, significant progress has been made to produce less active zinc-based coatings with increased corrosion resistance. Zinc can be alloyed with more noble iron-group metals (i.e. iron, cobalt and nickel) by electroplating from different solutions. For the Zn-Ni system, previous studies have shown that its corrosion resistance increases as the nickel content raises to approximately 14 wt %, where the optimum corrosion resistance is achieved.[12, 15]

According to Zn-Ni phase diagram in **Figure 15**, deposits with up to 86wt.% zinc should consist of (γ) phase with an orthorhombic structure.[57] Generally, electrodeposited zinc-nickel alloys containing approximately 10-16 wt. % nickel are known to exhibit mainly the γ phase, whereas those containing higher or lower nickel levels shows binary or multiphase characteristics.[58] Co-deposition of zinc-14%nickel alloys can be performed from zinc and nickel cyanides,[56, 58] sulphates,[12, 15, 60] sulphate-acetates[61] or chlorides based electrolyte solutions.[59, 62, 63]

Moreover, comparisons of electrolyte baths for different industrial processes have been previously carried out.[64]

Z. Wu *et. al*,[59] showed that when the ratio Ni^{2+}/Zn^{2+} was maintained between 0.5 and 1 in chloride baths, deposits with 10-15% nickel content were readily obtained. Further X-rays diffraction studies confirmed that the alloy consisted of either the (γ) phase (Ni_5Zn_{21}) or a mixture of the two phases Ni_5Zn_{21} and Ni_3Zn_{22} (δ).

Similarly to cadmium electroplating, co-deposition of Zinc-14%Nickel sacrificial coating on steel substrates produce some level of hydrogen embrittlement mostly depending upon electrolyte and baths conditions. Lower hydrogen uptake of some zinc-nickel coatings relatively to cadmium electroplating, has been associated with the low hydrogen diffusivity in nickel, zinc and zinc hydroxide phases during electroplating.[65, 66]

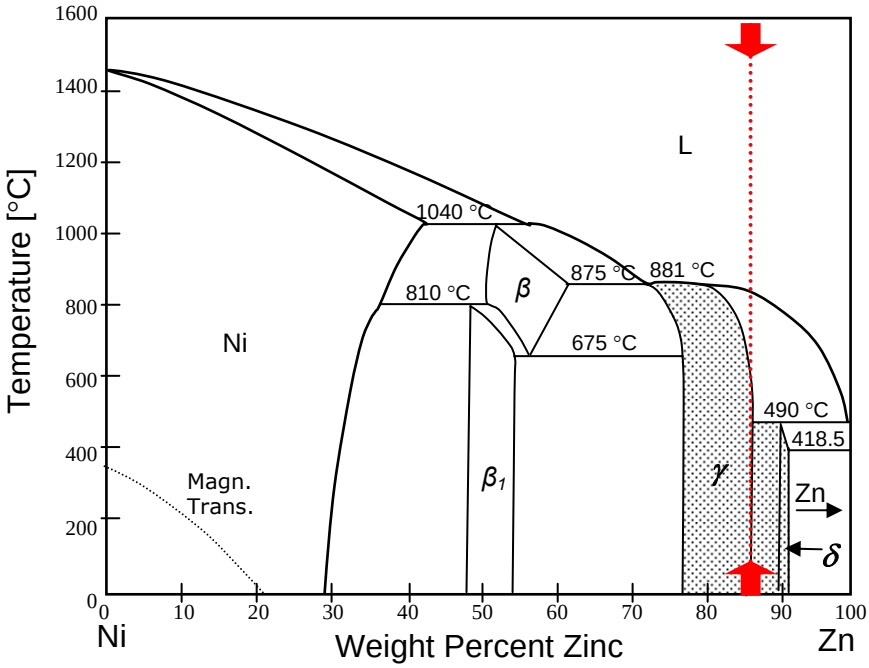

Figure 15. Zinc-Nickel Phase Diagram.(Arrow represents approximately 14 wt%Ni).[57]

E. M. K. Hiller *et al*.[66] showed that the electroplating of zinc-10%nickel coatings produce a relatively low embrittlement of AISI-4340 high strength steels. But regardless of the plating conditions, damage caused

by hydrogen uptake during electroplating of zinc-nickel still has to be eliminated by baking the steel components at 200°C for 24 hours.

2.3.4. Chromium Conversion Coatings

The term '*conversion coatings*' is associated with the formation of thin oxides or hydroxide coatings following the reaction of the metal substrate.[51, 55] They are normally applied to zinc and cadmium sacrificial coatings to retard the formation of white corrosion products following exposure to saline atmospheres. The protective action of the chromate film is due both to its barrier effect and the inhibiting action of chromium and its compounds with respect to the dissolution of the metal substrate by the reduction of oxygen at its surface. Moreover, chromate ions when used as inhibitors in aqueous solutions, passivate the substrate by forming a coherent oxide film on the coating surface.[51, 56, 60]

Heydarzadeh *et al*,[60] has compared the corrosion resistance of chromated zinc-nickel coatings to zinc-nickel deposits without chromating using neutral salt spray test (5% NaCl, temperature 35°C). **Figure 16** shows that chromate conversion treatments improve the corrosion resistance significantly and the best protection is achieved by a nickel content of approximately 14 wt%. In this particularly case, white rust represents zinc corrosion products whereas the red rust corresponds to steel corrosion.[60]

Chromate passivation films also improve the adhesion of paints including epoxy and polyurethane or acrylic top-coats. Nevertheless, these protective properties depend upon thickness and methods of drying the chromate layer. Normally these films are applied by dipping in acid solutions which contain hexavalent chromium salts or dissolved chromium in the form of sodium dichromate, $Na_2Cr_2O_7$.

The composition of the coating is particularly complex and vary for different metal substrates, but the predominantly active species is a slightly soluble hydrate chromium, $Cr_2^{III}(Cr^{VI}O_4)_3$, which is the source of the oxidizing anion $Cr^{VI}O_4^{-2}$.[10, 51]

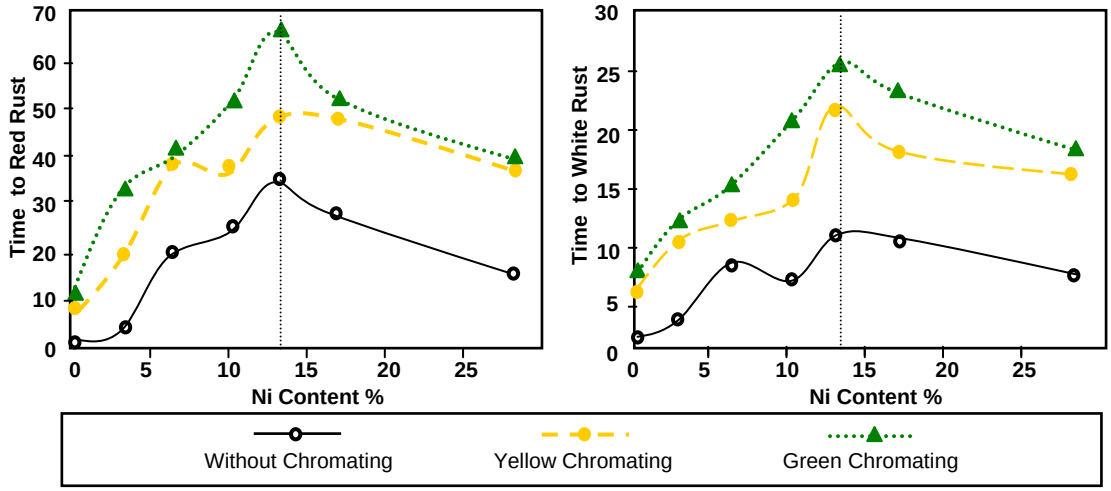

Figure 16. The appearance of white and red rust for chromated and non-chromated Zn-Ni coatings, modified from M. Heydarzadeh *et al*.[60]

Appearance and hardness of these films depends on bath compositions, temperature, *pH* and duration of the treatment. Finishing are divided by British Standards[67] in two main classes, each of which comprise two groups of films depending on the appearance and the total mass deposited per unit area, as is listed in **Table 1**.

Class	Designation*	Type	Appearance	Coating mass per unit area [g/m^2]
1	A	- Clear	-Transparent clear, with bluish tinge	≤ 0.5
	B	- Bleached	-Transparent with slight iridescence	≤ 1.0
2	C	- Iridescent	-Yellow Iridescent	0.5 -1.5
	D	- Opaque	-Olive green, shading to brown or bronze	>1.5

* In addition, black coatings can be produced by several methods. Such coatings may have different degrees of corrosion protection and may also differ in coating mass per unit area.[67]

Table 1. Classification of chromate conversion layers on zinc and cadmium sacrificial coatings.[67]

Following immersion in the electrolyte solutions, drying of the specimens is carried out at a temperature not exceeding 60°C to prevent cracking due to dehydration of the chromate coating. Any heat treatment or baking for the relief of hydrogen embrittlement is carried out before the chromate conversion layer is deposited.[67]

2.3.5. Aluminium Based Coatings

Metals like aluminium and magnesium cannot be electroplated from aqueous solutions since their deposition potentials, $E_{\phi,Al}$ ~ -1.66 Volts, are significantly more negative than that for hydrogen, $E_{\phi,H}$. Hence, the cathode cannot be polarised sufficiently to reach the potentials needed for metal deposition.[51] Primary aluminium is produced by electrolysis of fused salts, Na_3AlF_6, and dissolved alumina, Al_2O_3. However, this process is carried out at temperatures above 660°C, which are too high for deposition on steels. Nevertheless, it has been shown that aluminium can be electroplated in laboratory conditions from aluminium borides, $AlBr_3$, and aluminium chlorides, $AlCl_3$, in complex organic solvents like C_2H_5Br and *n*-butylamine, respectively.[11, 53]

Alternative techniques to deposit aluminium include spraying, hot dipping, vapour deposition, chemical deposition, cementation and mechanical bonding. Sprayed coatings commonly consist on small flattened globules of metal surrounded by a binding material that forms 1 to 3% of the coating.[11] SermeTel®1140/962 is a ceramic-aluminium sprayed coating which consists of densely packed aluminium particles in a chromate/phosphate binder together with an epoxy-polyamide urethane topcoat paint system, commercially known as SermeTel-1140. This coating has been designed to provide sacrificial corrosion protection and extended erosion protection for all ferrous alloys.[17, 68]

The dense packing characteristic of the aluminium pigment particles reduces the porosity, allowing the deposition of thin coatings with relatively good corrosion resistance. SermeTel®1140/962 coatings are sprayed on as slurry to produce thickness ranging between 400 to 500 μm, with curing temperatures between 232 and 343°C. In addition, the fluorocarbon modified silicon top-coating is thermally cured at 175°C. Therefore, it is suitable for use on alloys such as 300M and components that can tolerate 274°C cure temperatures.[17, 68, 69]

These coatings have been shown to be less anodic than pure zinc, but they are active enough to cathodically protect low alloy and stainless steels fasteners in saline environments. Moreover, this coating system has been used in aerospace applications varying from landing gear bodies for military aircrafts to axels for commercial aviation.[68]

It has been reported that the deposition of SermeTel®CR962, without the topcoat polymer system SermeTel®1140, on AISI-4340 high strength steels do not produce direct hydrogen embrittlement as a result of the application process.[68, 69] However, the corrosion of similar coatings like SermeTel®CR984-LT, have been shown to produced substantial amounts of hydrogen re-embrittlement of this steel when is exposed to marine-like conditions.[18]

3. Hydrogen Embrittlement

Hydrogen embrittlement can be defined as the *loss of ductility* or *delayed fracture* caused by absorbed hydrogen within the material during the application of load. In this process, the material manifests a non-ductile fracture mode or loss of ductility sometimes together with a reduction of tensile strength due to the hydrogen locked into its microstructure. The susceptibility of steels to hydrogen embrittlement usually increases as the tensile strength increases. Therefore, high strength steel components are particularly susceptible to this phenomenon by failing prematurely and abruptly with serious consequences.[6, 70, 71]

Before hydrogen can produce any embrittlement to the steel, it has to be located within the vicinity of the surface, then to be absorbed and finally transported to the the bulk of the alloy. This evolution and entry of hydrogen into the metal is the preliminary stage of the hydrogen embrittlement process.

3.1. Hydrogen Evolution and Entry into the Metal

The evolution of atomic hydrogen, previously described in *reaction 2*, is accomplished following consecutive steps depicted in **Figure 17**. McCright *et al*,[72] proposed the following sequence for the hydrogen evolution reaction, *HER*: 1) Transport of the hydrated proton (H_3O^+) to the electrical double layer that exists at the iron-electrolyte interface, 2) loss of water of hydration shield in the vicinity of the double layer, 3) adsorption of the proton to the electrode surface, 4) discharge of the proton to an adsorbed hydrogen atom.

The following step, 5) include a possible formation of molecular hydrogen by chemical combination of adjacent atoms and/or and adsorbed hydrogen atom can combine with a proton forming a hydrogen molecule. Afterwards, steps 6 and 7 involve either desorption of hydrogen molecule, which will evolved as hydrogen bubbles, *HER*, or absortion of atomic hydrogen, *HAR*, and subsequent diffusion into the metal bulk. Step 5,

which involves discharge followed by chemical or electrochemical combination, is considered the most important for *HER* and could be either rate-determine step or may proceed in as coupled discharge-recombination reactions.[72]

Only a fraction of the evolved hydrogen actually diffuses into the lattice to remain in the bulk of the alloy as is shown in step 7. Taking this observation into account, it is crucial to determine the amount of hydrogen uptake by the steel that will produce embrittlement problems. In this field, many researchers have attempted to establish a correlation between hydrogen evolving from the surface and hydrogen uptake by iron membranes.[73, 74, 75]

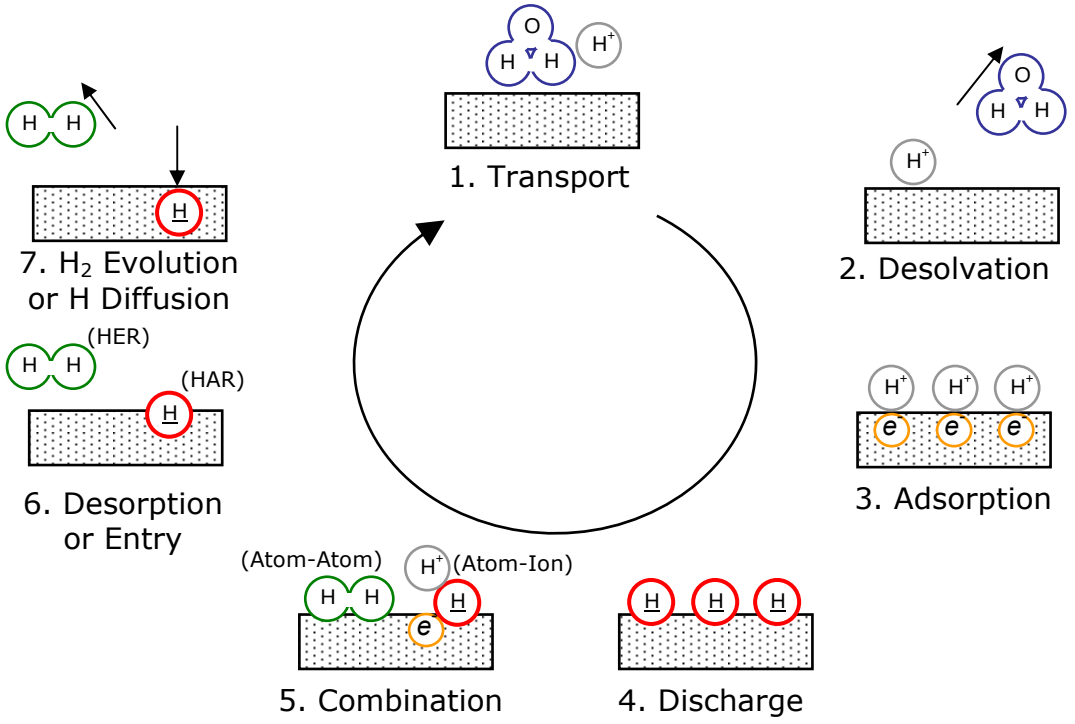

Figure 17. Mechanistic steps involved during the hydrogen evolution reaction.[72]

It has been shown that *HER* on α-iron occurs via coupled discharge-recombination reactions followed by a Tafel recombination mechanism at relatively low over-potentials, ($\eta = E_{applied} - E_{\phi}$), and low hydrogen surface

coverage, θ. This mechanism has been proposed to follow a reaction sequence at the cathode surface in the form:[73, 74, 75]

$$H_3O^+ + e + Fe \xrightarrow{K_I} FeH_{AD} \xleftrightarrow{K_{III}} FeH_{AB} \qquad \begin{matrix} \nearrow \xrightarrow{+\,FeH_{AD}} 2\,FeH_{AD} \xrightarrow{K_{II}} H_2 + 2\,Fe \\ \end{matrix} \qquad [9]$$

Where FeH_{AD} refers to adsorbed hydrogen on the metal surface, FeH_{AB} refers to absorbed hydrogen directly beneath the metal surface, k_I, k_{II} and k_{III} are the rate constants for the corresponding reactions.

This mechanism shows that after hydrogen is adsorbed on the metal surface, two possible reactions might take place. Firstly is the subsequent absorption of hydrogen below the metal surface which could be a reversible process. Secondly, the reaction with additional atomic adsorbed hydrogen to generates molecular hydrogen that escapes from the metal surface.[73, 74, 75]

3.2. Hydrogen Embrittlement Mechanisms

Hydrogen embrittlement or hydrogen related cracking phenomena depends upon different factors that include: environmental variables which define sources of hydrogen, temperature, load and strain rates, materials variables like microstructure and alloy content and finally the hydrogen embrittlement mechanisms itself.[76]

Several theories and mechanisms have been proposed to explain hydrogen embrittlement of steels. The mechanisms that have been postulated are the internal pressure theory,[77] reduction in the lattice cohesive force (de-cohesion mechanism),[78] reduction in surface energy (adsorption mechanism),[79] hydride induce cracking,[80] brittle crack tip[81] and localised slip model.[82] However, due to the complexity of the process and the variability of factors involved, it is a simplistic thought to assume that a single mechanism might define and describe the embrittlement

process for all conditions. On the contrary, there might be simultaneous mechanisms taking place for a specific alloy or material at determined environmental and operational conditions.

In general, on the basis of these theories two main effects of hydrogen can be identified: A) Hydrogen can decrease the strength of the metal-metal bond, facilitating brittle fracture (Both decohesion and the surface energy model are based on this premise), or B) Hydrogen can increase the stress required to emit dislocations from the crack tip, thereby making ductile fracture more difficult. A brief description of the aforementioned mechanisms is given in the following sections.

3.2.1. Internal Pressure Theory

The internal pressure theory is based on the approach that embrittlement of the steel is due to internal pressures generated by stabilised molecular hydrogen trapped within voids or defects such as interfaces, carbides and inclusions within the alloy.[77] However, the fact that low (sub-atmospheric) pressures of hydrogen gas can rapidly propagate cracks in high strength steels, suggest that the model proposed by Zapffe *et. al*[77] is not the essential mechanism for hydrogen embrittlement in these alloys.[83]

In addition, it has been observed that cracking of high strength steels can occur in dry molecular hydrogen at low pressures, leading to the conclusion that is not possible to produce high internal pressures in such conditions.[84] Nevertheless, pressure enhanced void growth can take place at high fugacity environments, demonstrated by blister formation in absence of external load on low strength AISI-1090 steels. Therefore, at low temperature, a dislocation-enhanced large super-saturation in voids is possible.[85, 86]

3.2.2. Lattice Decohesion

First proposed by Troiano *et al*,[78] this model suggested that interstitial elements diffuse to regions of large triaxial stresses ahead the crack (approximately 1-2 times the diameter of the crack tip), leading to large solute concentrations, as is depicted in **Figure 18.A**. Thereafter, once the hydrogen concentration critical value is reached, the reduction of the cohesive strength results in a brittle crack nucleation (**Figure 18.B**), which rejoins the crack front continuing out the region of hydrogen accumulation and becoming arrested by plastic deformation (**Figure 18.C**). This process is considered to be repetitive, producing a discontinuous propagation.

Troiano *et al*[78] proposed that electrons from hydrogen atoms enter the d-band (conduction band) of iron, and the increased electron density raises the inter-atomic spacing and reduces the cohesive strength. This model requires a stress concentration, approximately three times the yield strength, ahead of the crack tip to produce accumulation of hydrogen.

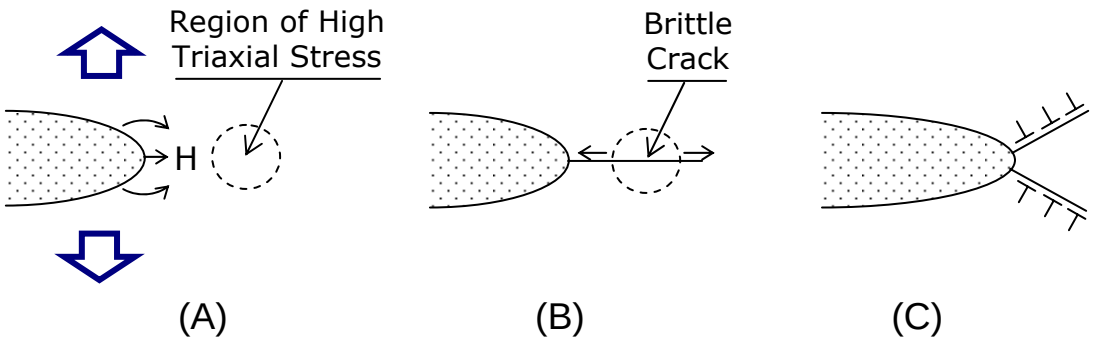

Figure 18. Schematic illustration of the decohesion model for hydrogen embrittlement proposed by Troiano.[78]

Nevertheless, Oriani *et al*.[83] suggested that this stress value was not sufficient to promote hydrogen concentrations levels for embrittlement. He pointed out that the amount of elastic stress necessary to produce sufficient hydrogen concentrations at the crack nucleation sites could be

as large as E/10. This statement was later disputed by Pugh *et al*.[87] for ductile materials, where these stress levels are suppressed by plastic flow.

In this model the local stress balances the maximum cohesive force per unit area of the crack tip and therefore the crack will propagate in a brittle mode. **Figure 19.A** shows this process in an atomic level, where stretched bonds in the linear stress-strain region are represented by straight lines, whereas, stretched bonds in the non-linear regions corresponded to zigzag lines.

Oriani's model was based in two primary assumptions: 1) The rapid increase in hydrogen concentration as the elastic strain rate raises, leading to a maximum value, (**Figure 19.B**); and 2) that large concentrations of dissolved hydrogen reduce the bonding or cohesive force, F_z, between iron atoms in the lattice, as is depicted in (**Figure 19.C**). This model differed from Troiano's proposal with respect to both the sites of embrittlement and the crack propagation. Hydrogen accumulation will rather take place at 'few atomic distances' from the crack tip and the crack propagation is continuous, at a rate determined by hydrogen transport and accumulation.

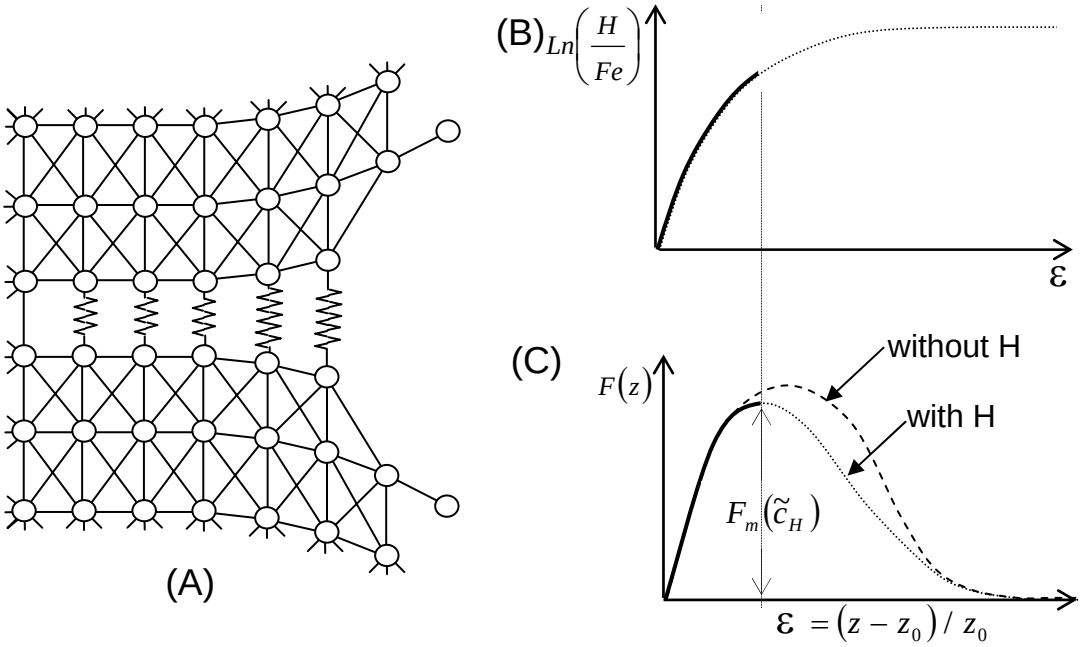

Figure 19. A) Atomic model of the crack edge and the relationship between strain and B) hydrogen concentration, and C) cohesive force.[83]

3.2.3. Surface Energy / Adsorption Model

A second model which is based on the hypothesis that hydrogen reduces the cohesive strength of iron atoms is the surface energy model. This model, initially proposed by Petch *et al*,[79] suggest that the surface energy, γ_s, of the metal is thermodynamically decreased by the adsorption of hydrogen on the surface of the crack tip, leading to a reduction in the energy required to produce brittle fracture. It involves a reduction in bond strength due to the absorption of hydrogen and its interactions with strained bonds at the crack tip, as **Figure 20** depicts.[87]

It basically differs from the decohesion model on the site where embrittlement occurs. In this case, hydrogen will be preferentially adsorbed on the surface itself rather than at few atomic distances below the surface, as was pointed out by Oriani.[83] In this context, the adsorption theory has the advantage that the hydrogen surface concentration is intrinsically large, and there are not large elastic stresses required to promoted hydrogen accumulation.[79, 83, 87]

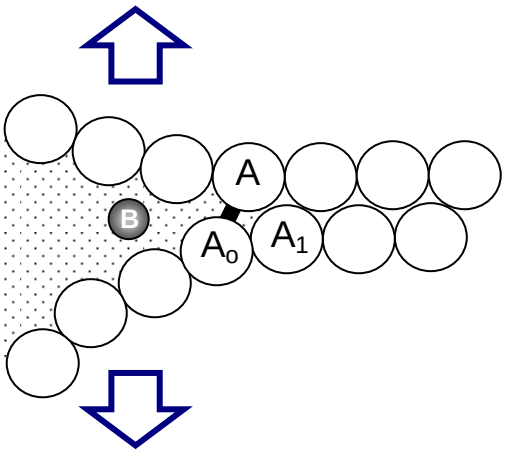

Figure 20. Schematic illustration of the adsorption model. The model requires that a specific ion from the environment, *B*, interacts and reduces the cohesive strength of the strained bond A-A_0 at the tip of the brittle crack.[87]

Uhlig *et al*[88] considered that the adsorption takes place at dislocations and other mobile imperfections in the vicinity of the crack tip. Moreover,

he also defined a critical potential below which the adsorption of ions does not occur. Nevertheless, Bockris *et al*[89] dismissed this proposal and suggested that the adsorption begins at the potential of zero charge and increases gradually with a shift in potentials.

In addition, Oriani *et al*[83] considered that the thermodynamic argument in which this model has been made was insufficient since the mechanistic path was not specified. He also considered that the crack propagation is a continuous process and thus, there is a lack of explanation on how cracks can propagate at low velocities without becoming blunted by plastic deformation. As a result, the idea that plastic relaxation does not prevent embrittlement has led to the proposal of a model involving the formation of surface hydrides.[87]

3.2.4. Hydride Induced Cracking

The hydride induced cracking model was originally proposed by Westlake *et al*[80] and suggests the formation of a localised hydrogen enriched phase (metal hydride) at regions of high stress triaxiality such as the crack tip. This hydride phase affects the mechanical properties of the metal leading to a brittle crack. More specifically, Gilman *et al*[90] proposed an speculative model which considered the strong interactions of hydrogen with free atoms and surfaces leading to chemisorption at all available sites nearby the crack tip in most metals.

The formation of surface hydrides tends to suppress the plastic deformation (glide of dislocations), increasing the tendency for cleavage and hence embrittlement. Therefore, a surface compound might substantially increase the formation energy of a glide surface step in relation to the energetic requirements for a cleavage surface step. Taking into account this model for ferrous alloys, a possible hydride would have the composition of FeH_2, schematically represented in **Figure 21.A**. Shear might change one row of iron atoms from FeH_2 to FeH, **Figure 21.B**, suppressing plastic deformation by increasing the surface resistance.[87, 90]

Hydride formation has been widely confirmed for the groups of metals IVB (Ti, Zr, Hf) and VB (V, Nb, Ta) as well as rare earth such as La, Ce, and Nd.[91] However, the lack of thermodynamically stable hydrides of iron together with insufficient evidence of the formation of hydrides in iron-based alloys for instance has led to dismissing the theory for steels. Nonetheless, the lack of stability of surface hydrides at the crack tip may be the result of a cyclic process of cracking of the hydride, crack arrest and reformation of the hydride.[92, 93]

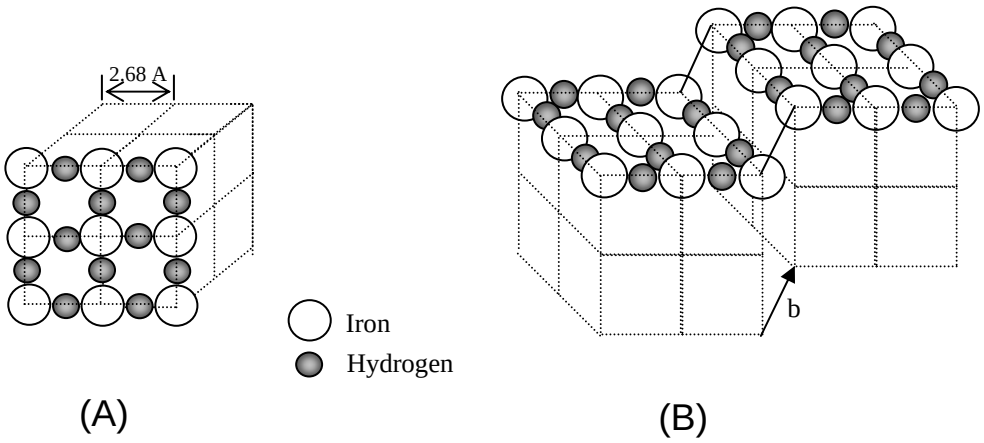

Figure 21. A) Chemisorption of hydrogen on the face of an iron crystal and B) Step produced by plastic glide on the surface of a hydrated iron crystal.[90]

3.2.5. Brittle Crack Tip Theory

Thompson *et al*.[81] suggested that in the presence of hydrogen, the surface energy in iron is sufficiently lowered that a sharp crack becomes stable against spontaneous blunting and dislocation formation at the crack tip. In addition, the dislocation density in the vicinity of the crack tip has to be significantly smaller than one dislocation per atom in order to promote an atomically sharp configuration. Under these conditions, the plastic zone around the crack tip can act to shield the brittle crack propagation in ductile materials like high strength steels. The crack configuration for this model is schematically represented in **Figure 22**.

In this model it is assumed that the dislocation density near the crack tip is limited by strain hardening (slip of dislocations). Moreover, Gilman *et al.*[90] proposed that strong chemisorptions would tend to prevent dislocation emission at the crack tip, favouring a brittle crack. However, further studies remain to be done regarding calculations to estimate the real effect of hydrogen on the lattice trapping barrier.[86]

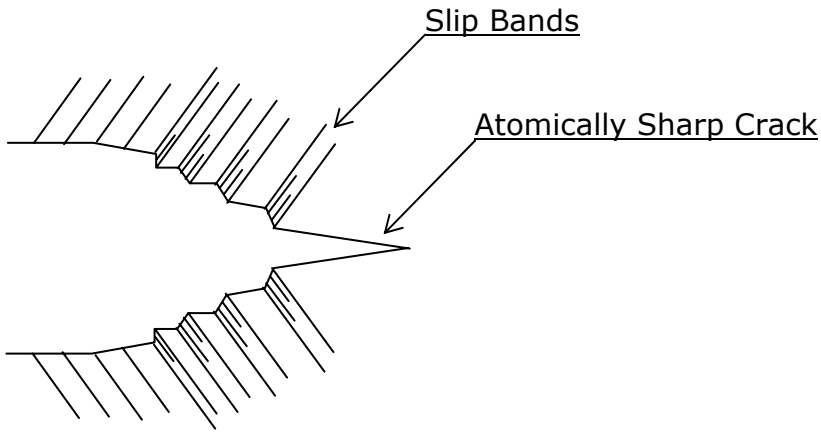

Figure 22. Sharp crack in a inhomogeneous field of dislocations.[81]

3.2.6. Localised Slip Model

This model proposed by Beachem *et al*.[82] is based on two assumptions: A) that the crack tip plasticity is promoted by the entry of hydrogen in the metal lattice, and B) that the plastic deformation aids the hydrogen entry near the crack tip. Based on experimental observations on AISI-4340 high strength steels, three different fractures modes were presented during hydrogen assisted cracking, *HAC*: micro-void coalescence, *MVC*, quasi-cleavage, *QC*, and intergranular fracture as is shown in **Figure 23**.[82, 94]

When the increasing plastic region is large enough to cover inclusions which acts as voids nucleation sites the resulting fracture mode displays micro-void coalescence, *MVC*. When the plastic region is not large enough to include large numbers of inclusions the quasi-cleavage, *QC*, fracture mode takes place. At still longer cracks, both *MVC* and *QC* modes cannot

operate and much less plastic deformation occurs, promoting inter-granular fracture mode, *IG*. Trans-granular fracture displays brittle cleavage (separation along specific crystallographic planes) whereas inter-granular fracture shows interface separation, depending on the relative strength of the grain boundaries.

This model assumes that fracture modes are produced by sub-microscopic plastic flow mechanisms and that hydrogen promotes these processes. It has been proposed that the intensity factor, *K*, and the hydrogen concentration at the crack tip determine the crack mode. By gradually decreasing *K* values the microscopic plasticity decreases showing *MVC*, *QC* and finally *IG* fracture modes. For high *K* levels fracture proceeds by the initiation and coalescence of microvoids which appear identical to the microvoids resulting from fracture under a rapid tensile overload. At intermediate *K*, the fracture is by quasi-cleavage, while at low *K* the fracture path is completely intergranular along the prior austenite grain boundaries.

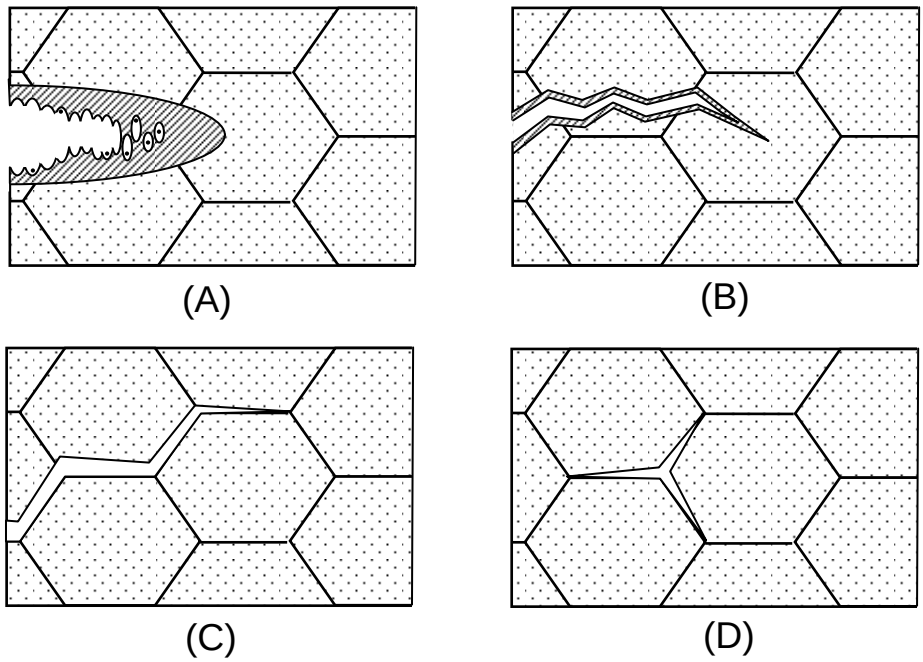

Figure 23. Schematic representation of the fractures modes observed as a function of decreasing stress intensity factor and decreasing cracking rate: A) High *K* (*MVC*), B) intermediate *K* (*QC*), C) low *K* (*IG*), D) *IG* cracking with assistance from hydrogen pressure.[82]

In addition, hydrogen can only aid the fracture mode that the microstructure of the metal will allow and the rate of hydrogen entry determines the concentration of the hydrogen in the crack tip region. Hence if hydrogen is insufficient for a particular mode of fracture, it cannot take place.[82]

On the contrary, with this model there is evidence that hydrogen impedes dislocation motion as has been shown by strain ageing and internal friction observations.[83] Nevertheless, atomic calculations for pure iron in vacuum have shown that the effect of hydrogen in promoting the injection of dislocations at the crack tip is feasible.[86]

Alternatively, evidence supporting the idea that hydrogen enhances the generation and mobility of dislocations through the hydrogen–shielding effect mechanism has been recently shown by Robertson *et al*.[95] During *in-situ* studies performed in a transmission electron microscope he showed that solute hydrogen increases the velocity of dislocations and therefore the crack propagation for 310 stainless steels. Whether this model occurs on alloys like high strength steels is not clear and it cannot be dismissed until further atomic scale studies at the crack tip have been done.

4. States of Hydrogen in Steels

Hydrogen can be present in a number of different ways in the metal, including the crystal lattice, voids and other defects where hydrogen atoms are not mobile at room temperature. Besides, there is evidence that not all hydrogen within the metals is available to contribute and cause damage by hydrogen embrittlement.[96] The assignment of hydrogen states particularly for steels is mainly determined by its microstructure, which itself defines the hydrogen *solubility*, *transport* and *trapping* characteristics of the alloy. These three concepts are explained in the following sections.

4.1. Hydrogen Diffusivity and Solubility

At an atomic level, hydrogen dissolves interstitially in virtually all metals. Consistent with this characteristic, hydrogen is transported or *diffuses* with high mobility in iron and particularly in *bcc* unit cells like ferrite, α. The mobility or diffusivity of hydrogen in *fcc* (i.e. austenite, γ) and *hcp* structures is considerably lower due to smaller interstitial sites and close packing of host atoms. Hence the rate of hydrogen diffusion depends on its mobility through the metal lattice. In the case of α-iron, indirect evidence indicates tetrahedral interstitial site occupancy of hydrogen at room temperature.[97] Nevertheless, other parameters such as spacing and interstitial bonding or activation energies, might restrict the number and distribution of hydrogen atoms that can be fitted into a specific unit cell.[91]

On the other hand, the hydrogen *solubility* of a specific microstructural phase determines hydrogen concentration levels within the steel. The solubility of hydrogen in the lattice of iron follows Sievert's law and its equilibrium concentration could be as low as $2x10^{-8}$ in the atomic ratio at room temperature under one atmospheric pressure of hydrogen gas.[98] It is known that austenite has higher hydrogen solubility than martensite;

and the diffusivity of hydrogen is an order of magnitude lower in *fcc* structures than in martensite *bct* or distorted *bcc* unit cells.[99]
The solubility of hydrogen is ideally governed by the heat of solution, that for hydrogen in α-iron is approximately 28.7KJ/mol with solubility values of C_o=3x10^{-4}wppm at 25°C. Noticeable, the hydrogen solubility in martensitic AISI-4135 steels (σ_y=1380MPa) is approximately 0.4wppm, which is considerably higher than that for α-iron due to trapping related phenomena.[100]

To produce embrittlement of martensitic high strength steels it is not necessary that hydrogen concentrations reach levels above the solid solution solubility limits. Martensitic and ferritic structures can become embrittled with relatively low average hydrogen concentrations. It has been suggested that local concentrations of hydrogen at microstructural defects are rather more critical than the average hydrogen content to cause embrittlement of these alloys. [71]

4.2. Hydrogen Trapping

Hydrogen in steels is not homogeneously distributed and could be found either in normal interstitial lattice sites or *trapped* in microstructural imperfections such as vacancies, dislocations, grain boundaries, second phase particles interfaces and voids.[97, 101, 102]

Whether a microstructural feature can act as a trapping site, *A*, is governed by a potential energy well or binding energy, E_b, relative to the normal interstitial position, *B*, in the iron lattice as describes **Figure 24**. E_t and E_s represent the trap activation energy and the saddle point energy around the trapping, respectively. Traps sites can be classified according to the number of hydrogen atoms that can be accommodated in the trap and to the binding energy of the traps. If the rate of hydrogen capture and release in the trap are large enough to match the relaxation time for a hydrogen atom to diffuse through the material, trapped hydrogen is assumed to be in equilibrium with the lattice diffusing population and the trap is classified as *reversible*.[97, 103, 104]

A reversible hydrogen trap has short residence time with corresponding low interaction energy, while an *irreversible* trap has negligible probability of releasing its hydrogen without the application of thermal energy. It is considered that if $|E_t| >> |E_b|$ the trap is thought to be irreversible.[104] It has been suggested that in pure annealed α-iron, reversible trap sites with $|E_b| > |E_n| = 7$[kJ/mol] create an 'effectively' higher barrier to hydrogen movement by increasing the residence time of the diffusing hydrogen atom.[105]

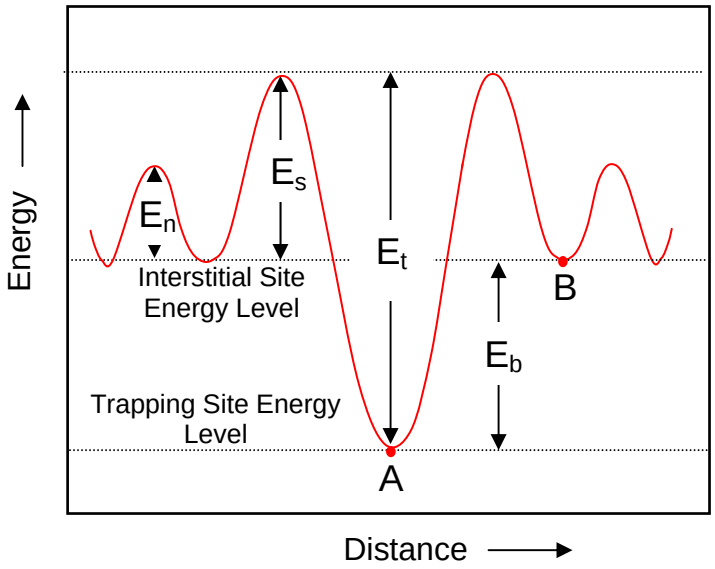

Figure 24. Energy levels of hydrogen around trapping sites. (E_n= Activation energy of hydrogen in normal lattice site, E_s= Saddle point energy around trapping site, E_t= Trap activation energy and E_b= Potential well of trapping site).[104]

4.2.1. Trapping Sites in High Strength Steels

The interaction energy between hydrogen atoms and potential traps is determined by its coherency, which is defined as the degree crystallographic match with the lattice of the matrix. For example, lower energy interactions exists for coherent precipitates like MC, M_2C and ε-carbides, but higher energies for both incoherent interfaces like Fe_3C and semi coherent (metal-carbides) precipitates in some high strength steels.[38]

It has been suggested that the predominant trapping with low binding energy corresponded to dislocations, vacancies, lath interfaces and prior austenitic grain boundaries for low carbon steels at room temperature.[106] Kumnick *et al.*[105] suggested that dislocations and microvoids acted as the main trap sites of hydrogen in Armco iron. What is more, alternative studies determined the binding energy at dislocation cores to be as high as 58[KJ/mol].[107] In addition, several studies have established that grain boundaries act as hydrogen reversible traps with similar binding energies of 59[KJ/mol]. Alternatively, Hong *et al*.[108] suggested that hydrogen in iron was trapped at the stress field around dislocation and not at the core of dislocations itself.

Lee *et al*.[104] proposed that the main hydrogen traps for cold worked AISI-4340 were dislocations. He found that the activation energies for evolution of hydrogen at ferrite-carbide interfaces, dislocations and microvoids in AISI-4340 high strength steels were approximately 48.3[KJ/mol]. This value corresponded to reversible or relatively low energy traps and was comparable to those reported by other researchers between 71.4 and 88.2[KJ/mol] for TiC interfaces, suggesting similar trapping effects.

On the other hand, Lee *et al*.[104] have suggested that additional factors such as alloying elements that form solid solutions and the degree of cold work would enhance the amount of dissolved hydrogen in AISI-4340 high strength steel by introducing additional traps within the microstructure by enhancing dislocation density. But Oriani *et al*.[103] pointed out that although dislocations furnish trapping sites, solid-solid interfaces possibly are more important in a non-cold worked steel for the trapping of hydrogen at room temperature.

J. Tien *et al*.[109] found that large pressures developed at small inclusions were associated to void formation in ductile fracture. Similarly, Lee *et al*.[104] showed that microvoids formed at the interfaces of sulphide-rich inclusions, *MS*, might be directly related to hydrogen embrittlement of AISI-4340 high strength steels. The trap activation energy of hydrogen

evolution from MnS interfaces was approximately 72.3[KJ/mol].[104] Moreover, his results demonstrated that hydrogen exits in molecular form in microvoids.

Although the previous information about traps and their corresponding binding energies were applicable to iron and mostly to AISI-4340 high strength steels, the complexity of the trapping phenomena depends upon a wide variety of factors including heat treatments, alloying elements, cold work and hydrogen sources due to environmental conditions. Therefore, it is feasible that trapping characteristics easily vary even for a particular alloy at different conditions. For example, *MS* inclusion and matrix boundaries (high angle prior austenite grain boundaries) should provide the predominant *irreversible* traps in AISI-4340 steel at very high yield strengths (above 1379MPa) and heterogeneities such as Fe_3C may become the principal traps as the yield strength is decreased.[38] Taking into account differences and classification of the high strength steels studied in the present research project, the nature and characteristic of traps is expected to differ for each alloy.

4.2.2. Trapping Effects on Hydrogen Diffusion

It has been defined that hydrogen diffusion in the absence of traps is described by ideal lattice diffusivity, D_L, (governed by lattice migration energy, E_n, between interstitial sites). Whereas, the trap affected or apparent diffusivity, D_H, is up to three orders of magnitude lower than D_L, depending on the nature and extent of trapping.[100] Both parameters can be related as the following equation shows:[110]

$$\frac{D_L}{D_H} = 1 + \frac{N\,k}{p} \qquad \text{[IV]}$$

Where N represents the number of traps per unit volume, k the trapping parameter of the material and p corresponds to the hydrogen release rate dependent on the trap nature. Trapped hydrogen must acquire an energy level substantially larger than the lattice migration energy to escape the

trap, as was previously depicted in **Figure 24**. Therefore, the mean residence time of a diffusing hydrogen atom is considerably longer in the trap than in the lattice, making the apparent diffusivity lower than lattice diffusivity.[97]

However several modifications of the previous model proposed by Mc. Nabb *et al.*[110] have been developed taking into account the effect of parameters such as trap hydrogen concentrations[103] and interaction for reversible and irreversible traps at various degrees of occupancy.[102] Considering reversible and irreversible traps, it is assumed that in a lattice containing only irreversible traps that can be saturated, the diffusivity decreases to D_H values during hydrogen charging until the traps become filled.

Once filled, the irreversible traps ideally do not interact with dissolved hydrogen in the lattice and consequently the diffusivity increases back to lattice diffusion values, D_L. On the contrary, hydrogen in reversible traps is in dynamic equilibrium with the dissolved hydrogen in the lattice and could disrupt the hydrogen transport. Consequently, D_H values in a lattice with reversible traps are always less than D_L.[100]

4.2.3. Trapping Effects on Hydrogen Embrittlement

It has been proposed that diffusible hydrogen causes embrittlement of low alloy steels but strongly trapped hydrogen does not.[106] Several authors suggested that reversible traps with low binding energy provide a reservoir of mobile hydrogen that diffuses to areas of lower hydrogen chemical potential such as the dilated region under triaxial tensile stress ahead the crack tip during application of load.[100]

Actually, numerous theories have suggested that hydrogen is preferentially transported to regions of high stress triaxiality assisting hydrogen induced cracking.[109] Moreover, it have been shown that low energy traps exacerbate hydrogen embrittlement by decreasing the

threshold stress intensity with increasing hydrogen concentrations in high strength steels.[38, 100]

Similarly, hydrogen embrittlement can take place after the hydrogen concentration exceeds a critical value enough to achieve certain hydrogen pressure that overcomes the cohesive strength of the atoms in the crystal lattice.[111] In addition, it has been considered that a critical stress concentration at trap sites might be also necessary to induce hydrogen embrittlement.[112]

Using an alternative approach, Pound *et al*.[38] considered that the type of heterogeneities plays a crucial role in determining an alloy's intrinsic susceptibility to *HE* for high strength steels, with large irreversible (high binding energy) traps often imparting a high susceptibility. He associated hydrogen embrittlement susceptibilities of high strength steels to their corresponding irreversible trapping constant, *k*, and found that by decreasing *k* values the hydrogen susceptibilities of high strength steels decreased. Moreover, the inverse of *k* values for AISI-4340 steels correlate with the stress intensity factor for stress corrosion cracking, K_{ISCC}, in 3.5% NaCl solutions.

The inverse of *k* (1/*K*) has been regarded as a measure of the intrinsic resistance to hydrogen embrittlement for this alloy. This inverse relationship supported the general view that hydrogen plays the predominant role in stress corrosion cracking of martensitic steels.[38]

4.3. Hydrogen Transport Measurements

As dissolved hydrogen in steels causes embrittlement, it is important to assess the intrinsic hydrogen transport characteristics of the alloy in terms of diffusivity. In a general definition, diffusion is the process by which matter is transported from one part of a system to another as a result of random motion of particles. Fick's first law describes that in an isotropic medium, the rate transfer of diffusing species expressed as a flux

J [mol/cm²s] through a unit area of a section is proportional to the concentration gradient, $\partial C / \partial x$ [mol/cm³], and the diffusion coefficient, D[cm²/s], as follows:[113]

$$J = - D \frac{\partial C}{\partial x} \qquad [V]$$

According to equation [V], the driving force which compels the diffusion process to occur is the concentration gradient. Diffusion is a time-dependent process and in this particular situation the diffusion flux does not change with time, therefore *steady-state* conditions are established.

Nonetheless, most practical diffusion situations are *non-steady*, implying that the diffusion flux and the concentration gradient at some particular point in the solid vary with time with a resulting accumulation or 'trapping' of the diffusing species. Under these conditions the Fick's second law is applied:[113]

$$\frac{\partial C}{\partial t} = - D \frac{\partial^2 C}{\partial x^2} \qquad [VI]$$

Clearly, solutions for both mathematical interpretations of the diffusion process, described in equations [V, VI], will depend upon boundary conditions defined by a particular physical situation.

4.3.1. Hydrogen Permeation Method

Devanathan and Stachurski,[114] developed an electrochemical technique that allows the detection of the hydrogen permeation flux through relatively thin metallic membranes. In this technique a concentration gradient is created by cathodically charging one side of the membrane with hydrogen, and holding the other side at potentials at which hydrogen is oxidised.

Figure 25 shows a schematic representation of the permeation double cell used to record hydrogen permeation rates through metallic membranes. The charging side of the cell is held at cathodic potentials to promote the generation and uptake of hydrogen on the surface of the membrane. Hydrogen diffused through the metal and is oxidised and detected on the depletion or anodic side. The electrolyte used in both cells is commonly 0.2 M NaOH solutions to maintain the passive condition of the iron membrane preventing additional oxidation currents to alter the electrochemical hydrogen measurements.[114]

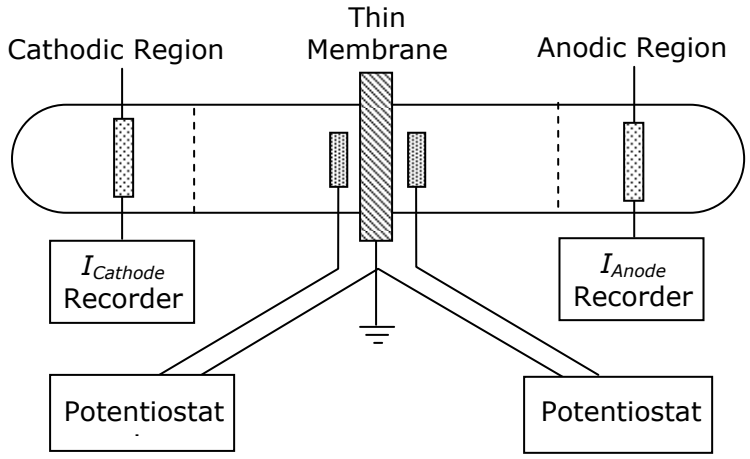

Figure 25. Devanathan and Stachurski permeation double cell, modified from Devanathan *et al*.[114]

The hydrogen flux permeating through the membrane can be represented by the Fick's law for diffusion, previously showed in equation VI. The solution for this equation depends upon boundary conditions applied which can be potentiostatic[114] and galvanostatic hydrogen charging.[115, 116] It is considered that the potentiostatic conditions correspond to a constant hydrogen concentration at the surface of the membrane whereas the galvanostatic method represents keeping a constant hydrogen flux at the surface with variable potentials.[115, 116] In the following sections the mathematical solutions used to analyse the corresponding permeation fluxes for both charging methods are described.

4.3.1.1. Potentiostatic Permeation Charging

For the potentiostatic permeation charging conditions one face ($x=O$) is kept at a constant hydrogen concentration C_o, the other face ($x=L$) at C_L and the membrane is initially at a constant concentration C_i. These conditions can be represented as:

- $C = C_o$; $x = 0$ $t>0$
- $C = C_i$; $0 \le x \le L$ $t=0$
- $C = C_L$; $x = L$ $t\ge 0$

Where C is concentration at a time t and X represents the distance through the membrane of thickness L. There is a finite period of time during which the steady-state condition is reached and during this period of time the hydrogen concentration changes as equation [VII] describes. Under these conditions, the concentration gradient is as follows: [113]

$$C - C_o = (C_L - C_o)\frac{x}{L} + \frac{2}{\pi}\sum_{1}^{\infty}\frac{C_L\ Cos(n-\pi) - C_0}{n}\ Sin\frac{n\ x\ \pi}{L}\ Exp\left(\frac{-D\ n^2\ \pi^2\ t}{L^2}\right) +$$

$$\ldots + \frac{4\ Ci}{\pi}\sum_{1}^{\infty}\frac{1}{2m+1}\ Sin\frac{(2m+1)\ \pi\ x}{L}\ Exp\left(\frac{-D\ (2m+1)^2\ \pi^2\ t}{L^2}\right) \quad [\text{VII}]$$

From the permeation experimental arrangement, C_i and C_L are zero since the membrane was initially at zero hydrogen concentration and the concentration at the depletion side of the cell was kept at zero level. Therefore, the concentration gradient in the membrane is:

$$C - C_o = C_o\frac{x}{L} + \frac{2}{\pi}\sum_{1}^{\infty}\frac{-C_0}{n}\ Sin\frac{n\ x\ \pi}{L}\ Exp\left(\frac{-D\ n^2\ \pi^2\ t}{L^2}\right) \quad [\text{VIII}]$$

It can be noticed that as time approaches infinity reaching steady state condition, the exponential part of equation [VIII] vanishes and the resulting hydrogen concentration distribution becomes linear. This

behaviour is depicted in **Figure 26.A**, where a normalised concentration profile is shown. The rate at which hydrogen emerges from the membrane per unit area at (X=L) corresponds to the permeation transient. Hence by differentiating equation [VIII] with respect to x, and knowing that the flux, J, when time tends to infinitive, $t \rightarrow \infty$, is $J_\infty = DC_0 / L$, then:

$$J = J_\infty \left\{ 1 + 2 \sum_{1}^{\infty} Cos(\pi n)\, Exp\left(\frac{-D\, n^2\, \pi^2\, t}{L^2} \right) \right\} \qquad [IX]$$

Equation [IX] theoretically describes hydrogen permeation curves assuming lattice diffusion with no effects of hydrogen trapping.[113, 114] The typical hydrogen permeation transient with constant hydrogen concentration on the charging side is shown in **Figure 26.B**. It can be seen that the breakthrough time, t_b, is the time for the first hydrogen to penetrate the membrane and the time to reach 0.63 of the steady-state value of the permeation current, J_∞, is represented by the t_{lag}.

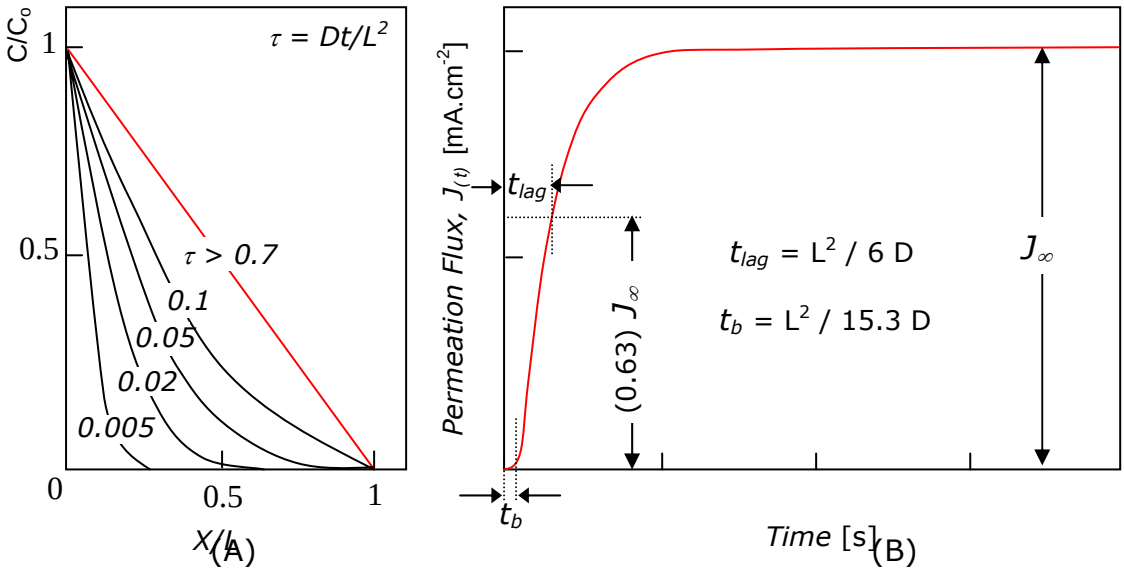

Figure 26. A) Normalised hydrogen concentration profile through a thin membrane under potentiostatic charging and B) Typical hydrogen permeation transient.[113, 114]

To determine the breakthrough time, t_b, and time lag, t_{lag}, to reach 0.63 times the steady-state current density, $(0.63)J_\infty$, is necessary to obtain

the total amount of diffusing hydrogen, Q_t, which has passed through the membrane in time, t, by integrating equation [VII] with respect to time. The resulting equation is as follows:

$$Q_t = D\,(C_o - C_L)\frac{t}{L} + \frac{2\,L}{\pi^2}\sum_{1}^{\infty}\frac{C_o\;Cos(n-\pi) - C_L}{n^2}\left\{1 - Exp\left(\frac{-\,D\,n^2\;\pi^2\;t}{L^2}\right)\right\} + \ldots$$

$$\ldots + \frac{4\,C_i\;L}{\pi}\sum_{1}^{\infty}\frac{1}{(2m+1)^2}\left\{1 - Exp\left(\frac{-\,D\,(2m+1)^2\;\pi^2\;t}{L^2}\right)\right\} \quad [X]$$

Under permeation experimental conditions, C_i and C_L are zero, and by approaching time to the infinitive value, the resulting expression is:

$$Q_t = \frac{D\,C_o\;L}{L}\left(t - \frac{L^2}{6\,D}\right) \quad [XI]$$

This function has an intercept t_{Lag} on the t-axis which corresponds to the time when 0.63 of steady-steady permeation flux is reached and detected on the depletion side of the Devanathan and Stachurski cell. This value is given by:

$$t_{lag} = \frac{L^2}{6\,D} \quad [XII]$$

A graph of (Q_t / LC_o) as a function of (Dt / L^2) for the case when C_i and C_L are zero depicted in **Figure 27** shows that the steady state condition is reached when (Dt / L^2 = 0.5) approximately. In addition, the time at which the first hydrogen penetrates the membrane is given by (Dt / L^2 = 0.0654), therefore the breakthrough time, t_b, is represented as equation [XIII] shows. Equations [XII] and [XIII] have been used to obtain hydrogen diffusion coefficients on steel membranes.[113, 114]

$$t_b = \frac{L^2}{15.3\,D} \quad [XIII]$$

Both t_{lag} and t_b are graphically determined from the permeation transients. t_{lag} is take when 0.63 times of the steady-state permeation flux is reached

whereas the t_b is taken by extrapolation of the linear part of the rise transient or from the point of inflection.

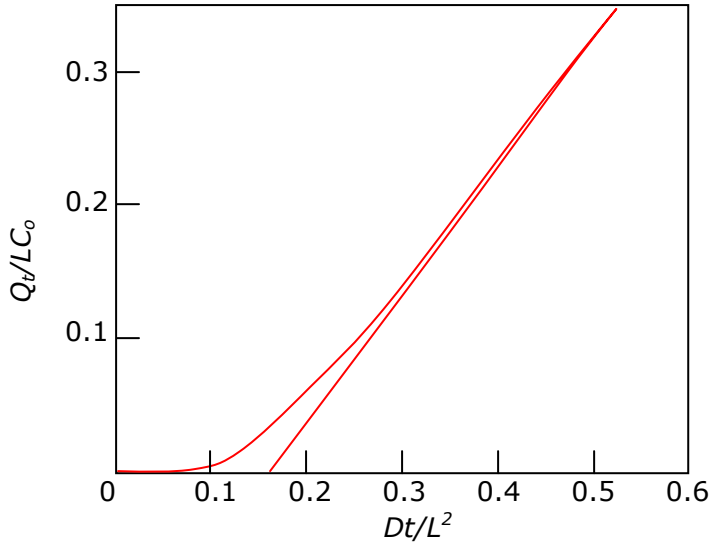

Figure 27. Approach to steady-state flow through a plane sheet.[113]

4.3.1.2. Galvanostatic Permeation Charging

For the case of constant hydrogen flux through a steel membrane, where one face (x=O) is kept at a constant hydrogen flux J_o, and the hydrogen atoms rapidly exit the other face (x=L). These conditions can be represented as:

- $C = 0$; $x = L$ $t>0$
- $C = 0$; $0 \leq x \leq L$ $t=0$
- $J_o = J_\infty = C_oFD/L$; $x = 0$ $t=\infty$

Where J_∞ is the hydrogen flux at steady-state conditions which is the same as J_o, and X represents the distance through the membrane of thickness L. The solution of equation [VI] following these boundary conditions describes the distribution of hydrogen through the steel membrane where the concentration gradient is as follows: [115]

$$C = \frac{J_o}{FD}(L-x) - \frac{8\,J_o L}{FD\pi^2}\sum_{1}^{\infty}\frac{(-1)^n}{(2n+1)^2}\,Sin\frac{(2n+1)(L-x)\,\pi}{2L} \quad \ldots$$

$$\ldots Exp\left(\frac{-D\,(2n+1)^2\,\pi^2\,t}{4L^2}\right) \qquad \text{[IXX]}$$

Moreover, the permeation current as a result of holding the surface hydrogen concentration at the depletion side, (X=L), at zero is given by:

$$J_t = J_0\left\{1+\frac{4}{\pi}\sum_{0}^{\infty}\frac{(-1)^n}{(2n+1)}\,Exp\left(\frac{-D\,(2n+1)^2\,\pi^2\,t}{4L^2}\right)\right\} \qquad \text{[XX]}$$

Figure 28 depicts a the normalised concentration profile through a membrane of thickness L and the typical hydrogen permeation transient for constant hydrogen flux on the charging side.

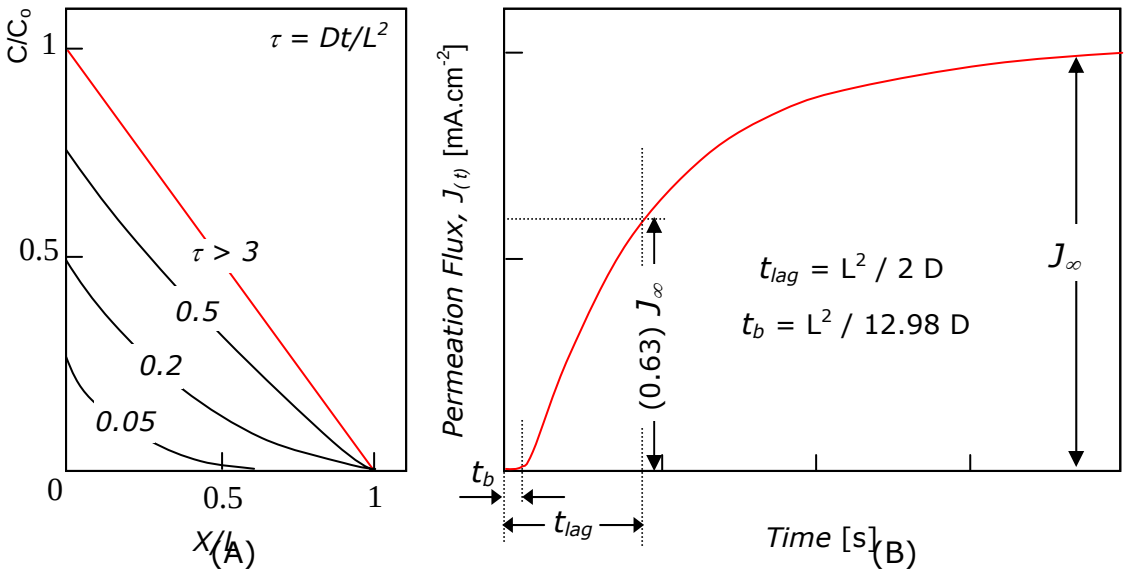

Figure 28. A) Normalised hydrogen concentration profile through a thin membrane under galvanostatic charging and B) Typical hydrogen permeation transient. Modified from Archer *et al.*[115]

Under galvanostatic charging conditions, the breakthrough time, t_b, and t_{lag}, are given by the following equations:[115]

$$t_b = \frac{L^2}{12.98\,D} \qquad [XXI]$$

$$t_{lag} = \frac{L^2}{2\,D} \qquad [XXII]$$

4.3.2. Galvanostatic or Chrono-potentiometric Method

One of the limitations of the permeation method is the preparation of a very thin membrane of steel with relatively large effective area in order to carry out the hydrogen charging. Hence, an alternative technique is presented where relatively small rectangular specimens of steel are used to determine hydrogen diffusion coefficients by galvanostatically charging its surfaces. This technique is referred as *galvanostatic charging* or *constant current chrono-potentiometry* in which by applying a constant current to the working electrode causes the electroactive species (i.e. hydrogen) to be reduced and produce H^+. C.J. Wen *et al*,[117] described this alternative technique where the potential difference between the steel electrode and a platinum anode is monitored as a function of time, as depicted in **Figure 29**.

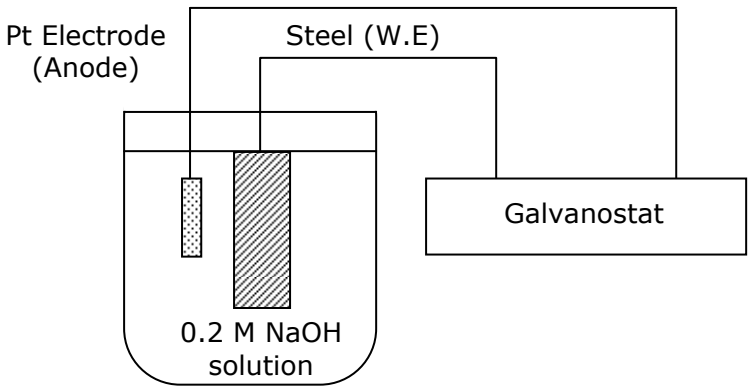

Figure 29. Schematic representation of the electrolytic cell used in the galvanostatic charging method.

Applying a constant current to the electrode causes the hydrogen to be reduced at a constant rate to produce atomic hydrogen, *H*. Considering that no additional corrosion reactions takes place in the simple cell, it is

assumed that the recorded potential differences provided a measure of the activity of the hydrogen diffusion in the steel specimen.[118, 119, 120]

The potential of the electrode moves to values characteristic of the couple and varies as the H/H^+ concentration ratio changes at the electrode surface.[117 - 119] The time dependent potential is related to the hydrogen concentration gradient at the electrode-electrolyte interface by the Fick's second law of diffusion corresponded to equation [VI]. At the electrode/electrolyte interface, assuming that the steady-state is reached (i.e. the amount of hydrogen discharged is constant), the current at the electrode surface at any time is described by the following equation:

$$I(t) = -\,z\,F\,S\,D\left(\frac{\partial C}{\partial x}\right)_{x=0} \qquad [\text{XXIII}]$$

Under the experimental conditions mentioned above, the initial boundary conditions are: [113, 117]

- $C = C_o$; $0 \le x \le L$ $t=0$
- $-D\frac{\partial C}{\partial x} = \frac{I}{zFS}$; $x = 0$ $t>0$
- $\frac{\partial C}{\partial x} = 0$; $x = L$ $t\ge 0$

The solution of the Fick's second law under these conditions is given as trigonometric series as:

$$C_{(x,l)} - C = \frac{I\,t}{z\,F\,S\,L} + \frac{I\,L}{z\,F\,S\,D}\left\{\frac{3\,(L-x^2)-L^2}{6\,L^2} - \frac{2}{\pi^2}\sum_{1}^{\infty}\frac{(-1)}{n^2}\cdots\right.$$

$$\left.\cdots Cos\left[\frac{n\pi\,(L-x)}{L}\right] Exp\left(-\frac{n^2\pi^2 D\,t}{L^2}\right)\right. \qquad [\text{XXIV}]$$

And error functions, where $ierfc\,(x) = \pi^{-1/2}\;Exp\,(-x^2) - x + (x)\,erf\,(x)$;

$$C_{(x,l)} - C = \frac{I\,t}{z\,F\,S\,L} + \frac{I\,L}{z\,F\,S\,D}\left\{\frac{3\,(L-x^2)-L^2}{6\;L^2} - \frac{2}{\pi^2}\sum_{1}^{\infty}\frac{(-1)}{n^2}\cdots\right.$$

$$\left.\cdots Cos\left[\frac{n\pi\,(L-x)}{L}\right] Exp\left(-\frac{n^2\pi^2 D\,t}{L^2}\right)\right\} \quad [\text{XXV}]$$

Where *z* is the charge of the diffusing element, *I*, the applied current, *t*, time, *F*, the faraday constant, *S* and *L* the surface area and the specimen thickness respectively, and *D* is the diffusion coefficient.

For small values of time, ($t << L^2/D$), the time variation of the hydrogen concentration at the electrode-electrolyte interface can be approximated to: [117]

$$Cs_{(l)} - C_0 = \frac{2\,I}{z\,F\,S}\left(\frac{t}{\pi\,D}\right)^{1/2} \text{; if } t << \frac{L^2}{D} \quad [\text{XXVI}]$$

This has a form identical to the well known *Sand*[117, 120] equation for ions diffusion in a semi-infinite medium of liquid electrolyte. By differentiating equation [XXVI] with respect to $t^{1/2}$ and then both sides of the equation multiplied by $\partial E/\partial t$, we obtain equation [XXVII].

$$\left(\frac{\partial E}{\partial t^{1/2}}\right) = \frac{2\,I\,Vm}{F\;S\;(\pi.D)^{1/2}}\left(\frac{\partial E}{\partial \delta}\right); \text{ if } \quad t << \frac{L^2}{D} \quad [\text{XXVII}]$$

The $\partial E/\partial t^{1/2}$ value represents the slope of the linear plot of $E_{(t)}$ *vs* $t^{1/2}$, $\partial E/\partial \delta$ is the variation in potential of the steel electrode with change in the hydrogen concentration, and V_m is the steel molar volume, 7.092 [cm^3/mol].

For long times, ($t > L^2/D$), the hydrogen concentration on the steel surface, ($x=0$), can be approximated by the first two terms of the equation [XXIV]. By differentiating the resulting expression with respect to time and expanding it by ∂E, we have the following equation: [117]

$$\left(\frac{\partial E}{\partial t}\right) = \frac{I\,Vm}{F\,S\,L}\left(\frac{\partial E}{\partial \delta}\right) \text{ ; if } t > \frac{L^2}{D} \qquad [\text{XXVIII}]$$

The quantity $\partial E / \partial t$ can be taken from the slope of the linear plot of $E_{(t)}$ *vs* *t*, and resulting $\partial E / \partial \delta$ value is substituted in the equation [XXVIII] to obtain the hydrogen diffusion coefficient *D*. Dimensionless hydrogen concentration-distance curves using equation [XXIV] for various times are shown in **Figure 30.A**. The total amount of diffusing hydrogen taken up by unit area of the steel sheet in a time, *t*, is (2.*I*.*t* / *z*.*F*.*S*). Moreover, a typical potential as a function of time plot is shown in **Figure 30.B**, where the *short time* and *long time* segments are described.

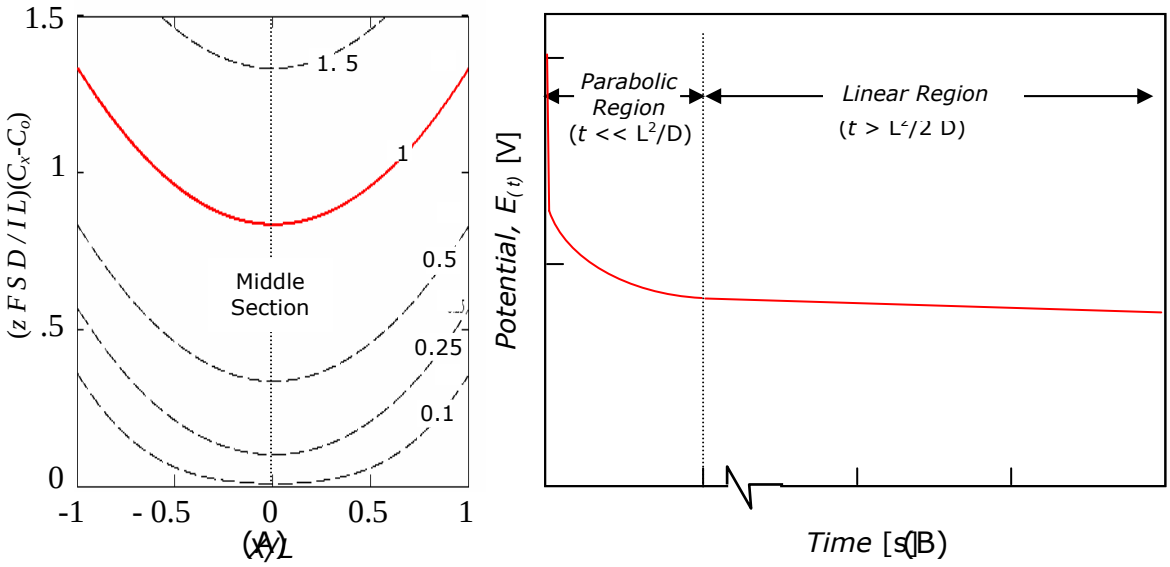

Figure 30. A) Dimensionless hydrogen concentration distribution in a plane sheet for constant flux at the surface. Numbers on curves are values of ($D\,t\,/\,L^2$), and B) Typical potential as a function of time trend from galvanostatic charging method.[113, 117]

In addition, by eliminating the ohmic voltage drop from equation [XXVIII] (by subtraction the extrapolation of *E vs* $t^{1/2}$ data to zero, i.e. $t^{1/2}=0$), together with the assumption that the variation in potential of the steel is linearly dependent on time over the concentration range involved in the current pulse, the hydrogen diffusion coefficient *D* can be also obtained from the following expression:[117]

$$\left[E_{(t)} - E_{(t=0)}\right]_{(t=0)} = \frac{I\ L\ Vm}{3\ F\ S\ D}\left(\frac{\partial E}{\partial \delta}\right);\ \text{if}\ \ t > \frac{L^2}{D} \qquad [\text{XXIX}]$$

The quantity on the left-hand side of equation [XXIX] is the extrapolated intercept of the linear portion of the $E_{(t)}$ *vs* t curve at $t=0$. Whereas, $E_{(t=0)}$ is the net voltage after eliminating the ohmic voltage drop when the current is switched on and can be obtained from the intercept of E *vs* $t^{1/2}$ at zero time.[117]

5. MECHANICAL TESTING

There is a wide diversity of mechanical testing methods used to evaluate the susceptibilities of metals and alloys to stress corrosion cracking, *SCC*, and hydrogen embrittlement, *HE*. The aim of these tests is to provide information of the predictable behaviour during service. Nevertheless, some of the tests attempt to reproduce service conditions and others may be designed to study the mechanistic aspect of failure.[121]

The use of smooth and notched or pre-cracked specimens also depends upon the objective of the test and the nature of application. For example, pre-cracked specimens are commonly used to control the crack growth and reduce experimental scatter. The reduction of ductility for high strength steels is particularly significant in respect to stress concentrations at notched regions. Moreover, it is considered that crack initiation induced by diffusible hydrogen occurs above the threshold stress intensity factor, K_{ISCC} or K_{th}, derived from a specific specimen geometry and applied stresses.[10, 121, 122] However, the use of pre-cracked or notched specimens was not considered as un-notched specimens have the advantage that the failure occurs at the site of the largest microstructural flaws.

Concerning methods of loading smooth or pre-cracked tests specimens, two main techniques have been widely used to assess the extent of hydrogen embrittlement on steels, which are constant load and slow strain rate tests, *SSRT*. Both techniques are based on the principle that the specimens are subjected to stress during a period of time long enough to allow hydrogen to diffuse and embrittle the material.[121, 123]

As its name describes, for the constant load technique a constant load is applied on the specimens during the test. However, cracking has not been observed in some circumstances under constant load, showing poor reproducibility or taking prohibitively long experimental time. It has been reported that to promote *SCC* on carbon steel in boiling sodium hydroxide using the constant load technique is extremely difficult, but relatively

easily to do so by using constant strain-rate tets. Nevertheless, this observation may be related to the effect of strain rate. [123]

Moreover, for cases where a specimen does not fail after an arbritrary chosen time for the constant load method, the number of cracks per unit length of material is commonly used to compare susceptibilities for *SCC* or *HE*.[18] Whereas, the slow strain rate test, *SSRT*, has the advantage over the constant load method that failure of the specimens always occurs, allowing a direct comparison between different material-enviroment combinations.[124] The next section is dedicated to describe the main features of this useful technique.

5.1. Slow Strain Rate Test, *SSRT*.

Humphries and Parkins[124, 125] first developed the slow strain rate technique for the study of caustic cracking of mild steels. This technique involves the application of relatively slow strain rate to a specimen subjected to specific environmental conditions.[124, 125] The strain rate to promote *SCC* or *HE* is defined as $\dot{\varepsilon} = \partial \varepsilon / \partial t$, expresed in units of [s^{-1}] and depends upon the system alloy-enviroment in study.[122, 126]

This technique is an effective and rapid test where failures of tensile specimens of usual dimensions should occur in not more than a few days. [123] The *SSRT* require the use of tensile machines with relatively stiff frames to prevent variations in the results. A proportion of the total elongation measured during the *SSRT* might come from the machine frame if it is not stiff enough in relation with the alloy tested. Therefore, equipments with different frame stiffness or compliances might display different elongations for the same material.[18]

The most significant advantage of this technique is that by plotting the stress-strain, stress-time or load-time diagrams from the *SSRT*'s it is possible to evaluate mechanical properties and parameters such as time

to failure values, *TTF*, or the reduction in area percentage, *RA*%, for the embrittled and non-embrittled specimens.

Figure 31 schematically shows a general load-time diagram for embrittled and non-embrittled specimens after *SSRT*'s. From the information displayed in this graph it is feasible to assess the extent of *HE* by comparing one or more of the following parameters: A) time to failure, *TTF*, B) ductility in terms of reduction in area, *RA*%, or elongation to fracture, C) maximum load reached and D) area bounded by a nominal stress elongation curve.[10]

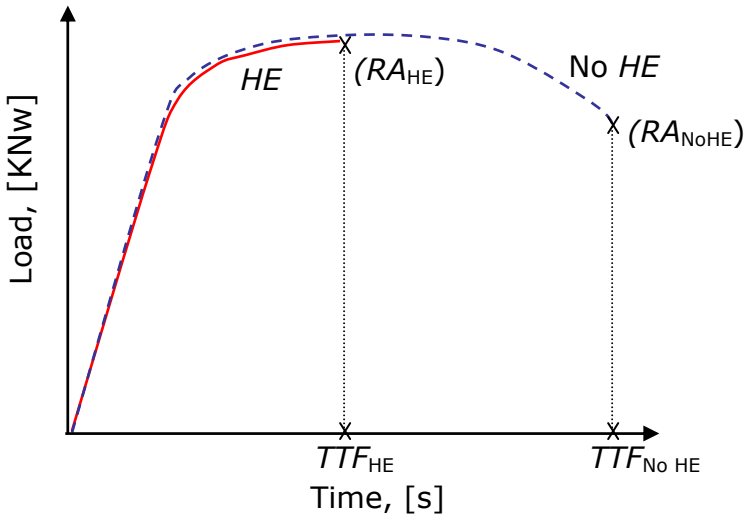

Figure 31. Applied load vs. time curves for slow-rate tests with and without *HE*.

It can be seen that the *TTF* for embrittled specimens is shorter than that of non-embrittled specimens. Because the specimens are strained constinuously at a given rate, *TTF* values are directly related to the percent of elongation. Therefore, in a similar way the *RA*% for embrittled specimens is smaller than that for non-embrittled specimens.

The strain rate is one of the most important experimental parameters in the slow strain rate test. Creep phenomena and necking after the ultimate tensile strength, *UTS*, might locally increase strain rate in the specimen. Nonetheless, adequate strain rates are possible to determine from

previous references associated to a specific environment-material system.[127, 128] For example, it has been reported that steels generally show severe *SCC* at a strain rate of about 10^{-6} s^{-1} regardless of the test environment.[126,127, 128]

Figure 32 shows schematically the responses to strain rate for *SCC*, *HE* and control specimens tested in air in terms of reduction of area, RA%. Remarkably, when the anodic dissolution mechanism is predominant and at extremely low strain rates, corrosion film formation could protect the metal surface from an active condition and as a result *SCC* susceptibility is suppressed. Whereas, at high strain rates there is not sufficient time for *SCC* to take place.[128]

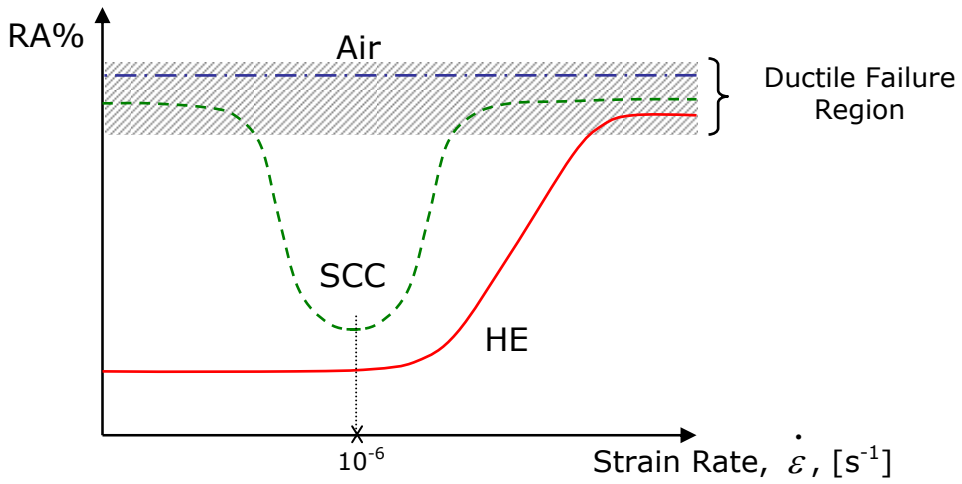

Figure 32. Schematic representation of the effect of strain rate on SCC and Hydrogen Induced Cracking.[128]

This behaviour is not observed for *HE,* where it is not required a film rupture process, but failure is promoted by occluded hydrogen in the steel. Instead, hydrogen is generated on the steel surface and absorbed by the steel up to the saturation limit.[128] Therefore, as the testing period increases by reducing the strain rate, the specimen becomes more susceptible to hydrogen cracking as more hydrogen penetrates the specimen. This trend is clearly shown in the previous figure.

Generally, it has been suggested that this *SSRT*'s overcome the limitations of alternavite techniques like constant load and is considered to be a test in which specimens are subjected to severe conditions to promote either *HE* or *SCC.* The *SSRT* technique have been widely used for many researchers like Parkins,[123, 125] Kim & Wilde,[129] and Scully. [130] Moreover, Pollock,[131] Robinson,[132] and Wright[16] have applied this technique to assess *HE* due to the electrodeposition or corrosion of metallic sacrificial coatings on high strength steels used for diferent structural applications. Hence, the validity of this method on the evaluation of *HE* susceptibility of high strenght steels have been widely corroborated.

5.2. Statistical Analyses

Mechanical-strength measurements of brittle fractures for steels show a variability of results which requires statistical analysis. Brittle failures display non reproducible results because of its random characteristic. The nature of this stochastic process shows dependence on the internal distribution of flaws and imperfections within the alloy where the critical crack length is sufficient to promote failure.

The most common frequency distribution in the case of hydrogen embrittlement is the Weibull[133] distribution. This technique was originally developed by Waloddi Weibull in 1951 to statistically represent the distribution of parameters like time to failure values, *TTF*, for a population of ceramic or glassy materials which showed brittle fracture mode. He defined the probability density function, $f_{(t)}$, for the Weibull distribution as equation [XXX] describes:

$$f_{(t)} = \frac{\beta}{\delta}\left(\frac{t-\gamma}{\delta}\right)^{\beta-1} Exp\left[-\left(\frac{t-\gamma}{\delta}\right)^{\beta}\right]; \qquad (t \geq \gamma)$$

[XXX]

$$f_{(t)} = 0; \qquad (t < \gamma)$$

Where γ is the location parameter, ($-\infty < \gamma < \infty$), δ is the scale parameter, ($\delta > 0$), and β the shape parameter, ($\beta > 0$). By tailoring these parameters the Weibull distribution could model and represent a specific experimental condition. Likewise, the Weibull density function displays an exponential distribution when $\gamma = 0$, $\delta = 0$ and $\beta = 1$ as is shown in **Figure 33**. Moreover, as β increases up to 4, the function progressively adopted a bell-shape distribution.

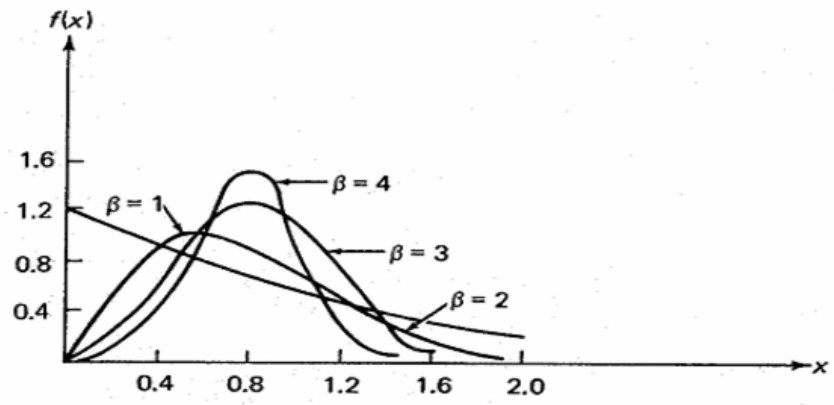

Figure 33. Weibull densities for $\gamma = 0$, $\delta = 1$, and $\beta = 1, 2, 3, 4$.[134]

The probability of a specimen to fail in a period of time, *t*, can be obtained by integrating equation [XXXI] with respect to time. Thus, the probability of survival is represented as follows:

$$F_{(t)} = \int_0^t f_{(t)}\, dt = 1 - Exp\left[-\left(\frac{t-\gamma}{\delta}\right)^{\beta}\right] \text{ ; if } t \geq \gamma \qquad [\text{XXXI}]$$

Subsequently, the probability of survival, P_s, for an specific period of time is represented by equation [XXXII]:

$$P_s = 1 - F_{(t)} = Exp\left[-\left(\frac{t-\gamma}{\delta}\right)^{\beta}\right] \text{; if } t \geq \gamma \qquad [\text{XXXII}]$$

Yokobori[135] adapted the Weibull distribution for the analysis of brittle failure of steels specimens. He demonstrated that for a stochastic process the probability of a specimen not failing or the probability of survival, P_s, within a period of time, t, was given by equation [XXXIII]:

$$P_s = e^{-xt} \qquad [XXXIII]$$

Where x is the probability per unit time that during a period of time, t, a crack with a sufficient size to cause failure will occur. The value of x can be obtained from the negative slope of the Weibull distribution graph in terms of time to failures values, *TTF*, against the natural logarithms of the probability of survival, Ln P_s, as is shown in **Figure 34**.

Robinson and Sharp[136] have modified equation [XXXIII] by introducing the crack incubation time parameter, t_i, which represents the time required for hydrogen to diffuse where the critical crack length was generated and reach the critical hydrogen concentration level to promote premature failure.

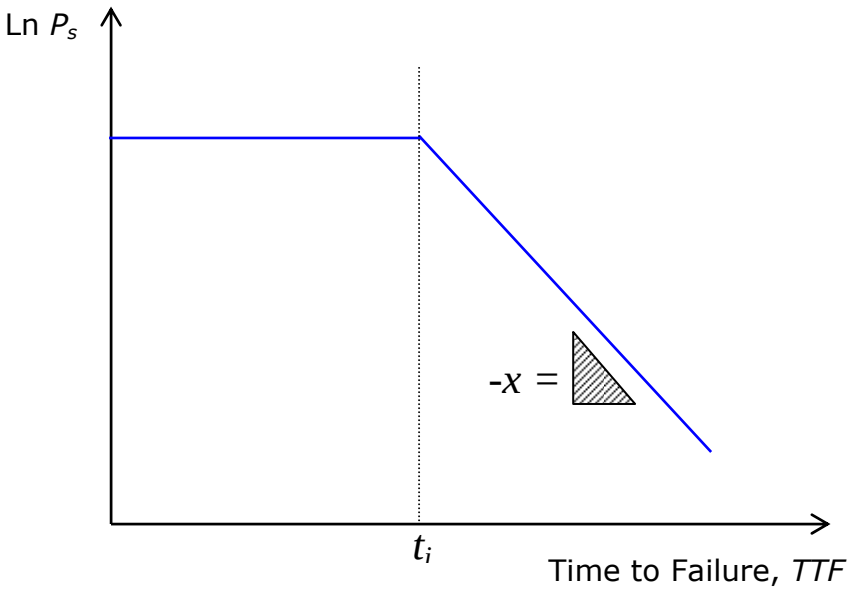

Figure 34. Schematic Weibull plot showing the natural logarithms of probability of survival, LnP_s, against time to failure, *TTF*.[66]

For crack incubation times below the minimum value, no failure take place and P_s = 1. Then, the probability of survival was defined as follows:

$$P_s = e^{-x(t - t_i)} \quad [XXXIV]$$

Where the mean time to failure, t, was defined as equation [XXXV] shows:

$$t = t_i + \frac{1}{x} \quad [XXXV]$$

5.2.1. Student t-Test

Student *t*-test analysis can be used to compare parameters like mean time to failure values of two batches of specimens tested using the *SSRT* technique at different experimental conditions. This analysis determines whether or not the two mean values are statistically different from each other. In this way, it is possible to assess the effect of the test conditions between two statistical populations.

The *t*-value is calculated considering the mean values and the variance of the two groups which represent different experimental conditions, i.e. un-treated and treated specimens, as is shown in **Figure 35**.

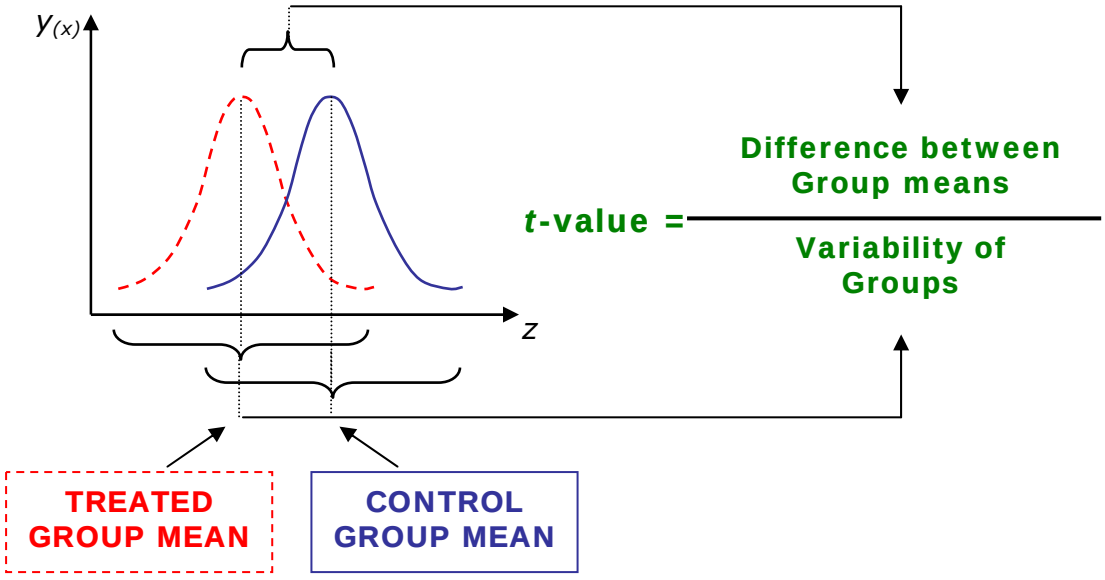

Figure 35. t-test analysis between control or untreated group and treated group.

It can be seen that the formula for the *t*-test is a ratio. The top part of the ratio is the difference between the two means or averages,μ, and the bottom part is a measure of the dispersion of those values, where S_d represents the standard deviation.[8, 137] If the analysed groups display normal statistical distributions this value is calculated from equation [XXXVI]:

$$t_s = \frac{(X_1 - X_2) - (\mu_1 - \mu_2)}{S_p \sqrt{\frac{1}{n_1} + \frac{1}{n_2}}} \qquad [XXXVI]$$

$$S_p = \sqrt{\frac{(n_1 - 1)^2 \; S_{d1}^2 + (n_2 - 1)^2 \; S_{d2}^2}{n_1 + n_2 - 2}} \qquad [XXXVII]$$

Taking a random sample from each of the two groups, labelled using the subscripts *1* and *2*, where *n* is the number of specimens and the mean value of the small samples is represented by *X*. **Figure 36** shows a normal distribution and some of the parameters for the student *t*-test, (σ represents S_d values).

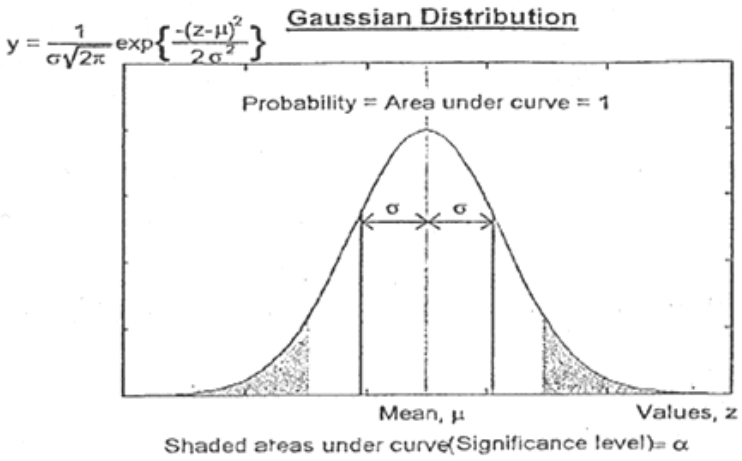

Figure 36. Normal distribution and the Student t-test.

Alternatively, where the analysed groups do not follow a normal statistical distribution the *t*-value is modified and calculated by the following equation:[137]

$$t_s = \frac{(X_1 - X_2) - (\mu_1 - \mu_2)}{\sqrt{\left(\frac{S_{d1}^2}{n_1}\right) + \left(\frac{S_{d2}^2}{n_2}\right)}} \qquad \text{[XXXVIII]}$$

Taking a significant level of α=0.05, if the calculated t_s from experimentally determined values is higher than the tabular value, t_t, then we are 100(1-α) % confident to assume that the two samples belong to different statistical populations.

Appendix 1 shows the tabular values, t_t, for the *t*-test at different degrees of freedom, υ, parameter which depends on the number of specimens of each group and is defined as:

$$\upsilon = n_1 + n_2 - 2 \qquad \text{[XXXIX]}$$

6. Materials

This section describes the high strength steels and the metallic sacrificial coatings used in the present research project. Although this work was mainly focused on the 300M and AerMet®100 high strength steels, alternatives alloys GifloM2000 and CSS-42L™ were also considered in some tests. The equipment and characterisation techniques used to study these materials are also described.

6.1. High Strength Steels

The elemental compositions of the high strength steels studied in the present project are shown in **Table 2**. It can be seen that 300M and GifloM2000 high strength steels were micro-alloyed. AerMet®100 was a high alloyed steel with Ni and Co. CSS-42L™ was a martensitic stainless steel with high alloying content of Cr, Ni and Co.

ALLOY	Fe	C	Ni	Cr	Si	Mo	V	Nb	Co	Mn
300M †	bal	0.4	1.8	0.8	1.6	0.25	-	-	-	0.7
AerMet®100†	bal	0.23	11.5	3.1	-	-	-	-	13.5	-
GifloM2000	bal	0.55	1.15	0.4	0.5	0.4	-	-	-	1.55
CSS-42L™†	bal	0.12	2	14	-	4.75	0.6	0.02	12.5	-

† Timken Latrobe. [4, 19, 22]

Table 2. Element nominal compositions (wt%) for 300M, AerMet®100, GifloM2000 and CSS-42L™ high strength steels.

Specimens for microstructural evaluation were sectioned from original tensile test specimens using a Buhler-Isomet2000 precision saw. The sections were mounted in bakelite using a Simplemet2000 automatic hot press. Subsequently, mounted specimens were ground using 120, 240 and 1200 grit silicon carbide paper and polished with 6 and 1 μm diamond suspensions.

To reveal the microstructural characteristics of the alloys, Nital (ethanol and nitric acid) and Vilella's (glycerol, nitric acid and hydrochloric acid) reagents were used to etch the low carbon and the stainless steels, respectively. Final micrographs were taken using a Nikon optical microscope connected to a JVC-3CCD digital camera recording system. Moreover, additional images and corresponding energy dispersive X-ray analyses, *EDAX*, were taken using a Stereoscan 250MK3 Cambridge Instruments and a Philips XL-Series scanning electron microscopes, *SEM*.

Figures 37, **38**, **39**, and **40** show the microstructures of the 300M, AerMet®100, GifloM2000, and CSS-42L™ high strength steels, respectively. The resulting microstructures displayed for all the alloys a sub-micron mixed lath and plate martensitic matrix.

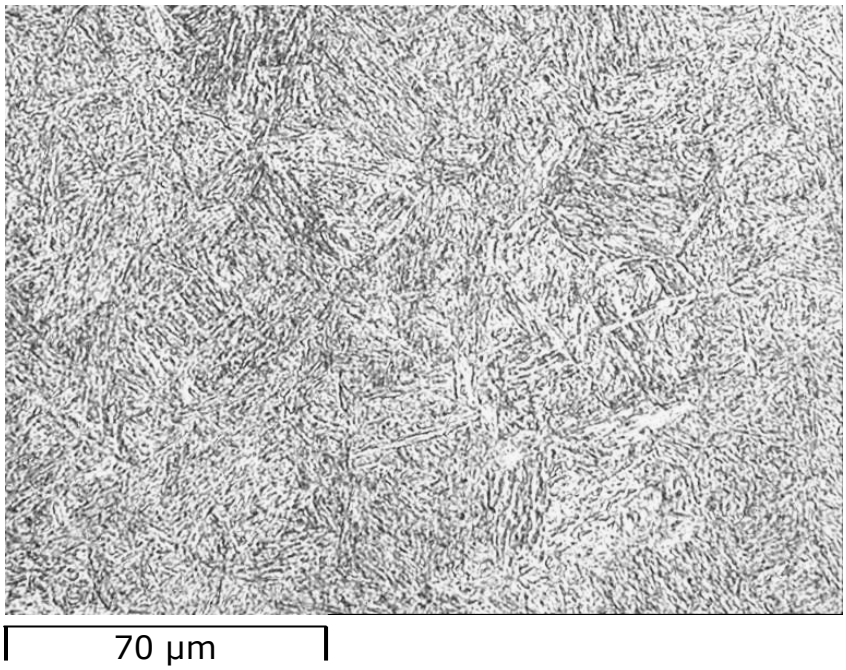

Figure 37. Optical micrograph of 300M steel. (2%Nital)

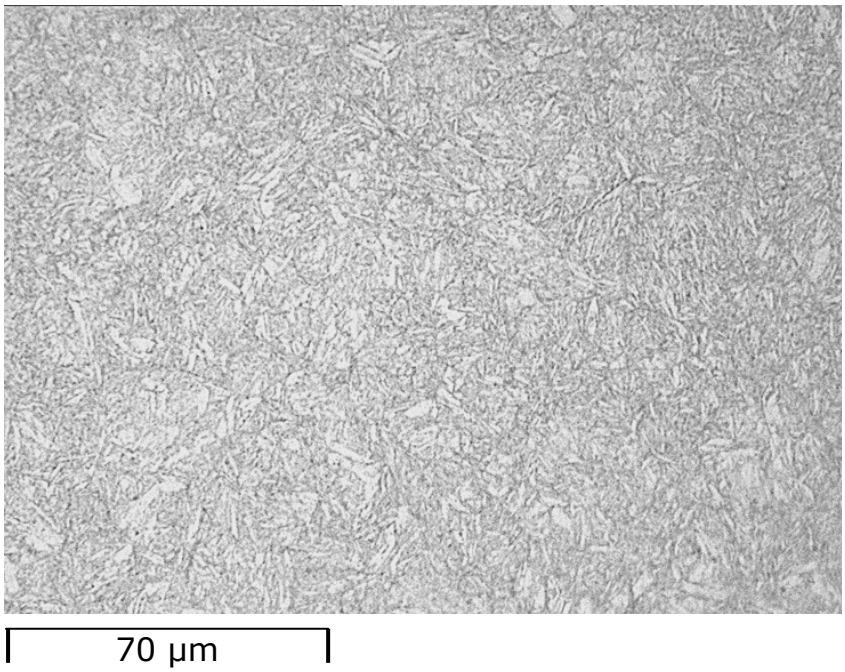

Figure 38. Optical micrograph of AerMet®100. (2% Nital)

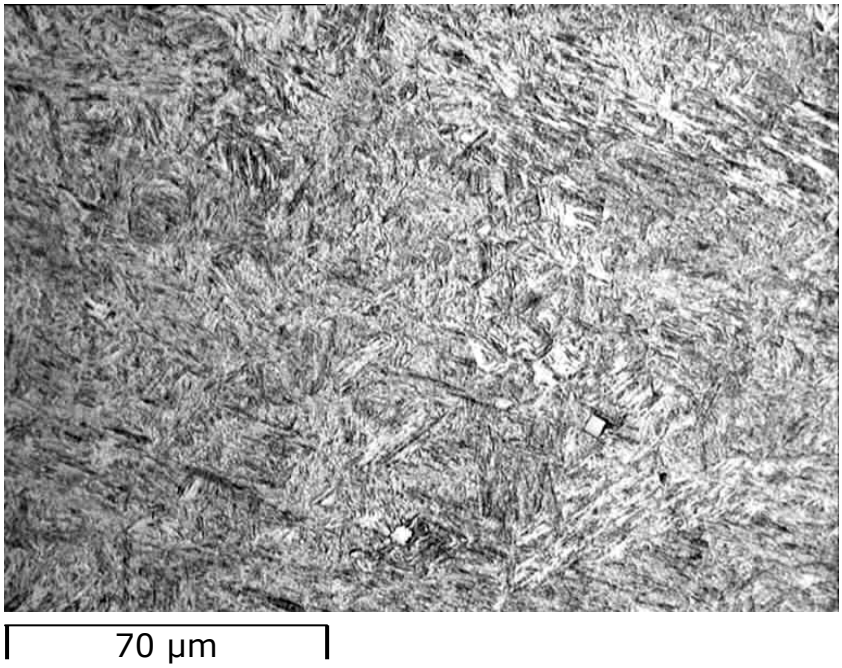

Figure 39. Optical micrograph of GifloM2000. (2%Nital)

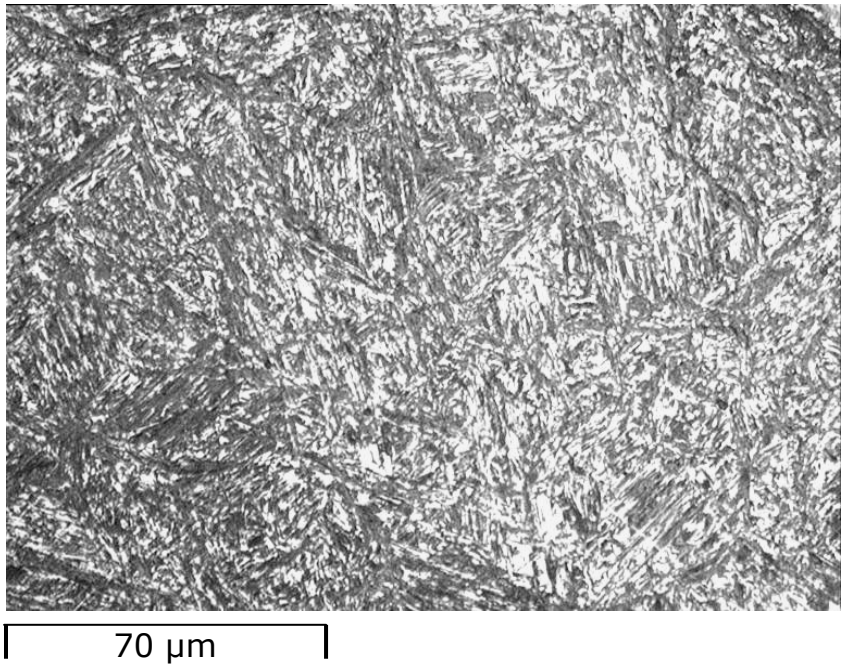

Figure 40. Optical micrograph of CSS-42L™ stainless steel. (Vilella's)

On the other hand, X-Ray quantitative analyses were carried out on AerMet®100 and 300M polished specimens to identify the amount of reverted and retained austenite within the martensitic matrix. The equipment used for this task was a Siemens D5005 X-ray diffractometer with a Co-K_α radiation source. The analysis consisted in the comparison of the relative intensities of the austenite with the martensite corresponding peaks. The X-Ray software package was used to reduced the fluorescence levels obtained in the patterns as well as to identify the different peaks taken into consideration.[138, 139]

6.2. Sacrificial Coatings

Three different metallic sacrificial coatings were selected for this project; electroplated Zinc-14%Nickel and aluminium based SermeTel®1140/962 coatings were compared with the conventional electroplated cadmium. The three coating materials were deposited on tensile specimens of 300M and AerMet®100 steels. In addition, cadmium was also electroplated on GifloM2000 and SermeTel®1140/962 was deposited on CSS-42L™ stainless steel tensile specimens.

Cadmium and Zinc-14%Nickel electroplated specimens were baked to allow hydrogen to diffuse from the steel after the electroplating process, whereas SermeTel®1140/962 coated specimens were only cured and being a non-electrochemical process no further treatment was required.

Metallographic analyses for the metallic sacrificial coatings were carried out following the methodology described in the previous section for the high strength steels. Further, *SEM*, and *EDAX* analyses were performed in order to assess the morphological characteristics and the barrier properties of the coatings in order to establish a correlation with the extent of hydrogen embrittlement or re-embrittlement for the high strength steels. In addition, cross sections of the sacrificial coating were also analysed using a focussed ion beam, *FIB,* workstation, model Philips FEI-FIB200.

6.2.1. Cadmium Coating

The electroplating of cadmium was carried out by Magellan Aerospace Corporation, Bournemouth, UK. Before the electroplating process, tensile specimens were degreased, demagnetised and stress relieved and finally alumina blasted. A chromium passivation layer was applied on top of the sacrificial coating. Some of the electroplated specimens were baked at 200°C for 24 hours whereas others were not baked in order to assess the extent of hydrogen embrittlement produced by the electroplating process.

The cross section of the electroplated cadmium coating is shown in **Figure 41**. It can be seen that the thickness of the electroplated cadmium is approximately 20 μm. Moreover, the degree of porosity within the coating layer has been deliberately designed to allow hydrogen to diffuse out from the steel during baking processes.

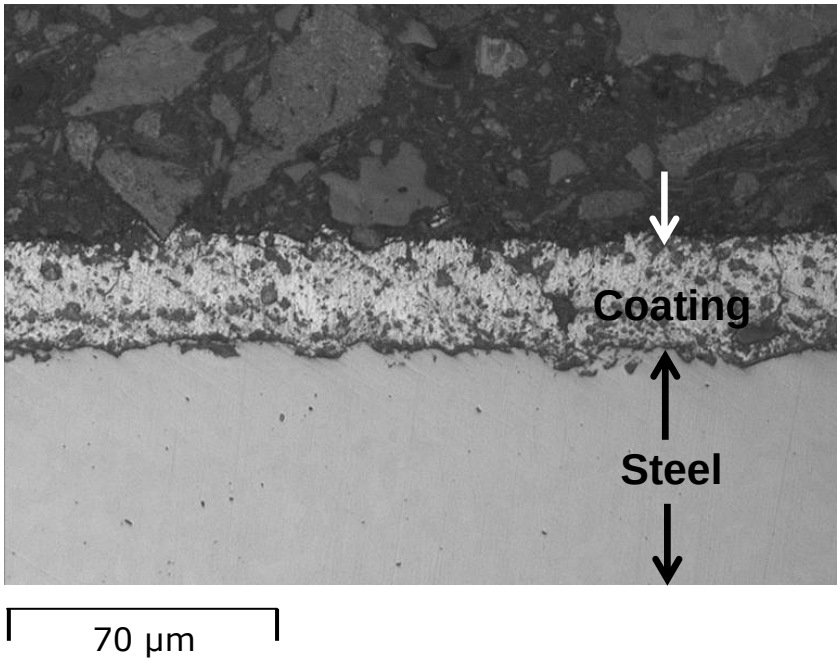

Figure 41. Optical microscopy showing the cross section of the electroplated cadmium coating.

6.2.2. Zinc-Nickel Coating

Electroplating of Zinc-14%Nickel coatings were carried out by South West Metal Finishers, U.K. Technical details about the electroplated process were not specified. A further chromium passivation layer was applied on top of the sacrificial Zinc-14%Nickel coating. Similarly to electroplated cadmium specimens, some of the Zinc-14%Nickel electroplated specimens were baked at 200°C for 24 hours and others were tested without baking to study the extent of direct hydrogen embrittlement produce by the electroplating process. **Figure 42** shows the cross section of the Zinc-

14%Nickel electroplated coating. According to the metallographic analysis the thickness of the electroplated layer was approximately 20 μm.

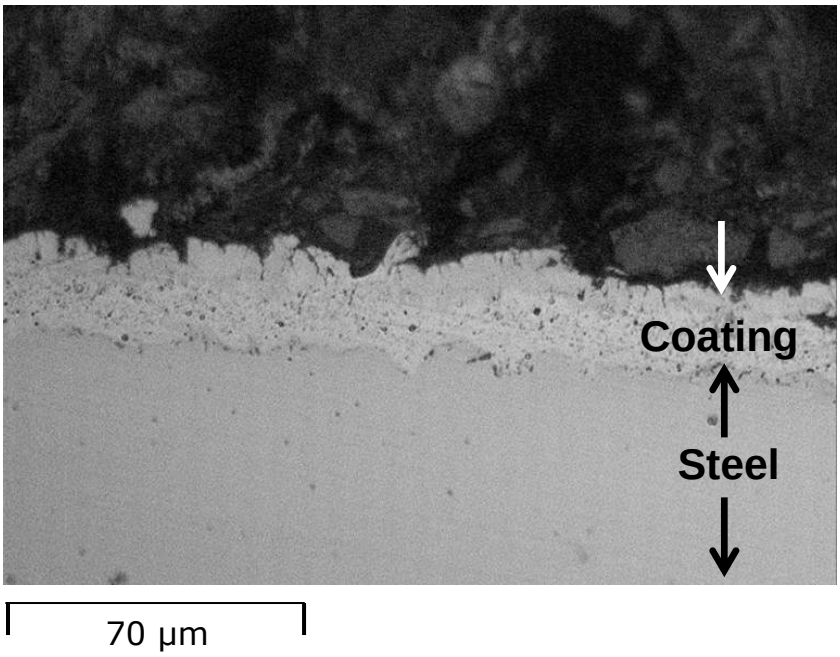

Figure 42. Cross section of the Zinc-14%Nickel electroplated coating.

6.2.3. SermeTel®1140/962 Coating

Tensile specimens of 300M, AerMet®100 and CSS-42L™ were coated with SermeTel®1140/962 at Sermatech International Inc. based in Lincolnshire, U.K. The aluminium based coating together with a ceramic inorganic binder (coating system 962) were applied by spray painting and subsequently cured at temperatures up to 315°C. Further application of a modified polyurethane top-coat layer (top-coat system 1140) was applied on the coating.[17, 68]

Figure 43 shows the cross section of the SermeTel®1140/962 coating. It can be seen that the thickness of the aluminium based coating was approximately 70 μm thick and the polymer topcoat layer 20μm.

Moreover, further *SEM* analysis in **Figure 44** showed that the coating consisted of spherical aluminium particles, with diameters up to approximately 5 μm, held in a chromate/phosphate binder. Corresponding *EDAX* elemental analyses displayed the chemical composition of both particles and binder.

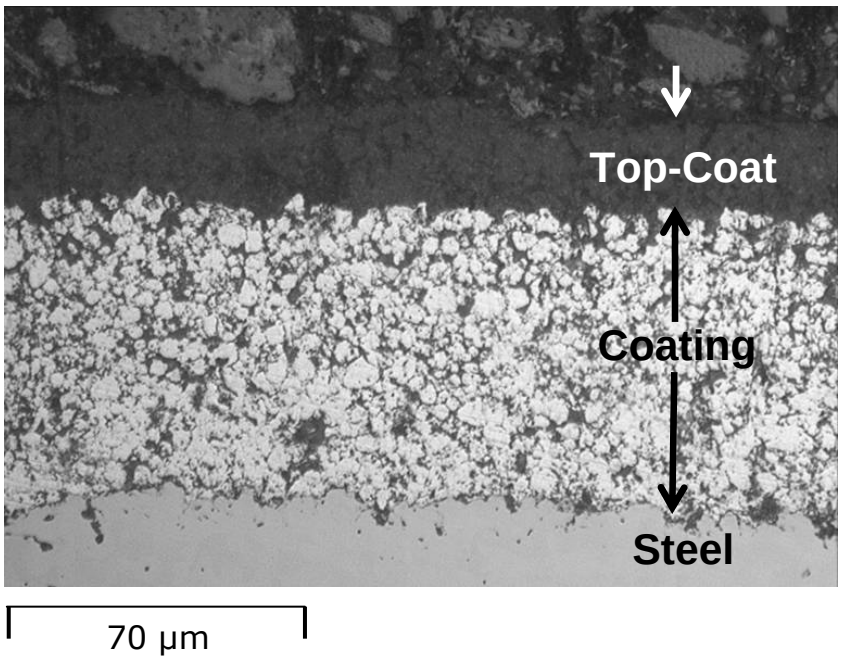

Figure 43. Optical micrograph of SermeTel®1140/962 coated specimen.

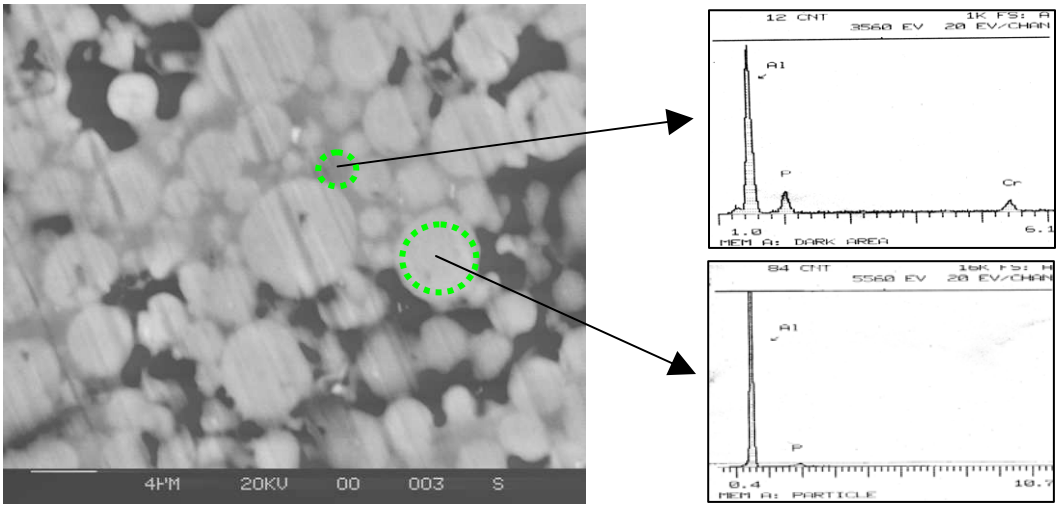

(A) (B)

Figure 44. A) Backscattered Electron *SEM* image for the cross section of SermeTel®1140/962 sacrificial coating, and B) *EDAX* analyses for aluminium particles and the inorganic binder.

6.3. Sacrificial Coatings Barrier Properties

Discontinuities in the sacrificial metallic coatings could lead to hydrogen re-embrittlement of the steel substrate. Porosity and cracks from high internal stresses are the main sources of these discontinuities in sacrificial coatings. These defects were studied for Zinc-14%Nickel electroplated 300M steel panel identified as MISC-1263-11, previously exposed for 6 months to a marine atmosphere, and cut sections from tensile specimens using chemical (colour) and electrographic tests. Moreover, flaws and discontinuities for cadmium and aluminium based SermeTel®1140/962 coatings specimens were assessed on sections from AerMet®100, GifloM2000 and CSS-42L™ tensile test specimens.

The colour chemical tests involved using chemical reagents which caused a colour change in the presence of corrosion products from the substrate, forming distinctive spots at each discontinuity such as pores or cracks.[140] Three main tests were used in these analyses:

6.3.1. Potassium Permanganate Test

In this test the specimens were immersed in a dilute solution of potassium permanganate, (0.15 gr of $KMnO_4$ per litre of distilled water), for 3½ hours. Formation of black markings or spots indicated porosity or discontinuities in the metallic coating.[141, 142] This particular test was used to study the three sacrificial coatings (Cadmium, Zinc-14%Nickel and SermeTel®1140/962).

6.3.2. Copper Sulphate (Preece) Test

Zinc-14%Nickel and cadmium plated specimens were immersed in a neutral copper sulphate solution, (36 g per 100ml distilled water) for 1 minute. After removal, specimens were brushed and rinsed with water to remove any copper deposit formed on the Zinc-14%Nickel or cadmium

coatings. The end point of the test was recognised by the appearance of a bright and adherent copper deposit. [140-142]

This test was not able to detect all the fine cracks and fissures particularly in the sacrificial Zinc-14%Nickel coating and an alternative potassium ferricyanide electrographic test were tried as well.

6.3.3. Potassium Ferricyanide Electrographic Test

In this technique exposed areas of steel substrate were detected by applying a current to promote corrosion and generate Fe^{2+} ions. Migration of Fe^{2+} ions to the coating surface was promoted by the current of 1.5 $\mu A/cm^2$ between the substrate and the electrolyte-soaked paper.[140, 141] **Figure 45** shows an schematic representation of the test.

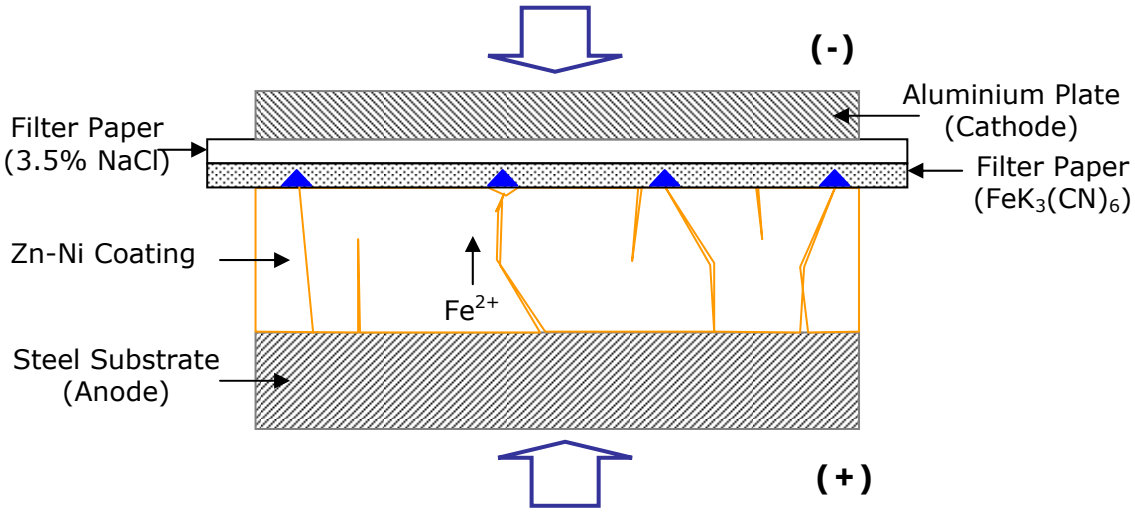

Figure 45. Schematic representation of the potassium ferricyanide electrographic technique.

After exposure, the reagent-soaked paper (0.05% $FeK_3(CN)_6$), was allowed to dry and blue markings or spots indicated coating discontinuities. *FIB*, *SEM* and metallographic analyses were carried out to study the grain size of the coating as well as crack network distributions.

Following British Standard EN ISO 10308:1997,[140] **Table 3** summarises the three chemical porosity tests performed for cadmium, Zinc-14%Nickel and SermeTel®1140/962 coatings on steel substrates:[140, 141, 142]

Tests	Coating Applied	Reagent	Time	Corrosion Products
Potassium Permanganate	• Cadmium • Zinc-14%Nickel • SermeTel®1140/962	$KMnO_4$ (0.15 gr/l)	2-4 hr	Black MnO deposit
Copper Sulphate (Preece Test)	• Cadmium • Zinc-14%Nickel	$CuSO_4$ (360 gr/l)	1-4min	Cu bright deposit
Potassium Ferricyanide	• Zinc-14%Nickel	$FeK_3(CN)_6$ (0.05 %)	1-2min	Blue deposit

Table 3. Porosity Test for Zinc based Coatings on steel substrates. [140-142]

6.4. Sacrificial Coatings Open Circuit Potentials

Cadmium, Zinc-14%Nickel and SermeTel®1140/962 coated specimens were immersed in 3.5% NaCl quiescent solutions for 1200 hours to evaluate variations in the open circuit potential and therefore identify the corresponding potential ranges during re-embrittlement. Moreover, the ennoblement behaviour of the Zinc-14%Nickel coating as well as potential-time changes of the SermeTel®1140/962 coating were also assessed. Complementary surfaces analyses before and after immersion were performed to establish possible morphological changes as the coatings undergo corrosion.

7. Mechanical Testing

Slow rate tensile tests were carried out using a Corrtest Incorporated, C.E.R.T. system Sensotec D-3971-03 *SSRT* equipment. In all cases, specimens were tested for each experimental condition at a strain rate of $9.7x10^{-7}$ s^{-1}. Original cross section areas at the gauge length of each tensile specimen were measured with a Multimoyo micrometer and a Profile Projector Type PJ-300. The dimensions of tensile specimens used for slow strain rate tests are described in **Figure 46**.

LONGITUDINAL VIEW

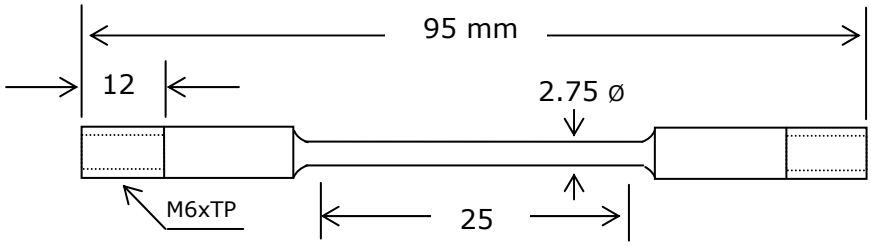

Figure 46. Dimensions of slow strain rate test specimens.

A preload of 50 KNw was applied to the specimens to avoid displacement from any of the equipment components that could affect the recorded data. Results were obtained in terms of Load vs. Time graphs from a Corrtest Incorporated analogue chart recorder and a PC computer connected to the tensile equipment.

Slow strain rate tests were performed both on uncoated tensile specimens and others that have received one of the coating treatments. Further tests were conducted on coated specimens to investigate the effectiveness of the de-embrittlement baking treatment designed to remove absorbed hydrogen. In addition, *SSRT* tests were carried out on coated specimens that had been scribed in the centre of the gauge length to expose the substrate.

These specimens were tested in 3.5% NaCl solution to investigate the extent of re-embrittlement caused by the freely corroding coating. In order to perform these tests, a region of 1mm width was scribed in the centre of the gauge length of the cadmium coated tensile test specimens, as shown in **Figure 47** below.

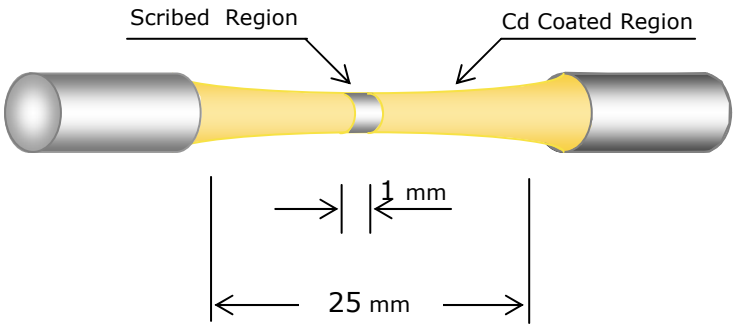

Figure 47. Diagram showing a scribed tensile specimen.

A corrosion cell was designed to contain the test solution, (3.5% NaCl). The cell was made of *PTFE* (Teflon) due to its inert characteristics. The design specifications are shown in following diagram, **Figure 48**.

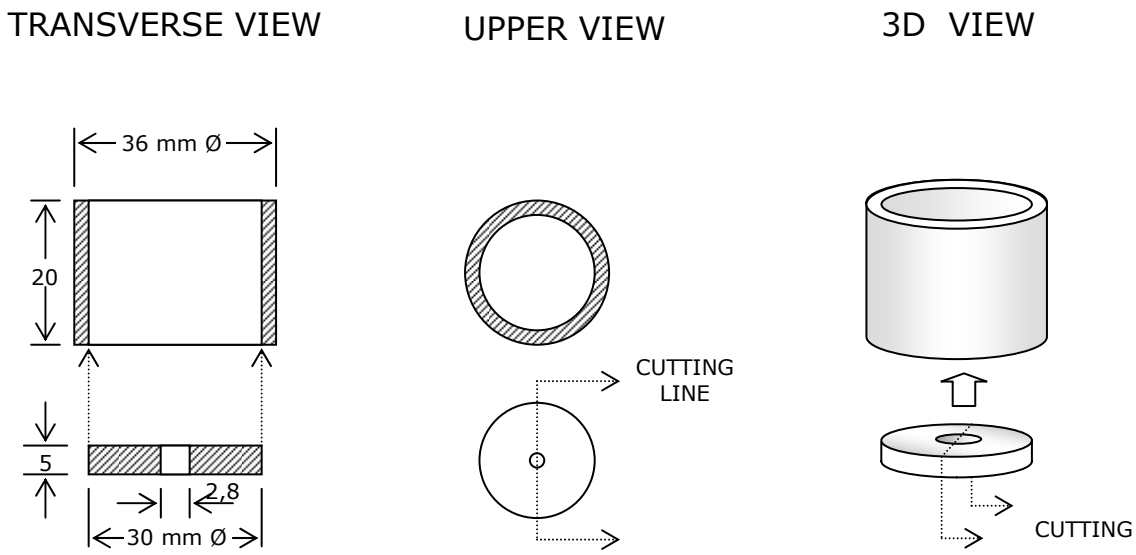

Figure 48. Corrosion cell design for re-embrittlement test.

The mechanical testing programme was carried out on 300M, AerMet®100, GifloM2000 and CSS-42L™ high strength steels at different conditions which are summarized in the following **Table 4**.

	Coating	Condition	Number of Specimens
300M	Uncoated	As Machined	4
	Cadmium	As Plated	4
	Cadmium	Plated + Baked	4
	Cadmium	Scribed, Test in NaCl	4
	Zn/14%Ni	As Plated	4
	Zn/14%Ni	Plated + Baked	4
	Zn/14%Ni	Scribed, Test in NaCl	4
	SermeTel®1140/962	As Coated + Cured	4
	SermeTel®1140/962	Scribed, Test in NaCl	4
AerMet®100	Uncoated	As Machined	4
	Cadmium	As Plated	4
	Cadmium	Plated + Baked	4
	Cadmium	Scribed, Test in NaCl	4
	Zn/14%Ni	As Plated	4
	Zn/14%Ni	Plated + Baked	4
	Zn/14%Ni	Scribed, Test in NaCl	4
	SermeTel®1140/962	As Coated + Cured	4
	SermeTel®1140/962	Scribed, Test in NaCl	4
GifloM2000	Uncoated	As Machined	4
	Cd	Plated + Baked	3
	Cd	Scribed, Test in NaCl	4
CSS-42L™	Uncoated	As Machined	4
	Uncoated	Test in NaCl	4
	SermeTel®1140/962	As Coated + Cured	2
	SermeTel®1140/962	Scribed, Test in NaCl	3

Table 4. Summary of the complete test programme for 300M, AerMet®100, GifloM2000 and CSS-42L™ specimens.

7.1. Analysis of the *SSRT* Results

The embrittlement indices, *EI*, were based on times to failure values, *TTF*, in the slow strain rate test for coated and uncoated or control specimens. This relation is described by the following equation:

$$EI = 1 - \left(\frac{TTF_{coated}}{TTF_{uncoated}} \right) \qquad [\text{XL}]$$

It can be seen from this expression that the lower *EI* values correspond to less hydrogen embrittlement susceptibility. If $EI \geq 0.6$, the specimen was considered to be highly embrittled. In the present research project, the hydrogen embrittlement susceptibilities of 300M, AerMet®100, GifloM2000 and CSS-42L™ steels were evaluated by comparing *EI* values, based on the criteria described above.

A Weibull statistical distribution was used to compare time to failure for all conditions. Results were plotted in terms of natural logarithm of probability of survival, *Ln* P_s, versus *TTF* values. It was shown previously that the probability of survival, P_s, is the complementary value of the probability of failure, P_f. The latter value for a specific environmental condition applied to a batch of 4 tensile specimens was calculated as follows:

$$P_f = \frac{n}{(n+1)}; \quad (\text{n} = 1, 2, 3, 4) \qquad [\text{XLI}]$$

In addition, student *t*-test analyses were performed in order to determine whether there was a statistically significant difference between two sets of data. Moreover, the mean value of embrittlement indices for each condition was used to compare the extent of hydrogen embrittlement for all conditions.

7.2. Fractographic Analyses

Fractographic analyses for the most embrittled cadmium plated 300M and AerMet®100 tensile specimens were carried out in order to identify the exact mode of fracture due to hydrogen embrittlement. The analyses involved a careful metallographic examination of the fracture surfaces after the *SSRT*'s using *SEM* and *EDAX* techniques.

It is known that the fracture mechanisms taking place along the fracture surface depended upon the stress intensity factor and the concentration of the hydrogen at the crack tip.[143] The fracture surfaces of embrittled tensile specimens exhibited a brittle to ductile transition failure. At the regions of inter-granular fracture, *IG*, occurring by interface separation of grain boundaries, were identified with a red colour. Meanwhile, outer and central regions with ductile failure modes were identified with green and yellow colours, respectively. Micro-void coalescence fracture mechanism corresponded to these latter conditions. Finally, ductile-to-brittle transition regions which generally displayed quasi-cleavage fractures were identified with orange colour. Quantitative analyses of the fracture mechanisms distribution were carried out using the *UTHSCA Image Tool* for *Windows* software, version 3.0. This methodology was carried out on the eight cadmium plated 300M and AerMet®100 specimens.

8. Hydrogen Transport Characteristics

This section describes the methods and equipment used to assess the hydrogen transport characteristics in terms of diffusivity for the high strength steels studied. Moreover, the techniques used to determine the total amount of hydrogen evolving on the steel surface during the re-embrittlement process are shown.

8.1. Hydrogen Evolution Reaction

Potentiodynamic measurements were carried out to plot the cathodic polarisation curve for the following reaction:

$$H_2O + e^- \rightarrow H + OH^- \qquad [10]$$

And thus the total amount of hydrogen that was generated at the steel surface at specific values of potential were determined. Some, but not all, of this hydrogen entered and diffused through the steel and was therefore detected during the permeation measurements. **Figure 49** shows a schematic representation of the cell used for this experiment.

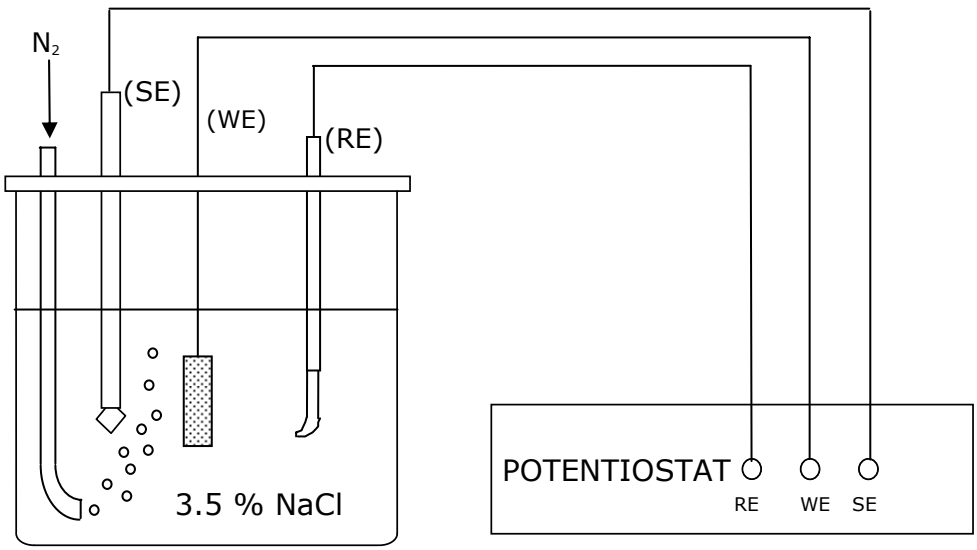

Figure 49. Experiment setup for cathodic polarisation measurements.

The potentiodynamic measurements were carried out in de-aerated 3.5% NaCl solution. Nitrogen bubbling was used to reduce levels of dissolved oxygen in the solution, suppressing the oxygen reduction cathodic reaction. Results from these measurements were reported by means of plots of potential, *E*, versus the logarithm of the current density, $Log_{10}(i)$. The gradients (Tafel slopes) were determined and used to establish a relationship between amount of hydrogen evolving on the steel surface and the amount of hydrogen that was taken up by the steel the during re-embrittlement process.

8.2. Hydrogen Diffusion Measurements

8.2.1. Permeation Technique

Hydrogen transport in the high strength steels was measured using the hydrogen permeation technique. The aim of these tests was to measure hydrogen uptake by the different high strength steels at the potential of the corroding sacrificial coatings. This electrochemical method determined the amount of electrolytic hydrogen diffusing through a thin steel membrane using a Devanathan and Stachurski [114] double cell, as is shown **Figure 50**.

The charging side of the cell was held at a range of potentials from –0.900 to -1.250 volts (SCE) to promote the generation and uptake of hydrogen on the surface of a low carbon steel shim as well as 300M and AerMet®100 steel membranes. As a result, hydrogen diffused through the steel and was oxidised and detected on the depletion side, which was held at -0.094 volts (SCE). To keep the potential values at the charging and depletion sides of the cell, a Sycopel Ministat Precision Potentisotat and a Sycopel Scientific portable electrochemical workstation AWE2 were used, respectively. The electrolyte in both sides of the cell was 0.2 M NaOH solution.

The experimental conditions required for the permeation measurements were established by carrying out initial tests using low carbon steel

membranes. These were in the form of 0.04 % C steel shim 57 μm thick. The membranes of the 300M and AerMet®100 steels were prepared using high precision grinding equipment at Cranfield University. Steel plates were supplied with a thickness of 6 mm and this was reduced to 1 mm by grinding material alternately from each side.

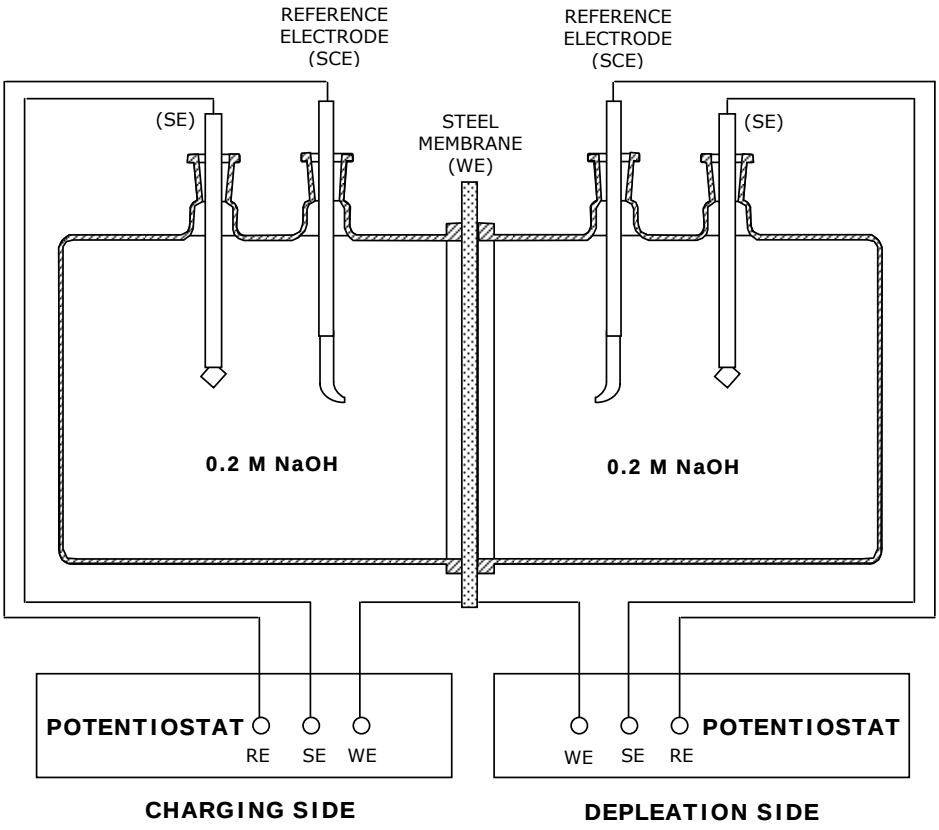

Figure 50. Modified Devanathan and Stachurski[114] permeation cell.

A Barkhausen[144] noise technique was used to detect any microstructural changes on the surface of each membrane that could have been caused by the grinding process. In the Barkhausen noise technique the magnetization of different domain regions on the surface are recorded by a conducting coil. Elastic stresses and the hardness of the material affect the recorded signal, providing information of its microstructural condition.

Residual stresses as well as microstructural changes induced by the grinding process can be detected by this technique. The measurements showed that there was no increase in the Barkhausen noise after the

plates had been ground and it can be concluded that no detectable grinding damage was introduced. **Figure 51** shows that the 300M and AerMet®100 steel membrane dimensions were 10 x 10 cm, and the effective area used in the tests was 50.3 cm^2.

The hydrogen diffusion coefficient of the steel can be calculated using the time lag, t_{lag}, and the breakthrough time, t_b, methods previously described in the literature review. In addition, the internal hydrogen concentration, C_o, just below the steel surface at the charging side of the cell was also determined by using the following equation:

$$C_0 = \frac{J_\infty L}{F D} \qquad [XLII]$$

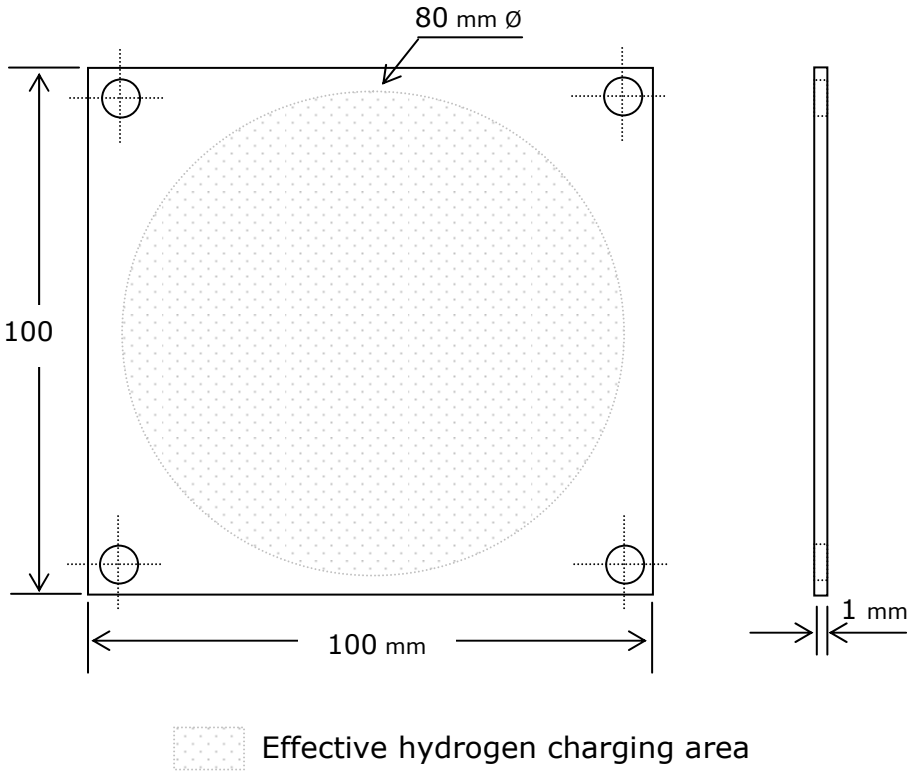

Figure 51. Steel membrane for the hydrogen permeation cell.

8.2.2. Effect of Residual Stresses on Hydrogen Diffusion

The effect of residual stresses on hydrogen transport characteristics were analysed for the 300M membrane. Compressive residual stresses due to surface treatments such as shot peening might affect the hydrogen solubility, diffusivity and the susceptibility to hydrogen embrittlement. It is well known that these treatments are commonly used to enhance fatigue resistance of the steel structural components.

The electrochemical permeation method was used to measure hydrogen diffusion coefficients and internal hydrogen concentrations for an untreated 300M steel membrane at a potential of -1.250 volts (SCE). The electrolyte used was 0.2 M NaOH. The results were compared to those obtained after charging the same membrane following a shot peening treatment. The surface treatment induced a degree of plastic deformation and therefore compressive residual stresses were produced on the membrane surface.

Shot peening of the membrane was carried out at Metal Improvement Company. LLC, Newbury, Berks. Compressive stresses induced by this surface treatment were reported to represent approximately 50% of the yield strength of the alloy. The process was monitored by use of the Almen test in which two samples of spring steel were peened at the same time as the membrane. The required stress level was achieved by peening the membrane on both sides with AF glass beads and the corresponding deflection produced in a N-type Almen strip was in the range 0.004-0.006 inch (100-150 μm).

8.2.3. Galvanostatic Charging

The galvanostatic electrochemical method was also used to determine hydrogen diffusion coefficients for 300M, AerMet®100, GifloM2000 and CSS-42L™ high strength steels. Hydrogen charging conditions were applied by maintaining a constant hydrogen flux at the electrode-electrolyte interface. **Figure 52** depicts the electrochemical cell used for this technique.

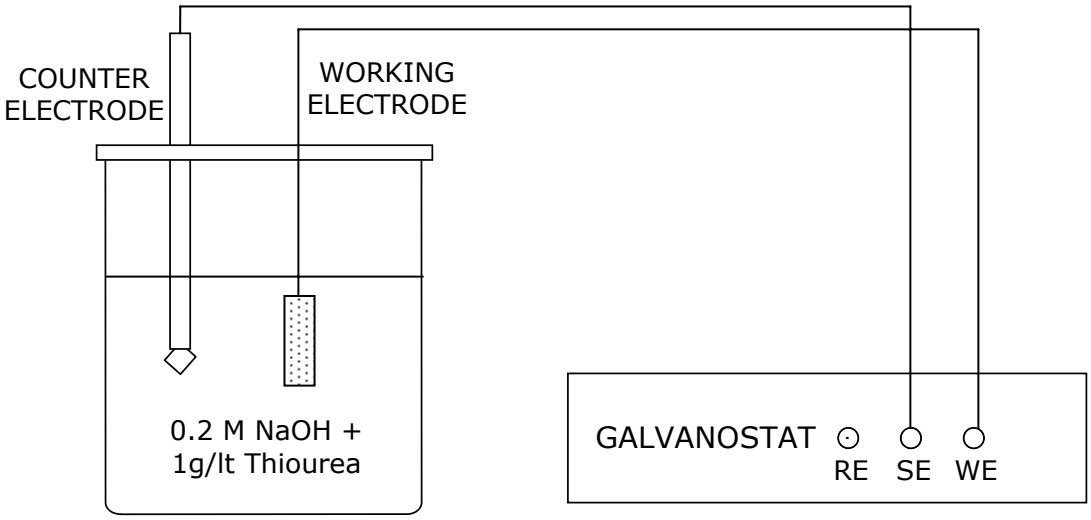

Figure 52. Galvanostatic hydrogen charging cell.

A charging current density of 1mA/cm^2 was applied to the steels for a period of time between 24 to 48 hours, to promote hydrogen evolution and uptake on its surfaces. The electrolyte used was 0.2 M NaOH with additions of 1g/l of thiourea, which acted as a hydrogen recombination poison.

The working electrode potential could be measured as a function of time either with respect to a standard reference electrode (i.e. SCE) or as the absolute value of cell voltage (against Pt counting electrode). It was assumed that $\left| \partial E_{Elcetrode} / \partial t \right| = \left| \partial E_{Cell} / \partial t \right|$. Hence, the potential difference

between the steel electrode and the platinum anode was monitored as a function of time.[119]

These potential differences at the cell provided a measure of hydrogen diffusion into the steel specimen. The fact that the hydrogen bubbling was suppressed using hydrogen recombination poisons and that no additional corrosion reactions occurred in the electrolytic cell, indicates that only diffusion of hydrogen is associated with the changes in potential, *E*. [117, 119]

The 300M, AerMet®100 steel specimens were cut in order to obtain effective hydrogen charging areas of 1.44 and 2.52cm^2. These rectangular samples were ground on all sides using 120, 240, 1200 grinding paper and polished to 1μm diamond finish.

The two opposite faces of these specimens were galvanostatically charged and the rest of the surfaces were coated with resistant lacquer (Lacomit). Effective specimen thicknesses used for diffusion calculations were 0.1 for 0.2 cm thick specimens.

8.2.4. Effect of Elastic Stresses on Hydrogen Diffusion

Hydrogen transport characteristics in terms of diffusion coefficients were analysed and compared for 300M, GifloM2000 and CSS-42L™ high strength steels. The constant current chrono-potentiometry electrochemical method was used to charge parallel faces of flat tensile specimens with hydrogen. The effect of applied elastic stresses on the diffusion coefficients was determined by simultaneously applying different tensile stress levels while maintaining a constant hydrogen flux at the electrode-electrolyte interface.

Figure 53 shows a schematic representation of the electrochemical cell used for this technique. A charging current density of 0.69 mA/cm^2 was applied to the steels for a period of 8 hours to promote hydrogen evolution and uptake. The electrolyte used was 0.2 M NaOH with 1g/l of thiourea, which acted as a hydrogen recombination poison.

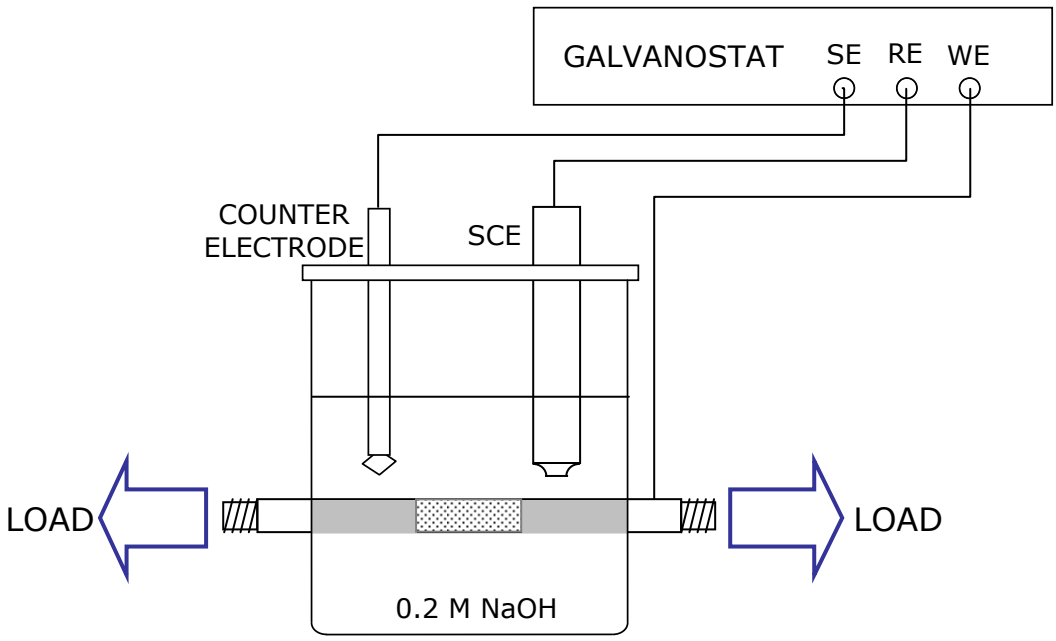

Figure 53. Galvanostatic hydrogen charging under elastic stresses.

The electrochemical cell was mounted in a Hounsfield tensometer with Sagamo Transducer Series-150 and a maximum load capacity of 13.3 KN. Current density was maintained by using the Sycopel Scientific portable electrochemical station AEW2.

For these experiments, cylindrical tensile specimens of 300M, GifloM2000 and CSS-42L™ steels were ground on parallel faces to produce a rectangular cross section with dimensions of 5.0 X 0.6 x 0.2 cm, as is depicted in **Figure 54**. Each of the surfaces were ground and polished using 120, 240, 1200 and 2400 grinding paper.

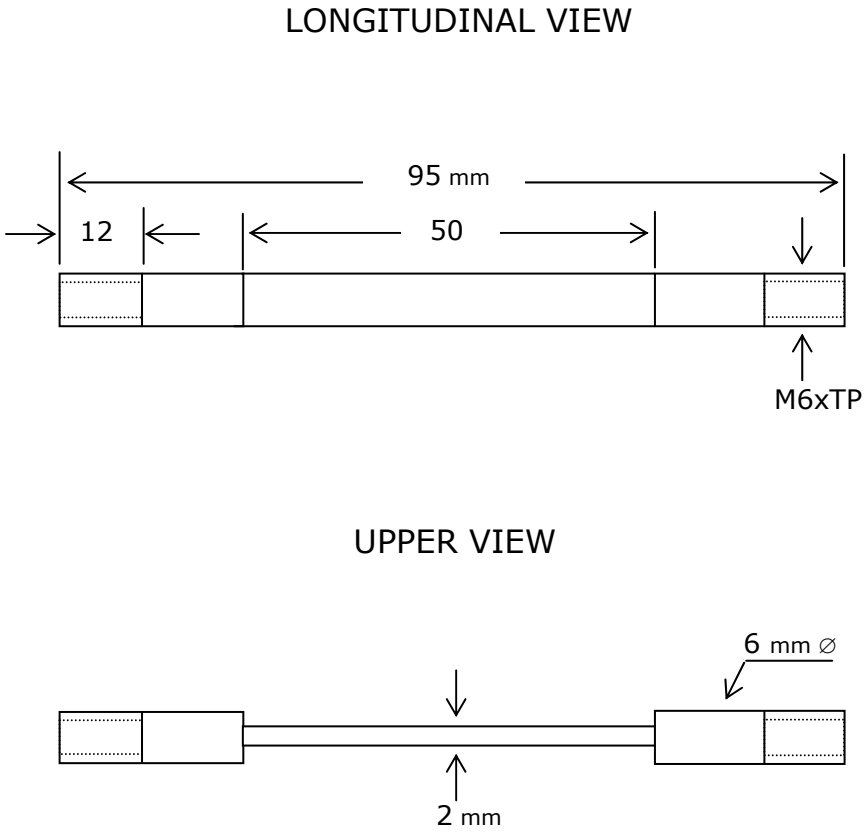

Figure 54. Steel specimens used for hydrogen charging experiments under elastic stress.

The two opposite faces had an effective hydrogen charging area of 1.44 cm^2 each and the rest of the surfaces were coated with an acid resistant lacquer (Lacomit). The specimen thickness was 0.2 cm but as hydrogen was charged on both faces, the effective thickness used for diffusion calculations was 0.1 cm.

9. Mechanical Testing

This section has been divided in three sets of analyses including: mechanical properties of the uncoated high strength steels, slow strain rate test results and the fractographic analyses of the most embrittled cadmium plated 300M and AerMet®100 tensile specimens.

9.1. Mechanical Properties of Steels

Mechanical properties of uncoated 300M specimens are shown in **Figure 55**. It can be seen that the ultimate tensile strength and the yield strength for this alloy were 2250 and 2000 MPa, respectively. It is important to mention that points randomly distributed out of the trend line were produced due to electronic noise from the data recording system.

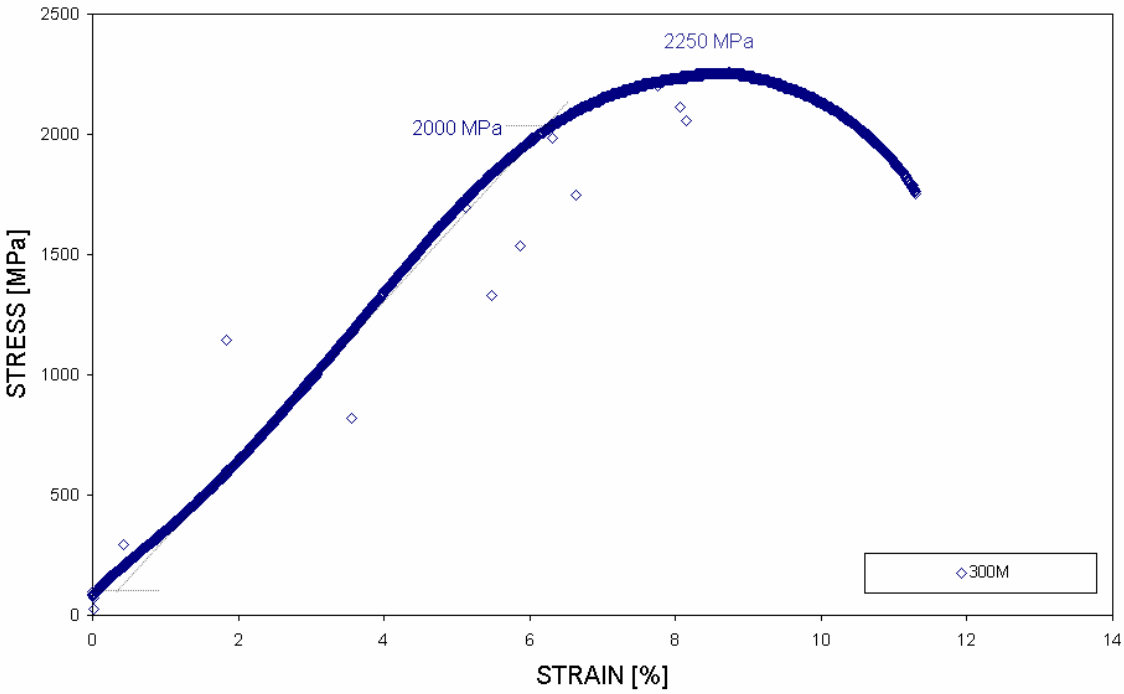

Figure 55. Stress-Strain graph for uncoated 300M steel specimens.

Moreover, the corresponding stress-strain graphs for uncoated AerMet®100, GifloM2000, and CSS-42L™ specimens are shown in **Figures 56**, **57** and **58**. It can be seen that the ultimate tensile strengths were 2093, 2066 and 2030MPa for AerMet®100, GifloM2000 and CSS-42L™,

respectively. In the same order, their corresponding yield strengths were 1900, 1800 and 1580 MPa approximately.

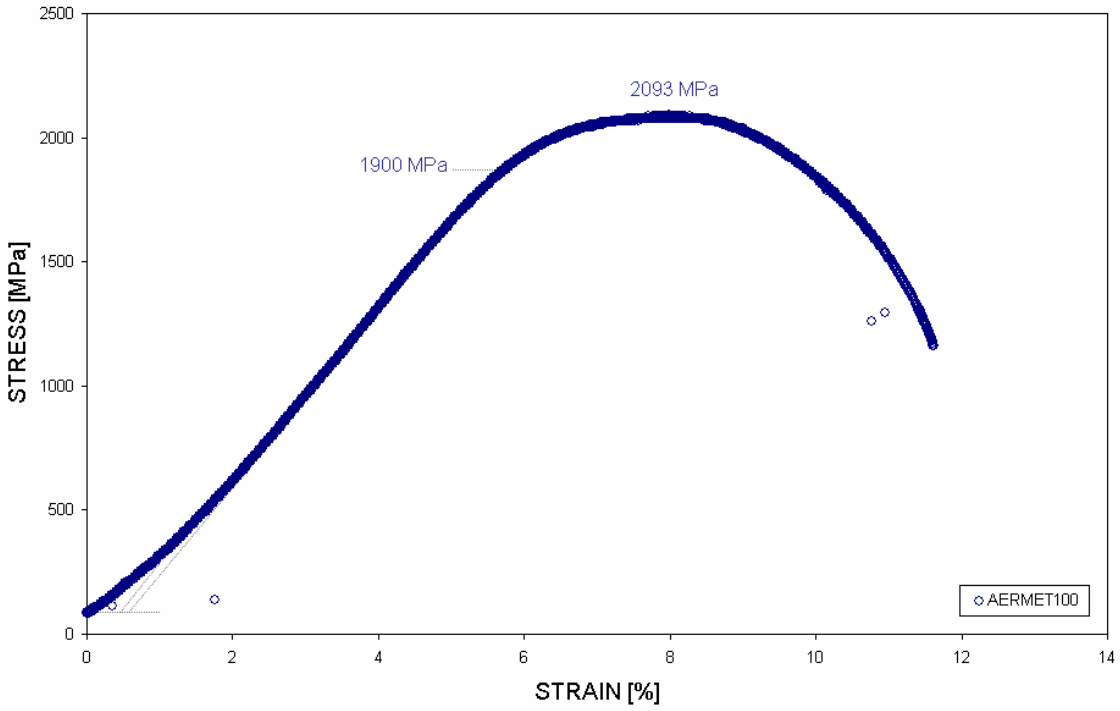

Figure 56. Stress-Strain graph for uncoated AerMet®100 steel specimens.

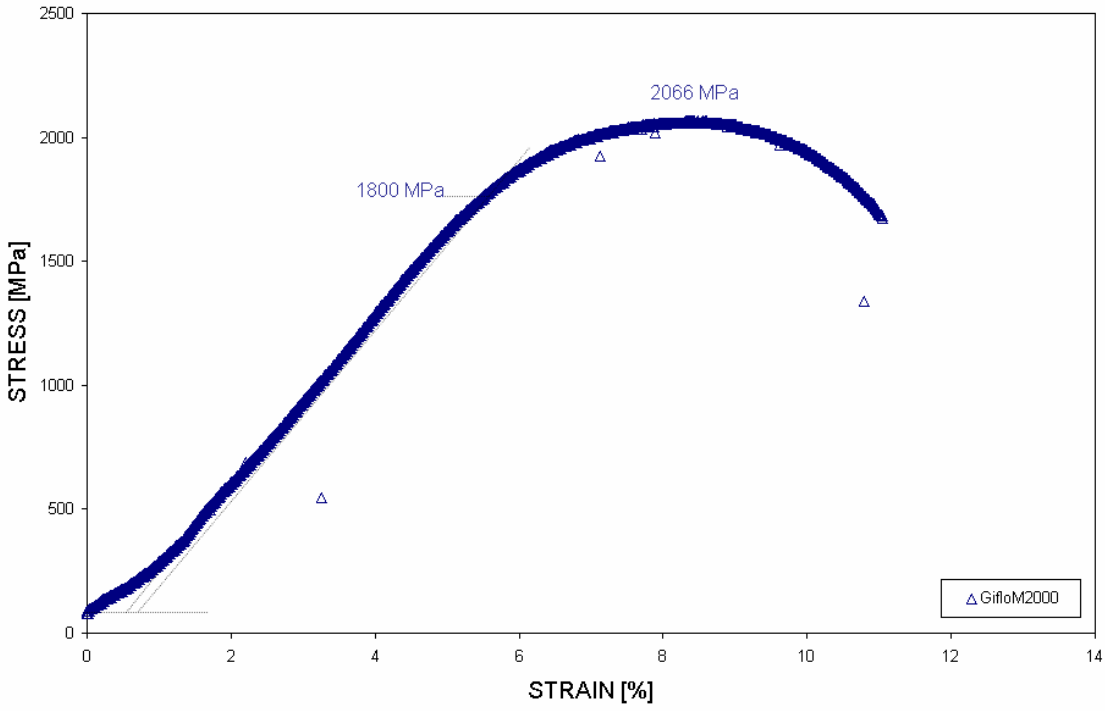

Figure 57. Stress-Strain graph for uncoated GifloM2000 steel specimens.

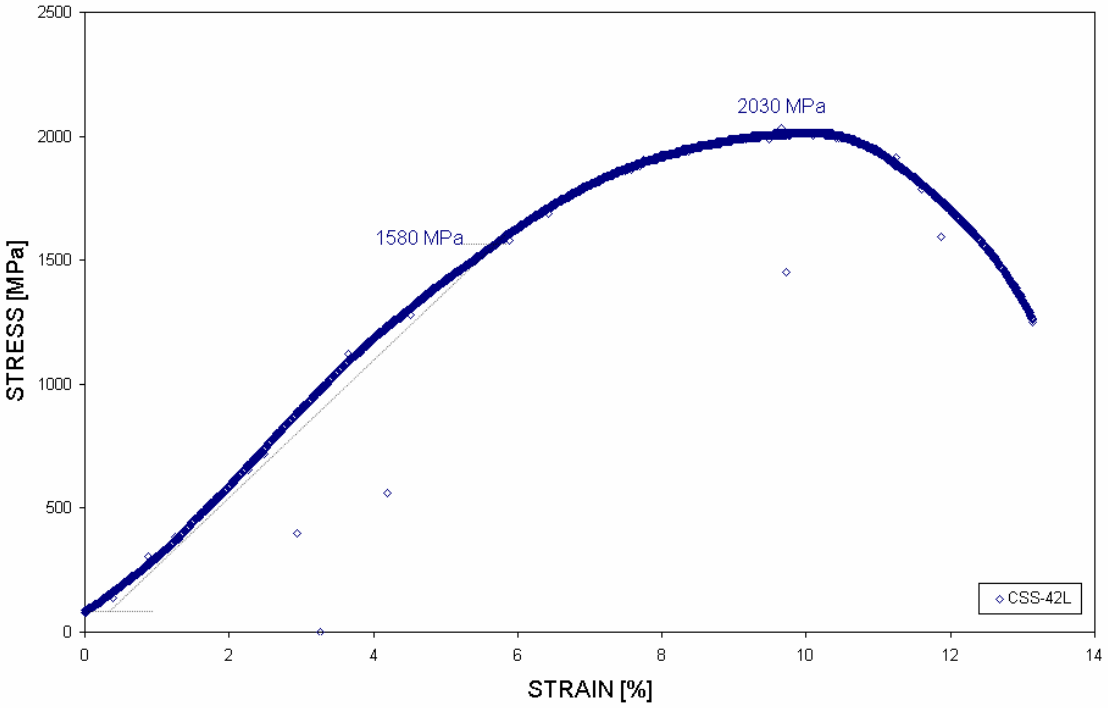

Figure 58. Stress-Strain graph for uncoated CSS-42L™ stainless steel specimens.

9.2. Slow Strain Rate Results, *SSRT*

The effect of the three sacrificial coatings at different test conditions, previously described in **Table 4**, are displayed in terms of Weibull graphs for the *SSRT* tests. In addition, the mean time to failure, *TTF*, embrittlement indices values, *EI*, as well as the student *t*-test statistical analyses between sets of conditions are displayed in tables following their corresponding Weibull plots. The complete excel spreadsheet containing the *SSRT* data is displayed in the **Appendix 2**.

9.2.1. 300M Specimens

The Weibull plot for uncoated, cadmium plated, cadmium plated and baked and cadmium plated baked and corroded 300M specimens is shown in **Figure 59**. It can be seen a substantial decrease in the mean time to failure value for 300M specimens due to cadmium electroplating.

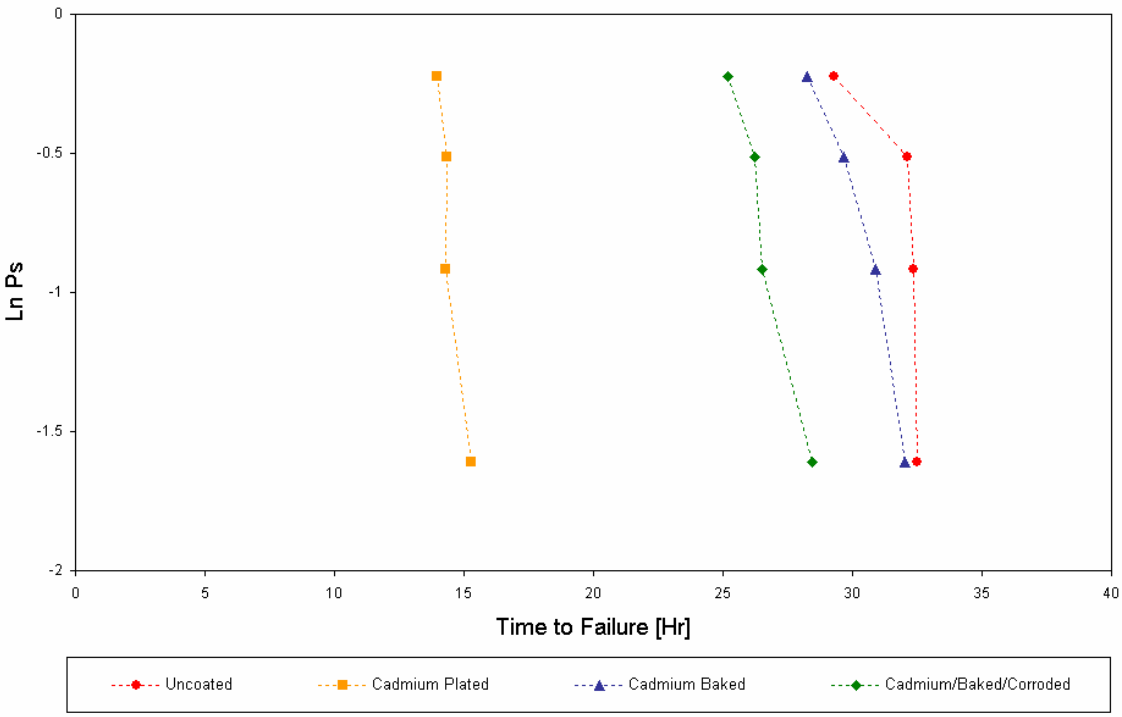

Figure 59. Weibull distribution for uncoated, cadmium plated, cadmium plated and baked and cadmium plated, baked and corroded 300M specimens.

The mean *TTF* value decreased from 31.6 hours, for uncoated specimens, to 14.5 hours when the specimens were cadmium plated. However, baking the cadmium plated specimens for 24 hours at 200°C gave almost a complete recovery, exhibiting a mean *TTF* value of 30.2 hours. A student *t*-test analysis has shown that this mean *TTF* value is not statistically different from the control group. The details of this analysis are described in **Table 5**. In addition, considerable re-embrittlement was found for cadmium plated 300M specimens that were baked and then corroded in 3.5 % NaCl solution. The mean *TTF* values decreased from 31.6 to 26.6 hours.

Specimens	*n*	Mean *TTF*, [Hr]	S_d	Mean *EI*	*t* tabular	*t* statistic	Result
Uncoated 300M Batch I	4	31.57	1.52	-	-	-	-
Cadmium Plated	4	14.46	0.56	0.54	2.447	21.10	$t_s > t_t$
Cadmium, Baked	4	30.20	1.62	0.04	2.447	1.23	$t_s < t_t$
Cadmium, Baked, Corroded	4	26.59	1.37	0.16	2.447	4.87	$t_s > t_t$

Table 5. Student *t*-test analyses for uncoated, cadmium plated, cadmium plated and baked and cadmium plated, baked and corroded 300M specimens.

Weibull plots for uncoated, SermeTel®1140/962 coated and SermeTel®1140/962 coated and corroded 300M specimens are shown in **Figure 60**. The mean time to failure values measured for these conditions were approximately 31.6, 33.8 and 23.2 hours, respectively. SermeTel®1140/962 coated and corroded 300M specimens showed a considerable reduction in the mean *TTF* values from 31.6 to 23.2 hours.

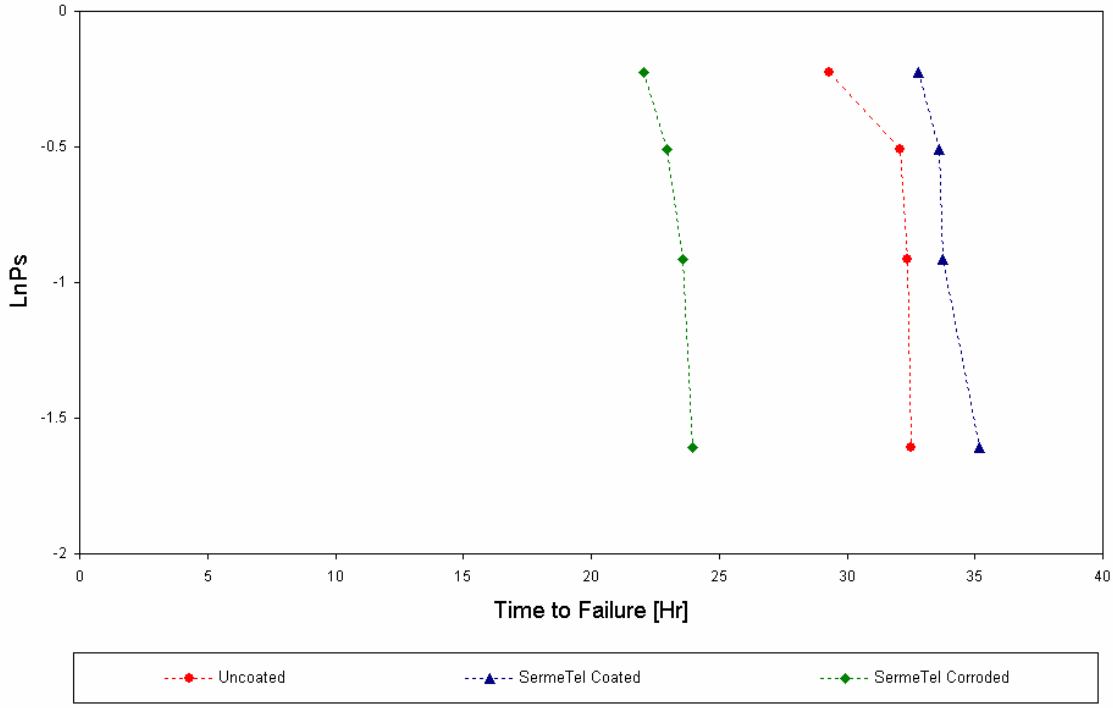

Figure 60. Weibull distribution for uncoated, SermeTel®1140/962 coated and SermeTel®1140/962 coated and corroded 300M specimens.

However, following the curing treatment between 191 and 343°C the mean *TTF* values slightly increased to 33.8 hours compared with the 31.6 hours for the uncoated controls. The student *t*-test, shown in **Table 6**, revealed with 95% of confidence level that this difference is considered to be statistically significant as these two groups of specimens do not belong to the same population.

Specimens	*n*	Mean *TTF*, [Hr]	S_d	*EI*	*t* tabular	*t* statistic	Result
Uncoated 300M Batch I	4	31.57	1.52	-	-	-	-
SermeTel1140/ 962	4	33.82	0.99	-0.07	2.447	2.47	$t_s > t_t$
SermeTel1140/ 962, Corroded	4	23.15	0.85	0.27	2.447	9.66	$t_s > t_t$

Table 6. Student *t*-test analyses for uncoated, SermeTel®1140/962 coated and SermeTel®1140/962 coated and corroded 300M specimens.

Figure 61 shows the Weibull plots for un-plated, Zinc-14%Nickel plated, Zinc-14%Nickel plated and baked and Zinc-14%Nickel plated, baked and corroded 300M specimens. The mean time to failure decreased from 31.6 for the controls to 17.4 hours for Zinc-14%Nickel plated specimens. Following baking the mean *TTF* recovered to 31.4 hours.

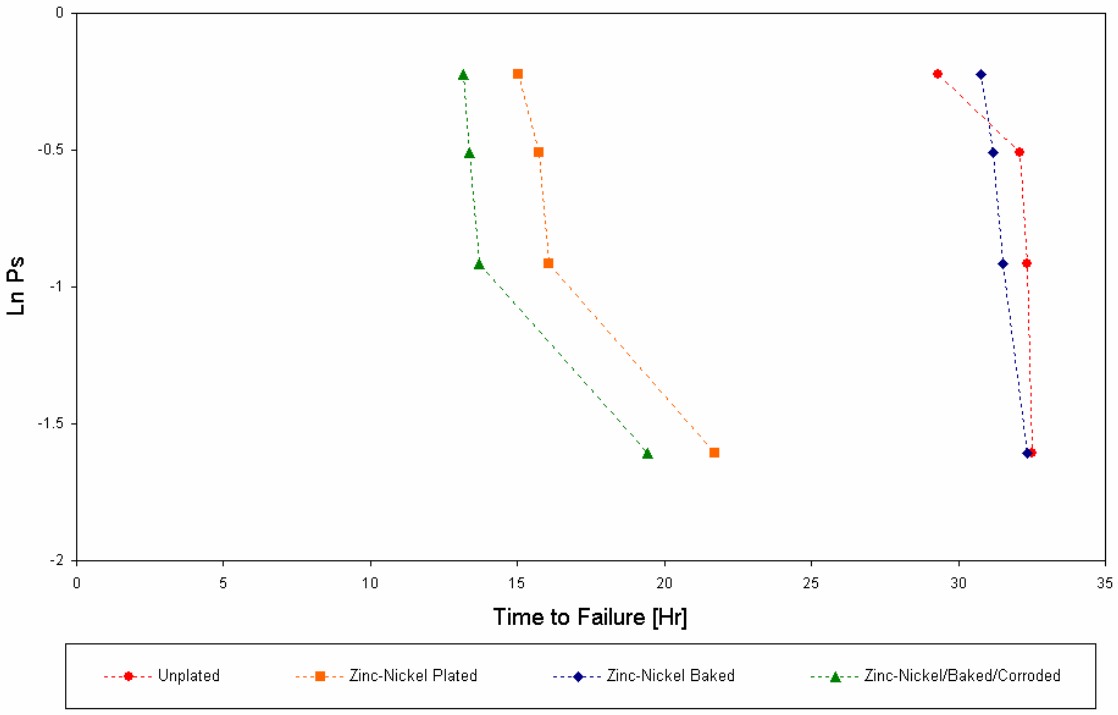

Figure 61. Weibull distribution for Zinc-14%Nickel plated, Zinc-14%Nickel plated and baked and Zinc-14%Nickel plated, baked and corroded 300M specimens.

When the Zinc-14%Nickel was exposed to 3.5% NaCl during the *SSRT* severe hydrogen re-embrittlement occurred and the mean *TTF* was reduced to 15 hours. Student *t*-test analyses displayed in **Table 7** showed that Zinc-14%Nickel plated and Zinc-14%Nickel, baked and corroded conditions showed with 95% of confidence level a statistically significant difference with the control unplated group. Therefore, these treated conditions belong to different statistical populations.

Specimens	*n*	Mean *TTF*, [Hr]	S_d	Mean *EI*	*t* tabular	*t* statistic	Result
Uncoated 300M Batch I	4	31.57	1.52	-	-	-	-
Zinc-14%Nickel	4	17.14	3.09	0.46	2.447	8.37	$t_s > t_t$
Zinc-14%Nickel, Baked	4	31.44	0.67	0.01	2.447	0.16	$t_s < t_t$
Zinc-14%Nickel, Baked, Corroded	4	14.92	3.02	0.53	2.447	9.84	$t_s > t_t$

Table 7. Student *t*-test analyses for Zinc-14%Nickel plated, Zinc-14%Nickel plated and baked and Zinc-14%Nickel plated, baked and corroded 300M specimens.

9.2.2. AerMet®100 Specimens

The corresponding results for the cadmium plated, plated and baked and plated, baked and corroded AerMet®100 are shown in **Figures 62**. It can be seen that there was only a slight reduction in the mean *TTF* values from 32.9 to 31.1 hours for uncoated and cadmium plated specimens, respectively. Moreover, cadmium plated and baked specimens showed a complete recovery of the mechanical properties with a mean *TTF* value of 32.0 hours.

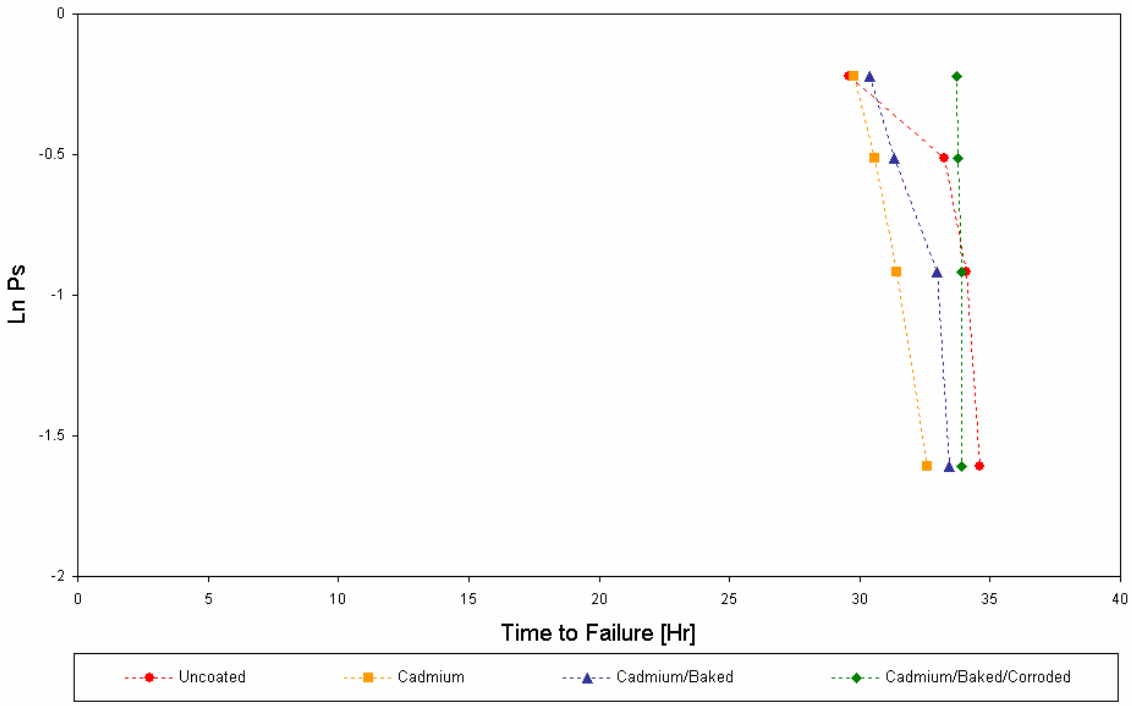

Figure 62. Weibull distribution for uncoated, cadmium plated, cadmium plated and baked and cadmium plated, baked and corroded AerMet®100 specimens.

Student *t*-test showed that there was not significant statistical difference between cadmium plated and cadmium plated and baked conditions compared with the control uncoated specimens. In addition, specimens that were exposed to 3.5% NaCl solution did not display any re-embrittlement and, in fact, there was a small increase in the mean *TTF* value.

Based on the 95% confidence limit for the statistical student *t*-test analysis, it has been shown that there was not a statistically significant difference between *TTF* values of the cadmium plated, baked and corroded specimens and the controls.

Specimens	*n*	Mean *TTF*, [Hr]	S_d	Mean *EI*	*t* tabular	*t* statistic	Result
Uncoated AerMet100	4	32.89	2.26	-	-	-	-
Cadmium Plated	4	31.10	1.20	0.05	2.447	1.40	$t_s < t_t$
Cadmium Plated/ Baked	4	32.03	1.43	0.03	2.447	0.64	$t_s < t_t$
Cadmium Plated/ Baked / Corroded	4	33.82	0.10	-0.03	2.447	0.83	$t_s < t_t$

Table 8. Student *t*-test analyses for uncoated, cadmium plated, cadmium plated and baked and cadmium plated, baked and corroded AerMet®100 specimens.

Weibull plots for uncoated, SermeTel®1140/962 coated and SermeTel®1140/962 coated and corroded AerMet®100 specimens are shown in **Figure 63**. These Weibull plots revealed negligible differences between mean *TTF* values of approximately 32.9, 33.5 and 33.9 hours respectively.

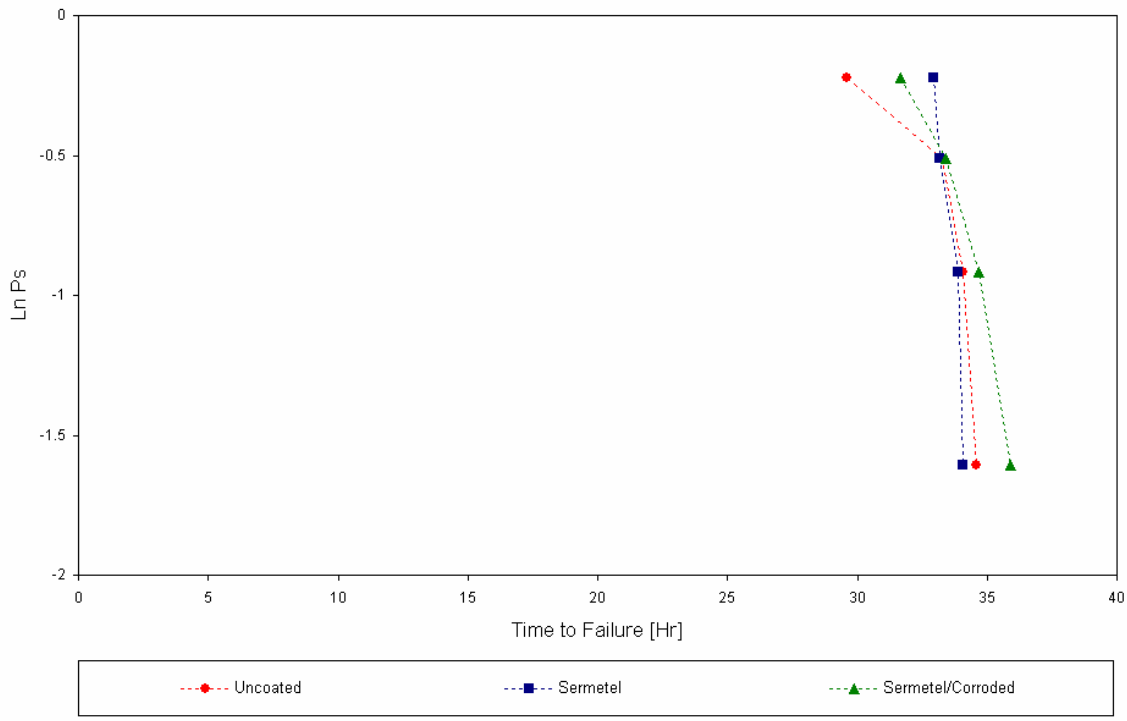

Figure 63. Weibull distribution for uncoated, SermeTel®1140/962 coated and SermeTel1140/962 coated and corroded AerMet®100 specimens.

The student *t*-test showed in **Table 9** revealed with 95% confidence level that the small differences between these three sets of results cannot be considered to be statistically significant.

Specimens	*n*	Mean *TTF*, [Hr]	S_d	Mean *EI*	*t* tabular	*t* statistic	Result
Uncoated AerMet100	4	32.89	2.26	-	-	-	-
SermeTel1140/962	4	33.52	0.55	-0.02	2.447	0.54	$t_s < t_t$
SermeTel1140/962 / Corroded	4	33.92	1.81	-0.03	2.447	0.71	$t_s < t_t$

Table 9. Student *t*-test analyses for uncoated, SermeTel®1140/962 coated and SermeTel®1140/962 coated and corroded AerMet®100 specimens.

Weibull plots for un-plated, Zinc-14%Nickel plated, Zinc-14%Nickel plated and baked as well as Zinc-14%Nickel plated, baked and corroded AerMet®100 specimens are shown in **Figure 64**. It can be seen that there was little difference between mean *TTF* values for un-plated, Zinc-14%Nickel, and Zinc-14%Nickel plated and baked specimens.

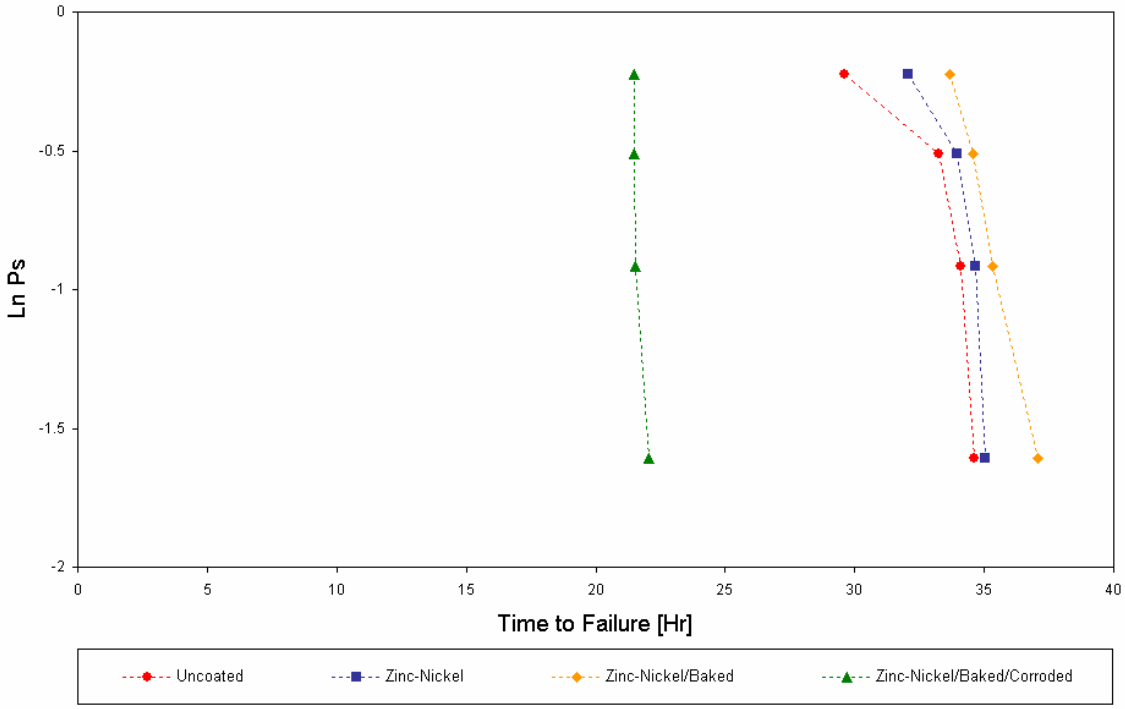

Figure 64. Weibull distribution for uncoated, Zinc-14%Nickel plated, Zinc-14%Nickel plated and baked and Zinc-14%Nickel plated, baked and corroded AerMet®100 specimens.

The corresponding *TTF* for these conditions were 32.9, 33.9 and 35.2 hours, respectively. Student *t*-test analyses for these groups of specimens showed with 95% confidence level that there were no significant statistical differences between these sets of results. In contrast, a considerable reduction in the mean *TTF* value from 32.9 to 21.6 hours was found for Zinc-14%Nickel baked and corroded AerMet®100 specimens.

Specimens	*n*	Mean *TTF*, [Hr]	S_d	Mean *EI*	*t* tabular	*t* statistic	Result
Uncoated AerMet100	4	32.89	2.26	-	-	-	-
Zinc-14%Nickel plated	4	33.94	1.31	-0.03	2.447	0.80	$t_s < t_t$
Zinc-14%Nickel /Baked	4	35.16	1.44	-0.07	2.447	1.70	$t_s < t_t$
Zinc-14%Nickel /Baked/Corroded	4	21.64	0.27	0.34	2.447	9.86	$t_s > t_t$

Table 10. Student *t*-test analyses for uncoated, Zinc-14%Nickel plated, Zinc-14%Nickel plated and baked and Zinc-14%Nickel plated, baked and corroded AerMet®100 specimens.

9.2.3. GifloM2000 Specimens

Figure 65 shows the Weibull analysis of the *SSRT* for cadmium plated and baked and cadmium plated, baked and corroded GifloM2000 specimens. The *TTF* for the control group tested in air was 31.5 hours approximately. Moreover, as expected, the mean *TTF* value for cadmium plated and baked condition did not show a reduction, with a value of 31.9 hours.

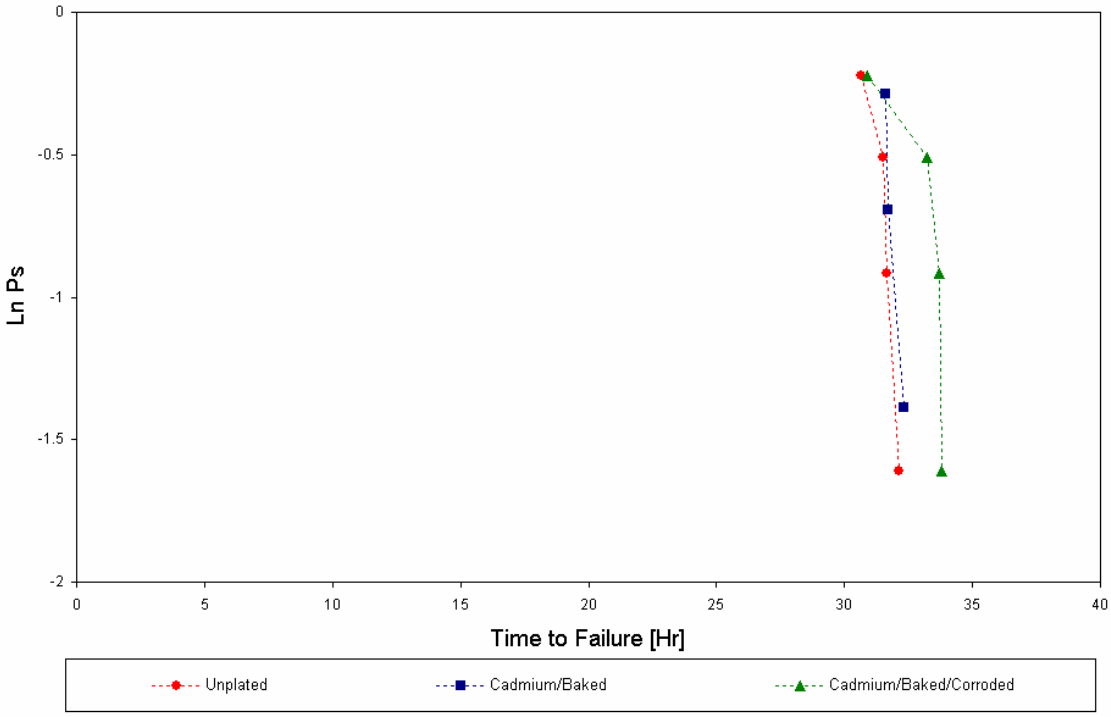

Figure 65. Weibull distribution of cadmium plated, plated and baked and plated, baked and corroded GifloM2000 specimens.

The mean time to failure value for the cadmium plated, baked and corroded specimens in 3.5% NaCl solutions was 32.9 hours. Moreover, student *t*-test results showed with a 95% confident level that there was no statistically significant difference with the uncoated specimens.

Specimens	*n*	Mean *TTF,* [Hr]	S_d	Mean *EI*	*t* tabular	*t* statistic	Result
Uncoated GifloM2000	4	31.49	0.61	-	-	-	-
Cadmium Baked	3	31.87	0.39	-0.01	0.571	0.93	$t_s < t_t$
Cadmium Baked/Corroded	4	32.90	1.37	-0.04	2.447	1.88	$t_s < t_t$

Table 11. Student *t*-test analyses for uncoated, cadmium plated and baked, cadmium plated, baked and corroded GifloM2000 specimens.

9.2.4. CSS-42L™ Specimens

Figure 66 displays the Weibull analysis of the *SSRT* results for uncoated, uncoated and corroded in 3.5% NaCl, SermeTel®1140/962 coated and cured, as well as SermeTel®1140/962 coated, cured and corroded CSS-42L™ stainless steel specimens. It can be seen that the mean time to failure for the control specimens was 38.9 hours.

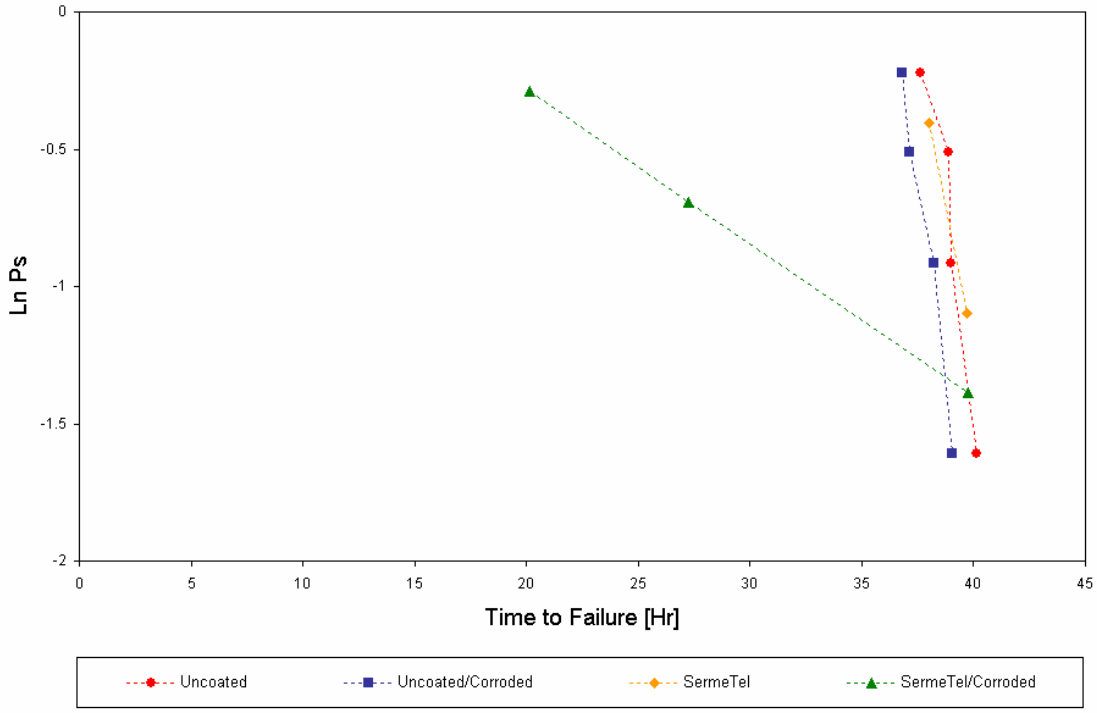

Figure 66. Weibull distribution for uncoated, SermeTel®1140/962 coated, SermeTel®1140/962 coated and corroded and uncoated and corroded CSS-42L™ specimens.

There was a slight reduction in the mean time to failure value from 38.9 to 37.8 hours, for uncoated and corroded specimens in 3.5% NaCl solutions. Although these results showed a small difference, the student *t*-test analyses revealed, with 95% confidence level, that this difference was considered to be not statistically significant.

In addition, the two SermeTel®1140/962 coated and cured specimens showed a mean time to failure of 38.9 hours, which was similar to the values for the previous conditions.

SermeTel®1140/962 coated and corroded specimens in 3.5% NaCl solutions displayed a significant reduction in the mean time to failure value from 38.9 to 29.1 hours.

Specimens	*n*	Mean *TTF*, [Hr]	S_d	Mean *EI*	*t* tabular	*t* statistic	Result
Uncoated CSS-42L	4	38.91	1.03	-	-	-	-
Uncoated CSS-42L/Corroded	3	37.81	1.03	0.03	2.571	1.51	$t_s < t_t$
SermeTel1140/962	2	38.87	1.19	0.00	2.777	0.04	$t_s < t_t$
SermeTel1140/962 / Corroded	4	29.05	9.93	0.25	2.447	2.04	$t_s < t_t$

Table 12. Student *t*-test analyses for uncoated, uncoated and corroded, SermeTel®1140/962 coated and SermeTel®1140/962 coated and corroded CSS-42L™ specimens.

9.3. Fractographic Analyses

This section presents the fractographic analysis for un-plated and cadmium plated 300M and AerMet®100 specimens. A quantitative analysis was performed in order to compare the fractures produced by hydrogen embrittlement in the two materials under similar conditions.

9.3.1. Cadmium Plated 300M Specimens

A typical ductile "cup and cone" fracture for 300M *SSRT* specimens tested in air is shown in **Figure 67**. In contrast, the cadmium plated but unbaked specimens failed with little reduction in area as shown in **Figure 68**. The initiation point of the fracture is clearly visible.

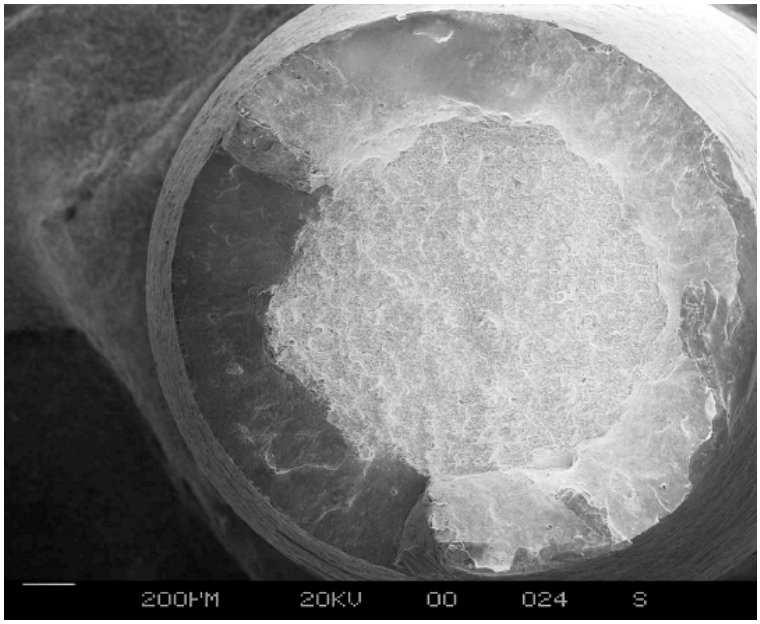

Figure 67. Fracture surface for un-plated 300M specimens.

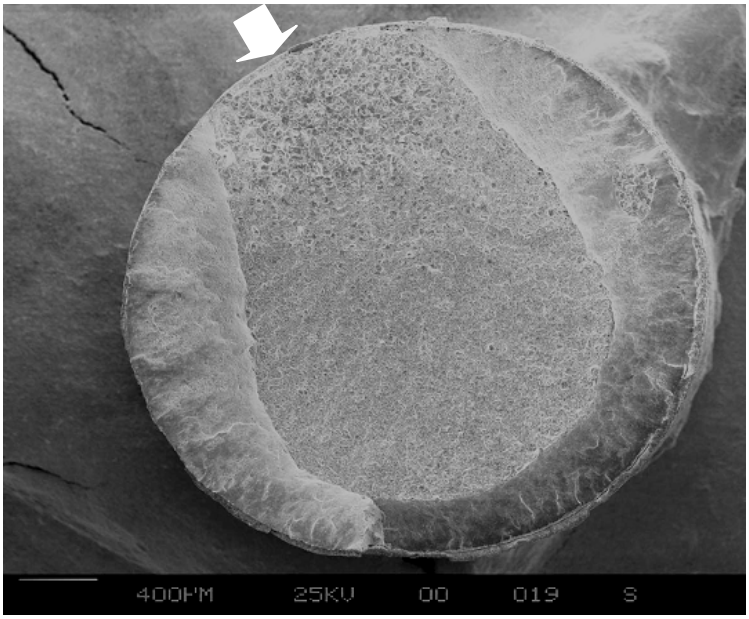

Figure 68. Fracture surface for cadmium plated 300M specimens (Arrow shows the point of crack initiation).

Hydrogen interactions lead to the appearance of brittle intergranular and transgranular fracture mechanisms, whereas micro-void coalescence indicated a ductile mode of failure. The different fractures modes present on cadmium plated 300M specimens are shown in **Figures 69**, **70** and **71**.

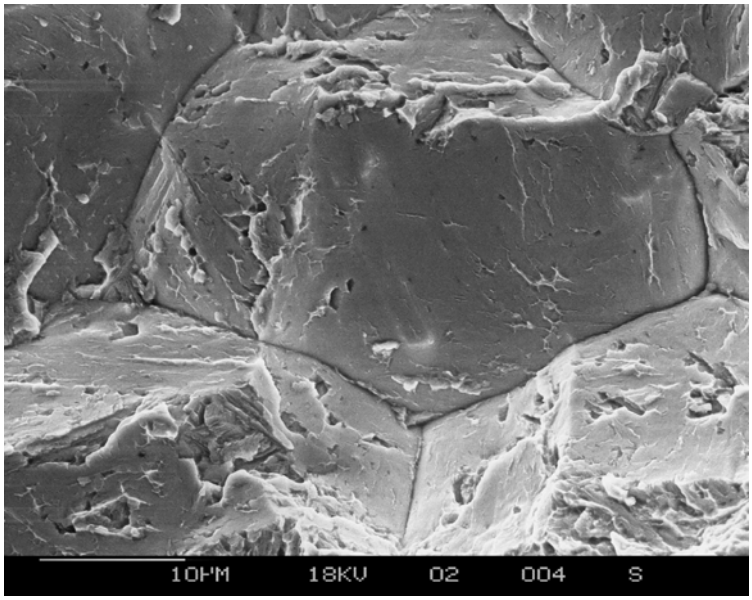

Figure 69. *SEM* Micrograph showing brittle intergranular fracture for cadmium plated 300M specimens.

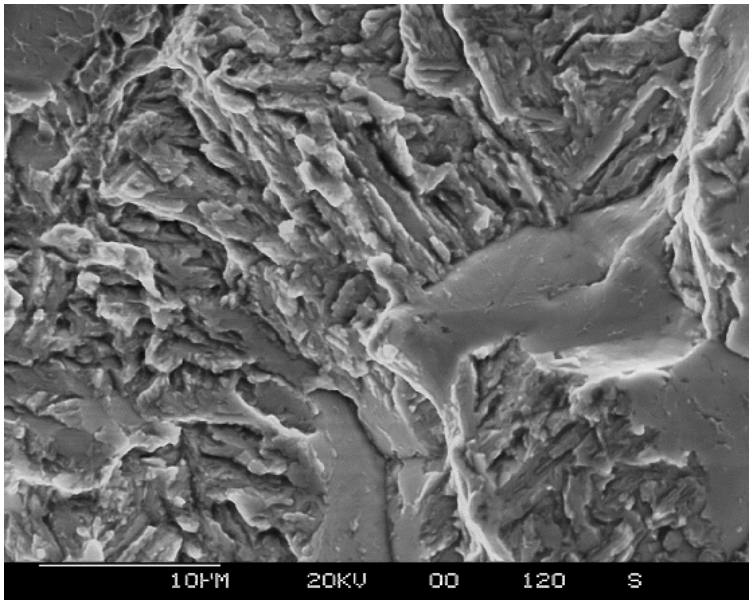

(A)

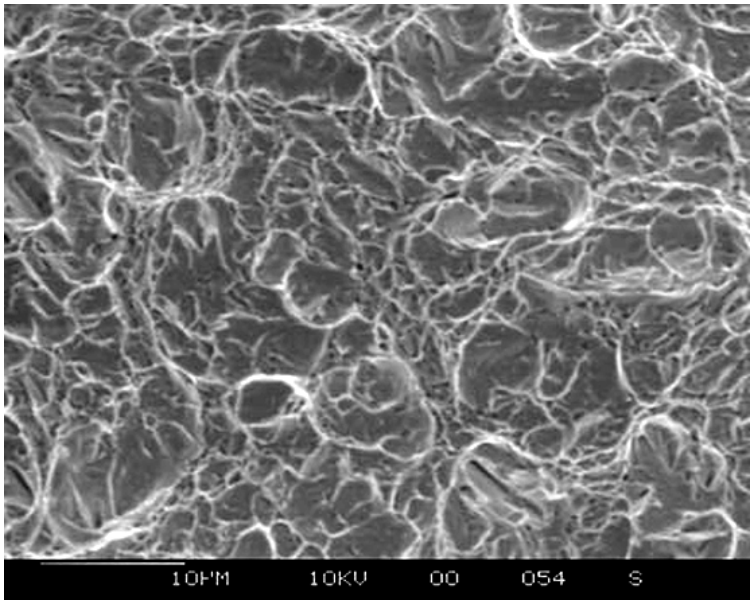

(B)

Figure 70. *SEM* micrograph showing A) mixed intergranular and brittle cleavage, and B) ductile central region for cadmium plated 300M specimens.

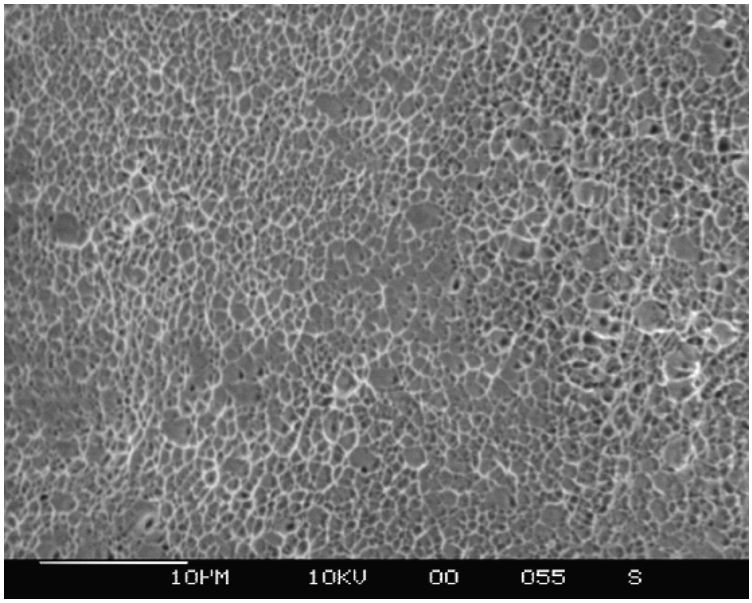

Figure 71. *SEM* micrograph showing the ductile central region for cadmium plated 300M specimens.

A typical brittle intergranular fracture was found in the most severely embrittled region near the edge of the 300M specimens, **Figure 69**, followed by a transgranular fracture containing some intergranular regions, **Figure 70(A)**. Ductile micro-void coalescence fractures were found on the rest of the fracture surface, **Figure 70(B)** and **71**.

Moreover, a quantitative fractographic analysis for 300M cadmium plated specimens is shown in **Figure 72**. Four different colours represent the characteristic fracture morphologies. It can be seen that the brittle inter-granular region (Red) ranged between 10 to 15%, the transition region (Orange) between 6-8% and the ductile region (Green-Yellow) ranged between 80 to 90% of the fracture surface. These proportions are consistent with a high hydrogen embrittlement mean index of *EI*= 0.54, found for these specimens.

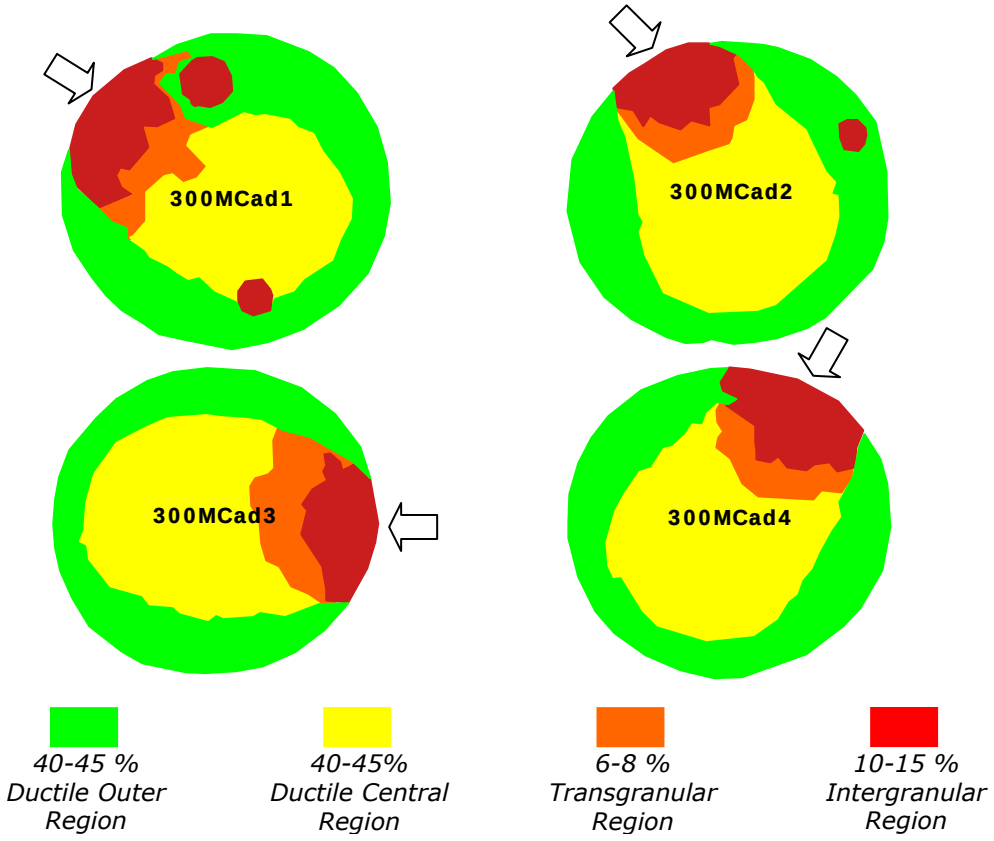

Figure 72. Quantitative fractographic analysis for cadmium plated 300M specimens (Arrows show initiation crack points).

9.3.2. Cadmium Plated AerMet®100 Specimens

Figure 73 shows the fracture surfaces of un-plated and cadmium plated AerMet®100 specimens. *SSRT* carried out on uncoated specimens showed a perfect "cup and cone" ductile fracture. These features were highly distorted on the cadmium plated specimens, although a large reduction in cross-sectional area occurred in both cases.

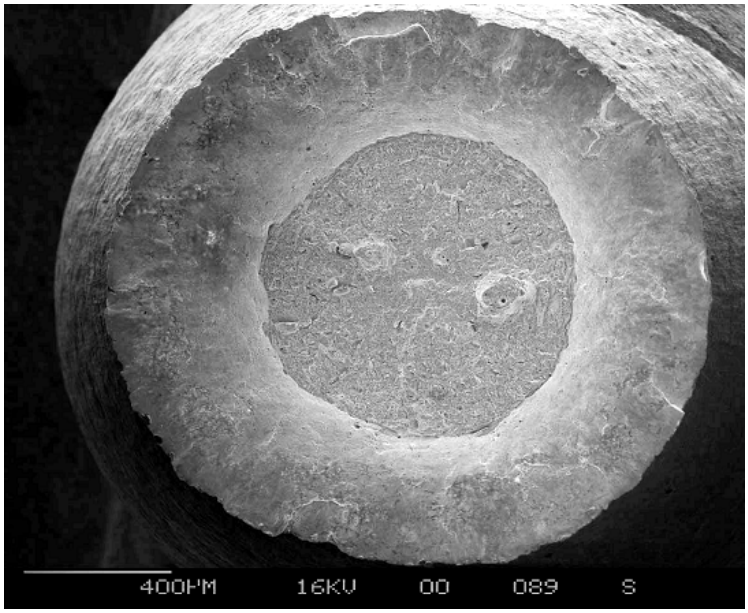

(A)

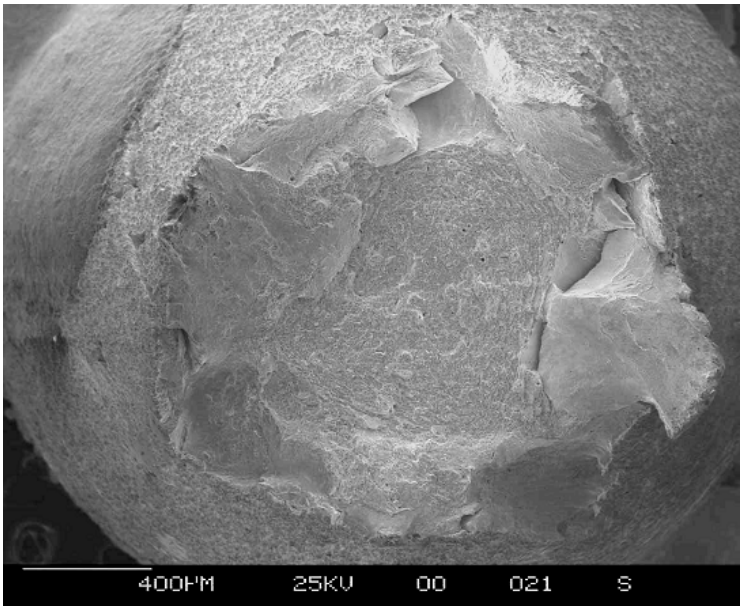

(B)

Figure 73. Fracture surfaces for A) un-plated and B) cadmium plated AerMet®100.

Three different fracture morphologies were identified on cadmium plated AerMet®100 specimens. Firstly, a region in direct contact with the electrolyte, close to the edge of the specimen, which was severely hydrogen embrittled and showed a brittle cleavage fracture, as shown in **Figure 74(A)**. In addition, characteristic central and outer ductile regions were identified, **Figure 74(B)**.

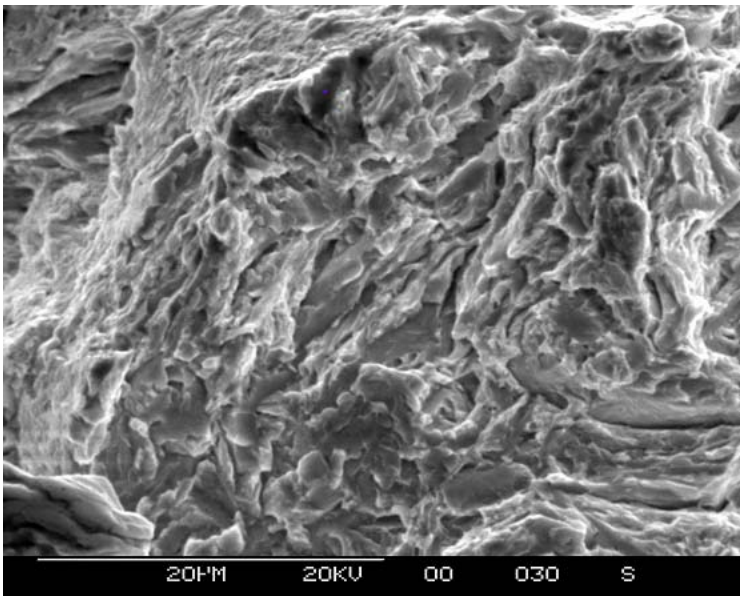

(A)

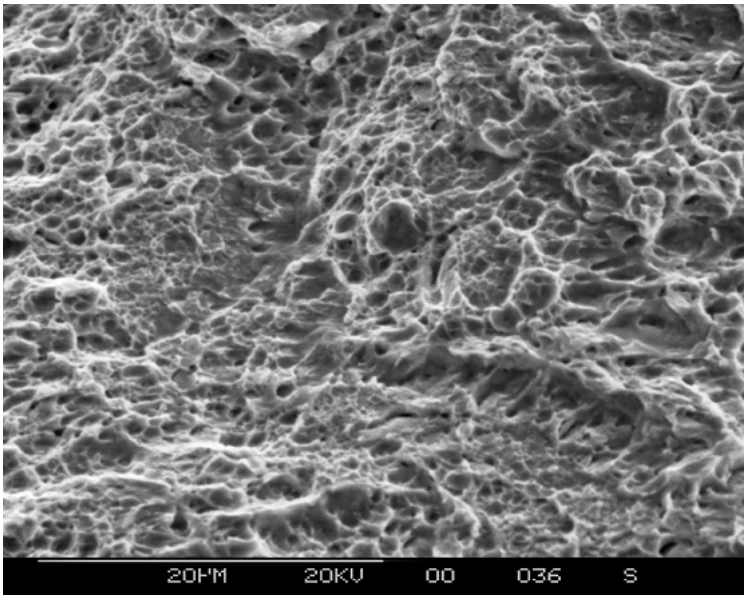

(B)

Figure 74. *SEM* micrographs showing A) brittle cleavage and B) ductile micro-void coalescence fracture for AerMet®100 steel.

From **Figure 75**, it can be seen that the brittle cleavage region (Red) ranged between 3 and 6% and the ductile regions (Green-Yellow) ranged between 94 and 97% of the fracture surface. A relatively low mean hydrogen embrittlement index of *EI*= 0.05 was measured for these specimens.

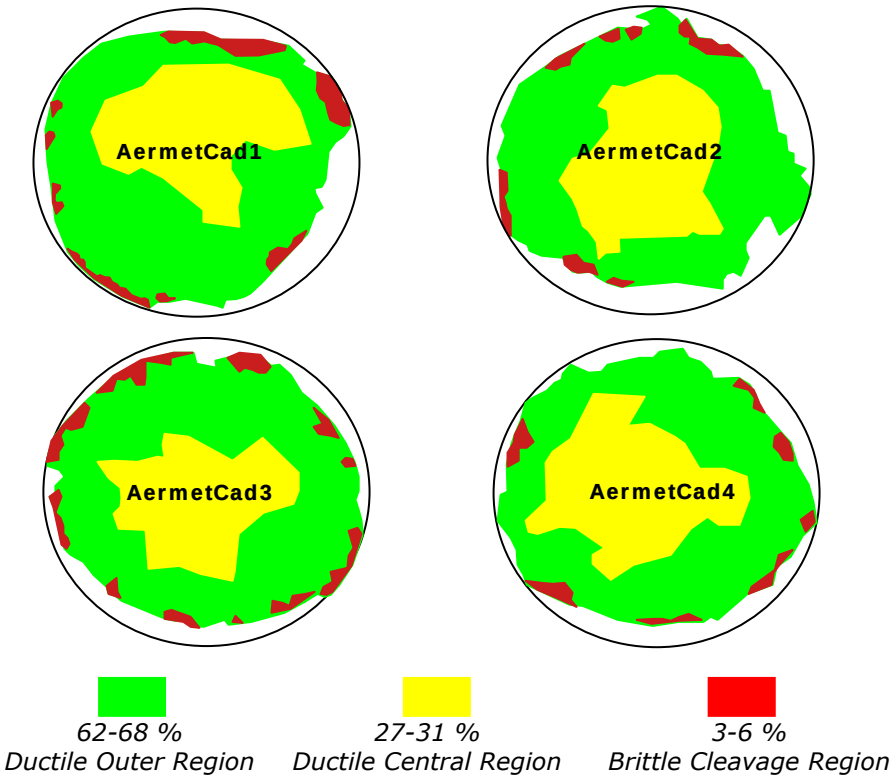

Figure 75. Quantitative fractographic analysis for cadmium plated AerMet®100 specimens.

10. Hydrogen Transport Characteristics

This section shows the results regarding the hydrogen transport characteristics for the high strength steels evaluated in the project. The first sets of results showed the cathodic polarisation experiments carried out to study the hydrogen evolution reaction on steel substrates. Subsequently, the hydrogen uptake by low carbon steel membranes at different cathodic potentials is shown. Later, the results for hydrogen diffusion coefficients, including the effect of residual and elastic stresses for 300M, AerMet®100, GifloM2000 and CSS-42L™ are described.

10.1. Hydrogen Evolution Reaction

Results from the cathodic polarisation experiments for the steel membrane in 3.5% NaCl solution are shown in **Figure 76**. It can be seen that at potentials between -0.65 and -0.90 V(SCE), the oxygen reduction cathodic reaction took place.

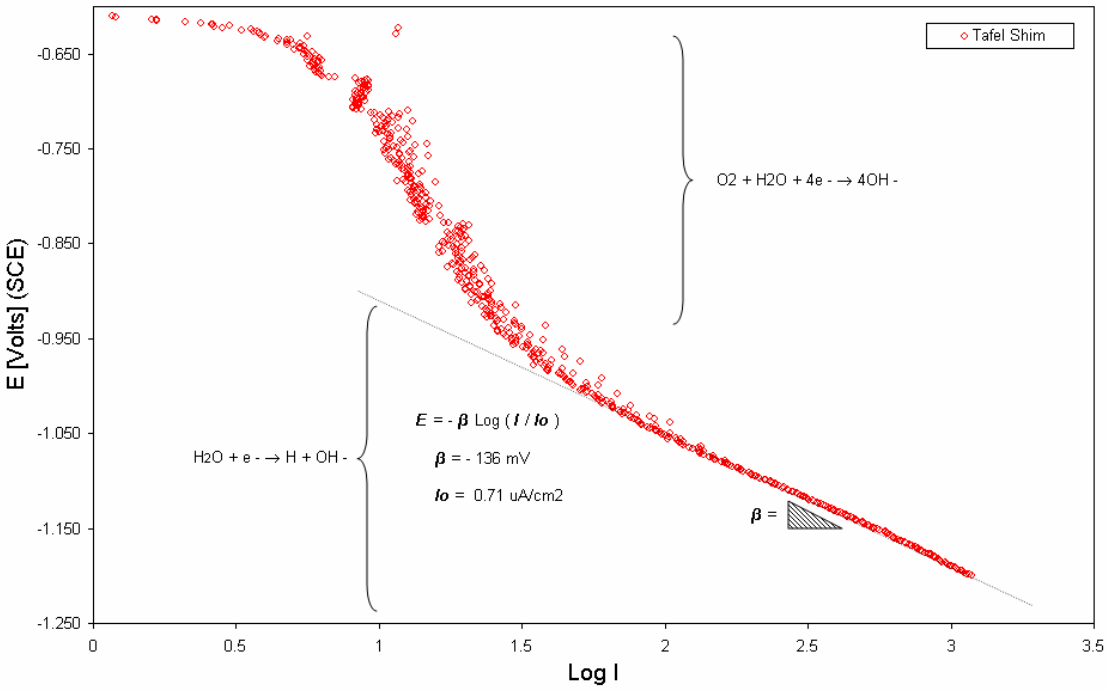

Figure 76. Potential, *E*, versus $Log_{10}(i_{charged})$ graph for low carbon steel membranes in de-aerated 3.5% NaCl solution.

In contrast, at more active potentials, E < -0.90 V(SCE), and as the oxygen concentration levels decreased in the solution, hydrogen evolution became the dominant reaction. For the hydrogen evolution reaction, the slope of the linear fit, β, was measured to be approximately -136 mV/decade.

10.2. Hydrogen Uptake by Low Carbon Steel Membranes

Figure 77 shows the hydrogen permeation transients for the low carbon steel membrane in 3.5% NaCl solutions. It can be seen that the steady state current densities, i_{∞}, were reached after approximately 7 hours of hydrogen charging. These values progressively increased at the more active (negative) potentials.

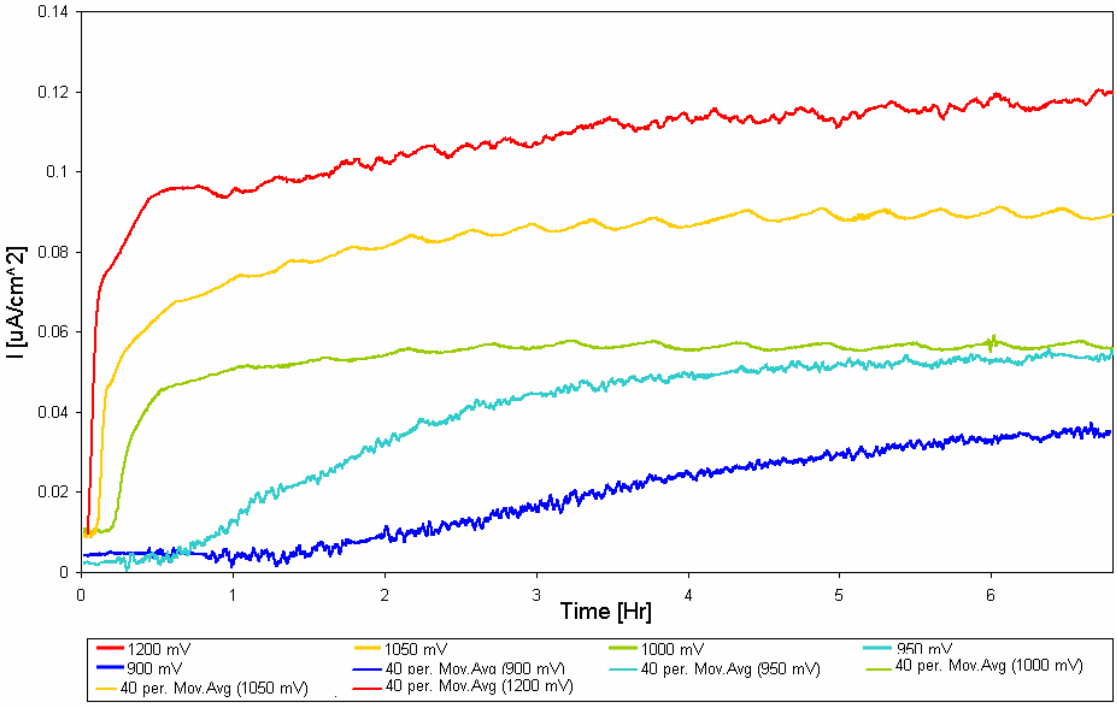

Figure 77. Hydrogen permeation transients for low carbon steel membranes in 3.5% NaCl solution at potentials between -0.90 to -1.2 V (SCE).

The steady state current densities, I_{∞}, for all applied potentials are summarised in **Table 13**. It can be seen that the steady state current densities, I_{∞}, as well as the internal hydrogen concentrations, C_o, constantly increased by lowering the potential from -0.90 to -1.15 V (SCE).

Potential, E [mV](SCE)	**Hydrogen Concentration, C_o** [mol/cm^3]	**Steady State Current Density, I_∞** [$\mu A/cm^2$]
-1200	2.62×10^{-8}	0.120
-1150	2.84×10^{-8}	0.130
-1100	2.40×10^{-8}	0.110
-1050	1.81×10^{-8}	0.083
-1000	1.03×10^{-8}	0.047
-950	1.16×10^{-8}	0.053
-900	0.68×10^{-8}	0.031

Table 13. Steady state current density values for each hydrogen permeation charging condition.

10.3. Hydrogen Diffusion Coefficients

Hydrogen diffusion measurements for the low carbon shim, 300M and AerMet®100 steels were carried out using the hydrogen permeation on relatively thin membranes. Moreover, the effect of residual stresses induced by shot peening treatments was assessed on 300M steel membranes. In addition, the alternative galvanostatic charging method was also used to calculate the hydrogen diffusion coefficients of 300M, AerMet®100, GifloM2000 and CSS-42L™ high strength steels. This hydrogen charging technique was used to assess the effect of elastic stresses on the hydrogen diffusivity of 300M, GifloM2000 and CSS-42L™.

10.3.1. Low Carbon Shim

Figure 78 shows the depletion transient for the low carbon steel shim. It can be seen that the hydrogen that was originally occluded within the shim was depleted in a period of approximately 12 hours, reaching a background current density of 0.029μA/cm^2. It has been established that background level for sensitive permeation transients should be below 0.03 μA/cm^2.

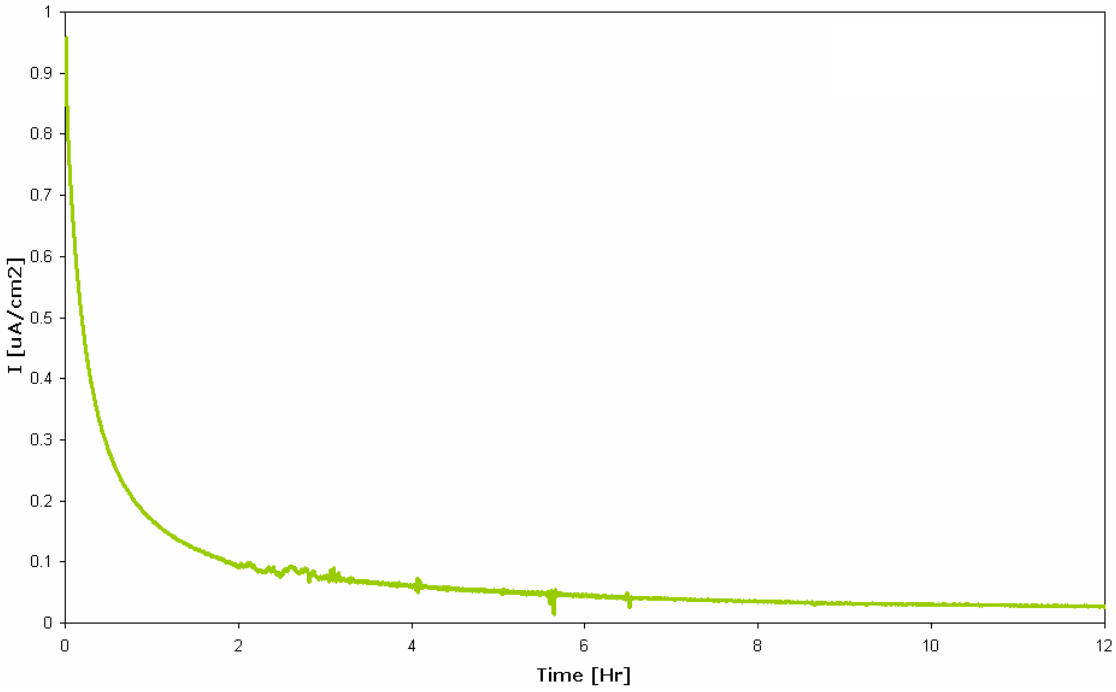

Figure 78. Depletion transient for the low carbon shim.

Figure 79 shows the permeation transient for the shim. It can be seen that the breakthrough time was approximately 2.41 min. The steady state current density, I_∞, was 0.327 μA/cm^2 after 120 min and the time lag value was graphically determined at 7.81 min.

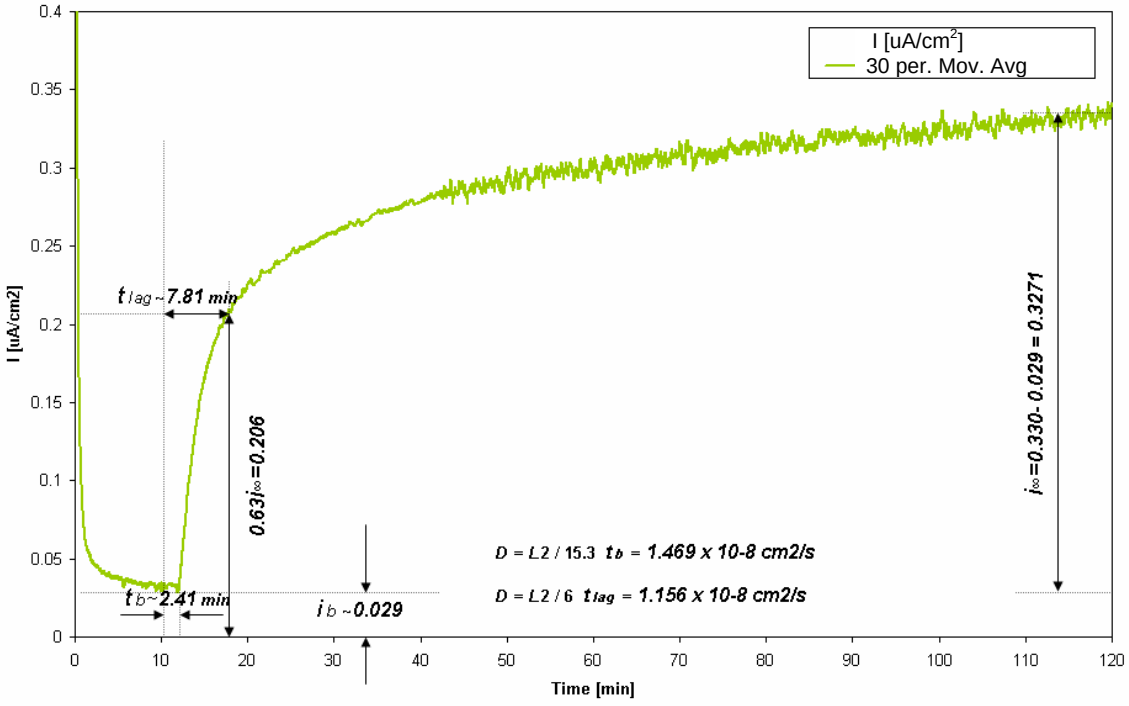

Figure 79. Permeation transient for the low carbon shim

From the time lag, t_{lag}, and breakthrough time, t_b, values the hydrogen diffusion coefficient was calculated by substituting all parameters involved in equations [XII] and [XIII], as follows:

- $$D = \frac{L^2}{6\,t_{lag}} = \frac{(0.0057\,cm)^2}{6\,(468.6\,s)} = 1.16\times10^{-8}\ cm^2 s^{-1}$$

- $$D = \frac{L^2}{15.3\,t_b} = \frac{(0.0057\,cm)^2}{15.3\,(144.6\,s)} = 1.47\times10^{-8}\ cm^2 s^{-1}$$

It can be seen that the hydrogen diffusivity calculated from the t_{Lag} and t_b methods were 1.16x10^{-8} and 1.47x10^{-8} cm^2/s, respectively. These values

and the mean hydrogen diffusion coefficient for the low carbon shim are summarised in **Table 14**.

$\mathbf{D}t_{Lag}$	1.16 x 10^{-8} cm^2/s
$\mathbf{D}t_b$	1.47 x 10^{-8} cm^2/s
DMean	1.31 ± 0.04 x 10^{-8} cm^2/s

Table 14. Hydrogen diffusion coefficients, D [cm^2/s], from the hydrogen permeation technique for the low carbon shim.

10.3.2. 300M Steel

The hydrogen depletion transient for the 1mm thick 300M steel membrane is shown in **Figure 80**. Hydrogen depletion was performed for 96 hours in order to obtain a very low hydrogen background level. After this time the current density reached a value of 0.01 $\mu A/cm^2$.

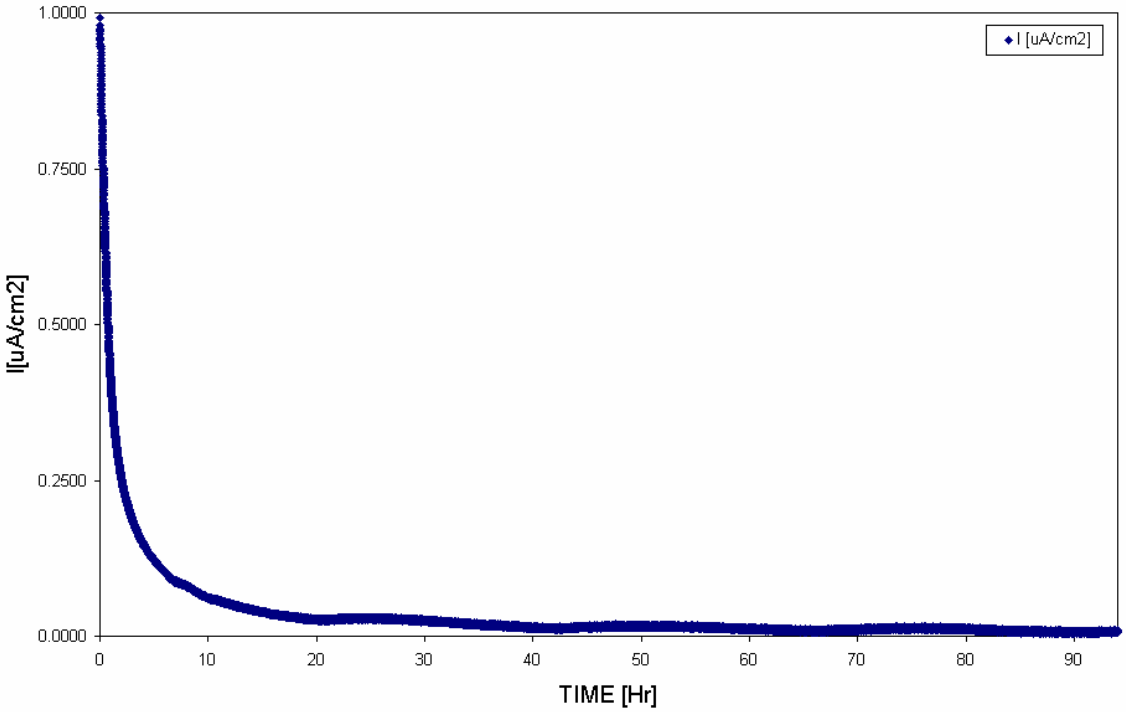

Figure 80. Hydrogen depletion transient for 300M steel membrane.

Immediately after the depletion, the charging side of the cell was connected to promote hydrogen permeation through the steel membrane.

Figure 81 shows the hydrogen permeation transient for 300M. After 23 hours of hydrogen charging, the steady state hydrogen current density reached the value of 0.337 μA/cm^2.

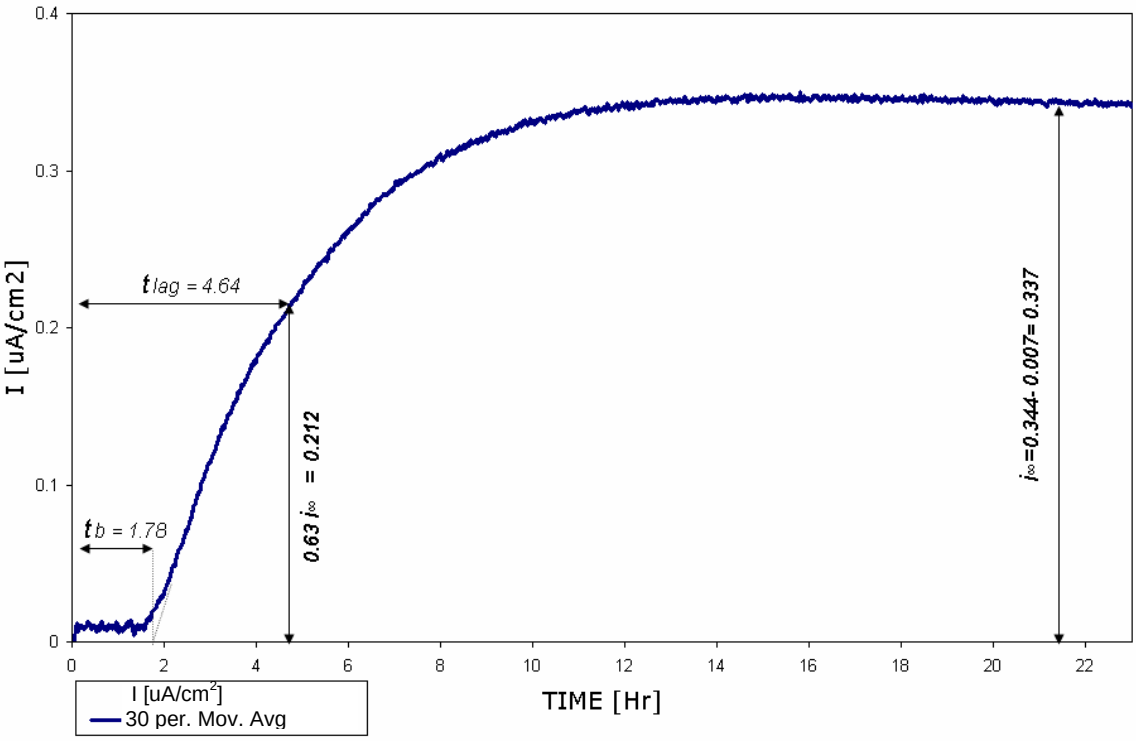

Figure 81. Hydrogen permeation transient for 300M steel membrane.

The time lag, t_{lag}, and breakthrough time, t_b, values obtained from the graph were 4.64 and 1.78 hours, respectively. The hydrogen diffusion coefficient was calculated by substituting all parameters involved in equations [XII] and [XIII], as follows:

- $$D = \frac{L^2}{6\,t_{lag}} = \frac{(0.1cm)^2}{6\,(16704\,s)} = 9.98\times10^{-8}\ cm^2 s^{-1}$$

- $$D = \frac{L^2}{15.3\,t_b} = \frac{(0.1cm)^2}{15.3\,(6408\,s)} = 1.05\times10^{-7}\ cm^2 s^{-1}$$

It can be seen that the hydrogen diffusivity calculated from the t_{Lag} and t_b methods were 9.98x10^{-8} and 1.05x10^{-7} cm^2/s, respectively. These values

and the mean hydrogen diffusion coefficient for the 300M steel membrane are summarised in **Table 15**.

$\mathbf{D}t_{Lag}$	9.98 x 10^{-8} cm^2/s
$\mathbf{D}t_b$	1.05 x 10^{-7} cm^2/s
DMean	1.02 ± 0.04 x 10^{-7} cm^2/s

Table 15. Hydrogen diffusion coefficients, D [cm^2/s], from the hydrogen permeation technique for 300M specimens.

Furthermore, the hydrogen concentration just below the charging surface, C_o, after 23 hour of potentiostatic hydrogen charging was calculated using equation [XLII] as follows:

- $$C_0 = \frac{J_\infty L}{F\ D} = \frac{(3.37\times10^{-7}\ Amp.cm^{-2})\ (0.1cm)}{(96500\,Coul.mol^{-1})\ (1.02\times10^{-7}\ cm^2.s^{-1})} = 3.42\times10^{-6}\,mol.cm^{-3}$$

The result from the galvanostatic hydrogen charging technique is shown in **Figure 82**. This graph consists on a plot of potential, *E*, against time for rectangular 300M specimens with dimension of (0.6x1.2x0.2 cm) and charged with a current density of 1mA/cm^2 for a period of 8 hours.

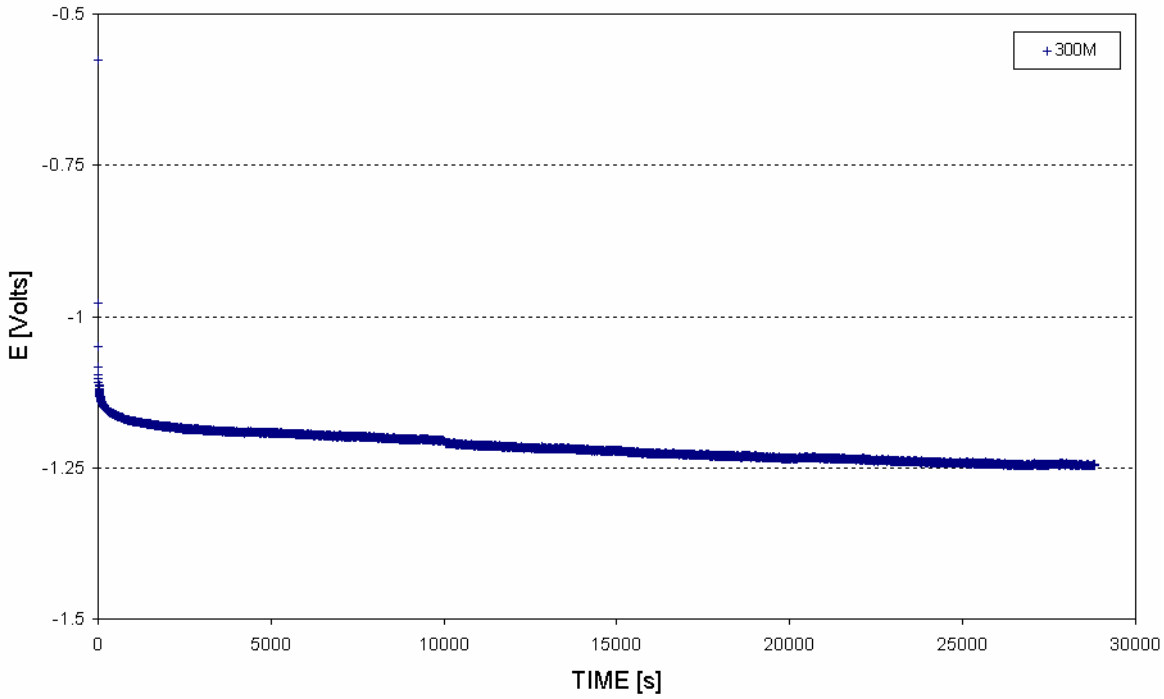

Figure 82. Potential, *E*, variation against time for 300M specimen in 0.2M NaOH solutions.

It can be seen that the potential decreased in almost a parabolic rate during the first 2500 seconds (approximately 42 minutes) of hydrogen charging. This segment of the trend corresponded to the '*short time*' period, $t << L^2/D$. Afterwards, the trend became linear for the '*long time*' period, theoretically defined when $t > L^2/D$. An extrapolation of the linear segment was applied to determine the slope of the linear fit at longer times.

Figure 83 shows the linear fit of the parabolic part of the *E* against the square root of time, $t^{1/2}$. In this graph the cell potential is a linear function of $t^{1/2}$, where the slope, $\partial E / \partial (t^{1/2})$, was approximately 8x10^{-4}V/s$^{-1/2}$ and the intercept at zero time was -1.147V. Furthermore, the linear fit at longer times is shown in **Figure 84**. From this graph it can be seen that

the slope of the linear fit, $\partial E / \partial t$, was approximately $2x10^{-6}$V/s and the intercept at zero time was -1.193V.

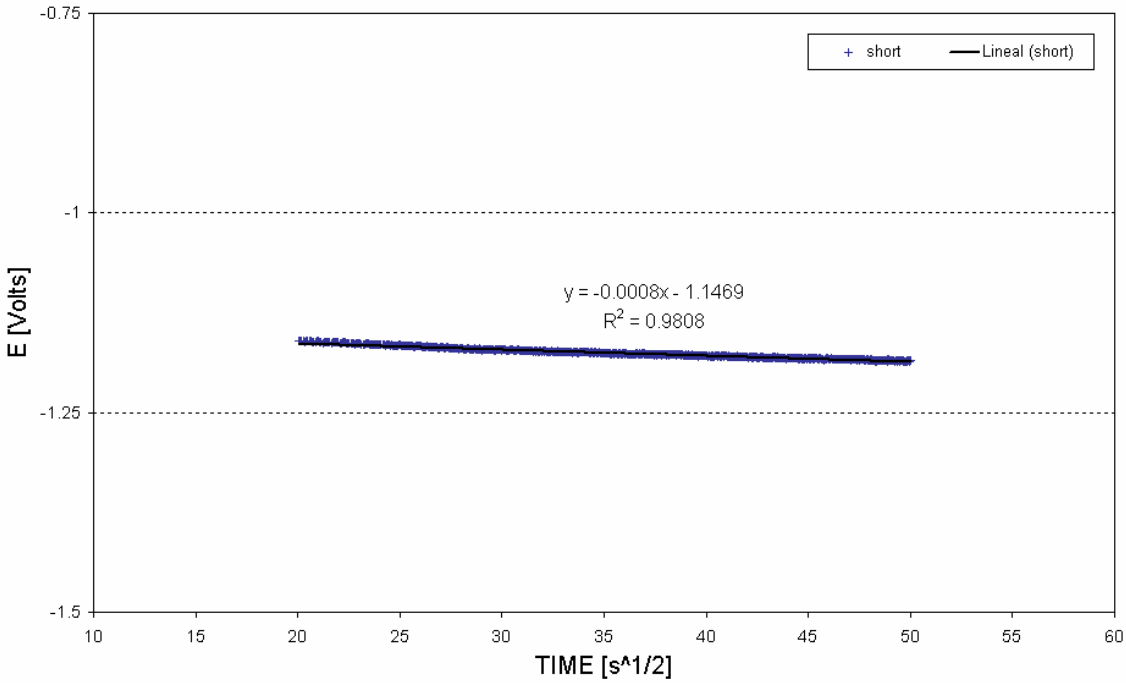

Figure 83. Linear plot of potential, *E*, as a function of $t^{1/2}$ at the 'short time' period for 300M specimens in 0.2M NaOH solutions.

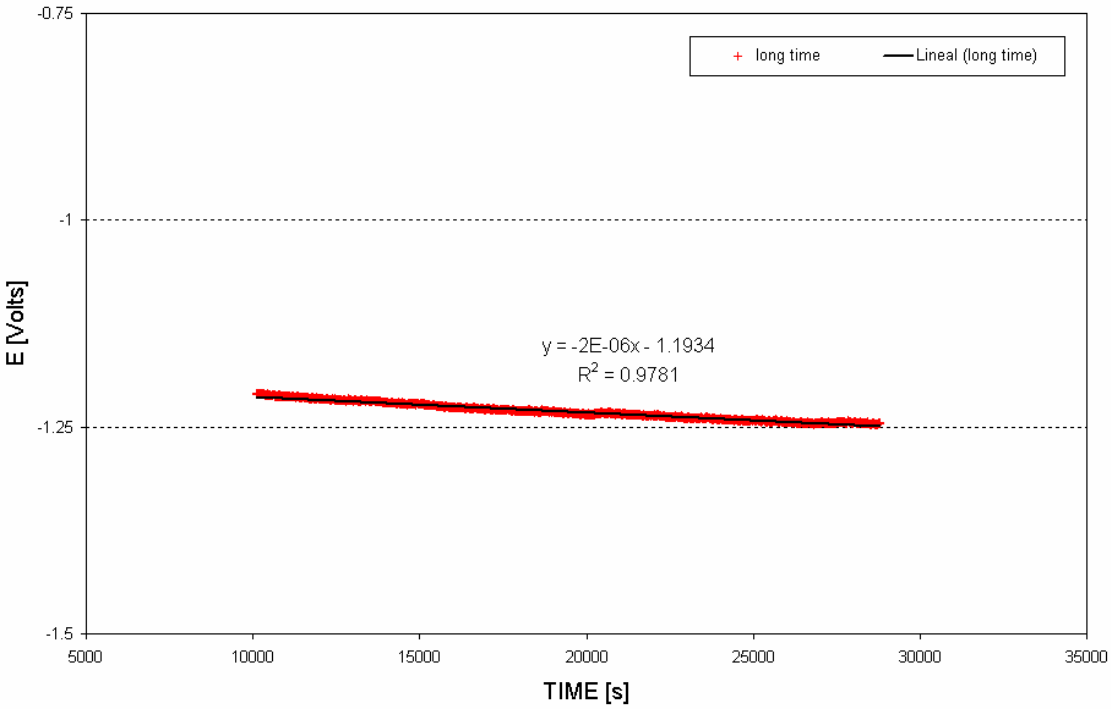

Figure 84. Linear plot of potential, *E*, as a function of time, at the 'long time' period for 300M specimens in 0.2M NaOH solutions.

The hydrogen diffusion coefficients for the galvanostatic hydrogen charging technique were calculated by substituting all parameters in equations [XXVIII], [XXVII] and [XXIX], as follows:

- $$\left(\frac{\partial E}{\partial \delta}\right) = \frac{F\ S\ L}{I\ Vm}\left(\frac{\partial E}{\partial t}\right) =$$

$$= \frac{(96500\,Coul.mol^{-1})\ (1.44\,cm^2)\ (0.1cm)}{(0.001\,Amp)\ (7.11cm^3.mol^{-1})}.(2\times10^{-6}\,V.s^{-1}) = -3.91V$$

- $$D_A = \left(\frac{2\ I\ Vm\ (\partial E/\partial\delta)}{\pi^{1/2}\ F\ S\ (\partial E/\partial t^{1/2})}\right)^2 =$$

$$= \left(\frac{2\ (0.001\,Amp)\ (7.11cm^3.mol^{-1})\ (3.91V)}{\pi^{1/2}\ (96500\,Coul.mol^{-1})\ (1.44\,cm^2)\ (8\times10^{-4}\,V.s^{-1/2})}\right)^2 = 7.96\times10^{-8}\ cm^2.s^{-1}$$

- $$D_B = \frac{I\ L\ Vm\ (\partial E/\partial\delta)}{3\ F\ S\ \left|E_{(t)} - E_{(t=0)}\right|_{(t=0)}} =$$

$$= \frac{(0.001\ Amp)\ (0.1\ cm)\ (7.11cm^3.mol^{-1})(3.91V)}{3\ (96500\,Coul.mol^{-1})\ (1.44\,cm^2)\ (0.0465V)} = 1.43\times10^{-7}\ cm^2.s^{-1}$$

The mean hydrogen diffusion coefficient was calculated taking into consideration values from equations [XXVII] and [XXIX]. **Table 16** displays these values for the 300M rectangular specimen. It can be seen that the resulting mean value was 1.12x10^{-7}cm^2/s, at approximately 18°C.

$\mathbf{D}_A$	7.96 x 10^{-8} cm^2/s
$\mathbf{D}_B$	1.43 x 10^{-7} cm^2/s
DMean	1.12 ± 0.45 x 10^{-7} cm^2/s

Table 16. Hydrogen diffusion coefficients, D [cm^2/s], from the galvanostatic charging technique for 300M specimens.

10.3.3. AerMet®100 Steel

The hydrogen depletion time for the AerMet®100 membrane was 96 hours. At the end of this period a background current level of 0.003μA/cm^2 was achieved, as shown in **Figure 85**.

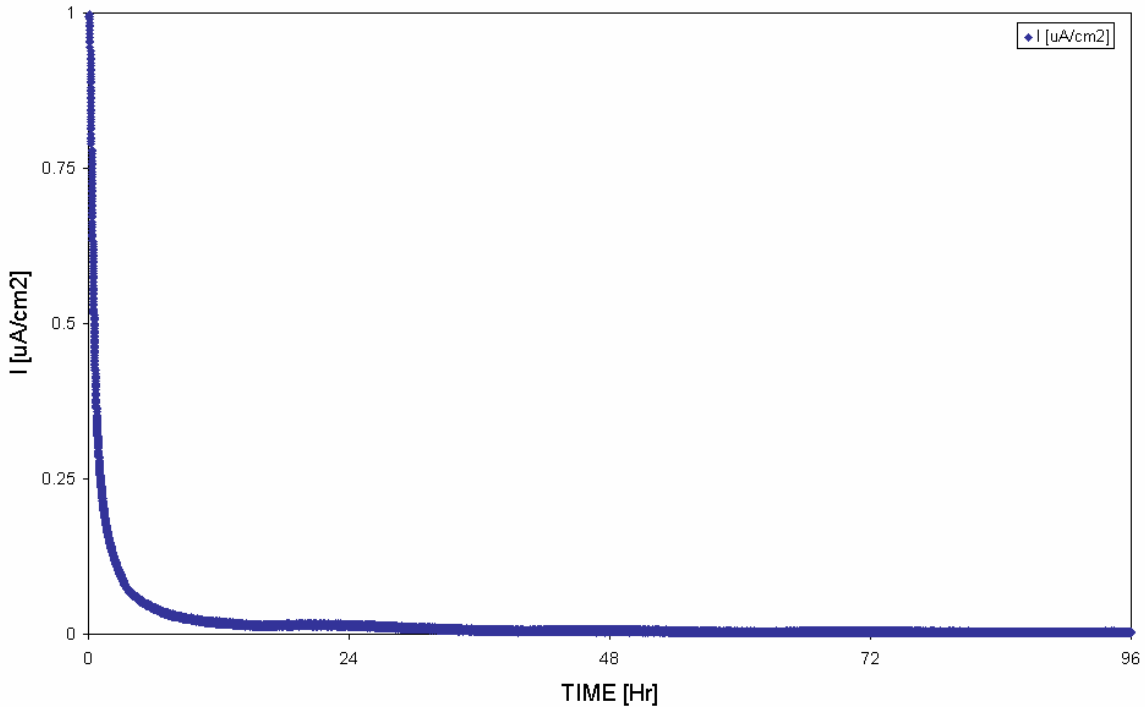

Figure 85. Hydrogen depletion transient for AerMet®100 steel membrane.

When the membrane was charged with hydrogen at a potential of -1.250 mV (SCE) no hydrogen was detected on the depletion side in a period of 48 hours, as shown in **Figure 86**.

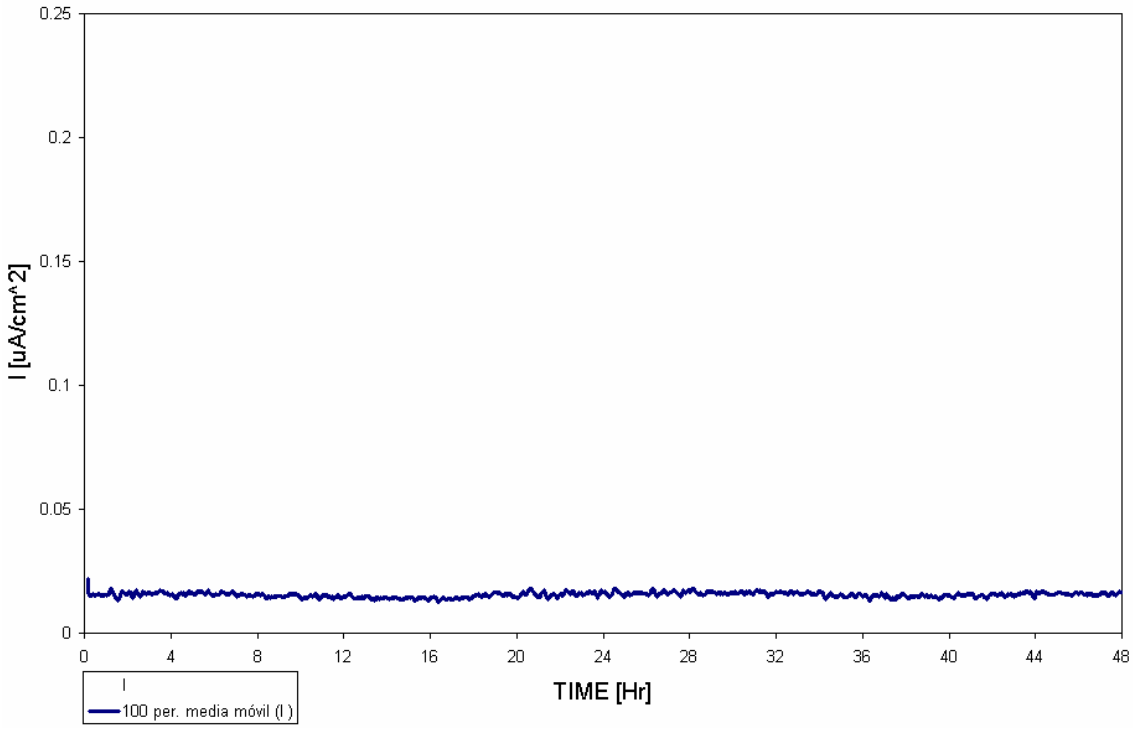

Figure 86. Hydrogen permeation transient for AerMet®100 steel membrane.

Alternatively, the result from the galvanostatic hydrogen charging method is shown in **Figure 87**. A charging current density of approximately 1mA/cm^2 was applied to the specimens for a period of 22 hours. The corresponding graph of potential, *E*, against time for AerMet®100 rectangular specimens with dimension of (0.6x2.2x0.1 cm) and charged with hydrogen in 0.2M NaOH solutions is shown.

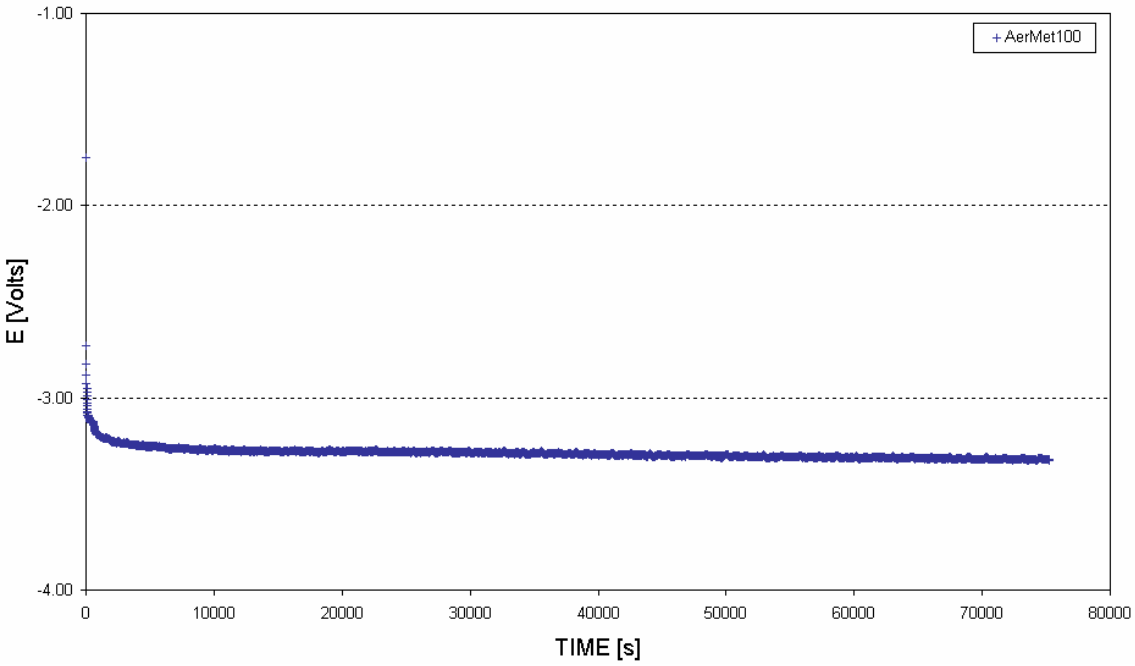

Figure 87. Potential, *E*, variation against time for 0.1 cm thick AerMet®100 specimen in 0.2M NaOH solutions.

This graph displayed the parabolic behaviour for the '*short time*' period, up to approximately 5000 seconds, and later became linear for the '*longer time*' period. An extrapolation of the linear segment was also applied to determine the slope of the linear fit at longer times.

The linear fit of the parabolic part of *E vs* $t^{1/2}$ for the '*short time*' period is displayed in **Figure 88**. It can be seen that the slope, $\partial E / \partial (t^{1/2})$, was approximately -1.14x10^{-3} V/s$^{1/2}$ and the intercept at zero time was -3.150V. Moreover, **Figure 89** depicts the linear approximation of *E* against time plot for the '*long time*' period. It can be seen that the slope of the linear fit, $\partial E / \partial t$, was approximately -8x10^{-7} V/s and the intercept of *E* at zero time was -3.261V.

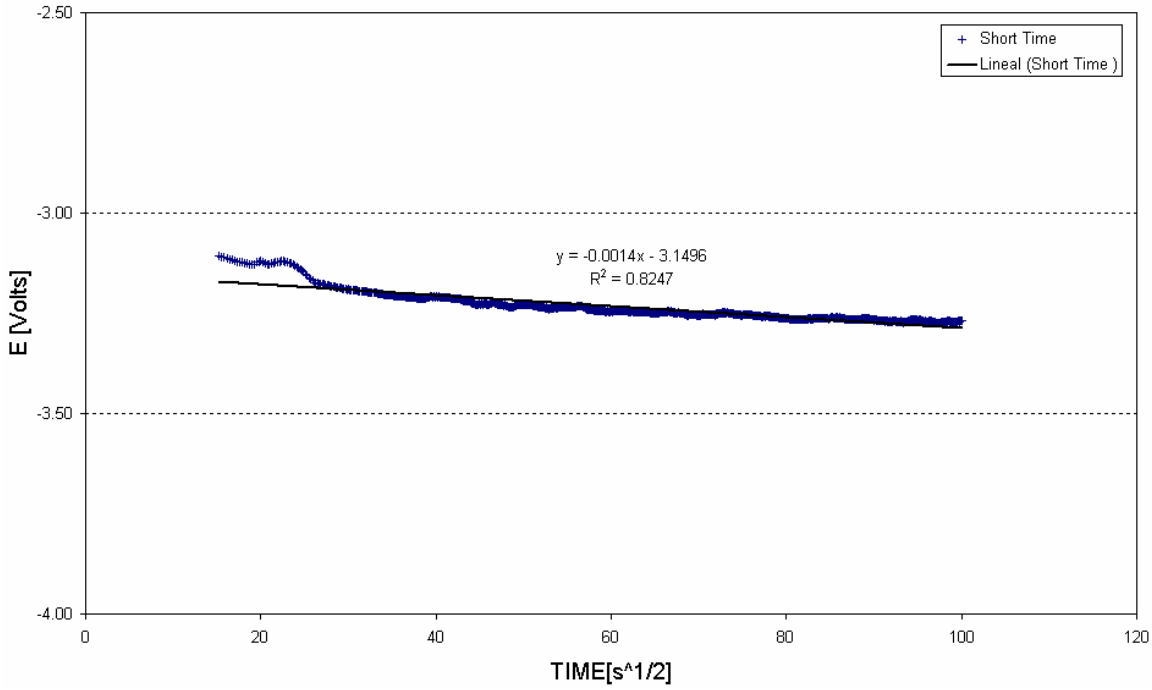

Figure 88. Linear fit of potential, *E*, as a function of $t^{1/2}$ at the '*short time*' period for AerMet®100 specimens in 0.2M NaOH solutions.

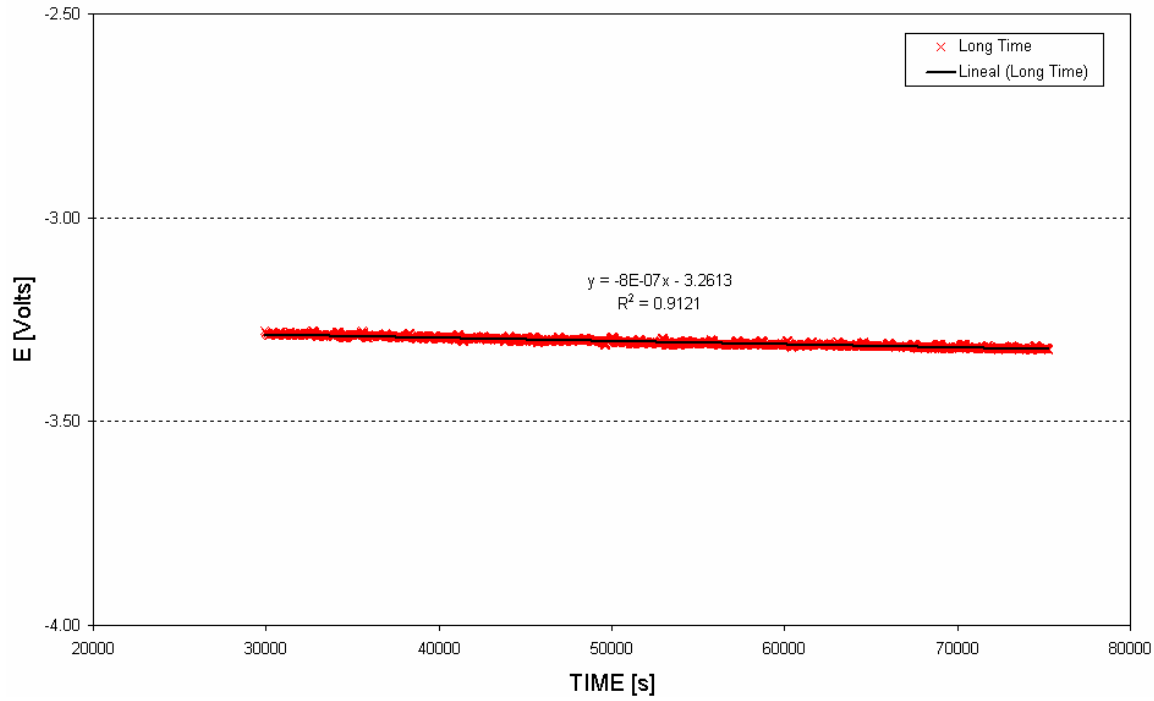

Figure 89. Linear fit of potential, *E*, as a function of time at the '*long times*' period for AerMet®100 specimens in 0.2M NaOH solutions.

The hydrogen diffusion coefficients for the galvanostatic hydrogen charging technique were calculated by substituting all parameters in equations [XXVIII], [XXVII] and [XXIX], as described below. Results are summarised in **Table 17**.

- $$\left(\frac{\partial E}{\partial \delta}\right) = \frac{F\ S\ L}{I\ Vm}\left(\frac{\partial E}{\partial t}\right) =$$

$$= \frac{(96500\,Coul.mol^{-1})\ (2.64\,cm^2)\ (0.05\,cm)}{(2.64\times10^{-3}\ Amp)\ (7.11 cm^3.mol^{-1})}.(8\times10^{-7}\ V.s^{-1}) = -0.543V$$

- $$D_A = \left(\frac{2\ I\ Vm\ (\partial E/\partial \delta)}{\pi^{1/2}\ F\ S\ (\partial E/\partial t^{1/2})}\right)^2 =$$

$$= \left(\frac{2\ (2.64\times10^{-3}\,Amp)\ (7.11 cm^3.mol^{-1})\ (0.543V)}{\pi^{1/2}\ (96500\,Coul.mol^{-1})\ (2.64\,cm^2)\ (1.4\times10^{-3}\,V.s^{-1/2})}\right)^2 = 1.04\times10^{-9}\ cm^2.s^{-1}$$

- $$D_B = \frac{I\ L\ Vm\ (\partial E/\partial \delta)}{3\ F\ S\ \left|E_{(t)} - E_{(t=0)}\right|_{(t=0)}} =$$

$$= \frac{(2.64\times10^{-3}\ Amp)\ (0.05\ cm)\ (7.11 cm^3.mol^{-1})(0.543V)}{3\ (96500\,Coul.mol^{-1})\ (2.64\,cm^2)\ (0.111V)} = 6.01\times10^{-9}\ cm^2.s^{-1}$$

$\mathbf{D}_A$	1.04 x 10^{-9} cm²/s
$\mathbf{D}_B$	6.01 x 10^{-9} cm²/s
DMean	3.53 ± 3.51 x 10^{-9} cm²/s

Table 17. Hydrogen diffusion coefficients, *D* [cm²/s], AerMet®100 specimens.

10.3.4. Effect of Residual Stresses on Hydrogen Diffusion

The effect of residual stresses induced by shot peening on the hydrogen diffusion coefficient and the hydrogen solubility of a 300M membrane is shown in this section. **Figure 90** shows a set of three hydrogen permeation measurements carried out before the shot peening process at a cathodic potential of -1.275 V(SCE).

It can be seen that the three permeation curves show similar characteristics, but some scatter is displayed in terms of the steady state current density values. Their characteristic parameters including the breakthrough time, t_b, time lag, t_{Lag}, the steady state current density, I_∞, the internal hydrogen concentration below the charging surface, C_o, and the hydrogen diffusion coefficients D_b and D_{Lag} calculated from the t_b and the t_{Lag} methods, are summarised in **Table 18**.

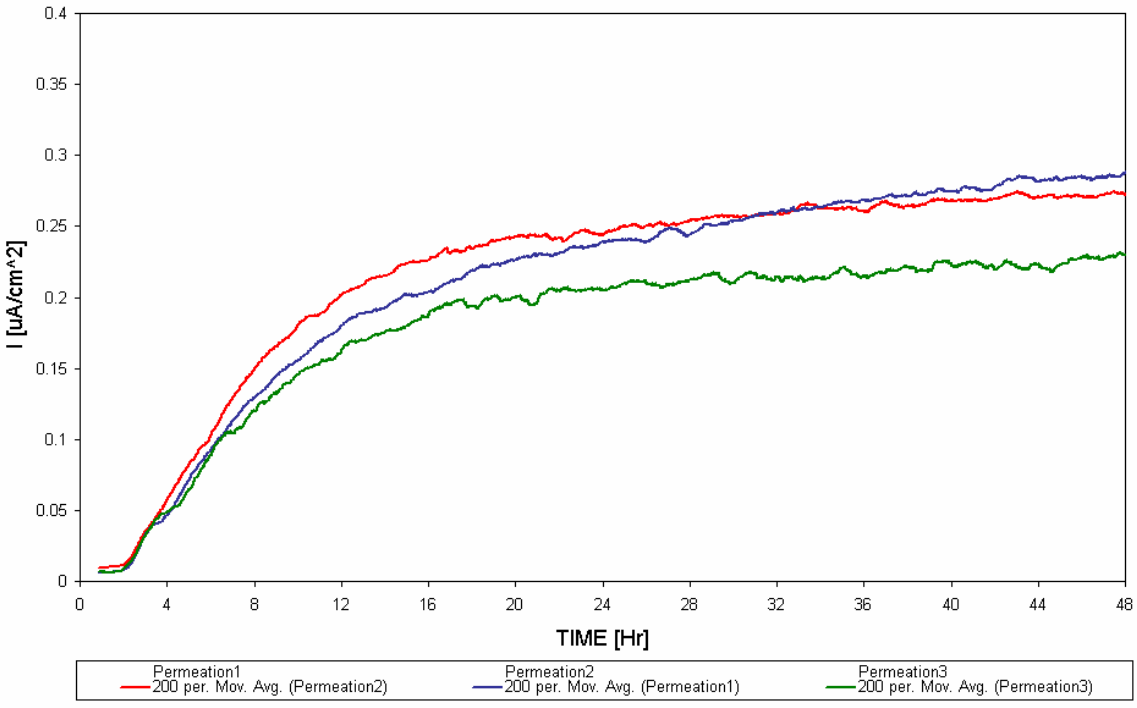

Figure 90. Hydrogen permeation transient for 300M steel membrane before the shot peening treatment.

It can be seen that the mean t_b and t_{Lag} values were 1.90 and 9.39 hours, respectively. By substituting these values in equations [XII] and [XIII], the mean hydrogen diffusion coefficient was calculated to be 7.32±2.32 x10^{-8} cm^2/s. In addition, the mean internal hydrogen concentration was approximately 3.81±0.05 x10^{-6} mol/cm^3.

Tests	t_b [Hr]	t_{Lag} [Hr]	I_∞ [$\mu A/cm^2$]	C_o x 10^{-6} [mol/cc]	D_b x10^{-8} [cm^2/s]	D_{Lag} x10^{-8} [cm^2/s]
1^{st}	1.85	8.14	0.26	3.48	9.81	5.69
2^{nd}	1.96	11.5	0.28	4.37	9.26	4.03
3^{rd}	1.88	8.53	0.24	3.57	9.66	5.42
Mean	1.90±0.06	9.39±1.84	0.26±0.02	3.81±0.05	9.58±0.28	5.05±0.89

Table 18. Parameters taken from the hydrogen permeation transients for the 300M membrane before shot peening.

Hydrogen permeation transients after shot peening the 300M membrane are shown in **Figure 91**. Parameters including the breakthrough time, t_b, time lag, t_{Lag}, the steady state current density, I_∞, the internal hydrogen concentration below the charging surface, C_o, and the hydrogen diffusion coefficients D_b and D_{Lag} calculated from the t_b and the t_{Lag} methods, are summarised in **Table 19**.

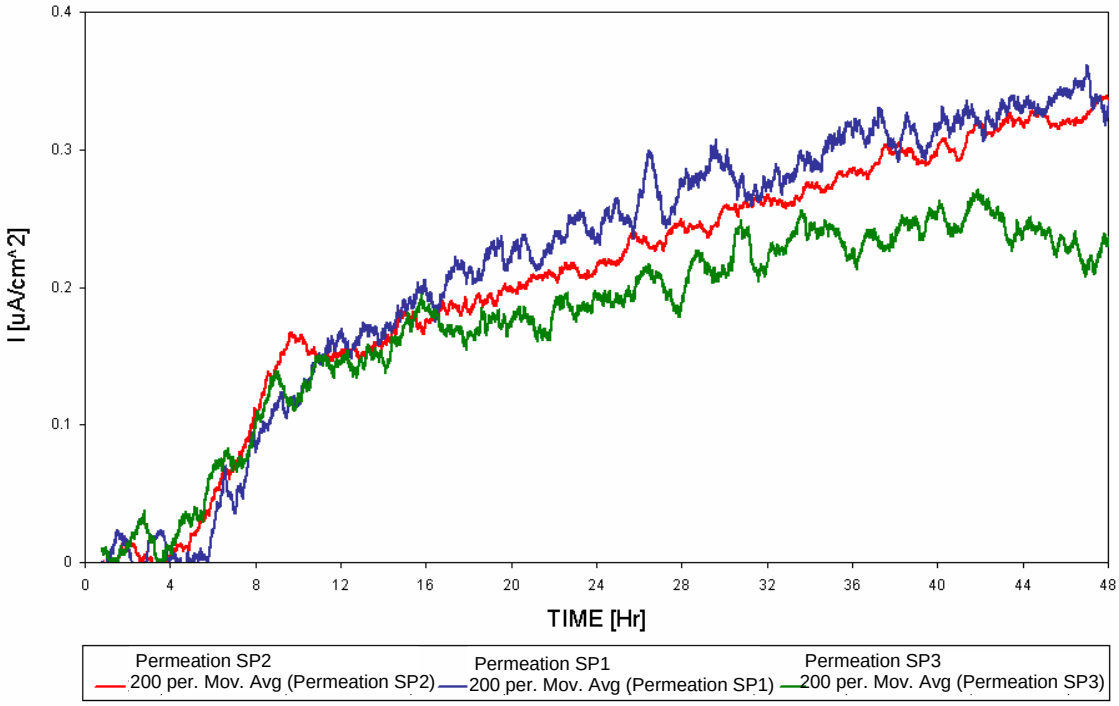

Figure 91. Hydrogen permeation transient for 300M steel membrane after the shot peening treatment.

The mean t_b and t_{lag} values were 4.33 and 16.7 hours, respectively. By substituting these values in equations [XII] and [XIII] the mean hydrogen diffusion coefficient was calculated to be 3.60×10^{-8} cm^2/s. In addition the mean internal hydrogen concentration was approximately 9.14×10^{-6} mol/cm^3.

Tests	t_b [Hr]	t_{Lag} [Hr]	I_∞ [$\mu A/cm^2$]	$C_o \times 10^{-6}$ [mol/cc]	$D_b \times 10^{-8}$ [cm^2/s]	$D_{Lag} \times 10^{-8}$ [cm^2/s]
1st	3.65	17.8	0.34	9.309	4.97	2.60
2nd	5.70	18.2	0.32	11.58	3.19	2.54
3rd	3.63	14.2	0.26	6.52	5.01	3.26
Mean	4.33±0.9	16.7±1.8	0.31±0.03	9.14±2.5	4.39±0.8	2.80±0.3

Table 19. Parameters taken from the hydrogen permeation transients for the 300M membrane after shot peening.

The student *t*-test shown in **Table 20**, revealed that there was a significant statistical difference in the mean hydrogen diffusion coefficient values after the shot peening treatment. The mean hydrogen diffusion coefficient was taken from the breakthrough time and time lag methods.

Condition	Mean $D_b \times 10^{-8}$ [cm^2/s]	*Sd*	*t* tabular	*t* statistic	Result
Untreated	7.31	2.28×10^{-8}	-	-	-
Shot Peened	3.60	1.02×10^{-8}	2.78	3.27	$t_s > t_t$

Table 20. Student *t*-test analysis for the hydrogen diffusion coefficients before and after shot peening of the 300M steel membrane.

Moreover, the student *t*-test showed with a confidence level of 95% that there was a significant statistical difference in the hydrogen concentration just below the charging surface, C_o, before and after shot peening of the 300M membrane, **Table 21**.

Condition	Mean C_o [mol/cm^3]	*Sd*	*t* tabular	*t* statistic	Result
Untreated	3.81×10^{-6}	0.05×10^{-6}	-	-	-
Shot Peened	9.14×10^{-6}	2.07×10^{-6}	2.78	3.58	$t_s > t_t$

Table 21. Student *t*-test analysis for the internal hydrogen concentration before and after shot peening of the 300M steel membrane.

10.3.5. Effect of Elastic Stresses on Hydrogen Diffusion

Results that showed the possible effect of elastic stresses on the hydrogen diffusion coefficients for 300M, micro-alloyed GifloM2000 and CSS-42L™ stainless steel are displayed in this section. Diffusion coefficients were calculated using the chrono-potentiometric charging technique when simultaneously different stress levels were applied on the specimens. Mathematical calculations for the recorded data are shown in **Appendices 3**, **4** and **5**.

10.3.5.1. 300M Steel

Table 22 shows the hydrogen diffusion coefficients calculated for 300M specimens under stresses of 0, 500 and 1000 MPa. These stress levels represented approximately 0, 25 and 50 percent of the yield strength, respectively.

Tests	GROUP A 0% Yield Stress 0 [MPa]	GROUP B 25% Yield Stress 500 [MPa]	GROUP C 50% Yield Stress 1000 [MPa]
1st	2.51×10^{-8}	3.73×10^{-8}	3.00×10^{-8}
2nd	3.83×10^{-8}	5.50×10^{-8}	2.98×10^{-8}
3rd	2.80×10^{-8}	3.37×10^{-8}	3.29×10^{-8}
4th	5.90×10^{-8}	3.50×10^{-8}	5.02×10^{-8}
Mean	$3.76 \pm 1.53 \times 10^{-8}$	$4.03 \pm 0.9 \times 10^{-8}$	$3.57 \pm 0.9 \times 10^{-8}$

Table 22. Hydrogen diffusion coefficients [cm^2/s] for 300M specimens under 0, 25 and 50% yield strength.

It can be seen that the mean hydrogen diffusion coefficient for 300M steel with no stress applied was approximately 3.76×10^{-8} cm^2/s. Moreover, there were no significant differences in the hydrogen diffusion coefficient by increasing the stress level to 25% and 50% of the yield strength.

Student *t*-test analysis to compare hydrogen diffusion coefficients at different stress levels for 300M specimens is shown in **Table 23**. This analysis revealed with a confidence level of 95% that there were no significant statistical differences between the three groups tested at 0, 500 and 1000 MPa, respectively.

Stress Applied	Mean *D* [cm^2/s]	*Sd*	*t* tabular	*t* statistic	Result
0% YS[0 MPa]	3.76×10^{-8}	1.53×10^{-8}	-	-	-
25% YS[500 MPa]	4.03×10^{-8}	0.90×10^{-8}	2.447	0.29	$t_s < t_t$
50% YS[1000 MPa]	3.57×10^{-8}	0.90×10^{-8}	2.447	0.21	$t_s < t_t$

Table 23. Student *t*-test analysis for diffusion measurements at different stress levels on 300M specimens.

10.3.5.2. GifloM2000 Steel

Hydrogen diffusion coefficient measurements without tensile stress applied for GifloM2000 micro-alloyed steel are shown in **Table 24**. For a set of four experiments the mean hydrogen diffusion coefficient corresponded to 4.40 x 10^{-8} cm^2/s at zero stress applied (0 MPa).

TEST	GROUP A 0% Yield Stress, 0 [MPa]
1st	4.71 x 10^{-8}
2nd	4.66 x 10^{-8}
3rd	3.90 x 10^{-8}
4th	4.31 x 10^{-8}
Mean	4.40 ± 0.37 x 10^{-8}

Table 24. Hydrogen diffusion coefficients [cm^2/s] for GifloM2000 low alloy steel specimens under 0% yield strength.

However, unexpected failure occurred when GifloM2000 steel specimens were galvanostatically charged with hydrogen under approximately 50% of yield strength. These specimens showed only one crack propagated at the point where the specimens failed. **Figures 92** and **93** shows a typical transverse crack found in the hydrogen charged specimens.

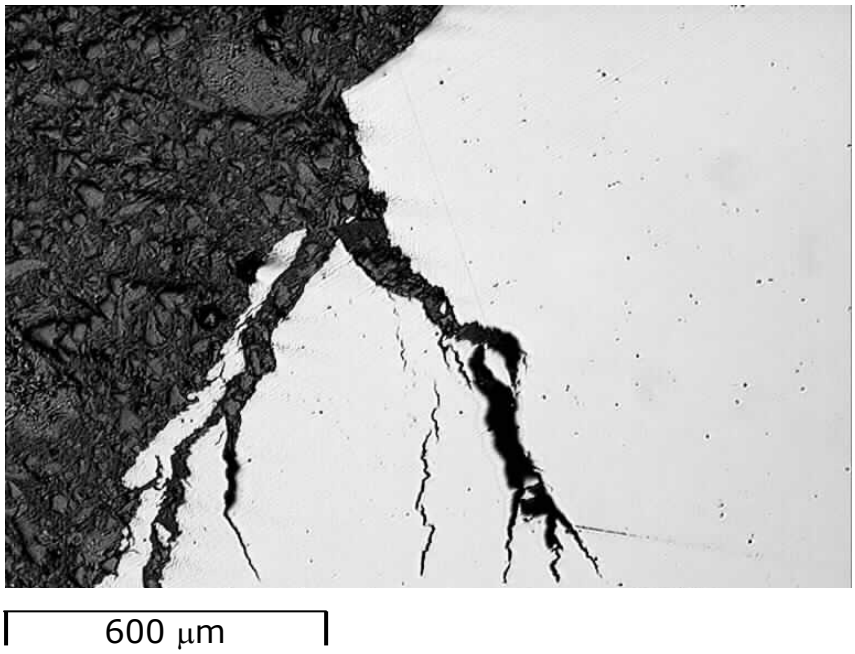

Figure 92. Transverse cracking found on GifloM2000 steel after simultaneous hydrogen charging and the application of 50% yield strength.

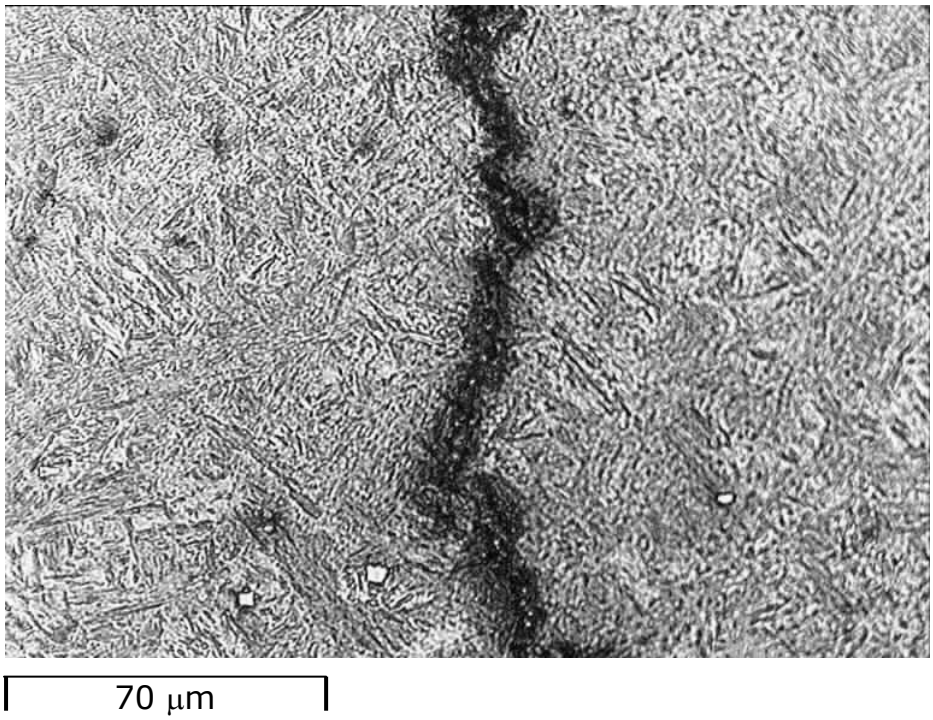

Figure 93. Transverse crack found on etched GifloM2000 steel after simultaneous hydrogen charging and the application of 50% yield strength.

10.3.5.3. CSS-42L™ Stainless Steel

Table 25 shows the hydrogen diffusion coefficient measurements under no applied tensile stress for CSS-42L™ stainless steel. The mean hydrogen diffusion coefficient was approximately 2.95 x 10^{-7} cm^2/s. This value was slightly higher than that for 300M steel and suggested that hydrogen penetrates the stainless steels faster than the low alloy 300M.

TEST	GROUP A 0% Yield Stress, 0 [MPa]
1st	2.07 x 10^{-7}
2nd	5.71 x 10^{-7}
3rd	2.06 x 10^{-7}
4th	1.95 x 10^{-7}
Mean	2.95 ± 1.8 x 10^{-7}

Table 25. Hydrogen diffusion coefficients [cm^2/s] for CSS-42L™ stainless steel specimens under 0% yield strength.

Following two consecutive hydrogen charging periods of 8 hours with no applied stress, CSS-42L™ specimens displayed transverse cracks (perpendicular to the stress direction). **Figure 94** and **95** shows a group of cracks parallel to each other on the previously hydrogen charged surface.

Figure 94. Transverse cracking found on CSS-42L™ stainless steels after two consecutive hydrogen charging periods of 8 hours with no stress applied.

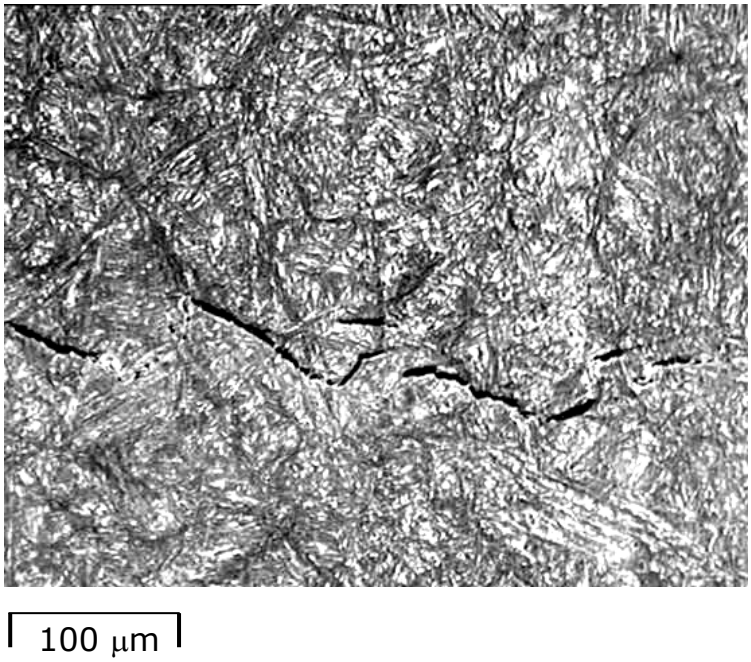

Figure 95. Transverse crack found on etched CSS-42L™ stainless steels after two consecutive hydrogen charging periods of 8 hours with no stress applied.

11. Sacrificial Coatings Results

This section has been divided in two sets of results. The first corresponded to the chemical porosity tests and metallographic analyses used to identify discontinuities in the electroplated cadmium, Zinc-14%Nickel and aluminium based SermeTel®1140/962 sacrificial coating. In addition, the second set of results describes the corrosion behaviour of the sacrificial coatings in terms of their open circuit potentials.

11.1. Barrier Properties

11.1.1. Cadmium Coating

In the potassium permanganate test, black markings indicated pores and cracks in the sacrificial coating. **Figures 96** and **97** show the surface of the cadmium coating before and after 3½ hours immersion in the reagent solution.

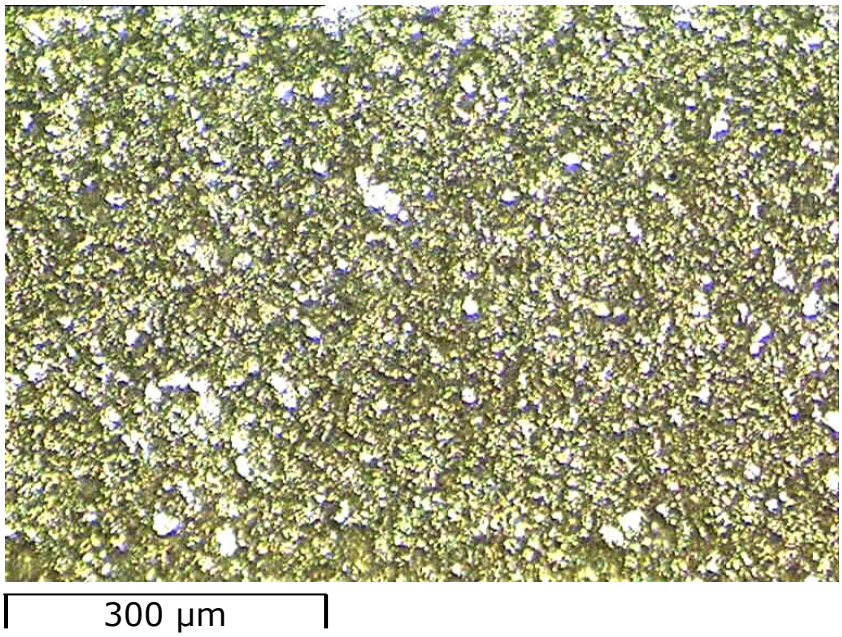

Figure 96. Surface characteristics of the cadmium coating before immersion in $KMnO_4$ solutions.

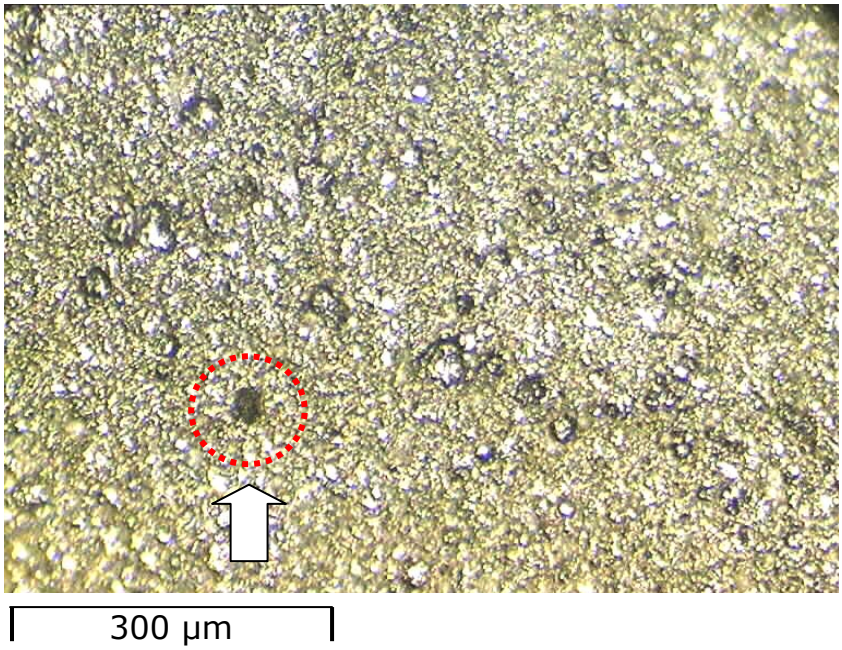

Figure 97. Surface characteristics of the cadmium coating after 3½ hours immersion in $KMnO_4$ solutions. (Arrows represent affected areas)

After immersion, isolated black manganese oxide spots were found on the surface of the coating. This product was located within some of the crater like irregularities on the coating.

Similarly, the copper sulphate or Preece test showed analogous results. **Figure 98** displays images of the cadmium coating after 6 and 8 minutes immersion in the copper sulphate solution. Bright adherent copper deposits started to appear within some isolated crater like features after 6 minutes immersion. By 8 minutes immersion the copper deposits had become more extensive and appeared to cover all the thinnest parts of the coating, which were evident from shallow depressions in the surface.

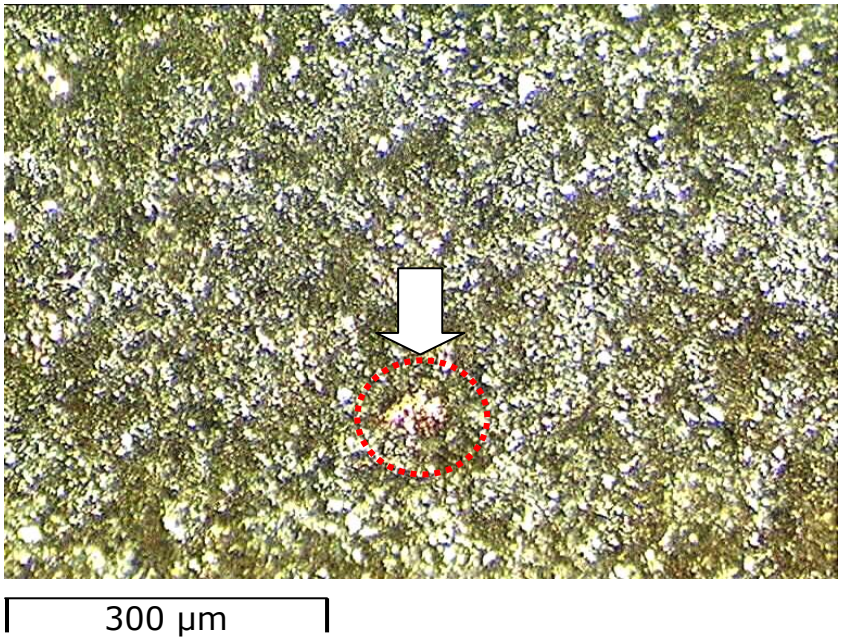

(A)

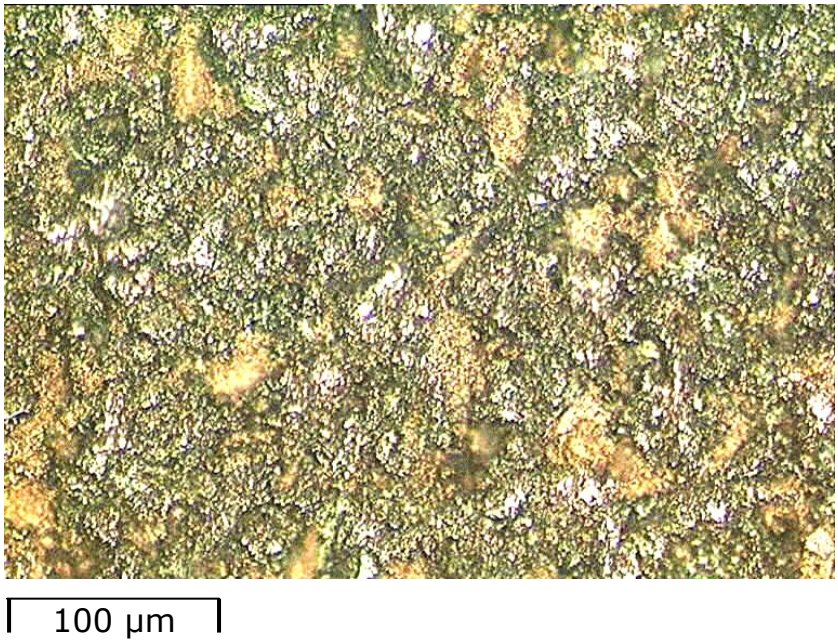

(B)

Figure 98. Micrographs from the Preece test, A) after 6 and B) 8 minutes immersion in copper sulphate solution. (Arrow indicates affected regions)

Finally, the metallographic examination of the cross section of the cadmium coating, shown in **Figure 99**, revealed the presence of closed pores.

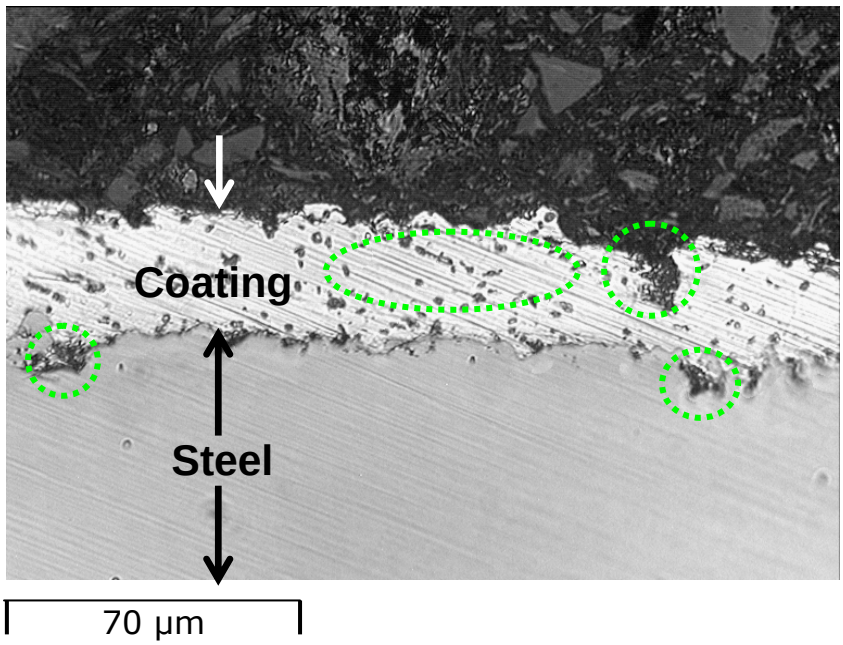

Figure 99. Closed pores in the cross section of the cadmium coated specimen. (Circles represent discontinuities in the coating)

11.1.2. Zinc-14%Nickel Coating

In the Potassium Permanganate test, black markings in the form of spots indicated pores and cracks on the Zinc-14%Nickel sacrificial coating. The end point of the test was recognized by the appearance of the black oxide deposit on the bottom of a previously scratched region.

Figures 100 and **101** show this reference point before and after 3½ hours of immersion in the reagent solution. After immersion, no significant changes were found on the colour fringes pattern from the chromium oxide passivation layer. Therefore, it was considered that during the test the Zinc-14%Nickel coating did not react with the potassium permanganate solution.

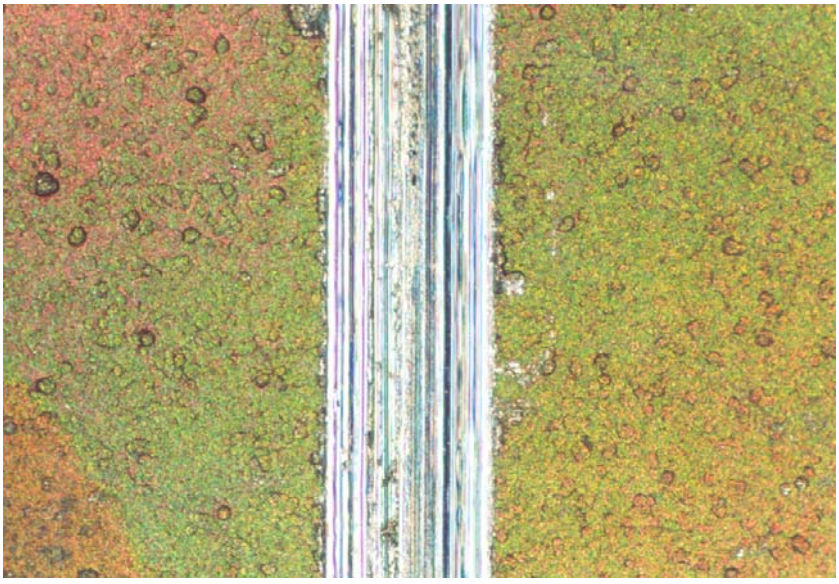

Figure 100. Scratched region on the Zinc-14%Nickel coating before immersion in $KMnO_4$ diluted solution.

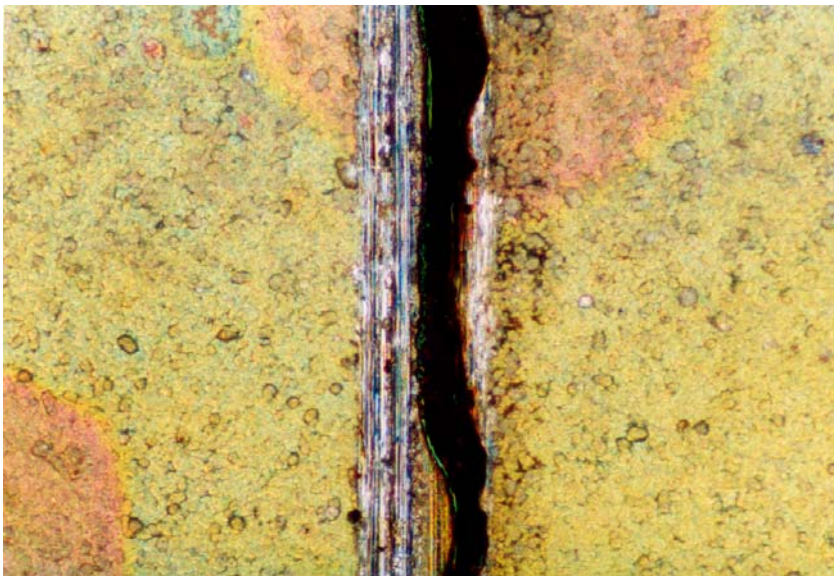

Figure 101. Scratched region on the Zinc-14%Nickel coating after 3 ½ hours immersion in $KMnO_4$ diluted solution.

From **Figures 102** and **103** it can be clearly seen well defined isolated black spots of *MnO* on the Zinc-14%Nickel coating. These features were localised on the bottom of *crater-like* indentations, approximately 50 μm in diameter, randomly distributed across the surface of the specimens.

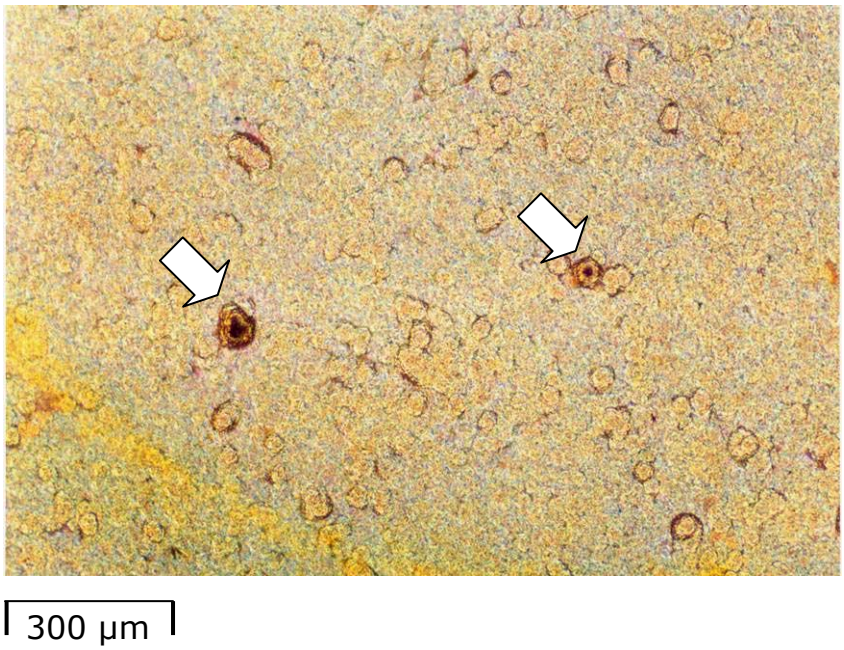

Figure 102. Micrographs showing two black spots on the Zinc-14%Nickel coating after 3½ hours immersion in $KMnO_4$ diluted solution.

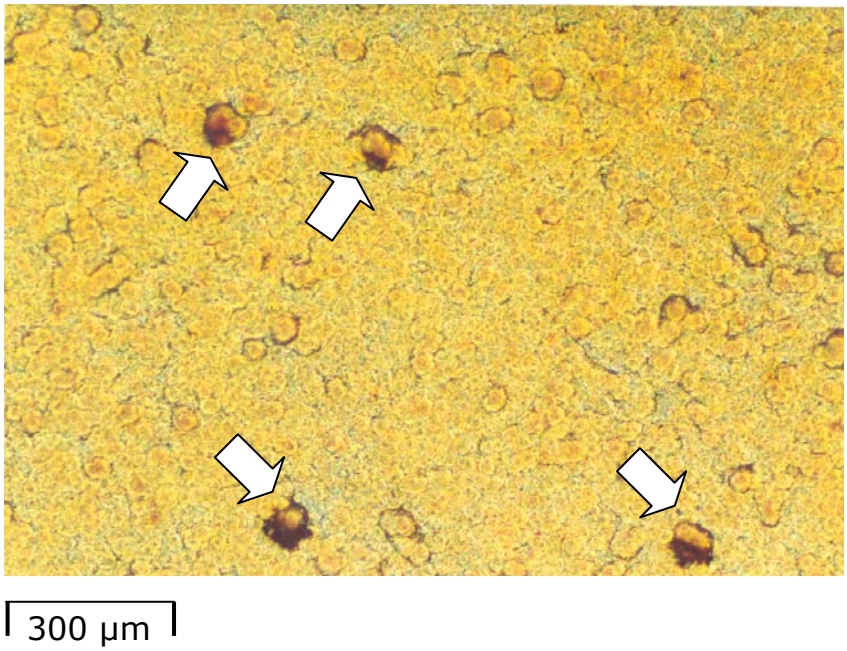

Figure 103. Micrographs showing four black spots on the Zinc-14%Nickel coating after 3½ hours immersion in $KMnO_4$ diluted solution.

On other hand, **Figures 104** and **105** displays images of the coating before and after 4 minutes immersion in the copper sulphate solution.

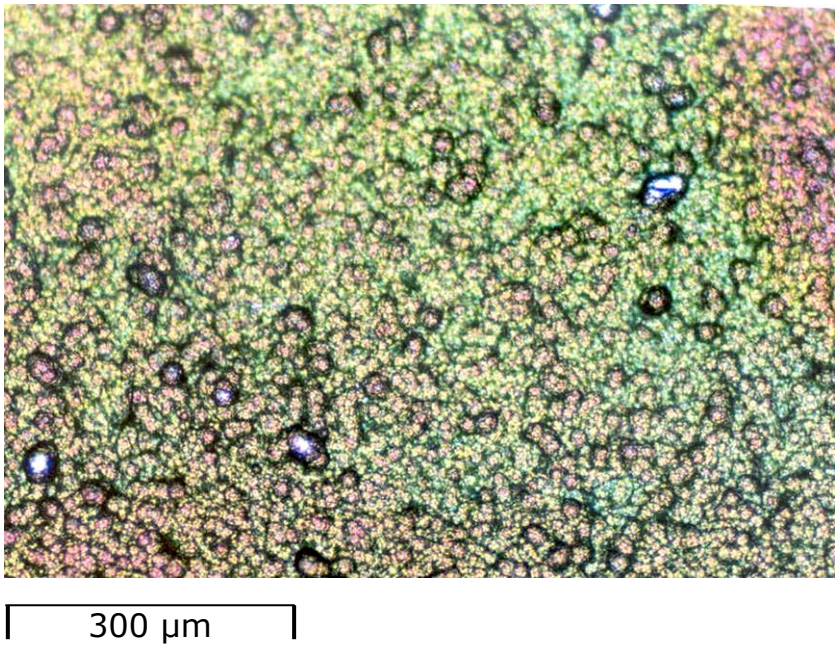

Figure 104. Micrograph from the Preece test before immersion in copper sulphate solutions.

From these figures, bright adherent copper deposits could be distinguished within most of the *crater-like* impression found on the coating surface.

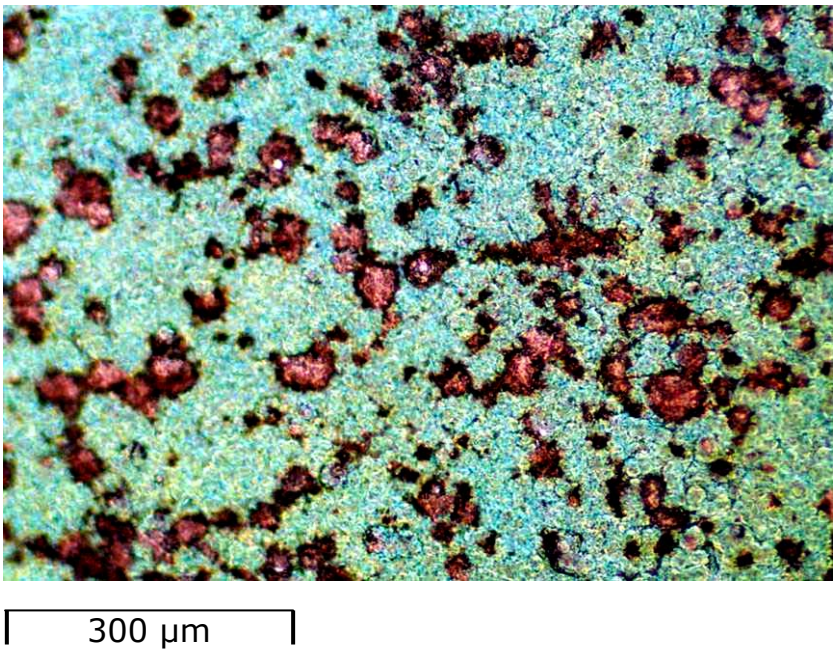

Figure 105. Micrograph from the Preece test after 4 minutes immersion in the copper sulphate solutions.

The Electrographic Sodium Ferricyanide prints were not successfully obtained using test conditions described in the experimental procedures. It was thought that low reagent concentration and tiny dimensions of cracks in the coating were the main reasons for this lack of results. Nonetheless, apparent dissolution of the coating was observed after 2 minutes exposure.

Due to the induced current flow between the coating and the electrolyte-soaked paper a progressive dissolution or etching of the coating took place. **Figure 106** displays a specimen treated in the electrographic test before and after 2 minutes exposure. It can be seen that the crack network became more evident as the coating was progressively dissolved.

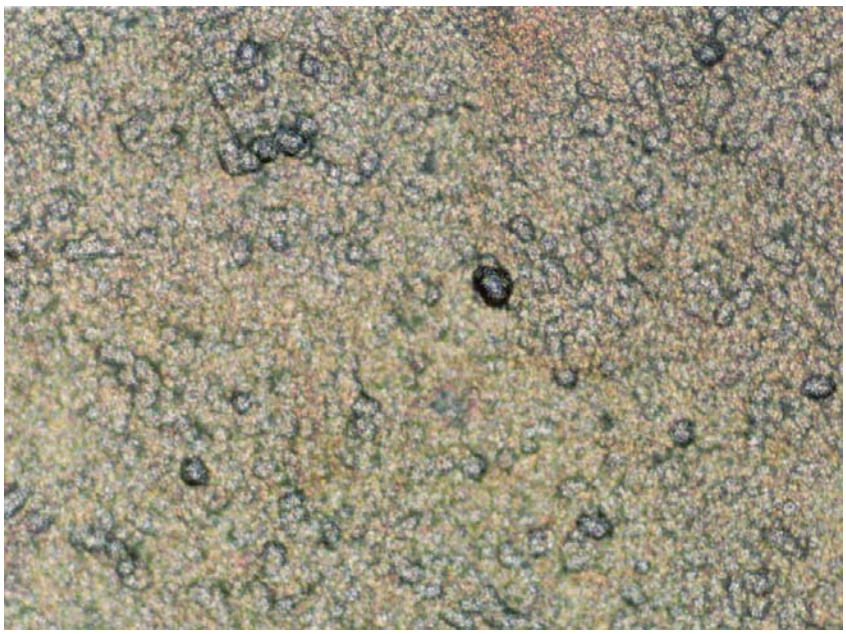

100 µm

(A)

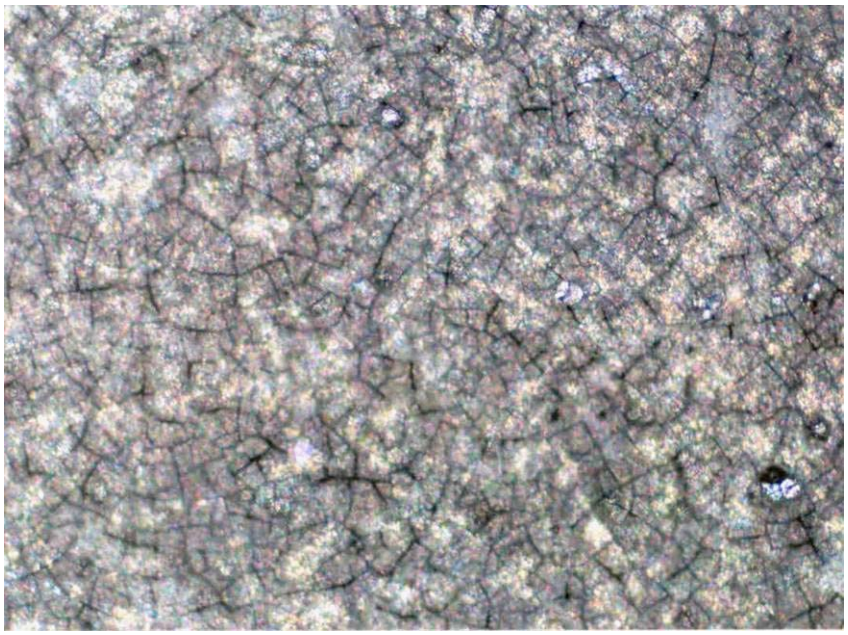

100 µm

(B)

Figure 106. Micrograph from the Electrographic test, A) before and B) after 2 minutes exposure.

Finally, a metallographic examination of the cross section area of the electroplated Zinc-14%Nickel coating, displayed in **Figure 107**, revealed a relatively large population of *through-thickness* pores.

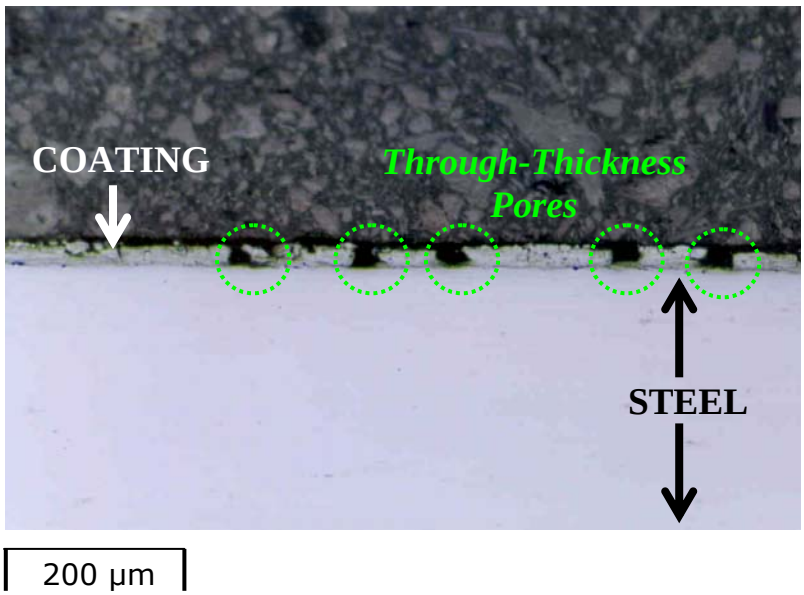

Figure 107. Through-thickness pores in the cross section of the Zinc-14%Nickel electroplated coating.

11.1.3. SermeTel®1140/962 Coating

Figure 108 and **109** show the surface of the aluminium based SermeTel®1140/962 sacrificial coating, before and after 3½ hours of immersion in a dilute potassium permanganate solution.

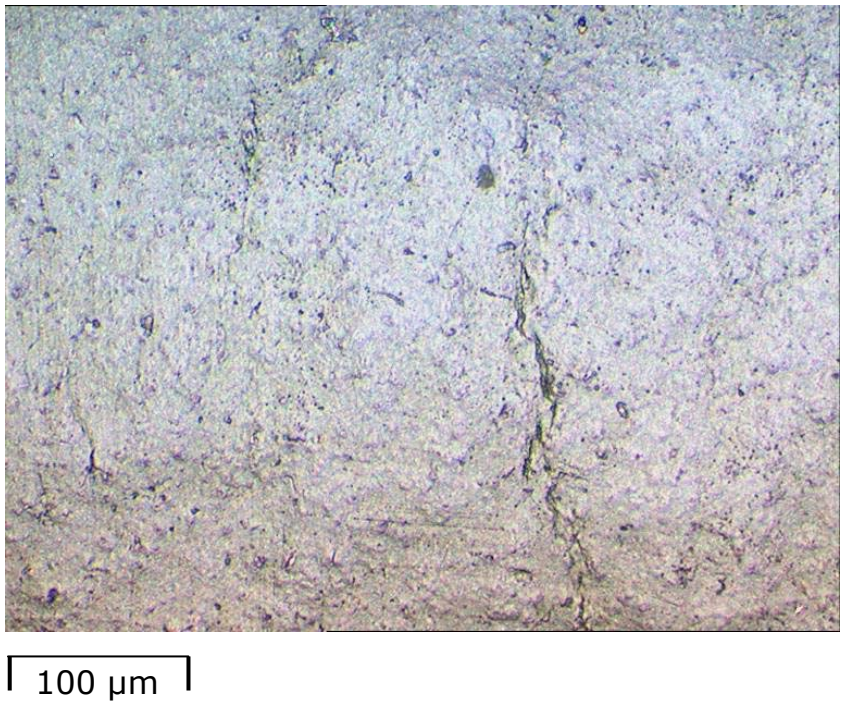

Figure 108. Surface characteristics of SermeTel®1140/962 coating before immersion in $KMnO_4$ solution.

It can be seen that no significant differences were found after the immersion period and no manganese oxide, *MnO,* products were identified on the coating.

The metallographic analysis of the cross section area of the SermeTel®1140/962, displayed in **Figure 110**, shows the presence of a high population of closed and bridged pores forming a randomly distributed network.

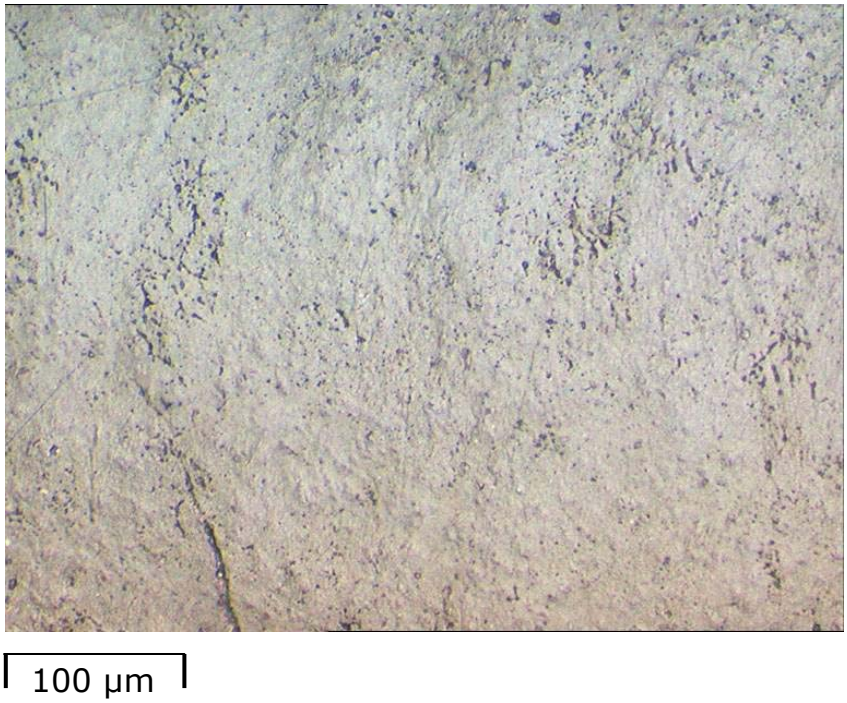

Figure 109. Surface characteristics of SermeTel®1140/962 coating after 3½ hours immersion in $KMnO_4$ solution.

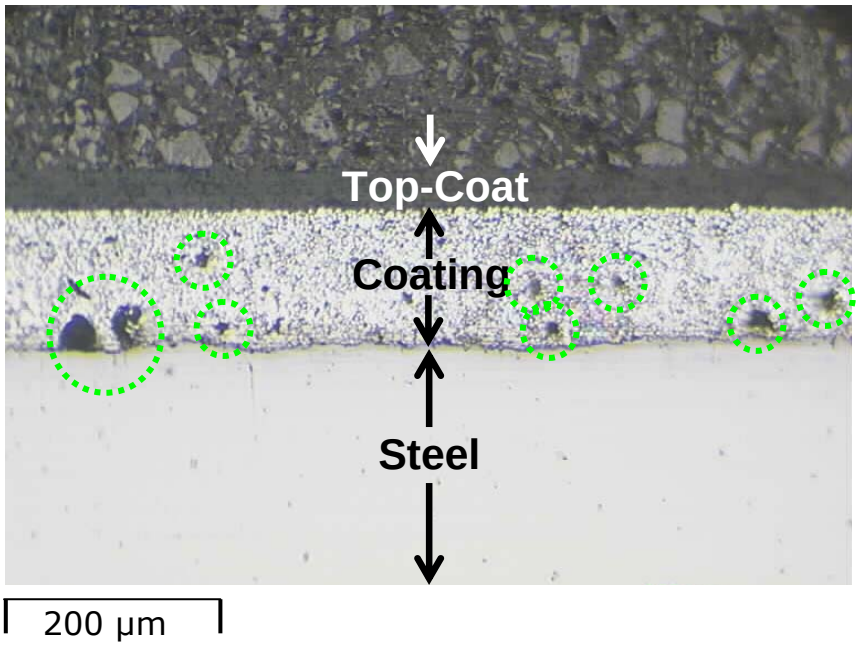

Figure 110. Closed pores in the cross section of the SermeTel®1140/962 coated specimen. (Circles indicate major closed and bridge type pores)

11.2. Sacrificial Coatings Open Circuit Potentials

Results from the open circuit potential measurements are presented in this section. Morphological examinations before and after immersion in 3.5% NaCl quiescent solutions were included in order to describe the surface morphology of the cadmium, Zinc-14%Nickel and SermeTel®1140/962 sacrificial coatings after partial dissolution.

11.2.1. Cadmium Coating

Figure 111 shows changes in the open circuit potential, *E*, with immersion time, *t*, for a sacrificial cadmium coating in a quiescent 3.5% NaCl solution. It can be seen that during the first 400 hours the open circuit potential slightly shifted from originally -750 to a more noble value of -725 mV (SCE). Afterwards, the potential remained fairly constant during 1200 hours of immersion.

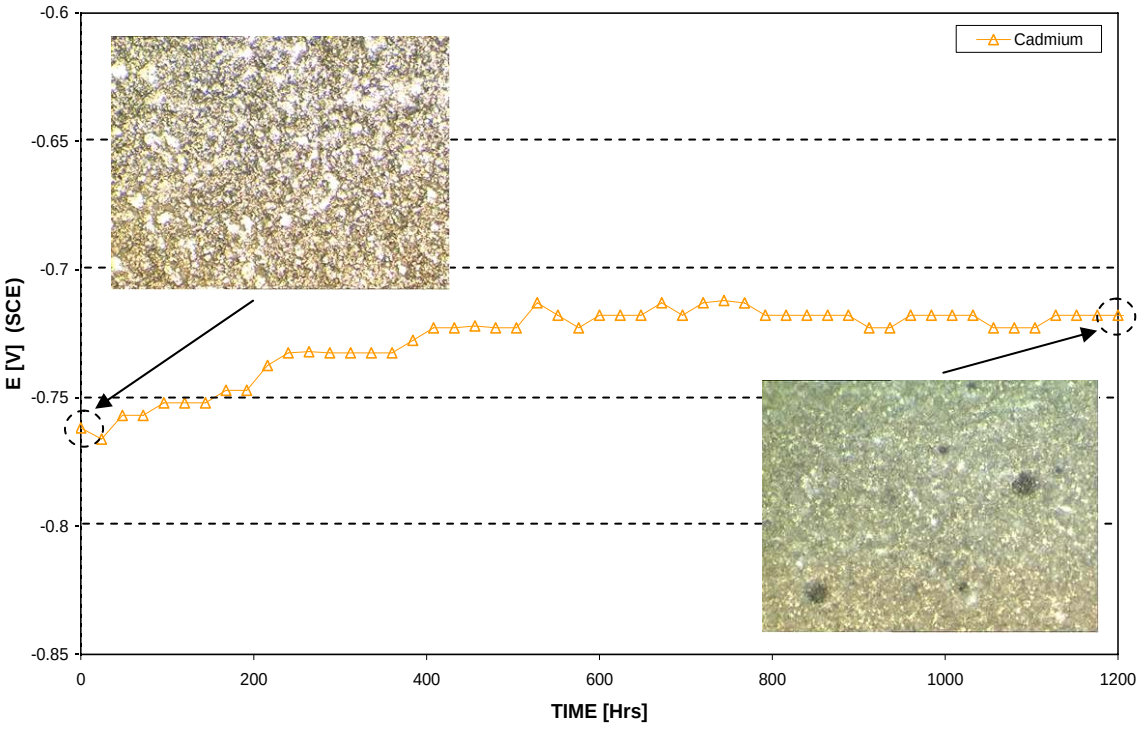

Figure 111. Changes in open circuit potentials for the cadmium coating in quiescent 3.5% NaCl solution.

A bright cadmium deposit can be seen before immersion in 3.5% NaCl quiescent solutions. Whereas, areas of dark brown or black corrosion

product were found in the coating surface within some of the crater like irregularities, after 1200 hours of immersion.

11.2.2. Zinc-14%Nickel Coating

Variations of the corrosion potential, *E*, with immersion time for the sacrificial Zinc-14%Nickel coating in a quiescent 3.5% NaCl solution are shown in **Figure 112**.

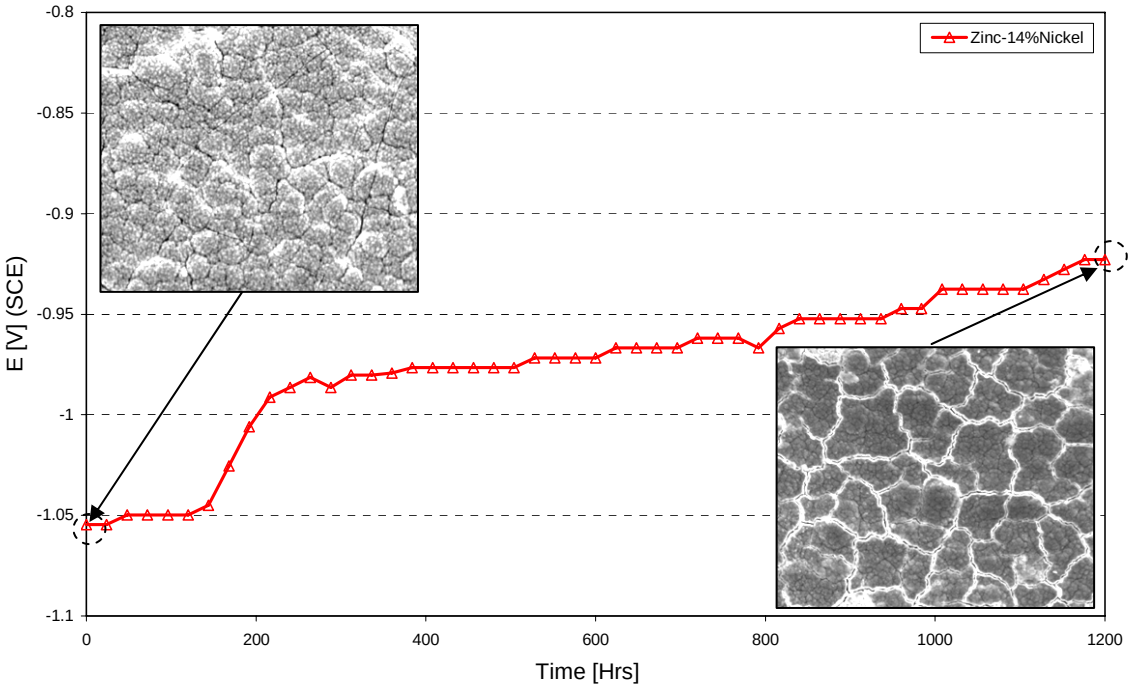

Figure 112. Changes in open circuit potentials for Zinc-14%Nickel coating in quiescent 3.5% NaCl solution.

It can be seen overall that the corrosion potential became more noble with time. Nonetheless, during the first 150 hours immersion *E* displayed a very stable value of approximately -1.05 V(SCE). Afterwards, *E* abruptly changed to a more noble value in a relatively short period of time. After approximately 300 hours, the sacrificial coating displayed a slow and constant ennoblement, reaching a final value of -0.960 V(SCE) following 1200 hours immersion.

By comparing the surface morphology before and after 1200 hours of immersion in 3.5% NaCl quiescent solutions, it can be seen that the Zinc-14%Nickel deposit corroded in a localized manner with the appearance of surface crack network.

11.2.3. SermeTel®1140/962 Coating

Figure 113 displays the open circuit potential trend for the aluminium based sacrificial coating SermeTel®1140/962 immersed in a 3.5% NaCl quiescent solution.

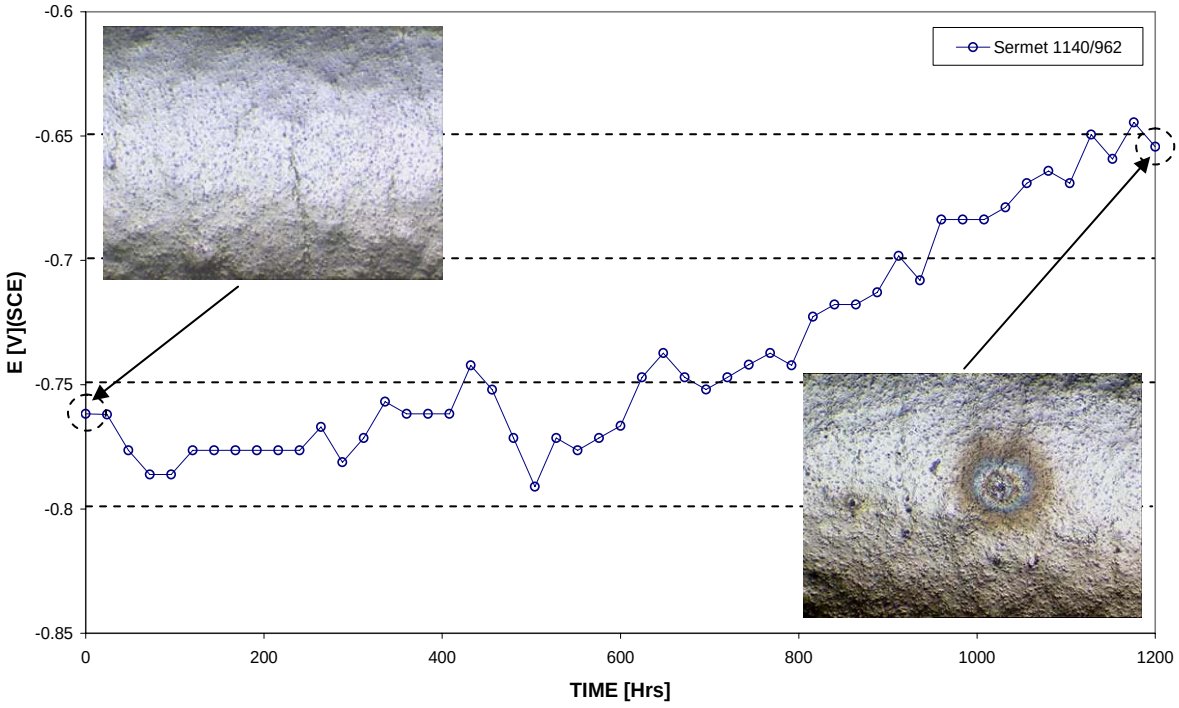

Figure 113. Changes in open circuit potentials for SermeTel®1140/962 coating in quiescent 3.5% NaCl solution.

During the first 600 hours of immersion the open circuit potential remained fairly constant within a range between -800 to -750 mV (SCE). Following this stage, a progressive ennoblement took place, reaching a value of approximately -650 mV (SCE).

It can be seen that the polymer topcoat degraded in a localised manner after 1200 hours of immersion in 3.5% NaCl quiescent solutions, displaying circular colour fringe patterns around the affected areas together with white corrosion products.

DISCUSSION

The discussion of the results has been conveniently divided in four main sections. First, hydrogen embrittlement and re-embrittlement susceptibilities of 300M and AerMet®100 high strength steels produced by the electroplated cadmium, Zinc-Nickel and aluminium based SermeTel®1140/962 sacrificial coatings are discussed. Only the effect of electroplated cadmium and the SermeTel®1140/962 sacrificial coating has been assessed for the micro-alloyed GifloM2000 and the CSS-42L™ stainless high strength steel, respectively.

In the second section hydrogen transport characteristic of the 300M and AerMet®100 high strength steels has been compared and related to the findings derived from the *SSRT* results. Analysis of the microstructural characteristics of the alloys has been also included. This section has covered the study of the results from the hydrogen permeation measurements as well as the alternative chrono-potentiometric charging method. Moreover, the effect of residual stresses, induced by surface treatments such as shot peening, on the hydrogen transport characteristics of 300M steel membranes is evaluated. The effect of elastic stresses on 300M, GifloM2000 and CSS-42L™ tensile specimens using the chrono-potentiometric charging method has been included.

The third section contemplates a comparison between the three sacrificial coatings by means of their barrier properties. This section includes an exhaustive study of the coating morphological characteristics, which contributed to the detection of regions where hydrogen uptake occurred for each particular sacrificial material.

Finally, a comprehensive analysis which covered all aspects described in the previous three sections has been considered. In this opportunity, different levels of hydrogen embrittlement or re-embrittlement were associated with two main factors: 1) the general characteristics of the high strength steels considered and 2) the sacrificial coatings used.

12. *SSRT* Results

To begin with the analysis of the *SSRT*'s results, the performance of the 300M high strength steel has been analysed when a conventional sacrificial cadmium coating was used. Afterwards, a comparison of these results with those obtained for the alternative new alloy AerMet®100 is considered. Later, the extent of hydrogen embrittlement and re-embrittlement of 300M and the alternative AerMet®100 are discussed when the Zinc-Nickel and the aluminium based SermeTel®1140/962 new sacrificial coatings were applied.

The performance of the micro alloyed GifloM2000 high strength steel has been only considered in terms of hydrogen re-embrittlement when the conventional cadmium sacrificial coating suffered corrosion. Similarly, the susceptibility to hydrogen embrittlement and re-embrittlement of the CSS-42L™ stainless steel has been only assessed when the aluminium based SermeTel®1140/962 coating was used. Afterwards, a final comparison between the performances of the four high strength steels is presented.

12.1. Effect of Cadmium Coating on 300M Specimens

300M high strength steel has been widely used for decades as the first material for structural applications in the aerospace industry. Similarly, electroplated cadmium has been considered the primary sacrificial system to protect high strength steel components from corrosion during the direct exposure to aggressive environmental conditions. In this respect, the two deleterious effects on the mechanical properties evaluated in this project were: 1) direct hydrogen embrittlement following electroplating processes, and 2) re-embrittlement when the coating suffered corrosion.

12.1.1. Direct Embrittlement

Initially, unplated 300M specimens considered as the control group, failed in average after 31.6 hours at a strain rate of 0.96×10^{-6} s^{-1}. A dramatic decrease to 14.5 hours in the mean time to failure, *TTF*, was found for the cadmium electroplated 300M specimens due to direct hydrogen embrittlement. This level of hydrogen embrittlement corresponded to an embrittlement index of 0.54. Bearing in mind that embrittlement indices of 0.60 are associated with severe embrittled conditions, cadmium plated 300M specimens were considered severely susceptible to delayed fracture due to occluded hydrogen. This effect can be noticed in **Figure 114**, which shows a comparison of stress vs. time plots for a representative unplated and cadmium plated 300M specimen.

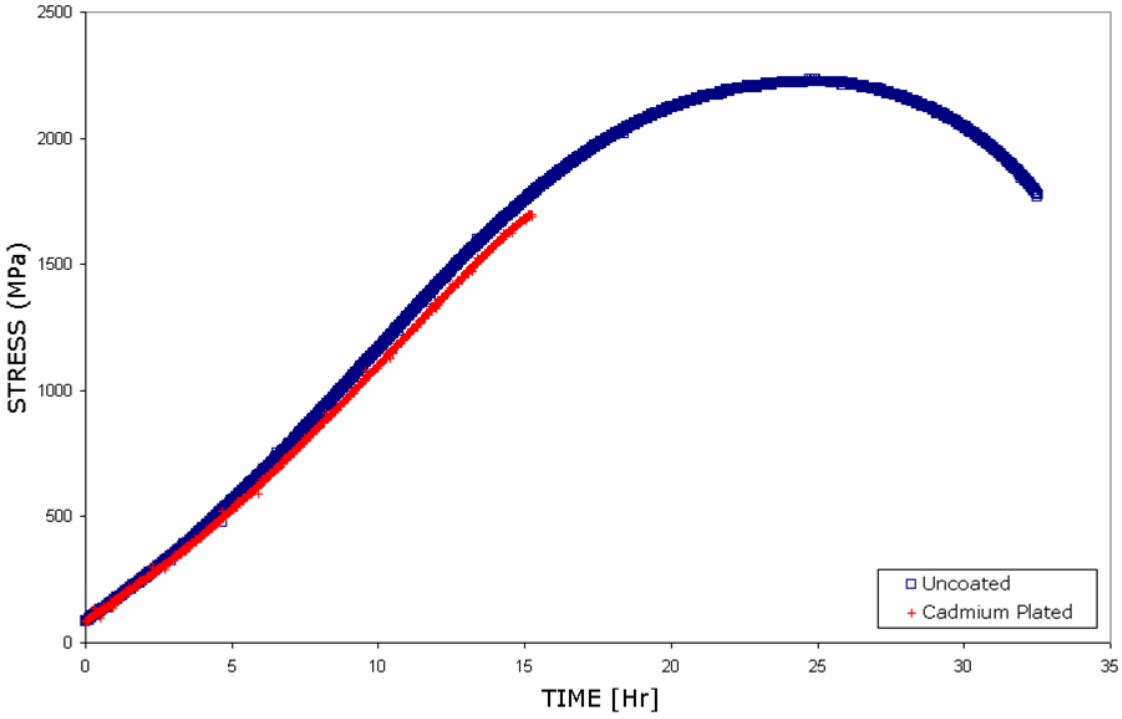

Figure 114. Stress v. time graphs for uncoated and cadmium plated 300M specimens.

It is known that electroplated cadmium promotes hydrogen uptake by steels as hydrogen is inevitably produced in the cathodic reaction during the electroplating process.[128, 132] Moreover, it has been widely proposed

that regardless of the hydrogen embrittlement mechanism, once atomic hydrogen had been taken up by the steel it diffuses to regions of high triaxial stresses, where the hydrogen concentration becomes sufficient to produce crack propagation.[78]

Interestedly, quantitative fractographic analyses carried out for cadmium plated 300M specimens, displayed in **Figures 67** to **72**, revealed the extent of embrittled regions across the fracture surfaces of tensile specimens. 300M steel displayed a staggering 10 to 15% of the total fracture surface with intergranular fracture, *IG*, and 6 to 8% with brittle transgranular cleavage fractures. These values were associated with the severe embrittlement displayed by 300M specimens due to cadmium electroplating.

Beachem *et al*[82] in the '*localised slip model'* for hydrogen embrittlement suggested that the stress intensity and the localised hydrogen concentration at the crack tip determines the fracture mode. He noted that at regions in direct contact to hydrogen (i.e. electrolyte-steel interface), fracture is generally *IG*, taking place by interface separation of the grain boundaries. Thereafter, a brittle-to-ductile transition failure is exhibited, ending in regions where unaffected material showed a ductile mode of fracture. The distribution of the fracture modes in 300M clearly followed this pattern.

Nevertheless, isolated *IG* regions were unexpectedly found in two of the cadmium plated 300M specimens, as was previously shown in **Figure 72** (coloured in red) and depicted in more detail in **Figure 115**. These isolated brittle *IG* areas were separated from other embrittled regions by ductile micro-void coalescence fracture mode. In this respect, Elias *et al*[71] had suggested that the effect of a localised internal hydrogen super-saturation might be significant for some high strength steels. This localised internal hydrogen super-saturation might take place at any major microstructural flaw within the material leading to a build up of an internal hydrogen pressure, which assists interface decohesion.

It is feasible to suggest that the fractographic evidence shown by two of the cadmium plated 300M specimens might be associated with localised hydrogen saturation at microvoids, microcracks or any additional microstructural flaw randomly distributed within the alloy.

Although the previous fractographic results have suggested that hydrogen embrittlement possibly followed this particular mechanism for 300M steel at the conditions tested, it is more likely to consider that not only one but a variety of mechanisms can simultaneously take place depending on the distribution of flaws, stress and localised hydrogen concentrations.

To illustrate this fact, T.D. Lee *et al*[85] proposed that hydrogen could promote the plastic deformation instability along characteristic slip lines which accelerates the formation of voids on spheroidized plain carbon steel. But, later on the same author has suggested that void formation at microstructural flaws has little effect on the fracture of AISI-4340 U-notch bend specimens, (this low alloy high strength steel is very similar to the 300M steel). Instead, it was considered that hydrogen distribution has a dominant effect on the decohesion at the crack tip.[145]

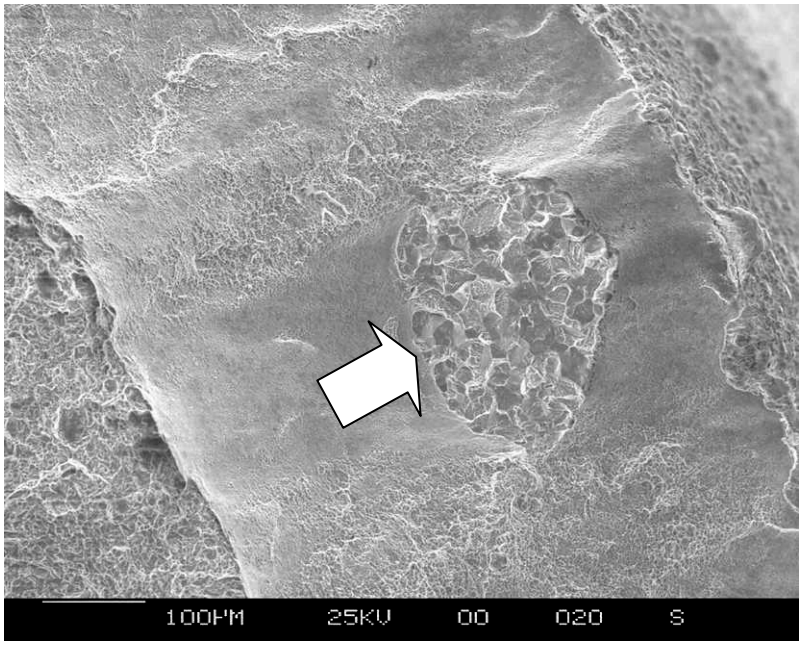

Figure 115. Isolated region displaying inter-granular fracture morphology in a cadmium plated 300M specimen.

On the other hand, results for the cadmium plated and baked 300M specimens have shown an acceptable recovery of the mechanical properties. The mean time to failure value for the cadmium plated and baked 300M specimens was approximately 30.2 hours. Nevertheless, this value still remained slightly less than that for the unplated controls (31.6 hours). The small difference in *TTF* values represented a very low hydrogen embrittlement index of 0.04. Therefore, baking the cadmium plated 300M steel for 24 hours at 200°C proved to be an effective means of removing most of the occluded hydrogen from the material. This process is commonly known as de-embrittlement and can be considered as reversible.

12.1.2. Re-Embrittlement

The last condition tested for the cadmium-300M system considered the extent of hydrogen re-embrittlement when the cadmium coating was freely exposed to 3.5%NaCl solutions. It was shown that 300M specimens were significantly susceptible to delayed failure due to re-embrittlement. The corresponding stress-time plot for this condition, depicted in **Figure 116**, shows a considerable reduction in the mean time to failure from 31.6 to 26.6 hours for the uncoated and the cadmium plated, baked and corroded specimens, respectively. Moreover, the cadmium plated, baked and corroded 300M specimen failed just after the *UTS*, showing relatively less reduction in area than that for the unplated specimen.

Open circuit potential measurements showed that the cadmium sacrificial coating remained at a potential of approximately -725mV(SCE) in 3.5%NaCl solutions after 1200 hours, (**Figure 111**). Taking into account that the 3.5%NaCl solutions displayed a *pH* value between 5 and 7, it is possible to notice from the *Pourbaix* diagram for the iron-water system, (**Figure 9**), that the hydrogen evolution reaction is taking place at potentials near -650mV(SCE). Therefore, it is possible to assume that thermodynamic conditions were favourable for hydrogen evolution and uptake by the steel at more active potentials. In addition, it can be

considered that during re-embrittlement only a fraction of the total hydrogen evolving on the steel substrate is taken up by the steel while the majority escapes from the surface as bubbles.

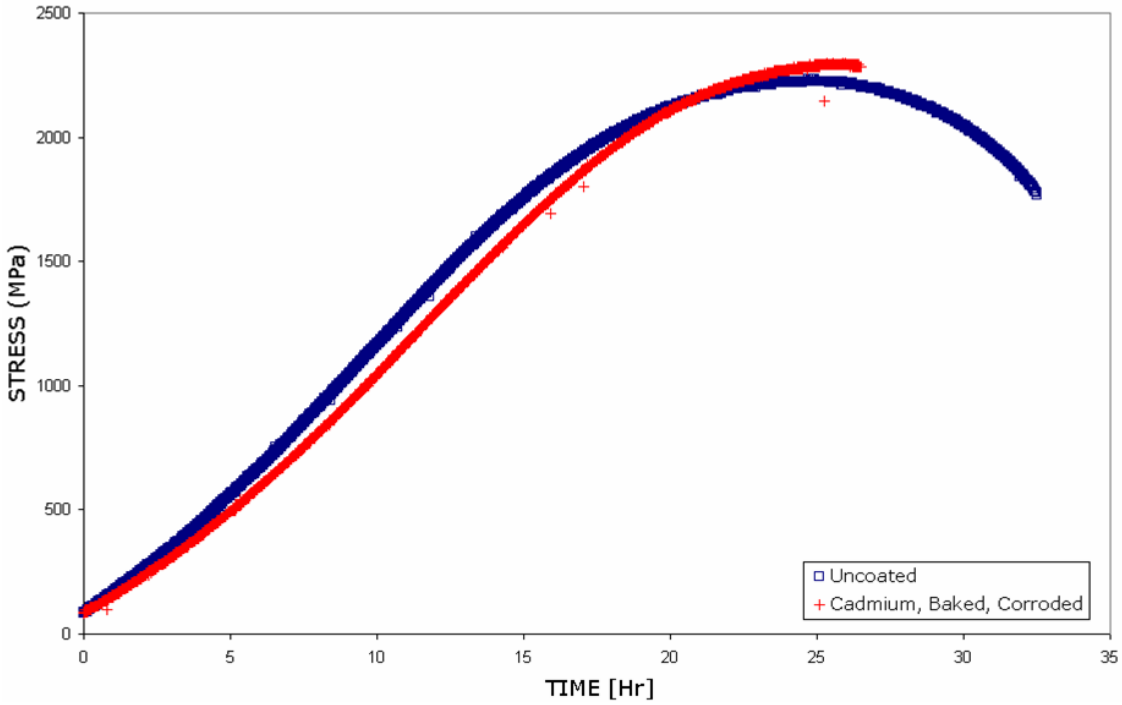

Figure 116. Stress v. time graphs for uncoated and cadmium plated, baked and corroded 300M specimens.

The level of re-embrittlement shown for the cadmium plated, baked and corroded 300M specimens was 0.16, a value that is much lower than that produced by direct embrittlement. However, it still represents a noticeable deleterious effect on the mechanical properties of the 300M steel. **Figure 117** graphically depicts the hydrogen embrittlement and re-embrittlement susceptibilities of 300M specimens due to the cadmium coating for all condition tested. Again, it can be noticed that the susceptibility to delayed failure is highly significant after the cadmium electroplating process, almost negligible following the baking process, but considerably important during the partial dissolution of the sacrificial coating.

Finally, it is important to point out that only 2 out of 4 cadmium plated, baked and corroded 300M specimens failed within the scribed region,

deliberately produced to promote hydrogen uptake where the steel substrate was freely exposed to 3.5%NaCl solutions. As possible reasons for this finding, two statements have been considered: First, failure might be defined by the distribution of flaws within the material, and secondly, hydrogen re-embrittlement occurred at sites of major discontinuities in the sacrificial cadmium coating. The distributions of these features might have an important influence on the hydrogen uptake by the steel substrate. Additional discussion on this particular topic has been given in further sections.

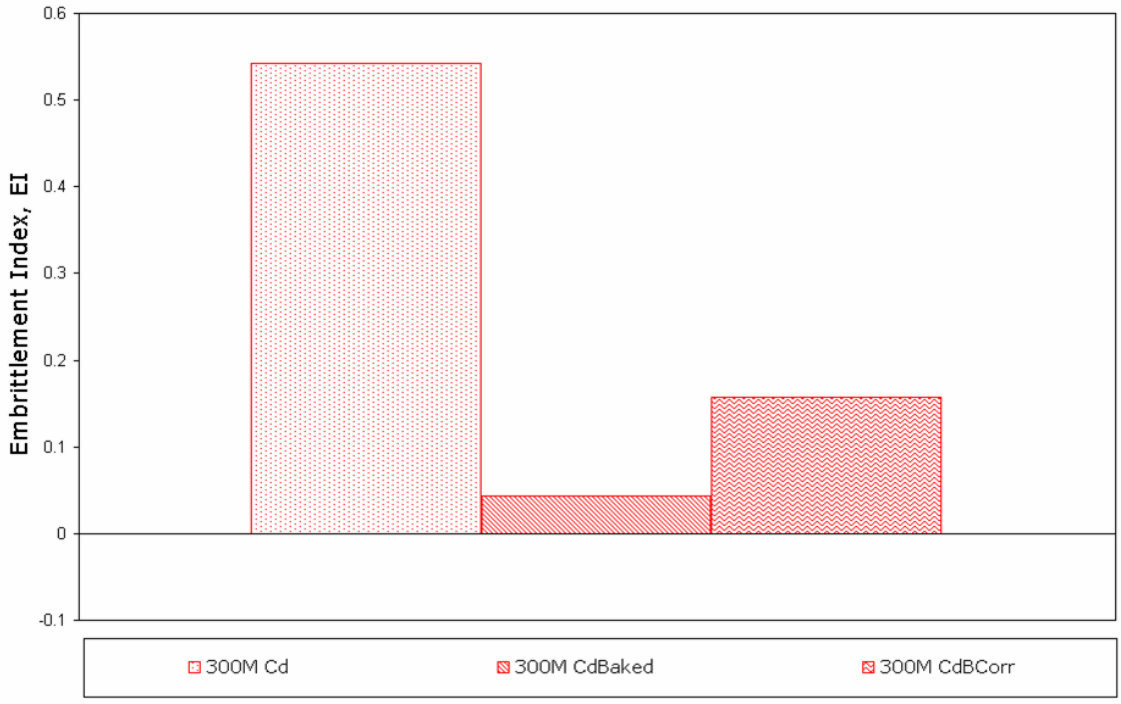

Figure 117. Bar chart of embrittlement indices for cadmium plated, cadmium plated and baked and cadmium, plated, baked and corroded 300M specimens.

12.2. Comparison to AerMet®100 Specimens

In this project AerMet®100 has been considered as an alternative alloy to the conventional 300M high strength steel. Therefore, it has been a priority to assess and compare the susceptibility to hydrogen related failure of this new material due to the cadmium sacrificial coating. Similar to the analysis made for 300M steel, the extent of hydrogen embrittlement and re-embrittlement are analysed separately.

12.2.1. Direct Embrittlement

SSRT results for unplated and cadmium plated AerMet®100 specimens have shown that the mean time to failure value, *TTF*, slightly decreased from 32.9 to 31.1 hours. Consequently, it is clear that AerMet®100 has a much lower susceptibility to direct hydrogen embrittlement than 300M after the cadmium electroplating process. This comparison is graphically depicted in **Figure 118**, where Weibull distributions for unplated and cadmium plated 300M and AerMet®100 specimens are shown.

It is evident that time to failure values were dramatically reduced for cadmium plated 300M specimens, whereas AerMet®100 specimens only suffered a small reduction under similar hydrogen charging conditions. Analogous results were shown after the fratographic analysis performed on AerMet®100 tensile specimens. Regions directly exposed to the electrolyte-steel interface, presented transgranular quasi-cleavage brittle fracture. Whereas, ductile microvoid coalescence fracture morphology was found in the central region of the cadmium plated specimens. It has been reported elsewhere[146] that embrittlement of AerMet®100 steels proceeds along martensite lath and packet interfaces, as well as cleavage planes through martensite laths, where hydrogen tends to promote cleavage-like cracking parallel to {100} and {112} planes in martensite. [146]

Cadmium plated AerMet®100 tensile specimens only displayed a tiny 3 to 6% of embrittled regions, which showed brittle cleavage fracture

morphology. In comparison, 300M specimens displayed between 16 to 23% of embrittled regions in total, including inter-granular and trans-granular morphologies. This comparison might indicate that AerMet®100 specimens were not as saturated with hydrogen as 300M specimens to reach the critical hydrogen concentration required to produce equivalent levels of hydrogen embrittlement at regions of high triaxiality.[147]

It was thought that these remarkable differences on the distribution of the embrittled regions were determined by the hydrogen distribution within distinctive microstructural features of the high strength steels. Alternatively, previous work done by E. U. Lee[147] had suggested that these kind of fractographic observations might indicate that the diffusivity of hydrogen in AerMet®100 steel is lower than for 300M steels.

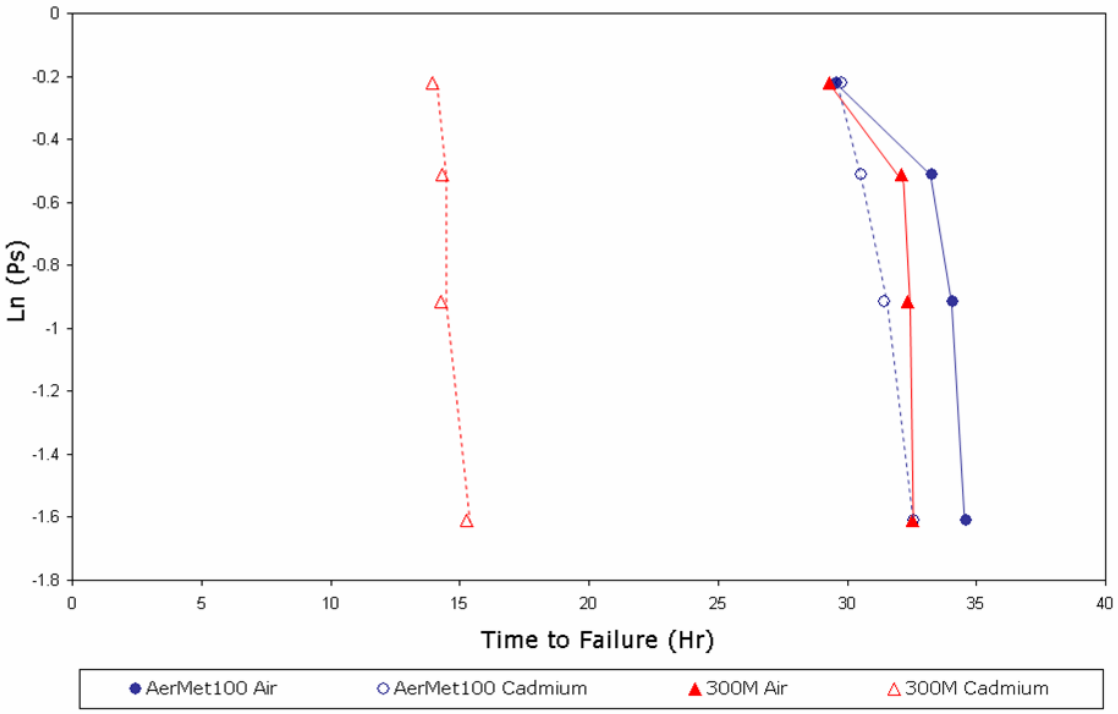

Figure 118. Comparison of the Weibull distribution for unplated and cadmium plated 300M and AerMet®100 specimens.

Following the statement which suggests that hydrogen embrittlement is produced when at a specific stress level, the critical hydrogen

concentration is reached; it is feasible to consider that the intrinsic hydrogen transport characteristic of the alloys plays a decisive role on their tendency to fail due to occluded hydrogen within the microstructure. An extensive discussion on this area has been developed in the next sections.

In addition, *SEM* examinations of the regions which showed ductile fracture morphology revealed the presence of cerium-rich inclusions randomly distributed on the fracture surface of AerMet®100 specimens. These spherical particles were inside the largest microvoids and they were thought to represent the sites for some void nucleation in AerMet®100. **Figure 119** shows one of these inclusions with its corresponding *EDAX* analysis.

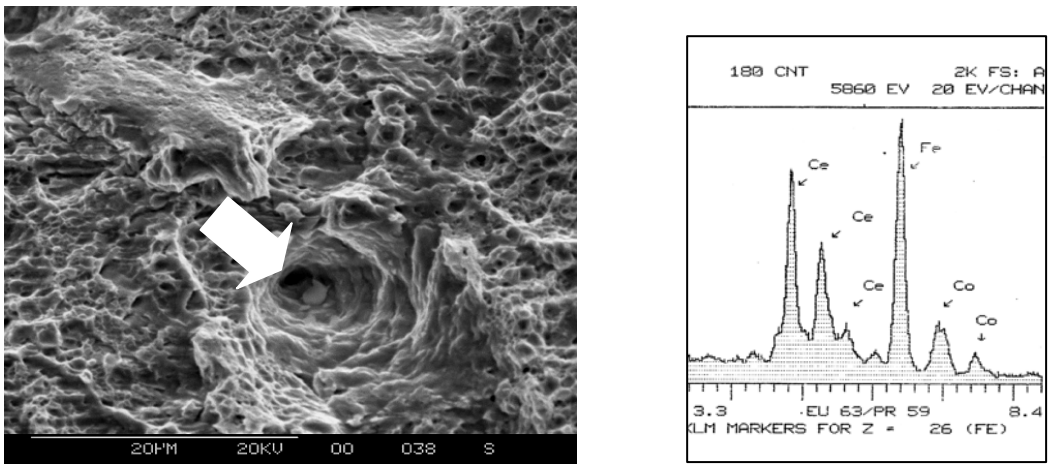

(A) (B)

Figure 119. (A) *SEM* micrograph showing cerium-rich inclusion, and B) the corresponding *EDAX* qualitative elemental analysis.

Additions of rare earth metals, such as lanthanum and cerium, are commonly used to modify the shape of non-metallic inclusions to avoid elongated stringers, which would be detrimental to the mechanical properties of the high strength steel.[148] Moreover, Olson *et al*.[149] postulated that intergranular hydrogen cracking is eliminated by rare-

earth element additions, which reduced the grain boundary impurity segregation on ultra high strength steels. Nonetheless, alternative micromechanical models of grain boundary decohesion suggests that the trapping of hydrogen and high stresses at the crack tip are sufficient to promote hydrogen embrittlement without a dominant contribution from the segregation of impurities at grain boundaries.[100]

The second condition discussed in the present section involved the cadmium plated and baked AerMet®100 steel. A small reduction in the mean *TTF* value was found for cadmium plated and baked AerMet®100 specimens, which was represented by an *EI* of only 0.03. This embrittlement index is very similar to that found for the 300M specimens in the same condition. Consequently, these results reinforce the idea that almost a complete recovery of the mechanical properties is effectively achieved after baking the cadmium plated AerMet®100 and 300M steels.

12.2.2. Re-Embrittlement

Contrasting with the performance of the conventional 300M steel, AerMet®100 proved to be not susceptible to hydrogen re-embrittlement due to the corrosion of the cadmium sacrificial coating. On the contrary, Weibull distributions for unplated and cadmium plated, baked and corroded AerMet®100 specimens showed a slight increment in the mean time to failure, *TTF*, value from 32.9 to 33.8 hours. It is feasible to assume that this increment is associated with the variability of results from the *SSRT*'s, since student *t*-test analyses corroborated with a 95% of confidence that both groups did not belong to different statistical populations. The comparison of the Weibull distributions for unplated and cadmium plated, baked and corroded 300M and AerMet®100 specimens is graphically depicted in **Figure 120**.

The amount of hydrogen that would be evolving during the cadmium electroplating is thought to be higher than that produced during the partial dissolution of the coating. Therefore, the amount of hydrogen to be

taken up by the high strength steel during re-embrittlement might be lower than that during electroplating, but it is still enough to produce delayed failure of at least the most susceptible 300M steel. Clearly, equivalent amounts of hydrogen are not sufficient to produce any measurable deleterious effect on the alternative AerMet®100 steel.

To summarise the performance of the cadmium plated, cadmium plated and baked and cadmium plated, baked and corroded AerMet®100 steel, a convenient comparison is graphically represented in **Figure 121**. In general, it can be seen that AerMet®100 is much less prone to hydrogen induced failure than the conventional 300M steel, when they are protected from corrosion with a sacrificial cadmium coating.

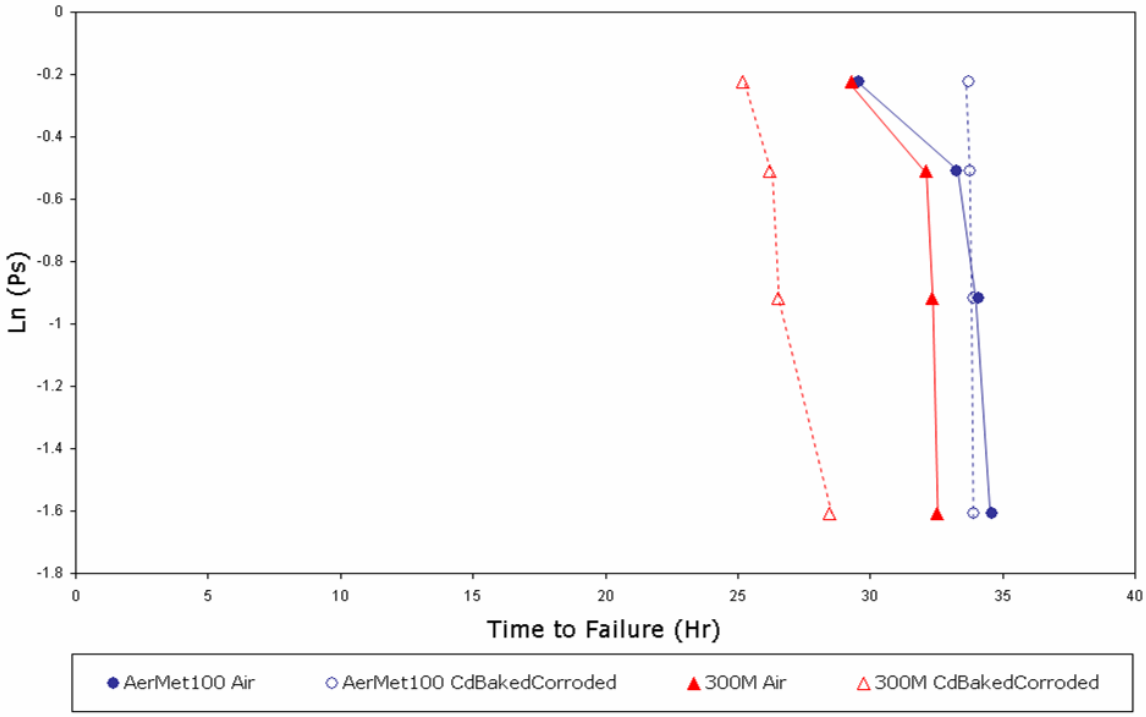

Figure 120. Comparison of the Weibull distribution for unplated and cadmium plated, baked and corroded 300M and AerMet®100 specimens.

However, cadmium coatings have been banned in the European Union for most engineering applications due to its toxicity and health related problems, specially those associated with the exposure to concentrations

above the recommended limit.[13, 14] What is more, the most recent publication from the Ministry of Defence, Standard 03-36,[150] describes a guidance for the use of alternative materials to cadmium on defence equipment including aerospace applications.

In this particular subject, one of the aims of this research project is to determine possible alternative replacements for the widely used cadmium sacrificial coating. Zinc-Nickel alloys have been considered by several researchers[58-65, 150, 151] as a promising material to substitute for cadmium. Therefore, the use of a Zinc-Nickel sacrificial coating was evaluated for both, 300M and the primary alternative alloy AerMet®100.

Figure 121. Bar chart of embrittlement indices for cadmium plated, cadmium plated and baked and cadmium, plated, baked and corroded 300M and AerMet®100 specimens.

12.3. Effect of Zinc-Nickel Coating on 300M Specimens

The effect of the alternative Zinc-14%Nickel sacrificial coating on 300M high strength steel has been evaluated in this section. Since the Zinc-Nickel coating displays different sacrificial characteristics than cadmium, the susceptibility of 300M steel to delayed failure has been considered taking into account that the Zinc-Nickel coating represents a different source of hydrogen either during the electroplating process or during its partial dissolution in service.

12.3.1. Direct Embrittlement

It was found that 300M displayed a high susceptibility to direct hydrogen embrittlement due to the electroplating of the Zinc-14%Nickel coating. Eventually, some of the Zinc-Nickel plated 300M specimens failed at almost the yield strength, as is shown in **Figure 122**. The corresponding reduction in the mean *TTF* value was from 31.6 to 17.1 hours for the uncoated and Zinc-14%Nickel plated 300M specimens, respectively. These results were associated to a severe embrittlement, with an *EI* of 0.46. Moreover, when these results are compared to those for the cadmium plated conditions, it is clear that the later coating produced more direct embrittlement than that for the alternative Zinc-14%Nickel coating.

The observation that both cadmium and Zinc-Nickel plated 300M specimens displayed such extents of direct embrittlement, (0.54 and 0.46, respectively), suggests that considerable amounts of hydrogen were evolving and taken up by the steel during the two electroplating processes. It is known that the efficiency of the electroplating processes is commonly affected by a variety of factors ranging from bath composition to parameters such as temperature, *pH* and applied current density.

For the Zinc-Nickel electroplating processes, Baldwin and Robinson[12, 15, 151] demonstrated that the acidity of Zinc-Nickel sulphates baths is a

critical variable which greatly influence the current efficiency at which the alloy is deposited. Specifically, they reported that when the *pH* is around 4.5, the current efficiency is nearly 100%. Whereas, for more acid compositions the efficiency decreases considerably and the amount of current lost is mainly due to hydrogen evolution reaction on the steel substrate, not all, but a fraction of which penetrates the steel and produces direct hydrogen embrittlement.

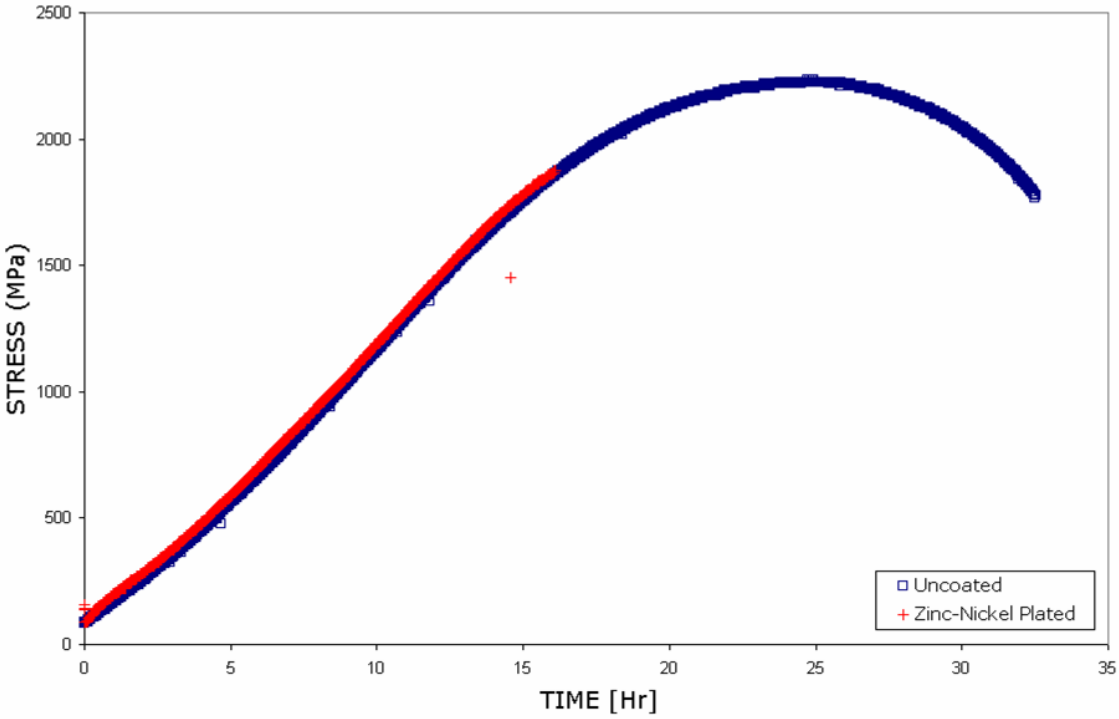

Figure 122. Stress v. time graphs for uncoated and Zinc-14%Nickel plated 300M specimens.

Similar observations were reported by Wu and Fedrizzi,[59] regarding the current efficiency during Zinc-Nickel electroplating using chloride baths. In this particular case when the ratio of cations, Ni^{2+}/Zn^{2+}, is between 0.5 and 1 the current efficiency of the alloy deposition reaches only 90%.

Indeed it is clear that even for high current efficiencies some hydrogen would be inevitably taken up by the high strength steel during electroplating. However, the effectiveness of the post-plating baking treatment in removing the occluded hydrogen from the steel has been

verified following the complete recovery of mechanical properties displayed by the Zinc-14%Nickel plated and baked 300M specimens. Moreover, a barely noticeable *EI* associated with the Zinc-14%Nickel plated and baked and cadmium plated and baked 300M specimens, corroborated this statement.

12.3.2. Re-Embrittlement

During the *SSRT* test carried out in quiescent 3.5%NaCl solutions, the severity of re-embrittlement displayed by the Zinc-14%Nickel plated, baked and corroded 300M specimens corresponded to a reduction in the mean *TTF* value from 31.6, for unplated condition, to 14.9 hours. This deleterious effect can be appreciated from the stress-time plot, depicted in **Figure 123**, in which the Zinc-Nickel plated, baked and corroded specimen failed far below the 300M's yield strength.

The corresponding *EI* for this condition was 0.53. This value is higher than that for the conventional cadmium sacrificial coating when suffered corrosion in 3.5%NaCl solutions. Although the amount of hydrogen taken up by the steel during the corrosion of the sacrificial coating might depend on several factors, it is known that the electro-negativity of the coating determines the amount of hydrogen generated at the steel surface.[18, 152, 153]

Since levels of re-embrittlement were greater than those displayed by the cadmium plated, baked and corroded 300M specimens, it has been considered that this effect resulted from the Zinc-14%Nickel in having a more electronegative corrosion potential. In relation to this statement, open circuit potentials measurements for the Zinc-14%Nickel coating showed that although the alloy suffered an ennoblement process, its potentials remained between -1050 and -960mV(SCE) for a period of 1200 hours immersion in 3.5%NaCl solutions. By comparison, the cadmium coating displayed a more noble potential of -725mV(SCE) for the same conditions.

Following this observation it is feasible to suggest that more hydrogen was generated and therefore taken up by the 300M high strength steel during the re-embrittlement of Zinc-Nickel than that when the cadmium was corroding. Likewise, Robinson and Kilgallon[153] have previously shown that the amount of hydrogen diffusing into low carbon steel membranes increases by making the hydrogen charging potentials more negative or cathodic in sterile and biologically active seawater.

To visualise the difference in hydrogen embrittlement and re-embrittlement susceptibilities of 300M steel due to the Zinc-14% Nickel coating, a comparison of the embrittlement indices is shown in **Figure 124**. It can be seen that the conventional 300M steel is severely affected by delayed failure due to both the Zinc-Nickel electroplating process and the corrosion of the sacrificial coating in 3.5%NaCl solutions.

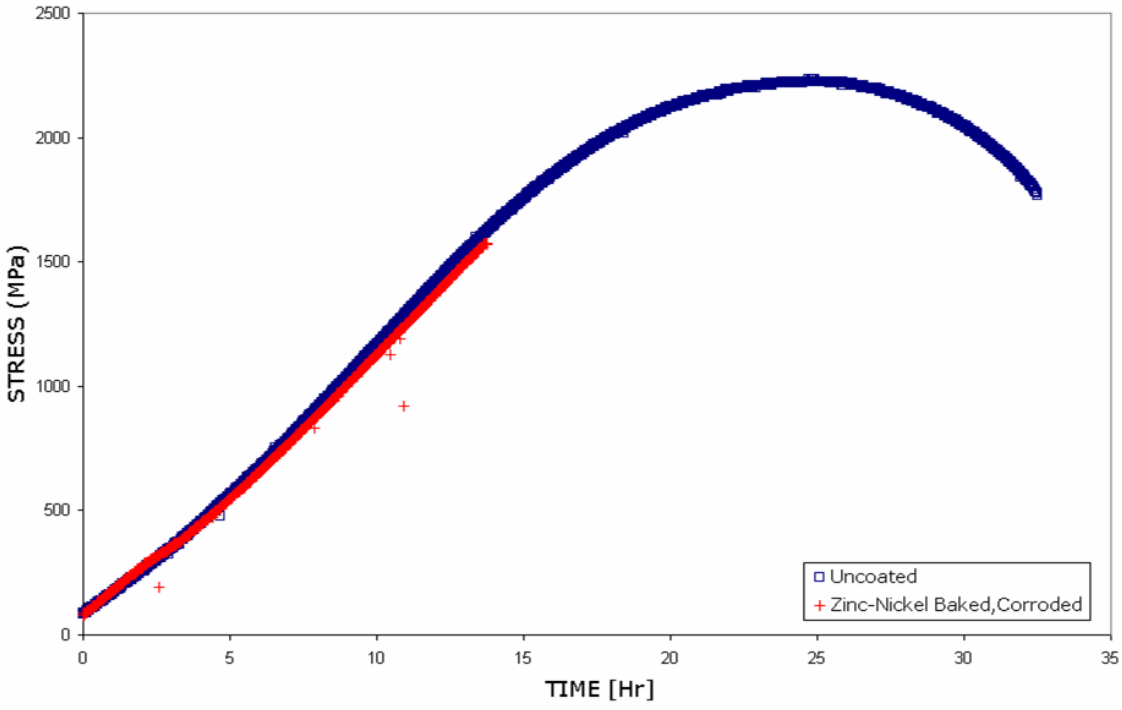

Figure 123. Stress v. time graphs for uncoated and Zinc-14%Nickel plated, baked and corroded 300M specimens.

Although the deleterious effect of direct embrittlement was effectively eliminated by the post-baking treatment, it has been estimated that the use of the alternative sacrificial Zinc-14%Nickel coating might pose delayed failure problems due to hydrogen re-embrittlement during service. Eventually, this detrimental effect was greater than that associated to the conventional cadmium sacrificial coating. However, before considering discarding the Zinc-14%Nickel coating as an alternative to the conventional cadmium, the extent of direct embrittlement and re-embrittlement on the alternative AerMet®100 high strength steel have to be considered.

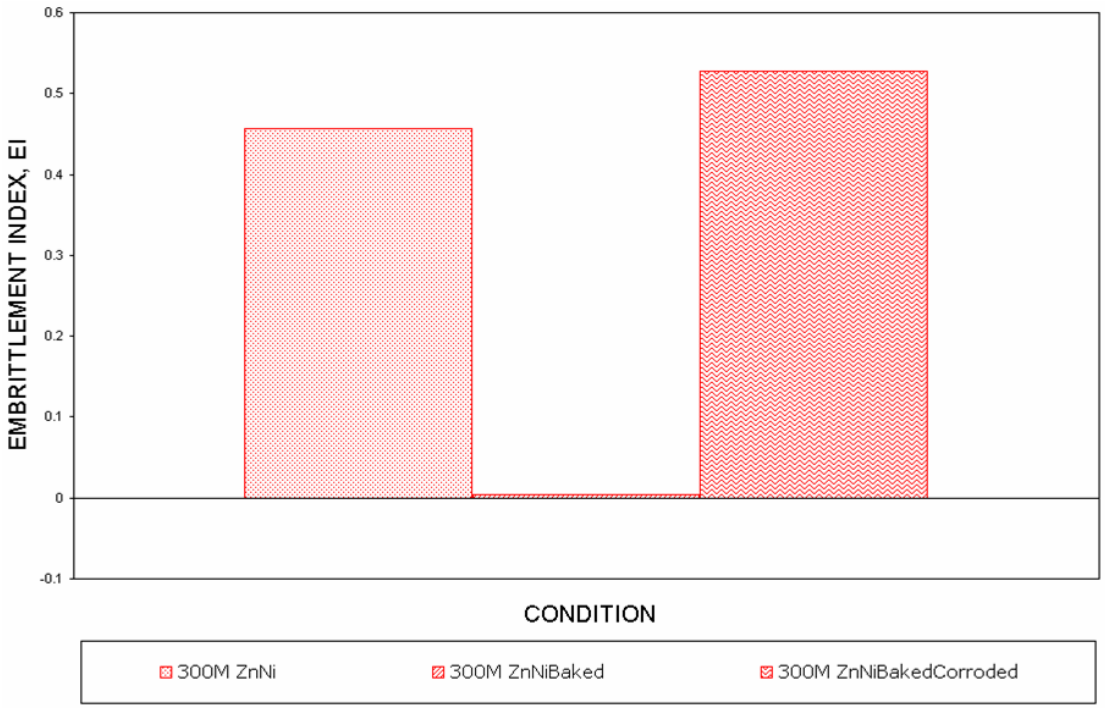

Figure 124. Bar chart of embrittlement indices for Zinc-14%Nickel plated, Zinc-14%Nickel plated and baked and Zinc-14%Nickel, plated, baked and corroded 300M specimens.

12.4. Comparison with AerMet®100 Specimens

In this section the susceptibility of direct hydrogen embrittlement and re-embrittlement of AerMet®100 high strength steel has been taken into

consideration when the alternative Zinc-14%Nickel sacrificial coating was used to protect it from corrosion processes.

12.4.1. Direct Embrittlement

Surprisingly, Zinc-14%Nickel plated AerMet®100 specimens did not suffer any direct hydrogen embrittlement effect due to the electroplating process. In fact, the mean time to failure value, *TTF*, slightly increased from 32.9 for unplated specimens, to 33.9 hours. On the contrary, Zinc-14%Nickel plated 300M specimens proved to be highly susceptible to delayed failure for the same condition. Therefore, AerMet®100 steel displayed a better performance than 300M steel. A comparison of the Weibull distribution for both alloys is displayed in **Figure 125**.

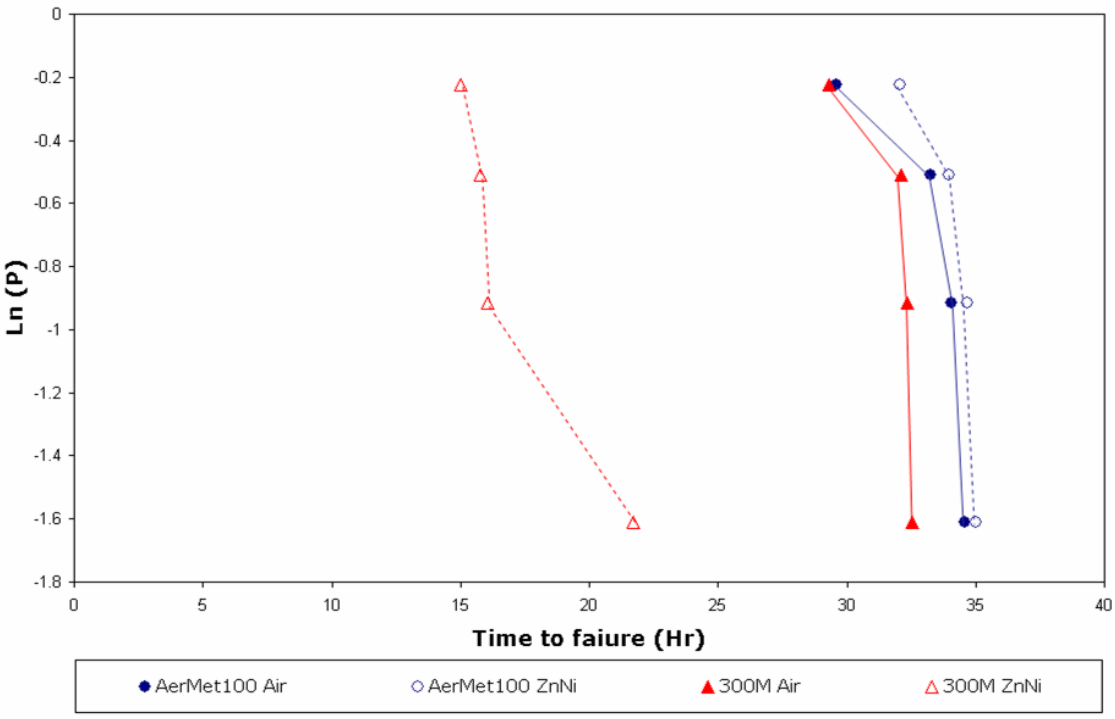

Figure 125. Comparison of the Weibull distribution for unplated and Zinc-14%Nickel plated, baked and corroded 300M and AerMet®100 specimens.

Zinc-14%Nickel plated AerMet®100 displayed an embrittlement index of -0.03. Again this negative *EI* value is thought to be the consequence of the

variability of results obtained from the *SSRT*, since student *t*-test analysis showed with a 95% of confidence that the unplated and Zinc-14%Nickel plated AerMet®100 groups did not belong to different statistical populations.

Although the electroplating of Zinc-14%Nickel did not produce any direct hydrogen embrittlement effect on AerMet®100, the conventional baking treatment was applied to remove any occluded hydrogen from the steel. As expected, *SSRT* results for this latter condition did not reveal any deleterious effect on the mechanical properties of the alloy. Similarly to the Zinc-14%Nickel plated condition, a negative embrittlement index of -0.07 was reported. Perhaps a deleterious effect with more engineering implications might be the extent of re-embrittlement when the Zinc-14%Nickel coating undergoes corrosion during service. This phenomenon is analysed in the next section.

12.4.2. Re-Embrittlement

Remarkably, a high susceptibility to hydrogen re-embrittlement was found for Zinc-14%Nickel plated, baked and corroded AerMet®100 specimens. It was reported a significant reduction in the mean *TTF* value from 32.9 for unplated, to 21.6 hours for the Zinc-14%Nickel plated and baked and corroded AerMet®100 specimens. The corresponding *EI* for this condition was approximately 0.34, which is the highest reached so far for the AerMet®100 steel in all conditions tested.

It is feasible to consider that the relatively active open circuit potential together with the presence of discontinuities in the barrier properties of the Zinc-14%Nickel coating might produce large amounts of hydrogen evolving and taking up by the steel during the direct exposure to 3.5% NaCl solutions. As for cadmium plated AerMet®100 specimens, the levels of re-embrittlement affecting the Zinc-14%Nickel plated specimens are still lower than that reported for the conventional 300M high strength

steel. This latter comparison can be appreciated in the bar chart depicted in **Figure 126**.

Following these observations, it has been considered that AerMet®100 represents a promising alternative alloy for 300M steel. However, the use of Zinc-Nickel sacrificial coatings proved to pose serious concerns due to re-embrittlement during service of electroplated structural components. Therefore, an alternative aluminium based SermeTel®1140/962 sacrificial coating has been evaluated to replace the conventional cadmium.

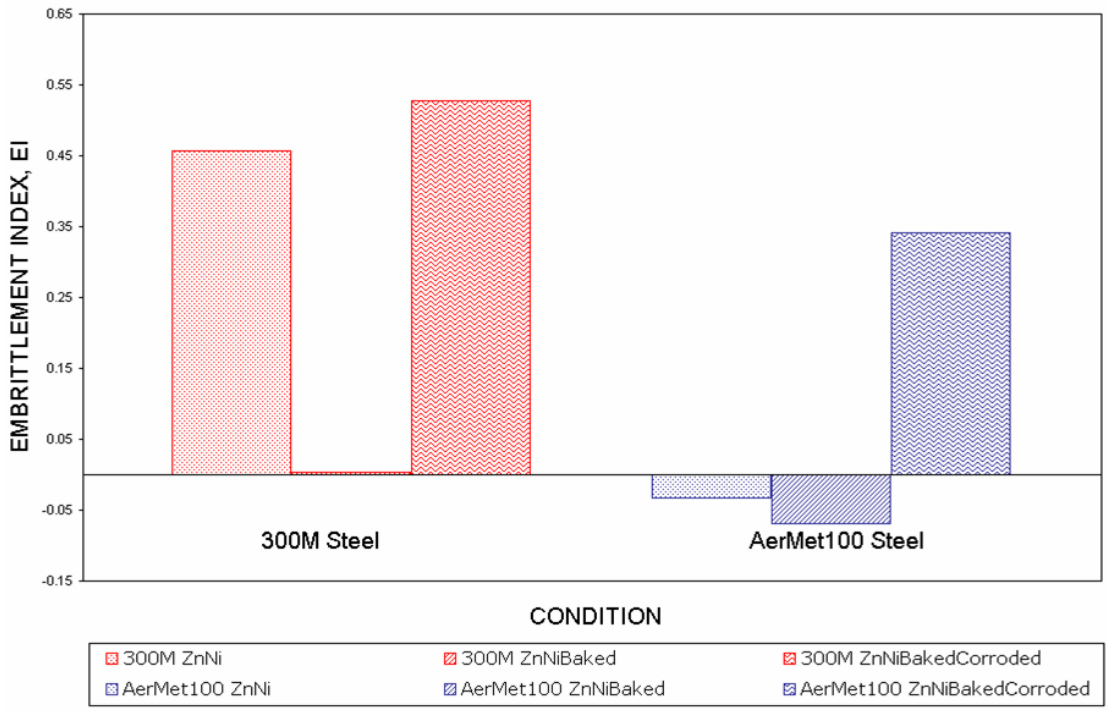

Figure 126. Bar chart of embrittlement indices for Zinc-14%Nickel plated, Zinc-14%Nickel plated and baked and Zinc-14%Nickel, plated, baked and corroded 300M and AerMet®100 specimens.

12.5. Effect of SermeTel®1140/962 on 300M Specimens

The second alternative sacrificial coating considered to replace the conventional cadmium was the aluminium based SermeTel®1140/962. One of the major advantages of this coating over the cadmium and Zinc-14%Nickel is the deposition method used to coat the steel with the

sacrificial layer. Instead of using electroplating conventional methods, tiny spherical aluminium particles are sprayed together with a phosphate ceramic binder on the 300M steel. Thereafter, a final curing process is carried out at temperatures between 191 and 310°C followed by the deposition of a fluorocarbon polymer top-coated layer on the sacrificial coating.[17, 68, 69]

12.5.1. Direct Embrittlement

As expected, no hydrogen direct embrittlement was found for the SermeTel®1140/962 coated and cured 300M specimens. These findings are associated with the lack of hydrogen evolution during the thermal spraying process and the subsequent curing treatment performed on the specimens.

In this occasion, the mean time to failure increased by approximately 1 hour with respect to the control specimens. Further student *t*-test analysis revealed with a 95% level of confidence that the SermeTel®1140/962 coated and cured 300M groups did not represented the same statistical populations as the control group. This finding suggests that the curing process carried out at temperatures close to the tempering temperature of 300M steel (315°C), produced an increase in ductility. Therefore, specimens displayed slightly different mechanical properties with a small reduction on the ultimate tensile strength. This event can be clearly appreciated in **Figure 127**, which compares the stress-time plots for uncoated and SermeTel®1140/962 coated and cured 300M specimens.

Several researches[17, 68, 69] have previously reported the non-embrittlement effect of similar dense pack metallic-ceramic sacrificial coatings commercially available. More recently, Chalaftris and Robinson[18, 132] demonstrated that an equivalent aluminium based sacrificial coating with a slightly different composition, specifically SermeTelCR984-LT, did not produce direct hydrogen embrittlement of AISI-4340 high strength steels due to the nature of its deposition process.

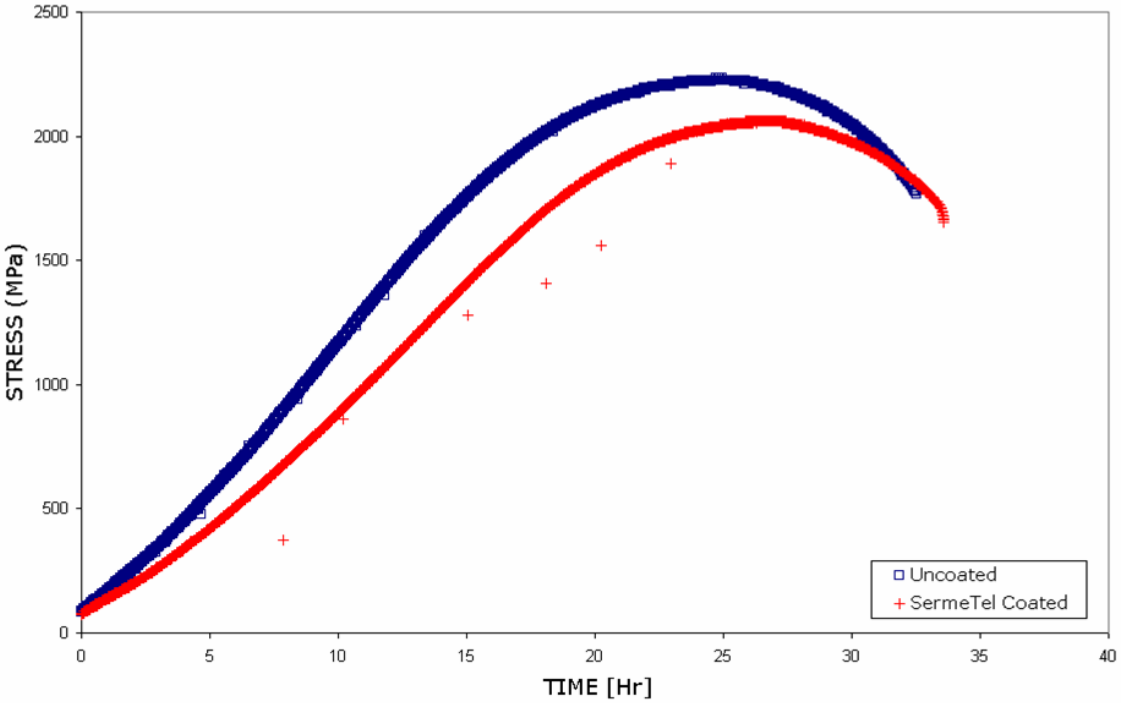

Figure 127. Stress v. time graphs uncoated and SermeTel®1140/962 coated and cured for 300M specimens.

12.5.2. Re-Embrittlement

SSRT results showed that hydrogen re-embrittlement problems recurred for the SermeTel®1140/962 coated 300M specimens. The mean *TTF* considerably decreased from 31.6 to 23.1 hours for the unplated and SermeTel®1140/962 coated, cured and corroded 300M specimens, respectively. The *EI* associated with these values was 0.27, as is shown in **Figure 128**.

Open circuit potentials recorded for SermeTel®1140/962 coatings in quiescent 3.5%NaCl solutions showed that although some variations did take place for long immersion periods, (at least significantly longer than the time to complete the *SSRT*), the potential remained slightly more active than that for cadmium. Therefore, it is expected that the amount of hydrogen evolving during re-embrittlement would be slightly higher to that produced during the corrosion of cadmium.

As expected, the extent of re-embrittlement produced by the dissolution of SermeTel®1140/962 coating was higher than that associated with the conventional cadmium coating. However, additional factors including the barrier properties of the coatings might also play an important role on the re-embrittlement process.

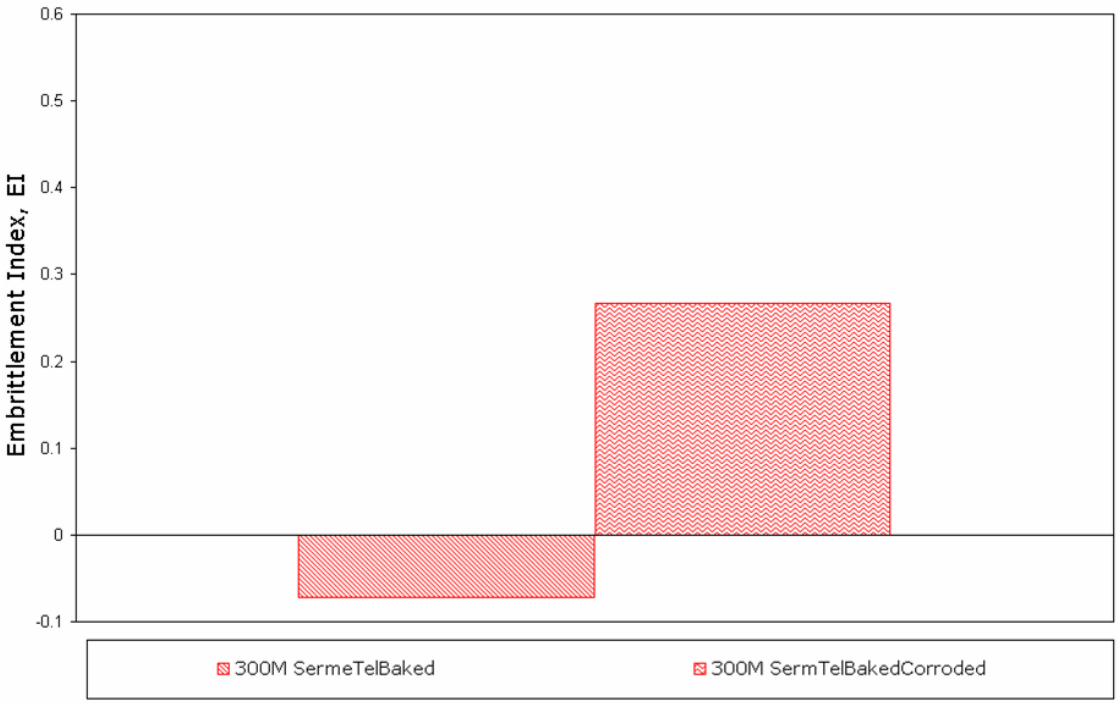

Figure 128. Bar chart of embrittlement indices for SermeTel®1140/962 coated and cured and SermeTel®1140/962 coated, cured and corroded 300M specimens.

Chalaftris and Robinson[132] reported analogous results for AISI-4340 tensile specimens coated with SermeTelCR984-LT, which showed *EI* of 0.51 on average after the exposure to 3.5%NaCl solutions during *SSRT*. But an important difference between this sacrificial coating and the SermeTel®1140/962 is the absence of the fluorocarbon polymeric topcoat. This top-coat system reduces the number of flaws or discontinuities that produce hydrogen re-embrittlement by sealing superficial porosities within the aluminium-phosphate dense packing.

12.6. Comparison to AerMet®100 Specimens

The effect of the SermeTel®1140/962 sacrificial coating on the AerMet®100 high strength steel is assessed in this section. Results obtained for the new alloy has been compared with the previously reported for the 300M steel.

12.6.1. Direct Embrittlement

Similarly to 300M steel*, SSRT* showed that SermeTel®1140/962 coated and cured AerMet®100 specimens did not suffered from direct hydrogen embrittlement after the deposition process. But, unlike 300M steel, no changes in the mechanical properties were found for AerMet®100 specimens due to the curing process. It is known that the tempering temperature for AerMet®100 is approximately 485°C,[19] a value higher than that for 300M steel, (315°C).[4] Hence, AerMet®100 is considered to be not susceptible to the curing process used for the SermeTel®1140/962 sacrificial coating.

12.6.2. Re-Embrittlement

AerMet®100 steel did not show any extent of hydrogen re-embrittlement due to the corrosion of the SermeTel®1140/962 sacrificial coating. In fact, student *t*-test analyses proved with a 95% of confidence that this test group did not belong to a different statistical population than the uncoated specimens. In comparison, 300M steel significantly suffered delayed failure problems due to hydrogen re-embrittlement under the same condition. **Figure 129** shows a comparison of the Weibull distribution for SermeTel®1140/962 coated, cured and corroded 300M and AerMet®100 specimens. The reduction in the mean *TTF* values for SermeTel®1140/962 coated, cured and corroded 300M specimens is evident, whereas *TTF* values for AerMet®100 remain unaffected.

The mean *EI* value for the re-embrittled condition for AerMet®100 was below zero (-0.03), indicating a very low probability of showing premature failure. This value is much lower than that corresponding to 300M steel, as is shown in **Figure 130**. It is considered that the negative *EI* values are not thought to be significant and they merely reflect the variability of results between different specimens.

Taking into account the previous results, it is feasible to suggest that SermeTel®1140/962 represents a promising sacrificial system to replace the conventional cadmium. Moreover, it was also demonstrated that AerMet®100 proved to be less susceptible to direct hydrogen embrittlement and re-embrittlement problems regardless the sacrificial coating used.

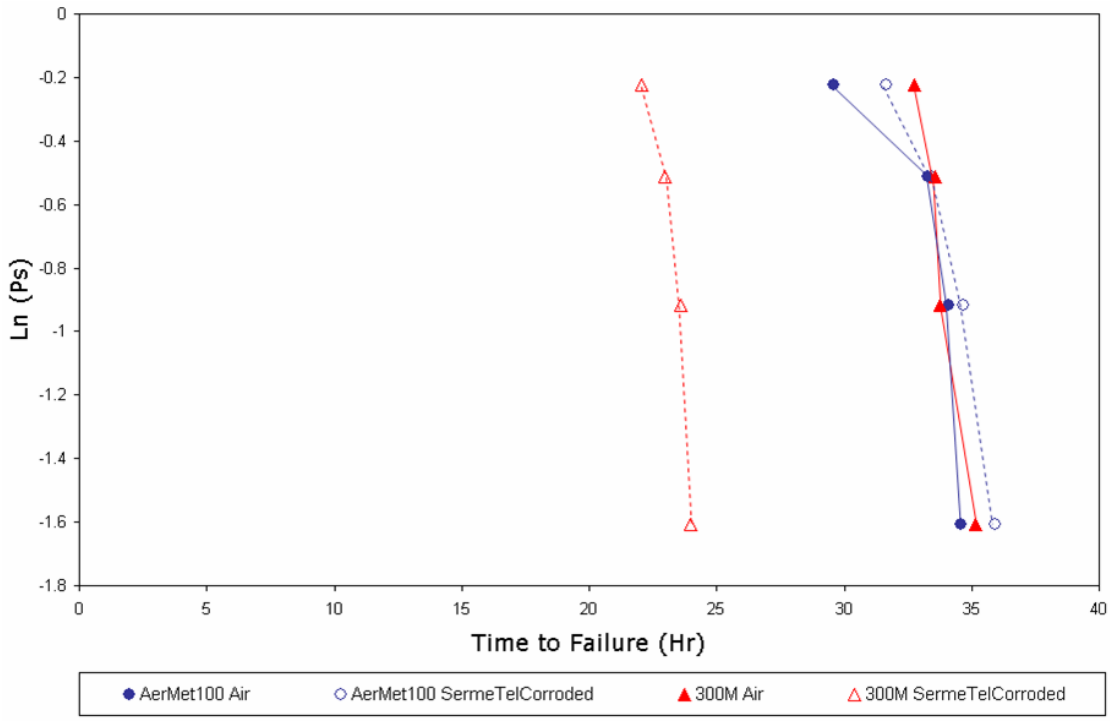

Figure 129. Comparison of Weibull distributions for uncoated and SermeTel®1140/962 coated and corroded 300M and AerMet®100 specimens.

From the previous analysis, it has been shown that hydrogen re-embrittlement might represent a more challenging problem to overcome than direct embrittlement. Therefore, the susceptibility to premature

failure of the two additional CSS-42L™ and GifloM2000 high strength steels have been assessed only for the re-embrittlement produced by the SermeTel®1140/962 and the cadmium sacrificial coating, respectively.

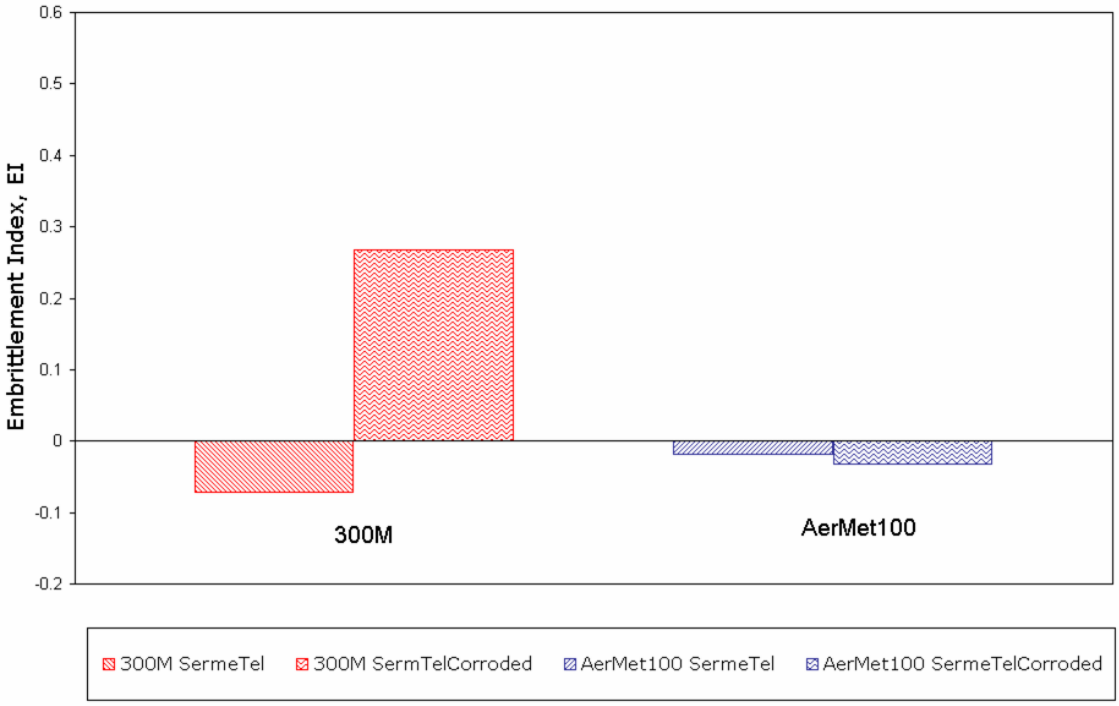

Figure 130. Bar chart of embrittlement indices for SermeTel®1140/962 coated and cured and SermeTel®1140/962 coated, cured and corroded 300M and AerMet®100 specimens.

12.7. Effect of SermeTel®1140/962 on CSS-42L™ Steel

SSRT results showed that no direct hydrogen embrittlement was produced after the spraying and subsequently curing of the SermeTel®1140/962 coated CSS-42L™ stainless steel. It was previously discussed that due to the nature of the spraying process, no hydrogen was produced and taken up by the steel during the deposition of this sacrificial coating.

Nevertheless, some but not all of the SermeTel®1140/962 coated and cured CSS-42L™ specimens were affected by hydrogen re-embrittlement, when the coating became partially corroded in quiescent 3.5% NaCl solutions. On average, the mean *TTF* value suffered a significant reduction from 38.9, for uncoated, to 29.1 hours. But, the individual time to failure

values for this condition were 20.1, 27.4 and 39.8 hours, as is shown in **Figure 131**.

The first two specimens failed in a brittle manner within the scribed region with a small reduction in area, *RA%*, whereas the latter did not fail within the scribe and instead displayed a typical cup and cone ductile fracture. In general, these results suggest that SermeTel®1140/962 coated CSS-42L™ stainless steel is susceptible to delayed failure due to hydrogen re-embrittlement. Nevertheless, a significant variability of results is evident.

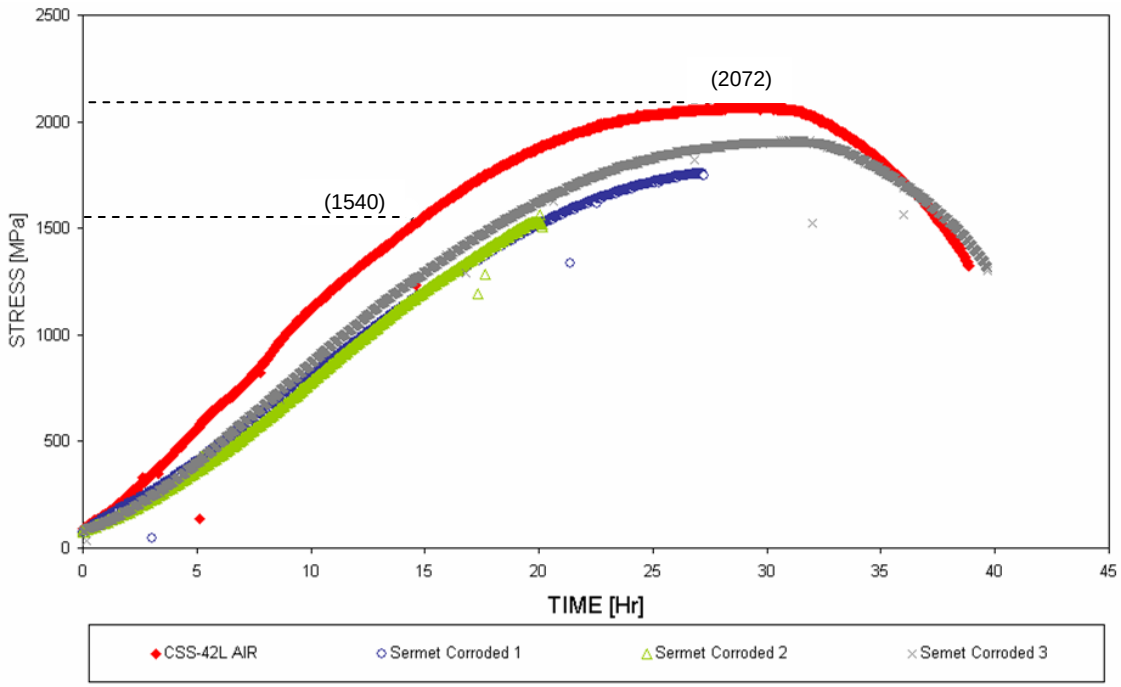

Figure 131. Stress-time plots for SermeTel®1140/962 coated, cured and corroded CSS-42L™ stainless steel specimens.

This variability of results was thought to be related to differences in the amounts of hydrogen absorbed by the steel from corrosion of the active SermeTel®1140/962 coatings. It is assumed that the specimen that failed in a ductile manner did not absorb sufficient hydrogen to cause embrittlement in the duration of the test. If the test had been conducted at a lower strain rate, however, then more time would have been available and a brittle failure may have occurred in this specimen too.

The mean *EI* value for the SermeTel®1140/962 coated, cured and corroded CSS-42L™ specimens was 0.25. However, the tests on uncoated CSS-42L™ did not display hydrogen embrittlement when tested in 3.5% NaCl, as **Figure 132** shows. The embrittlement index in this case was 0.03 and specimens displayed a relatively high *RA%* of 36.4.

Again, it is thought that insufficient hydrogen was generated to embrittle the CSS-42L™ steel at its free corrosion potential, -440 mV(SCE). On the contrary, the partial dissolution of the SermeTel®1140/962 coating occurred at a more cathodic potential, -750 mV(SCE). It is know that at more active potentials far more hydrogen would be available to produce hydrogen embrittlement in this test due to the partial dissolution of a sacrificial coating. Therefore, it was considered that CSS-42L™ stainless steel displayed a better performance in the uncoated condition.

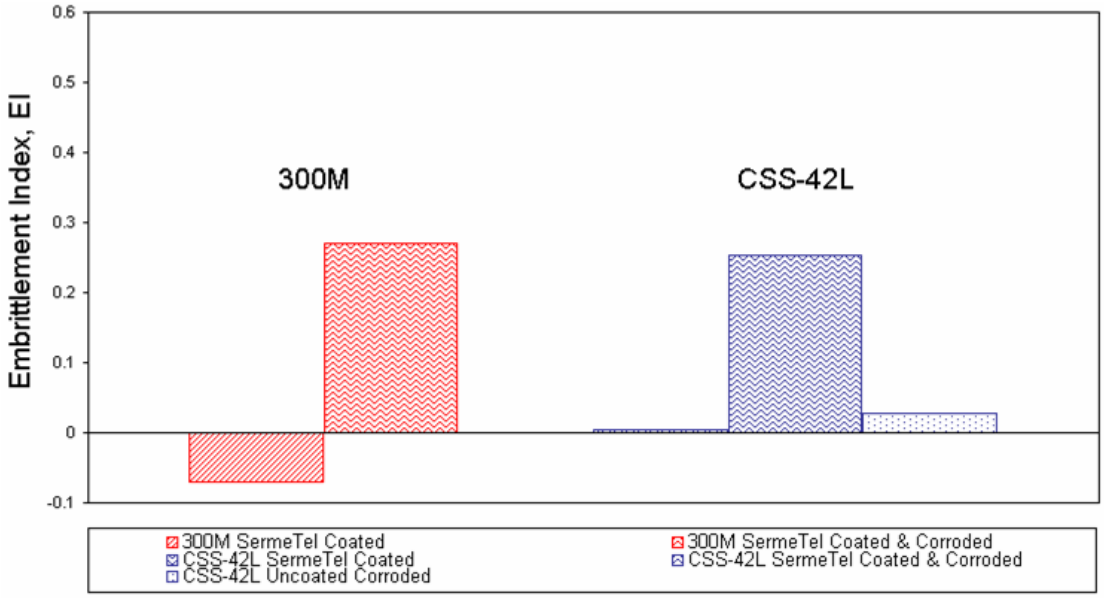

Figure 132. Embrittlement indices for un-coated and corroded, SermeTel®1140/962 coated and cured and SermeTel®1140/962 coated, cured and corroded 300M and CSS-42L™ stainless steel specimens.

By comparing these results with those previously reported for the conventional 300M steel under equivalent test conditions, it can be seen that the stainless steel showed similar hydrogen re-embrittlement susceptibilities. Nonetheless, the alternative CSS-42L™ stainless steel appeared to have a better performance when it is not coated with the

sacrificial coating. If the CSS-42L™ were to be used in service, however, longer exposure times might mean that the amount of hydrogen absorbed during the slow corrosion of the alloy could lead to brittle failure. For this reason, it was suggested that future tests should be performed at a lower strain rate of $3.8x10^{-8}$ s^{-1}.

Considering that uncoated and freely corroded CSS-42L™ specimens failed in 1.5 days (37 hours) at a strain rate of $0.97x10^{-6}s^{-1}$, it would be expected that this alloy might fail in approximately 38.5 days (925 hours) at a strain rate of $3.6x10^{-8}s^{-1}$, if no premature failure take place due to hydrogen embrittlement, *HE*, or stress corrosion cracking, *SCC*. If hydrogen embrittlement is the predominant mechanism for high strength martensitic stainless steels,[154] the latter *SSRT* performed at extremely slow strain rate ($3.6x10^{-8}s^{-1}$) should fail before the time predicted above showing little reduction in area, *RA%*. This phenomenon was previously depicted in **Figure 32**, where the effect of strain rate on *SCC* and *HE* was shown.

Unexpectedly, the slow strain rate test performed at a strain rate of $3.8x10^{-8}s^{-1}$ showed that the specimen failed in a period of time slightly longer than that predicted, (39.2 days). Moreover, metallographic examination at the fracture surface revealed that the failed specimen displayed ductile fracture with a *RA%* of 36.1%, which was equivalent to that obtained for specimens tested at higher strain rates. Therefore, it was considered that the uncoated and freely corroded CSS-42L™ martensitic stainless steel was not susceptible to hydrogen embrittlement.

12.8. Effect of Cadmium Plating on GifloM2000 Steel

Finally, the hydrogen re-embrittlement susceptibility of the low alloy GifloM2000 high strength steel was evaluated when the sacrificial cadmium coating became corroded. Surprisingly, the mean time to failure value for this condition did not show any major change. This result suggested that GifloM2000 is not susceptible to delayed failure due to hydrogen re-embrittlement under the conditions tested. The

corresponding stress vs. time plots for all specimens tested are shown in **Figure 133**.

This is an unexpected finding in the view of the levels of re-embrittlement displayed by 300M, which has been also classified as a low alloy high strength steel. Therefore, further work was carried out to seek an explanation. First, to check the validity of the tests the corrosion potential of the cadmium coated specimen was measured in 3.5% NaCl and shown to be -0.74 Volts(SCE). This potential is consistent with that previously reported and it was concluded that the results were not affected by unusual behaviour of the sacrificial coating.

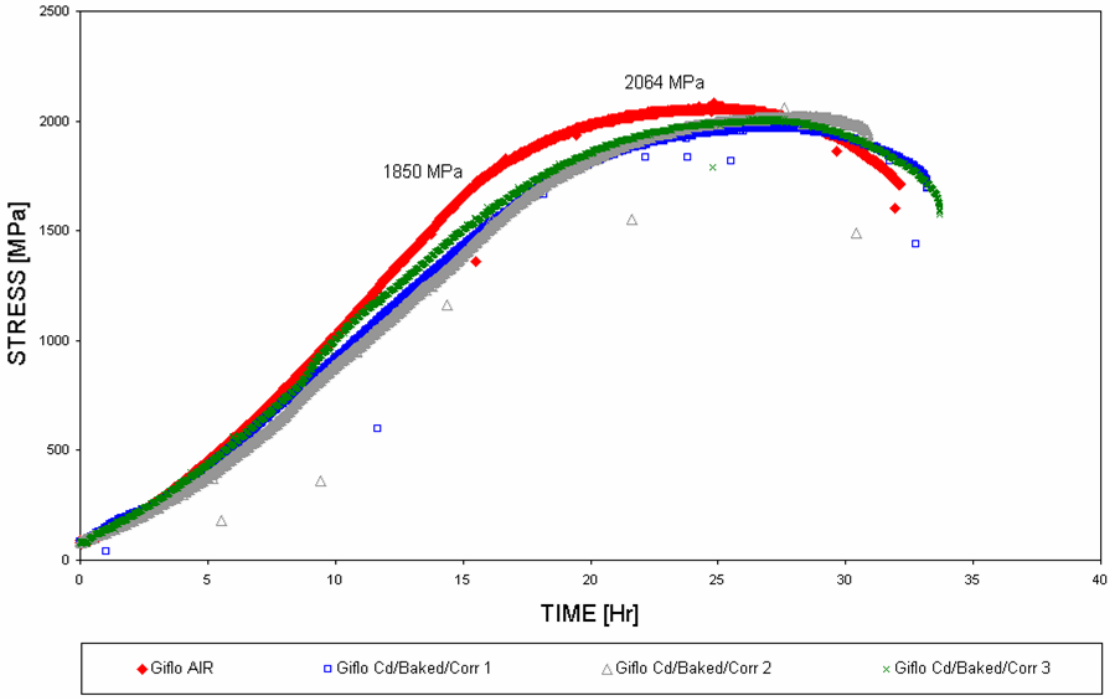

Figure 133. Stress-time graphs for unplated and cadmium plated, baked and corroded GifloM2000 specimens.

Second, a *SSRT* specimen was sectioned in the gauge length and the polished section was examined in a scanning electron microscope. Quantitative analysis at the interface of the steel and cadmium coating revealed a thin nickel layer, which had been inadvertently applied to the GifloM2000 specimens instead of the CSS-42L™ specimens. The

quantitative analysis at the interface of the steel and cadmium coating are shown in **Figure 134** and **Table 26**.

The analysis at the steel-cadmium interface showed nickel contents up to 7.5% compared to 1.5% in the steel. (The analysis included an area of the steel and an area of the cadmium so the percentage of nickel recorded should be much lower than that actually present in the layer at the interface). A very thin layer of nickel is often applied to stainless steel specimens before the cadmium plating process to improve the adhesion of the electroplated deposit. This process is known as '*Nickel Strike*' and is widely used in the electroplating industry.[155]

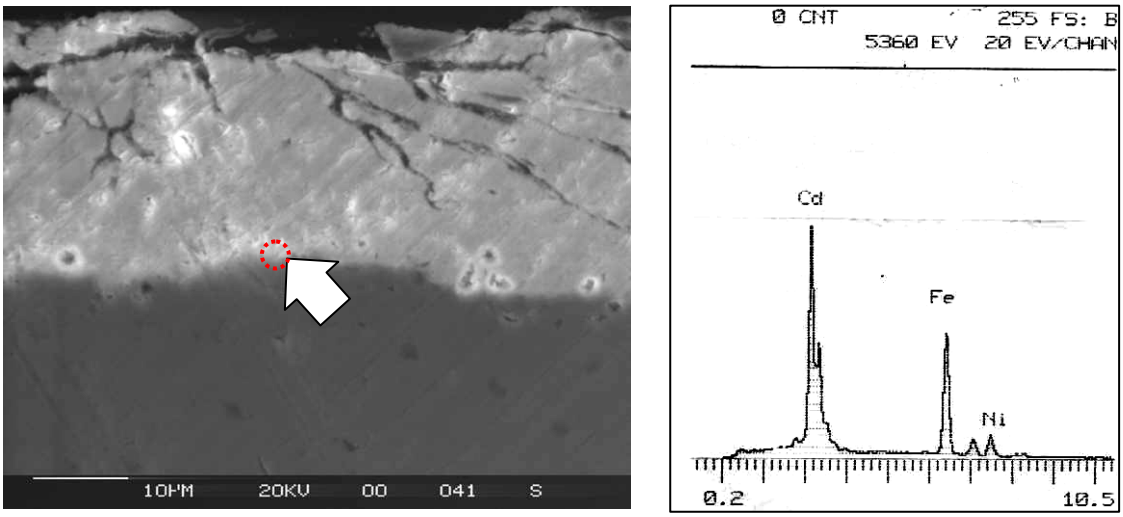

(A) (B)

Figure 134. A) Cross section of the cadmium coated, baked and corroded GifloM2000 high strength steel. Arrow indicates the area analysed at the coating-steel interface. B) Elemental analysis at the cadmium-steel interface.

The reason for the lack of re-embrittlement when the cadmium plated specimens were corroded in 3.5% NaCl is now clear. Nickel has a very low hydrogen diffusion coefficient ($8x10^{-10}$ cm^2/s compared to $4x10^{-8}$ cm^2/s for GifloM2000 as will be shown latter).[156, 157] Subsequently, the nickel layer acted as an effective barrier to hydrogen generated by corrosion of the cadmium.

	Fe	Cd	Cu	Ni	Cr	Mn
COATING	2.29	97.08	-	-	-	-
INTERFACE	32.54	58.50	0.98	7.51	0.20	0.30
STEEL	93.72	0.11	2.20	1.53	0.75	1.70

Table 26. Comparison of element compositions (wt%) at the cadmium coating, coating-steel interface and for GifloM2000 high strength steel.

What is more, it has been reported that a very thin layer of nickel could be more effective than a thicker coating in preventing hydrogen absorption as the hydrogen diffusion coefficient decreases as the coating thickness decreases. This phenomena had been corroborated by the experimental data previously reported by Song and Pyun,[157] displayed in **Figure 135**.

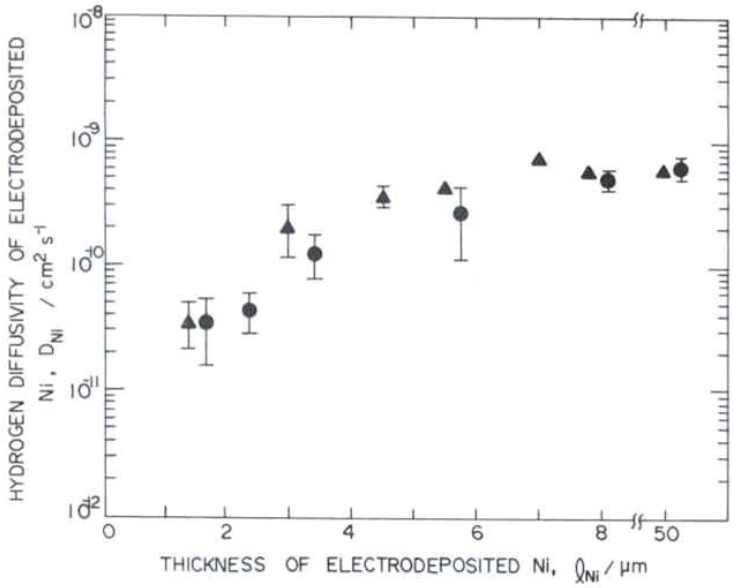

Figure 135. Hydrogen diffusivity in the electrodeposited Ni as a function of the thickness obtained under two different hydrogen charging conditions: galvanostatic boundary condition (Δ), and potentiostatic boundary condition (•).[157]

Similarly, Tolls *et al.*[155] have shown that applying a '*flash*' coating with nickel sulphanate prior a zinc electroplating process, considerably reduces

the hydrogen embrittlement of high strength steels used in the automotive industry. This reduction in the hydrogen embrittlement susceptibility has been explained in terms of the low hydrogen diffusivity of the nickel layer, approximately 3μm thick.

These results could have important practical implications. A thin nickel layer beneath the sacrificial coating seems to be the answer to both direct embrittlement and re-embrittlement problems. To corroborate this hypothesis, attempts were made to repeat the *SSRT*, ensuring that GifloM2000 specimens were cadmium plated and baked but did not receive the '*nickel strike'* treatment.

Figure 136 displays a comparison of the Weibull distributions for the cadmium coated, baked and corroded GifloM2000 specimens with the group that inadvertently received the '*nickel strike'* treatment.

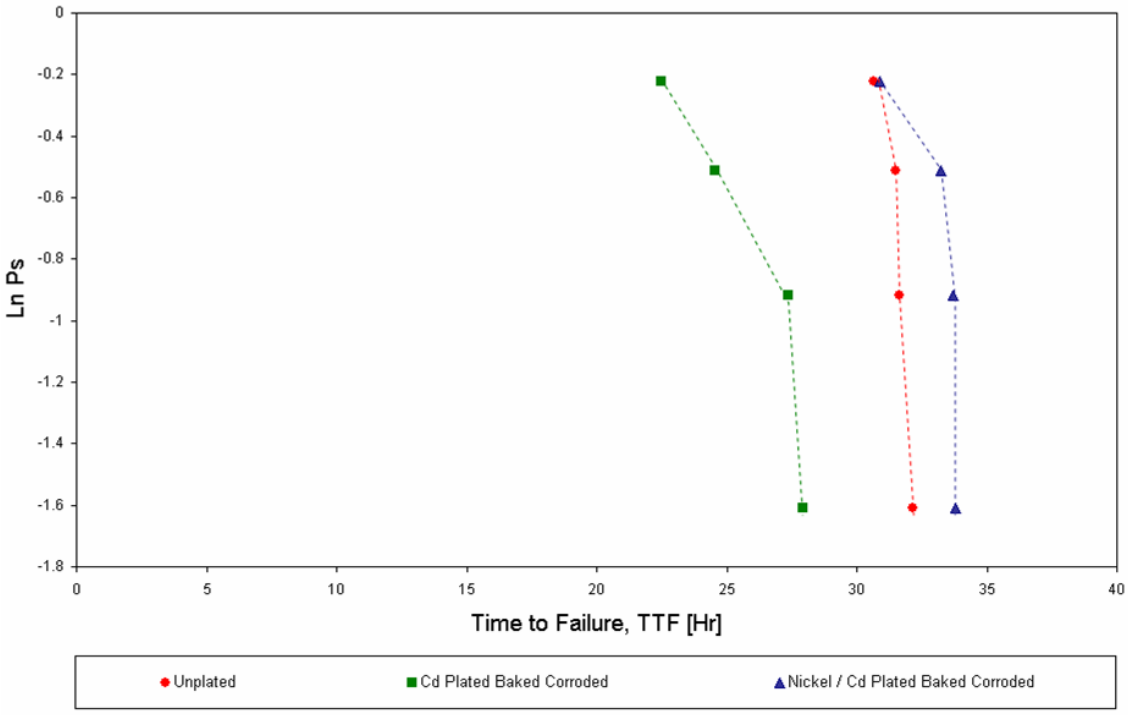

Figure 136. Comparison of Weibull distributions for uncoated, cadmium plated, baked and corroded and nickel plated followed by cadmium plated, baked and corroded GifloM2000 specimens.

Indeed, it can be seen that GifloM2000 specimens suffered from hydrogen re-embrittlement when the cadmium coating became corroded. The mean *TTF* value was reduced from 31.5 to 25.6 hours, and the *EI* associated with these values was 0.19.This level of susceptibility to hydrogen re-embrittlement was similar to that reported for the conventional low alloy 300M steel. In comparison, GifloM2000 specimens which have received the *'nickel strike'* treatment did not show any susceptibility to delayed failure problems.

12.9. Comparison of *SSRT* Results.

A comparison of the mean mechanical properties for 300M, AerMet®100, GifloM2000 and CSS-42L™ specimens, is shown in **Figure 137**. It can be seen that the four alloys displayed high strength levels, with *UTS* values above 2000MPa.

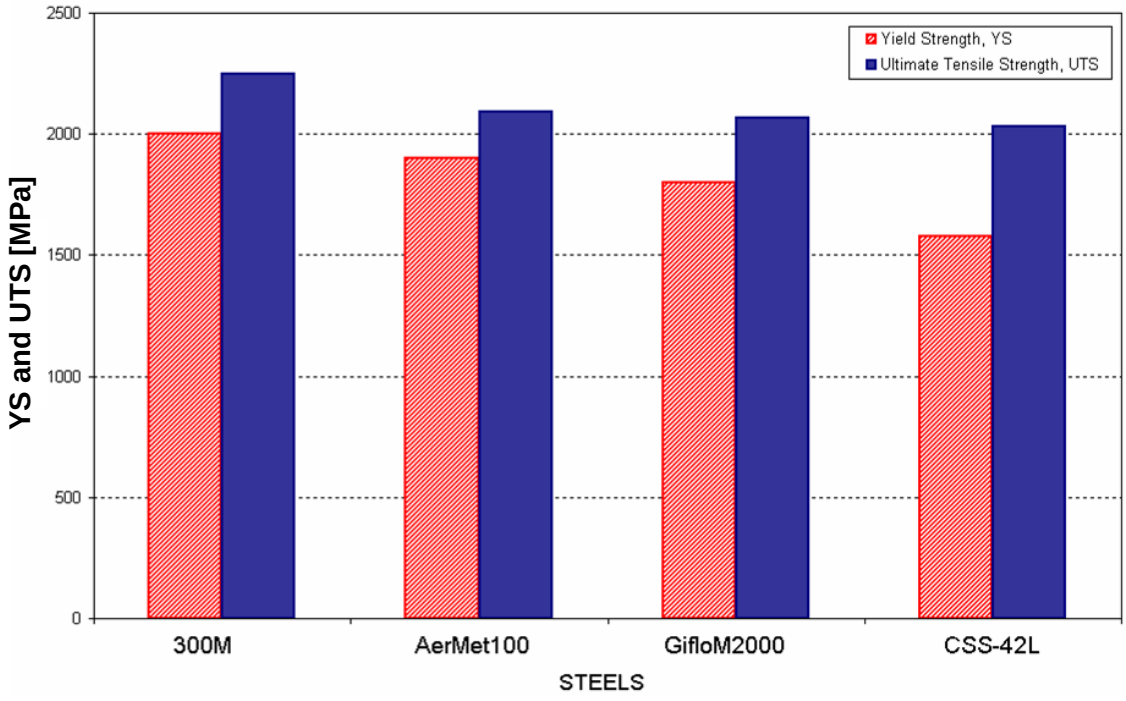

Figure 137. Comparison of the mechanical properties for the most representative 300M, AerMet®100, GifloM2000 and CSS-42L™ specimens.

Considerable improvements were made in the final mechanical properties when they were compared to the original data commercially available

from the corresponding manufacturers, previously showed in **Figure 5**. These improvements might have been achieved due to slight changes of the conventional heat treatments but further details of these modifications were not available. From the *SSRT*'s results it can be noticed that the mean *YS* values for 300M, AerMet®100, and GifloM2000 slightly decreased in the same order from 2000 to 1800MPa, but the most noticeable reduction was associated to the CSS-42L™ stainless steel. The *YS* for the later alloy was found to be approximately 1600 MPa.

Taking into account design safety factors, it is common to set maximum levels of load at approximately 2/3*YS* for structural engineering components. Hence, the application of the CSS-42L™ stainless steel for such parts might be significantly limited in comparison with the rest of the alloys considered. Specifically, CSS-42L™ components might only cope with 20% less than the maximum load applied to 300M steel. Therefore, the mechanical properties of the high strength steels studied have been ranked in the order: 300M > AerMet®100 > GifloM2000 > CSS-42L™ displaying the lowest.

12.10. Comparison of Embrittlement Susceptibilities

By comparing hydrogen embrittlement and re-embrittlement susceptibilities of 300M and AerMet®100 it can be appreciated that the later steel generally displayed far better performance in all conditions tested. However, relatively high re-embrittlement indices have been displayed by both alloys when a Zinc-14%Nickel sacrificial coating became corroded.

A comparison of the embrittlement indices for 300M, AerMet®100, CSS-42L™ and GifloM2000 high strength steels is graphically depicted in **Figure 138**. It can be seen that 300M and CSS-42L™ specimens displayed similar susceptibilities to hydrogen re-embrittlement when the SermeTel®1140/962 sacrificial coating became corroded. Moreover, CSS-42L™ showed better performance for the uncoated and freely corroded condition.

Alternatively, GifloM2000 displayed slightly higher re-embrittlement susceptibility than the conventional 300M steel during the corrosion of cadmium sacrificial coating. Nonetheless, it was proved that by the application of a '*nickel strike*' treatment prior the cadmium electroplating, led to a reduction of the re-embrittlement susceptibility. This observation has let us consider the possibility of applying a thin nickel layer (<1μm) under the electroplated sacrificial coatings like cadmium and Zinc-14%Nickel. This nickel layer reduces the hydrogen diffusion to the steel substrate, and consequently diminishes the susceptibility to hydrogen embrittlement and re-embrittlement.

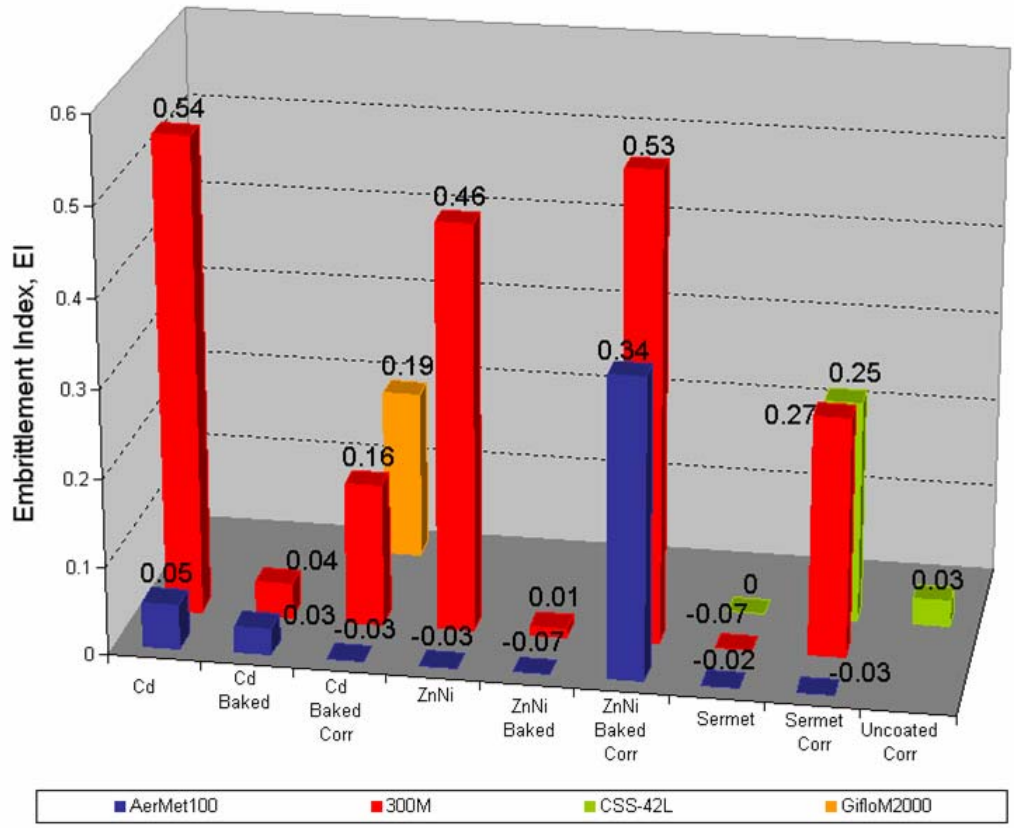

Figure 138. Comparison of embrittlement indices at different conditions for 300M, AerMet®100, CSS-42L™ and GifloM2000 tensile specimens.

On the other hand, the effectiveness of baking processes on removing hydrogen from the steels after electroplating was widely corroborated by the low embrittlement indices displayed for the cadmium plated and

baked and Zinc-14%Nickel plated and baked 300M and AerMet®100 specimens. In this particular area, SermeTel®1140/962 has proven to have the advantage over the rest of the coatings due to the lack of direct embrittlement after its deposition.

Perhaps, a more important technical implication can be associated to the extent of hydrogen re-embrittlement of high strength steels for structural components during service, due to the partial dissolution of different sacrificial coatings. However, AerMet®100 and SermeTel®1140/962 seem to represent a promising steel-coating combination because of the lack of susceptibility to direct hydrogen embrittlement and re-embrittlement of the substrate.

At this stage, a sensitive question rises: Why did AerMet®100 display lower hydrogen re-embrittlement susceptibility than 300M and CSS-42L™ high strength steels under similar test conditions? It was thought that intrinsic microstructural characteristics of each type of high strength steel (low alloy steels represented by 300M and GifloM2000, high alloy AerMet®100 and precipitation hardening CSS-42L™ stainless steel) might determine their performances in terms of hydrogen related failure. The elemental composition together with heat treatments determines the final microstructural characteristics that eventually define the hydrogen transport characteristic and hydrogen solubility of the alloys. This issue is widely discussed in the following section.

13. Hydrogen Transport Characteristics

Before the hydrogen transport characteristics of high strength steels are considered, first, it is important to establish a relationship between the electro-negativity of the sacrificial coatings and the amount of hydrogen produced during the hydrogen evolution reaction; and secondly determine the amount of hydrogen that could eventually penetrate the steel and produce embrittlement.

13.1. Hydrogen Evolution Reaction, *HER*

Cathodic polarisation experiments for the steel membrane in quiescent 3.5% NaCl solution showed that at potentials below -650mV(SCE), the cathodic oxygen reduction reaction occurred in preference to the hydrogen evolution reaction. However, at potentials more active than -900 mV(SCE) the controlling reaction shift to the hydrogen evolution.

It was also shown that the slope of the linear fit, β, was measured to be approximately -136mV/decade. This value is in reasonably good agreement with the theoretical value expected from the cathodic Tafel slope, which is -120mV/decade. The equation used to deduced this value has been described as follows:[74, 75, 158]

$$\frac{\partial E}{\partial Log\ i_c} = -\frac{2\ (2.303)RT}{F} = -120\ \ [mV/decade] \qquad [\text{XLIII}]$$

Where E is the potential, i_c is the current density, R, T and F are the gas constant, temperature and Faradays constant.[74, 75, 158] Moreover, it had been reported the same β value for hydrogen evolution on zinc in 1N HSO_4 solutions.[159] Therefore, it is feasible to assumed that a similar value can be expected during hydrogen re-embrittlement due to the dissolution of the sacrificial Zinc-14%Nickel coating.

13.2. Hydrogen Uptake by the Low Carbon Steel

It is known that only a fraction of the hydrogen evolving during *HER* eventually penetrates the steel and produces embrittlement. Results obtained from the hydrogen permeation measurements carried out on low carbon shim membranes at different cathodic polarisation levels, (**Figure 77** and **Table 13**), showed that the steady state current density, I_∞, as well as the internal hydrogen concentration just below the charging phase of the membrane, C_o, increased by making the potential more cathodic.

Steady state current densities represented the amount of hydrogen that was taken up and penetrated the steel membrane from the charging side of the cell at different cathodic potentials. It was also found that the steady-state current density, I_∞, increased at an almost exponential rate by lowering the potential from -0.90 to -1.15 V (SCE), as shown in **Figure 139**.

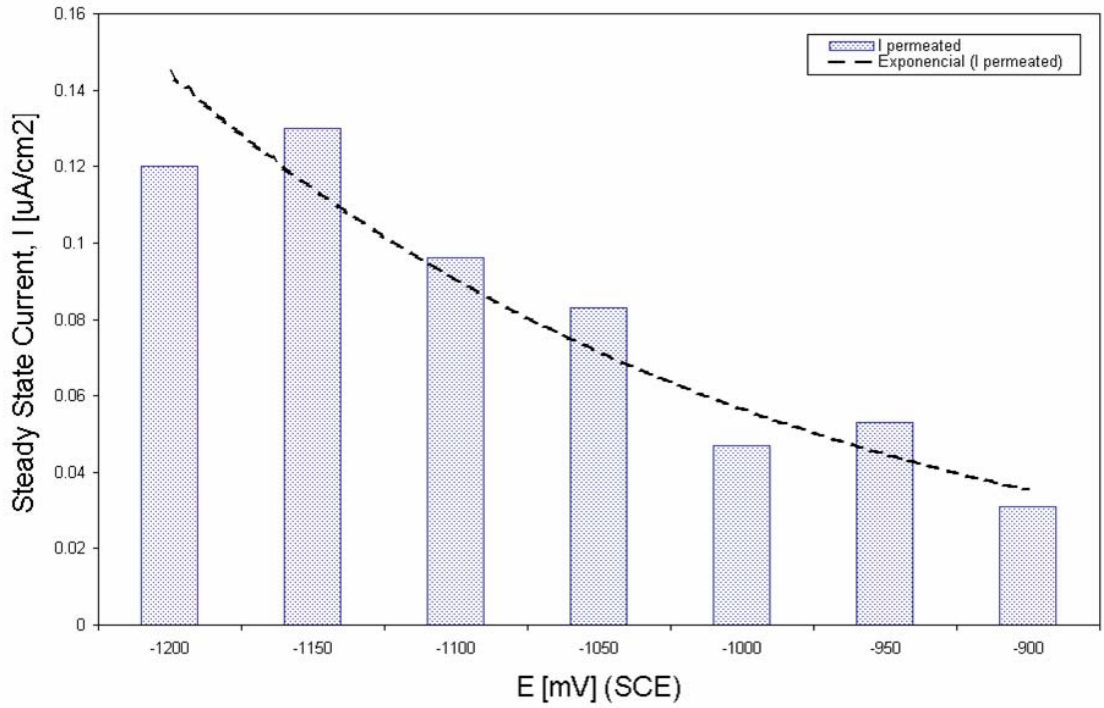

Figure 139. Bar chart showing the steady state current densities, i_∞ vs potential, E(SCE).

This observation is perfectly in agreement with the definition of the *Tafel* equation, which states that the activation overpotential (or activation energy) varies exponentially with the rate of charge transfer per unit area of the electrode surface. The *Tafel* equation is denoted as follows:[6]

$$\eta_a = a + b\ Log\ [i] \qquad [\text{XLIV}]$$

Where η_a is the activation overpotential, i is the current density, a is the intercept at zero current and b is the Tafel constant which vary with the nature of the electrode process and the electrolyte been used.[6] However, the current measured at -1.20 V (SCE) was consistently less that that at -1.15 V (SCE). The reason for this is that visible hydrogen bubbles were forming on the steel surface at potentials below -1.15 V (SCE) and this led to a drop in the hydrogen permeating through the steel membrane. Several consecutive experiments confirmed this observation.

Similarly, the electronegativity of the coatings measured by the open circuit potentials was used to estimate the amount of hydrogen that was produced in the cathodic reaction during re-embrittlement. In this context, a comparison of the open circuit potential for cadmium, Zinc-14%Nickel and SermeTel®1140/962 coatings immersed in quiescent 3.5% NaCl solutions is displayed in **Figure 140**. It can be appreciated, that the partial dissolution of the cadmium and SermeTel®1140/962 sacrificial coatings should generate similar amounts of hydrogen as their open circuit potentials (and over-potentials) during re-embrittlement are very similar, whereas the dissolution of the Zinc-14%Nickel sacrificial coating occurred at a more negative potential and should generate far more hydrogen during re-embrittlement.

Cadmium potential of -725 mV(SCE) determines the amount of hydrogen evolving on the steel substrate and this amount of hydrogen, in turn, would control the extent of re-embrittlement. But, from the ennoblement behaviour of the Zinc-14%Nickel coating, it is predicted that more hydrogen would evolve and permeate the steel during the first 150 hours

of exposure. At longer times, more noble potentials would develop, resulting in less hydrogen generation.

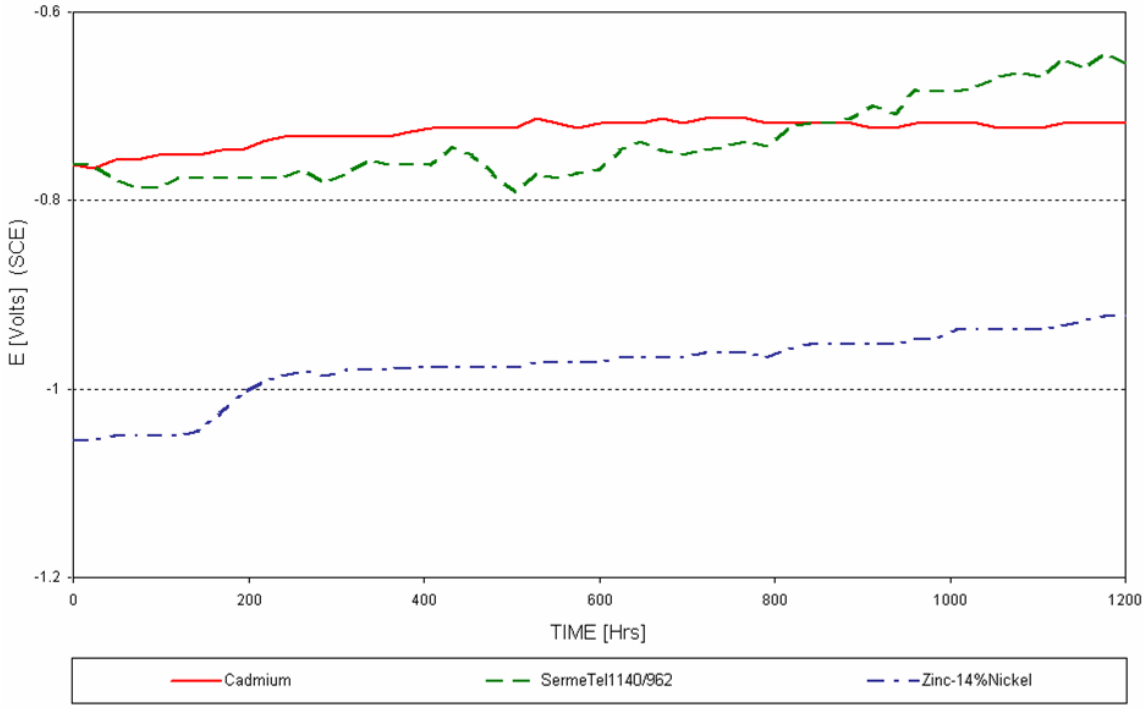

Figure 140. Comparison of the open circuit potentials for cadmium, Zinc-14%Nickel and SermeTel®1140/962 sacrificial coatings after 1200 hours immersion in quiescent 3.5% NaCl solutions.

From the apparent exponential relationship between the amount of hydrogen taken up by steel substrates and the electro-negativity of sacrificial coatings, it is expected to find a linear relationship between the logarithm of the permeating current density, $Log_{10}(I_\infty)$, and the potential, *E*. Indeed, **Figure 141** shows a linear fit of the *E vs* $Log_{10}(I_\infty)$ plot, where the slope is approximately -445 mV/decade and the intercept at zero current is -1.56 V(SCE).

It has been proposed that at low hydrogen surface coverage, θ, and for rate controlling hydrogen diffusion through the steel membrane the following premises applied: *1)* the permeated hydrogen flux, I_∞, should be proportional to the square root of hydrogen evolved on the charging surface $I_{charged}$, $\left(i_\infty \alpha \sqrt{i_{charged}}\right)$, and *2)* the slope of the linear fit for the *E vs*

$Log_{10}(I_\infty)$ plot can be theoretically represented by the following expression:[74, 75, 158]

$$\frac{\partial E}{\partial Log\ i_\infty} = \frac{\partial E}{\partial Log\,\theta} = -\frac{4\,(2.303)R\,T}{F} = -\,240\,[mV\,/\,decade] \qquad [XLV]$$

This theoretical value (-240 mV/decade) is lower than that obtained experimentally for the permeation hydrogen flux through the shim membrane. This observation suggests that less hydrogen was permeating through the steel membrane than that predicted.

To explain this assumption, it can be appreciated in **Figure 141** that for a hypothetical polarisation value, denoted as *E*, the amount of hydrogen permeating the steel membrane is far less for the experimental value, depicted as *A*, than that associated to the theory, *B*. This effect is thought to occur due to the relatively active potential range used in these experiments and the consequent loss of hydrogen by forming bubbles on the steel surface as the potential became more active.

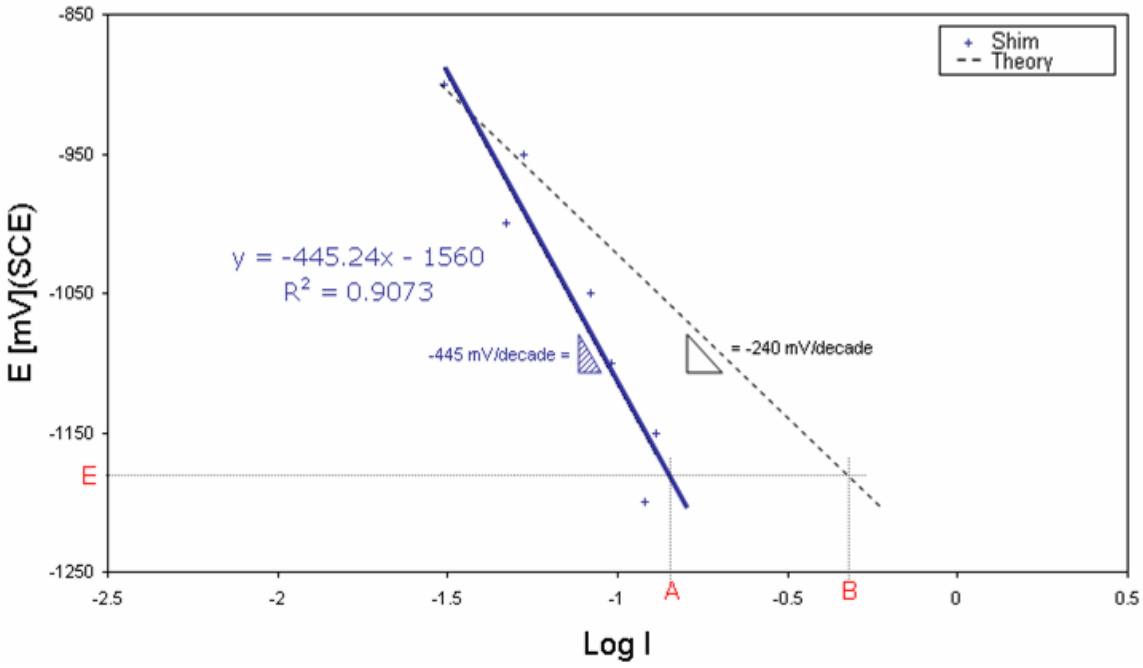

Figure 141. E vs. Log_{10} I_∞ graph for low carbon steel membranes in 3.5% NaCl solution.

To determine the proportion of hydrogen from the *HER* that eventually permeate the steel, the amount of hydrogen evolving during the cathodic reaction on the steel surface is represented by the slope of the linear fit of the *E vs* $Log_{10}(I_{charged})$ plot (Tafel slope); whereas the slope of the linear fit of the *E vs* $Log_{10}(I_{\infty})$ plot corresponds to the amount of hydrogen diffusing through the steel membrane. **Figure 142** clearly illustrates the relationship between steady state current densities, I_{∞}, and the cathodic Tafel behaviour, $I_{charged}$, for the hydrogen evolution reaction on the steel surface.

The displacement of the two lines represents a measure of the hydrogen escaping or bubbling from the surface together and the amount of hydrogen trapped within the steel membrane. Hence, from this relationship and knowing the amount of hydrogen permeating at low potentials, (*ie*.-0.90 Volts(SCE) where hydrogen bubbling is low), it would be possible to estimate the maximum I_{∞} value and therefore the highest amount of hydrogen that would permeate the steel during re-embrittlement.

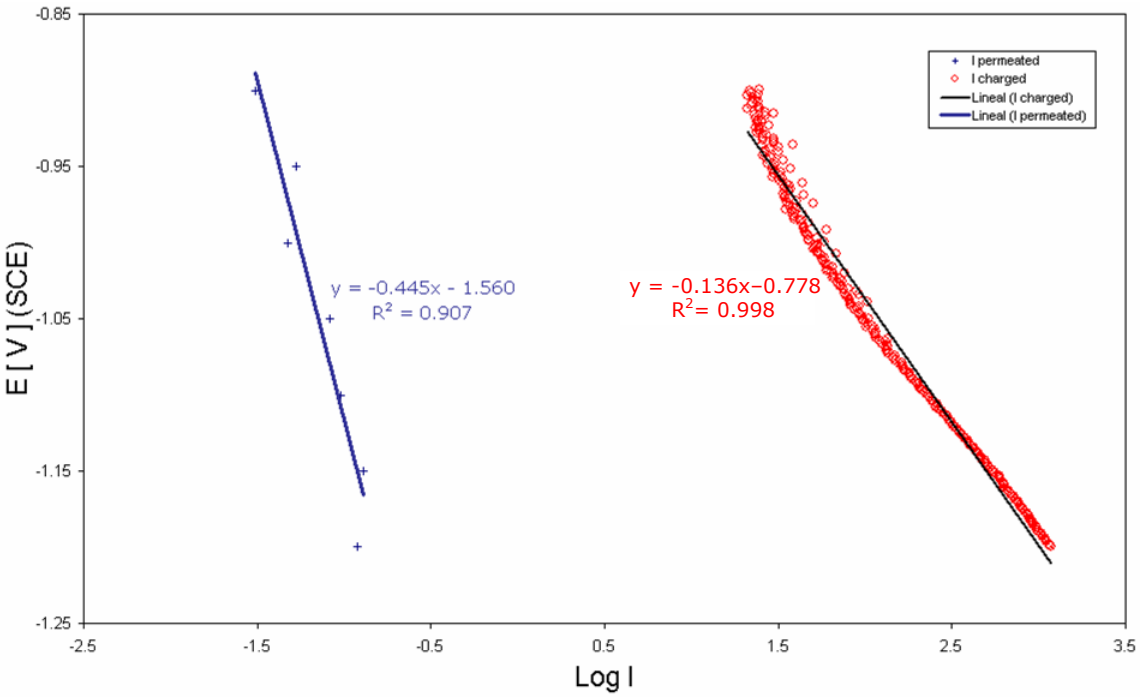

Figure 142. Potential vs. $Log_{10}(i_{\infty})$ and $Log_{10}(i_{charged})$ graph for low carbon steel membranes in 3.5% NaCl solution.

13.3. Hydrogen Diffusivity of 300M Steel

Hydrogen embrittlement and re-embrittlement of high strength steels occurs once the atomic hydrogen has been absorbed within the microstructure, filling reversible and irreversible traps and migrating to regions under triaxial stress ahead the crack tip.[100, 109] Therefore, it is important to establish an experimental method to quantify how fast the atomic hydrogen moves within the different steel microstructures. In relation with this observation, the hydrogen permeation technique was used to measure the hydrogen transport characteristic of the alloys in terms of hydrogen diffusivity.

Prior to the hydrogen charging of the 300M steel membrane, most of the hydrogen occluded within the microstructure was removed by depleting it for approximately 96 hours, until the current density detected, (proportional to the amount of hydrogen diffusing out from the membrane), reached values as low as 0.01μA/cm^2. Immediately after, the membrane was potentiostatically charged with hydrogen in the charging side of the cell. Following approximately 1.78 hours the first hydrogen atom permeated the steel membrane and was detected in the depletion side of the electrochemical cell.

Moreover, after 23 hours of charging a steady state current density value of 0.337μA/cm^2 was reached. From this latter parameter, the time to reach 0.63 of the steady state current density was calculated to be approximately 4.64 hours. The diffusion coefficients obtained using the breakthrough time and time lag methods were 1.07x10^{-7} and 9.98x10^{-8} cm^2/s, respectively. Considering these values, the resulting mean hydrogen diffusion coefficient for the 300M steel membrane was 1.02±0.04x10^{-7} cm^2/s.

Similarly, Beck *et al*[160] reported hydrogen diffusivity values of 2.7x10^{-7}cm^2/s for AISI-4340 high strength steel. This value is in good agreement with the results obtained for the 300M steel membrane, considering that

this alloy has been defined by some researchers as a silicon-modified AISI-4340 steel.[30, 32, 35] The AISI-4340 alloy is very similar to 300M, but slight differences in silicon and vanadium compositions might contribute to differences in hydrogen diffusivity.

Finally, the last parameter calculated from the permeation measurements was the hydrogen concentration just below the charging surface after 23 hours of charging, a parameter that reached a value of 3.42×10^{-6} mol/cm^3.

Ideally, in the absence of traps hydrogen diffusion takes place by random jump migration between the interstitials lattice positions, with a relatively short residence time.[161] From this assumption, it is feasible to assume that the flux of hydrogen permeating through the steel membrane can be predicted using the Fick's law of diffusion,[113] once the steady state condition is reached.

The behaviour of the experimental hydrogen permeation transient obtained for the 300M steel membrane was considered to be described by equation [IX], assuming lattice diffusion with no effects of hydrogen trapping. By substituting the hydrogen diffusivity (1.02×10^{-7} cm^2/s) and the steady state current density (0.337 μA/cm^2) values obtained from the 300M experimental permeation transient it is possible to compare the theoretical lattice diffusion model with the experimental values. This comparison shows a good agreement between the experimental transient and the ideal lattice diffusion model, as is graphically depicted in **Figure 143**.

There is a small difference in the breakthrough time, t_b, at which the first hydrogen permeated the 300M steel membrane. The t_b value for the experimental data was slightly longer than that for the lattice diffusion model by approximately 0.8 hour. It has been considered that the reason for this deviation is associated with the effect of hydrogen trapping in the 300M membrane.

Turnbull *et al.*[102] has shown that after consecutive hydrogen charging of AISI-410 stainless steel membranes, the breakthrough time of the second transients were shorter than the first. This observation was attributed to the filling of irreversible traps during the first transient; hence during the following permeations those traps were already filled resulting in faster rise on the current detected. Traps with relatively high energy create an effective barrier to the displacement of hydrogen atoms.[100] Therefore, the process of filling those traps delays the breakthrough time.

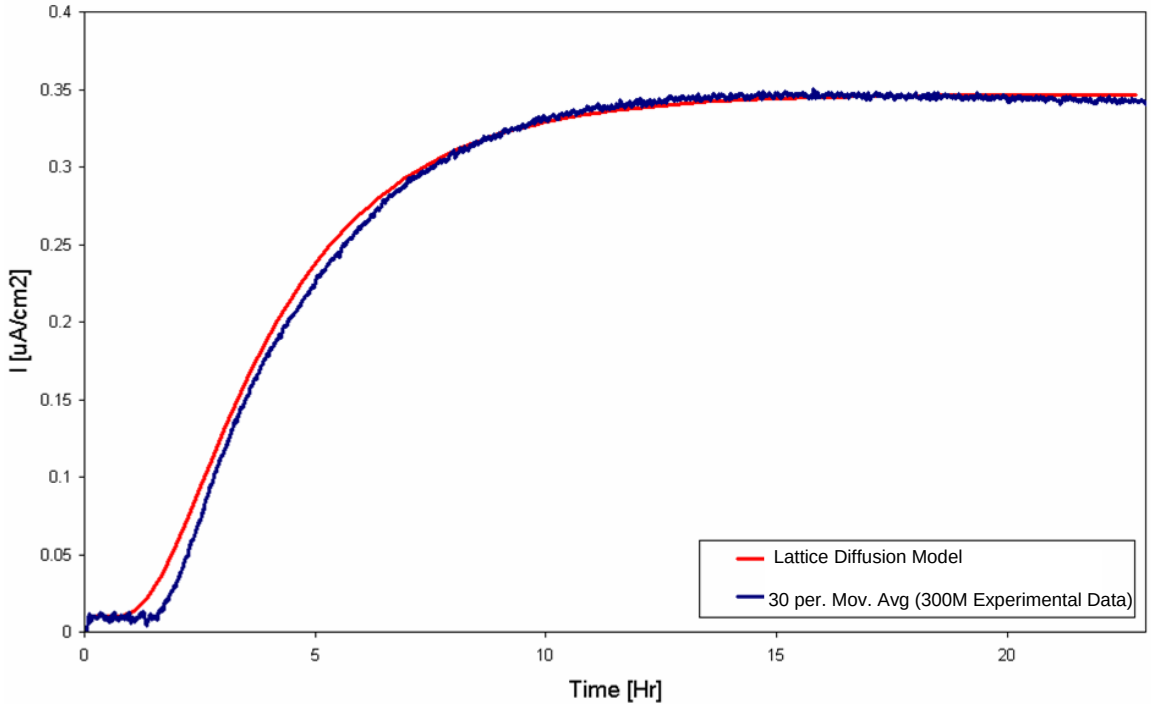

Figure 143. Comparison of the permeation lattice diffusion model and the experimental data for the 300M.

The microstructural characteristic of the steel determines the hydrogen transport characteristics of the alloy. For example, Robinson and Kilgallon[162] have suggested that the microstructure susceptibility to hydrogen embrittlement is in the order: lower bainite < quenched and tempered martensite < pearlite or spheroidized structures < untempered martensite is the most susceptible. Therefore, once the hydrogen diffusivity of the 300M steel has been measured, it was considered relevant to associate this characteristic with the microstructural features present in the high strength steel.

13.4. 300M Microstructural Characteristics

Initially, early metallographic analysis carried out on 300M high strength steels has shown a microstructure comprising a sub-micron plate or lath martensitic matrix. But later, additional microstructural features that might affect the mobility of hydrogen within the material became more evident when analyses were performed at higher magnifications. *SEM* micrograph showing this analysis is depicted in **Figure 144**.

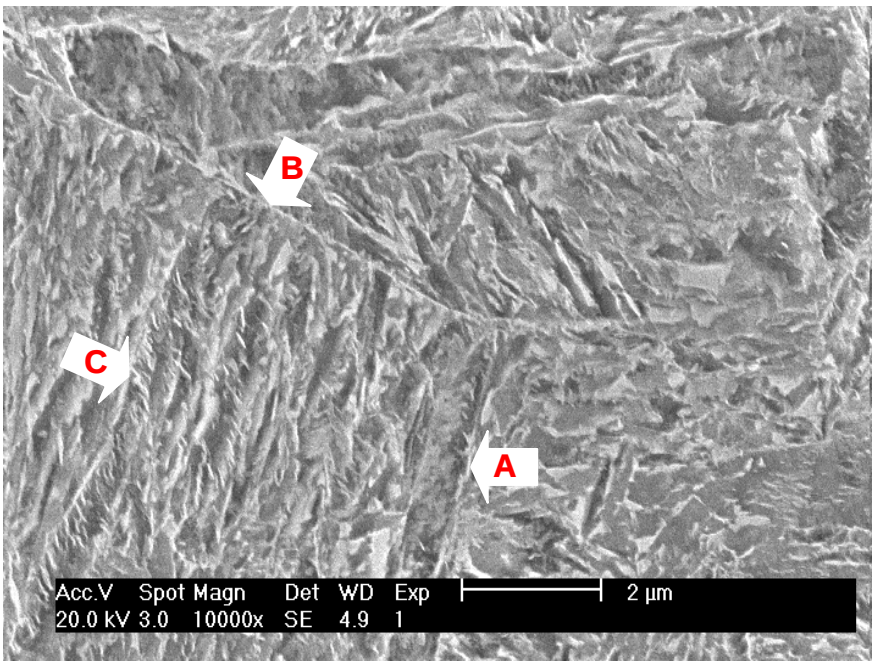

Figure 144. *SEM* micrographs for 300M high strength steel presumably showing: A) retained austenite at plates boundaries B) retained austenite at prior austenite grain boundaries; and C) ε-carbide precipitation within martensite laths.

It can be seen that the first important characteristic is the presence of retained austenite as thin films at some of the martensite laths or plates boundaries. T R. Padmanabhan[35, 99] has previously reported similar results following an extensive microstructural assessment for 300M steels that have received equivalent heat treatments to those used in the present project.

Secondly, it is clearly noticeable that some of the retained austenite presented in the microstructure is located at the prior austenite grain boundaries. It has been also reported that the segregation of P and S to the prior austenite grain boundaries reduces the intergranular cohesion, increasing the risk of *SCC*.[99] Considering that *SCC* of martensitic high strength steels in aqueous solutions involves a dominant role of hydrogen, it has been suggested that hydrogen become trapped at the grain boundaries as a result of segregated impurity elements.[163] At the same time, the interaction of these impurities and hydrogen atoms prevents the hydrogen diffusion into the bulk.

On the other hand, R. O. Ritchie *et al.*[163] has shown the beneficial role of retained austenite by comparing quenched and tempered 300M with AISI-4340 high strength steels containing less than 2% austenite. This beneficial role is attributed to a reduction in diffusivity of hydrogen in the steel. Austenite has a higher solubility of hydrogen than martensite and therefore the diffusivity of hydrogen is at least an order of magnitude lower than that for martensite.[99] Moreover, it is feasible to consider that retained austenite thin films located at either the plate interfaces or prior austenite grain boundaries, acts as sinks for interstitials and impurity elements which trap hydrogen atoms diffusing through the 300M martensitic matrix.[163]

The diffusion path for hydrogen ahead the crack tip should involve transport through austenite films around the martensite laths.[163] But a possible deleterious effect of stress-induced transformation of austenite to martensite, specifically in the plastic zone ahead the crack tip where austenite that might transform could released excess of dissolved hydrogen into the martensitic matrix, has also been proposed.[99] However, G. Thomas[164] proposed that if retained austenite films remained stable, it seems to have a beneficial role on the fracture toughness of medium carbon steels.

There is an abundance of literature on determining the percentage of the retained austenite using *XRD* analyses.[30, 32, 33, 163-167] Therefore, attempts

were made to quantify the amount of retained austenite presented in 300M steels using this technique. However, no retained austenite phase was revealed in the X-ray pattern obtained for 300M steel, as is shown in **Figure 145**. Only the austenite [111] peak was hardly noticeable, but the rest were thought to be below the background level.

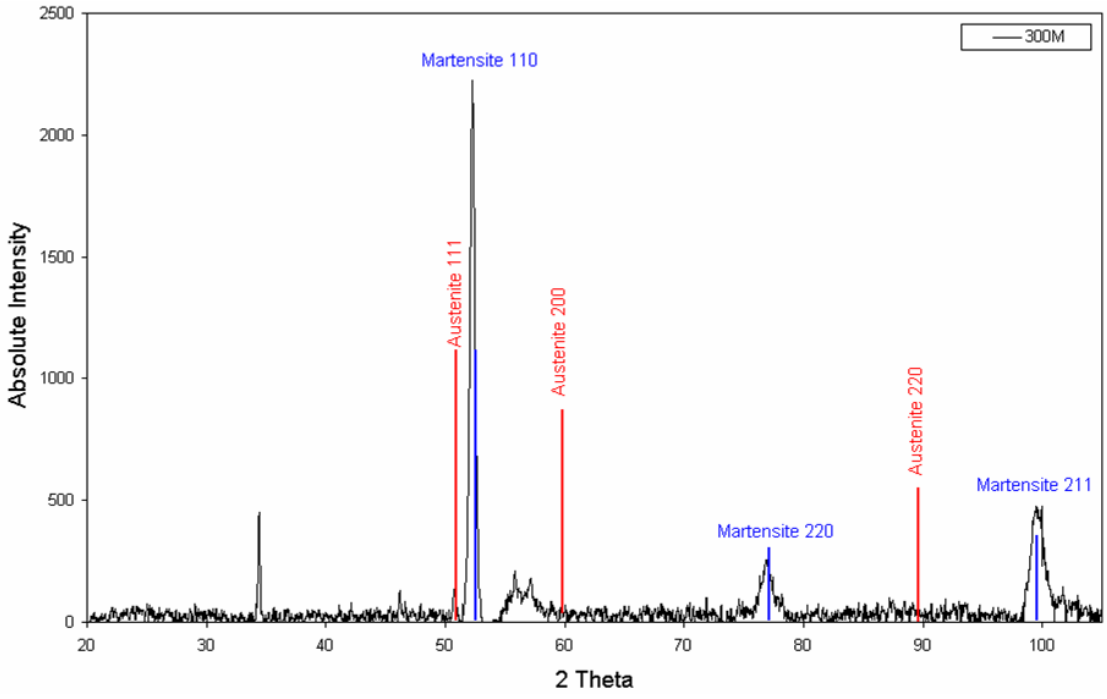

Figure 145. X-Ray diffraction pattern for 300M steel showing the corresponding angles for austenite (red) and martensite (blue) phases, using a Co-K_α radiation source.

The amount of retained austenite in 300M steel was below the detection limit of the technique, considering that a cobalt radiation source was used instead of the recommended molybdenum target.[30, 32, 33, 164, 167] Fluorescent phenomena might have contributed to those results as the background noise level increased as the incident angle θ increased.[165, 168] It is feasible to assume that the [200] and [220] austenite peaks, might easily become covered below the background level. Although an X-ray software analysis package was used to reduce this background effect, no other retained austenite peaks were found. Similar results were previously reported by Youngblood *et al,*[33] where the retained austenite phase in

300M steel was barely detected using the conventional molybdenum K_α X-ray radiation source.

The third microstructural characteristic revealed is the presence of a second phase, presumably cementite, Fe_3C, or ε-carbides within larger martensite laths. In relation to this observation, it has been speculated that ε-carbides formation depletes the carbon locally and therefore renders the carbide-matrix interface weak.[33]

Additional microstructural features, normally revealed using *TEM*, contemplate carbides such as M_7C_3, $M_{23}C_6$ and Mo_2C within martensite laths in 300M steels.[35] These precipitates act as reversible or irreversible traps with low or high interaction energies depending upon its coherency with the matrix.[35, 99] Nevertheless, it has suggested that the susceptibility to hydrogen degradation (in terms of loss in the mechanical properties) of '*low alloy*' high strength steels is more likely to be dependent on the amount of mobile hydrogen (diffusing) rather than the trapped hydrogen.[169]

13.5. Hydrogen Diffusivity of AerMet®100 Steel

Initially, the hydrogen permeation technique was used to determine the hydrogen diffusivity of AerMet®100 steel. Hydrogen depletion of the membrane was carried out for approximately 96 hours, as for the 300M steel membrane. Again the depletion was performed until the current density value detected was close to 0.01μA/cm^2. However, no hydrogen was detected on the depletion side of the cell after periods of potentiostatic hydrogen charging longer than 48 hours (**Figure 86**). In the first instance it was assumed that the hydrogen flux was below the detection limit.

The transients for the two steels were broadly as would be expected from the diffusion coefficients reported in the literature.[100,104,145,160] The steady

state flux, J_∞, and its equation, $J_\infty = C\ F\ D / L$, enabled the flux to be estimated for 300M and AerMet®100 steel membranes.

In other words, to predict the height of the permeation transient for 300M steel, the hydrogen diffusivity of a similar steel AISI-4340 (2.7×10^{-7} cm^2/s) was considered.[160] In addition, taking into consideration differences in membrane thickness, (0.1 and 5.7×10^{-3} cm for the 300M membrane and low carbon shim, respectively), and assuming that internal hydrogen concentrations reach equivalent levels for both alloys, the permeation transient for 300M was expected to be similar in height to that for the low carbon shim, which displayed a hydrogen diffusivity of 1.5×10^{-8} cm^2/s. This comparison was done as follows:

$$\frac{J_{\infty,300M}}{J_{\infty,SHIM}} = \frac{C\ F\ D_{300M}\ /\ L_{300M}}{C\ F\ D_{SHIM}\ /\ L_{SHIM}} = \frac{D_{300M}\ L_{SHIM}}{D_{SHIM}\ L_{300M}} = 1.03 \qquad [\text{XLVI}]$$

Steady state current density values obtained for the hydrogen permeation transients of both, low carbon shim and 300M steel membrane validated this prediction method.

In contrast, values reported for the apparent hydrogen diffusivity of AerMet®100 has been found around 3×10^{-8}cm^2/s.[100] Assuming that this value is correct, the height of the transient for the 1mm thick AerMet®100 membrane is expected to be approximately 0.03 μA/cm^2, only 0.11 of that for the low carbon shim, which is equivalent to the background level after depletion.

There are several possible methods to increase the steady state flux in order to raise it above the detection threshold. The most obvious is to increase the area of the steel membrane, as originally intended. For example, a membrane of 150mm diameter would increase the flux 2.25 times. But the practicality of producing bigger membranes was in doubt due to material availability. Therefore, it was also considered to increase the hydrogen charging conditions and increase the steady state current

density detected in the depletion side. However, it was known that by increasing the cathodic polarization, more hydrogen would escape from the membrane surface as the hydrogen bubbling became more violent, even using hydrogen recombination poisons such as thiourea.

Finally, the possibility of reducing further the membrane thickness was also discarded as residual stresses presented in the AerMet®100 membrane posed serious practical difficulties in reducing the thickness by conventional grinding processes.

Therefore, attempts were made using alternatives electrochemical techniques which required relatively small specimens, in order to determine the hydrogen transport characteristics of AerMet®100 steels. Among several techniques,[117-119,170,171] the alternative galvanostatic charging method[117-119] was used. This method has been also referred as constant current chrono-potentiometry[117-119,172,173] and involved a galvanostatic hydrogen charging of small rectangular specimens for relatively short periods.

This method is less familiar than the two-cell permeation technique, previously used for 300M steel, but the validity of its results has been corroborated by comparing diffusivity values obtained to that from the permeation technique. Although the hydrogen charging conditions were different and hence the boundary conditions at the electrolyte-steel interface, a good agreement in the hydrogen diffusion coefficient values was found. The mean hydrogen diffusion coefficients for 300M steel using the constant current chrono-potentiometry and the potentiostatic hydrogen permeation technique were 1.1×10^{-7} and 1.0×10^{-7} cm^2/s, respectively. Therefore, results from the alternative electrochemical technique proved to be consistent with those from the conventional hydrogen permeation.

Following this observation, the constant current chrono-potentiometry technique was used to determine the hydrogen transport characteristic of the AerMet®100 steel. Surprisingly, it was found that the hydrogen

diffusion coefficient of this high strength steel was two orders of magnitude lower than that for the conventional 300M steel. The mean hydrogen diffusion coefficient was $3.5x10^{-9}$ cm^2/s. This value is equivalent to that recently published by Sundaram *et al*[118] of $2.9x10^{-9}$ cm^2/s for AerMet®100 steels, using the same electrochemical method with different charging media.

Nevertheless, the obtained value is almost an order of magnitude lower than the '*apparent*' hydrogen diffusivity of AerMet®100 at 23°C, ($3x10^{-8}$ cm^2/s), previously reported by Thomas *et al.*[100,146] using thermal desorption spectrometry. The thermal desorption spectrometry (*TDS*) technique was used by Thomas *et al*[100,146] to measure the hydrogen egress from previously potentiostatically charged specimens, by heating the specimens at constant temperatures between 60 to 200°C. But values for hydrogen diffusivity at room temperature were extrapolated from the *TDS* data obtained at higher temperatures.

In addition, it is important to underline that the '*apparent*' hydrogen diffusivity is actually affected by the filling of hydrogen traps and hence this value tend to be lower by one or two order of magnitude than the lattice diffusivity.[100] Therefore, if the trap-affected or '*apparent*' hydrogen diffusivity value reported by Thomas *et al*.[100,146] was valid, it should be feasible to expect a lattice hydrogen diffusion coefficient for AerMet®100 steels in the order of 10^{-6} to 10^{-7} cm^2/s. In other words similar to that for 300M steel.

Nevertheless, these values did not correspond with previous SSRT results and specially with the fractographic analyses, which assessed the distribution of embrittled regions at the fracture surfaces of cadmium plated 300M and AerMet®100 steel. Specifically, when the little extent of affected regions of AerMet®100 specimens were compared to the extensive embrittled areas found for 300M specimens. It is thought that if AerMet®100 displays hydrogen diffusion coefficient in the same order as 300M, around 10^{-7} cm^2/s, AerMet®100 steel should displayed similar extent

of embrittled regions than for 300M. But this conjecture is in opposition to the fractographic evidence presented and discussed in previous sections.

Certainly, values obtained from the constant current chrono-potentiometry technique are more likely to explain such differences in brittle fracture distribution. These results support the view that the lower hydrogen embrittlement susceptibility of AerMet®100 is strongly related to its low rate of hydrogen transport, which has been confirmed to be two orders of magnitude lower than that for 300M steels.

At this point, it is possible to compare the hydrogen transport characteristics of both alloys using a common electrochemical technique. Consequently, **Figure 146** has been considered to visualise the differences in response of 300M and AerMet®100 steels to the galvanostatic hydrogen charging method, where changes in potential with time are depicted.

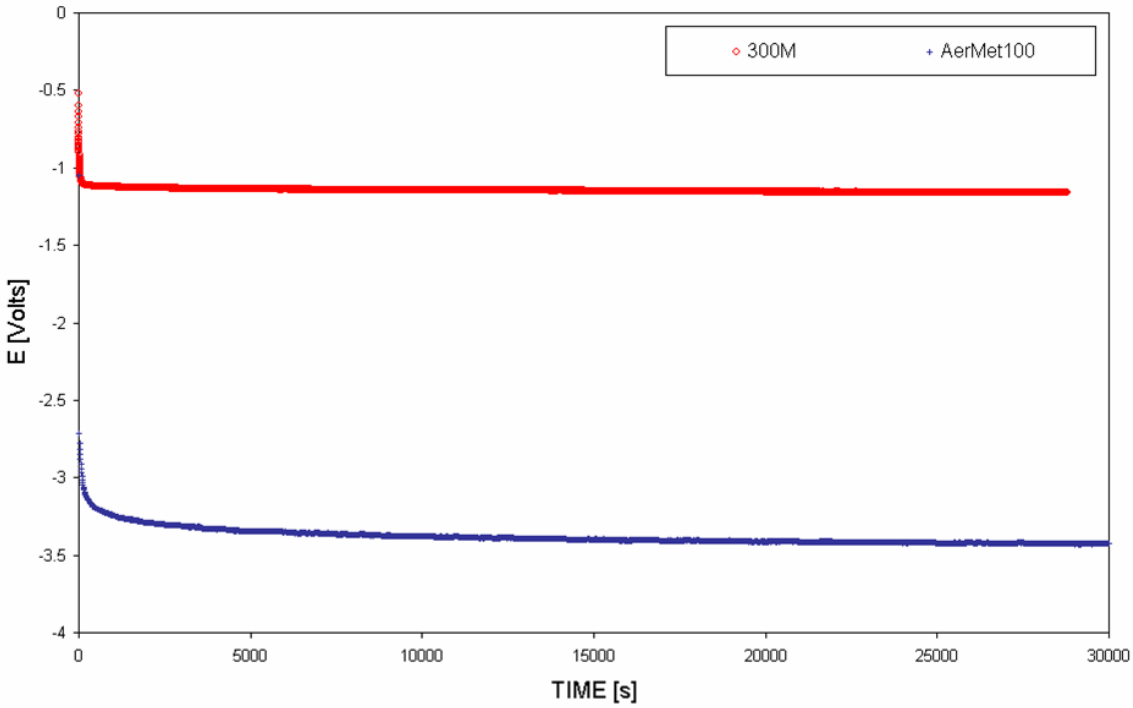

Figure 146. Comparison of potential, *E*, variation against time for 300M and AerMet®100 specimens in 0.2M NaOH solutions.

First, it can be appreciated that the equilibrium oxidation/reduction potential ($E_{H/H+}$) is far more negative for AerMet®100 than that for 300M steel under equivalent hydrogen charging density conditions. Considering, that the application of a constant current flux produces the passage of a constant flux of mobile hydrogen across the electrolyte-steel interface,[117] the different equilibrium potentials found for both alloys are thought to be associated with the intrinsic responses of each alloy at the electrode surface.

Initially, the potential response with time shows a parabolic relationship, which remarkably depends among different factors upon the hydrogen diffusivity of the steel, as equation [XXVI] showed. In addition, similarly to the permeation transients, the hydrogen diffusion process is assumed to obey the Fick's second law of diffusion.[117-119]

Remarkably, it was found that this initial parabolic section of the transient, defined as '*short time segments'*, was significantly shorter for 300M than that for AerMet®100 steel. In the same order, periods of time for the short time segments were 0.7 and 1.3 hours. Consequently, the potential parabolic response for AerMet®100 was much deeper than that for 300M. These effects are thought to occur as hydrogen diffusivity of AerMet®100 is far lower than that for 300M steel. If lower hydrogen diffusion values are substituted in equation [XXVI], bigger changes in potential should be produced in the electrochemical cell.

At longer times, the recorded trend is associated with changes in the working electrode potential as the hydrogen concentration increases within the material. AerMet®100 displayed smaller changes in potential than 300M, with potential-time slope values of $8x10^{-7}$ and $2x10^{-6}$ $V.s^{-1}$, respectively. Again, this difference is thought to be the result of less hydrogen been taken up by AerMet®100 than the by 300M steel during the galvanostatic charging.

The practical implications of the low hydrogen transport characteristics of AerMet®100 are clear. Considerably less hydrogen permeates through the

microstructure of this alternative alloy than through the 300M and this might contribute to its lower levels of hydrogen embrittlement previously reported. Therefore, it is feasible to assume that some microstructural features of AerMet®100 would restrict the transport of hydrogen through the material, reducing its susceptibility to delayed failure due to occluded hydrogen.

13.6. AerMet®100 Microstructural Characteristics

In addition to the martensitic matrix revealed from the metallographic analyses carried out on AerMet®100, *SEM* studies showed that some martensite lath or plates were approximately 8μm in length and 1μm width, as is shown in **Figure 147**. It can be seen that reverted austenite is present as thin film morphology at plate or laths boundaries, similar to the retained austenite observed in the 300M steels.

SEM analyses reported by C. H. Yoo *et al*,[40] has shown equivalent results, where the bright phase corresponded to reverted austenite and the darker phase to martensite. Moreover, *TEM* analyses carried out by R. Ayer. *et al*.[41] showed that reverted austenite thin films, found on quenched and tempered at 482°C AerMet®100 steel, were approximately 3nm width. It has been proposed that this reverted austenite is formed through a diffusionless mechanism which produces a strengthening effect in the resulting phase due to high density of defects.[42]

In the AerMet®100 steel, it is thought that the reverted austenite stops hydrogen from diffusing to the martensitic matrix like the retained austenite in 300M steel. However, reverted austenite slightly differs from retained austenite as its crystallographic orientation is not exactly the same.[42] Due to the high density of defects such as dislocations, stacking faults and twining, it is feasible to consider that reverted austenite might displays a slightly higher hydrogen solubility than retained austenite as such microstructural defects offer sites for reversible hydrogen traps.

Similar to 300M steel, reverted austenite was also found presumably at some of the prior austenite grain boundaries in AerMet®100. In addition, it was also revealed that AerMet®100 displayed far less amount of second phases (austenite, cementite or ε-carbides) in the martensitic matrix than 300M steel. This observation can be noticed by comparing **Figures 144** and **147**. R. Ayer. *et al*.[41] has suggested a complete absence of cementite in AerMet®100 and instead he noticed the formation of reverted and stable austenite as thin films around martensite laths and plates.

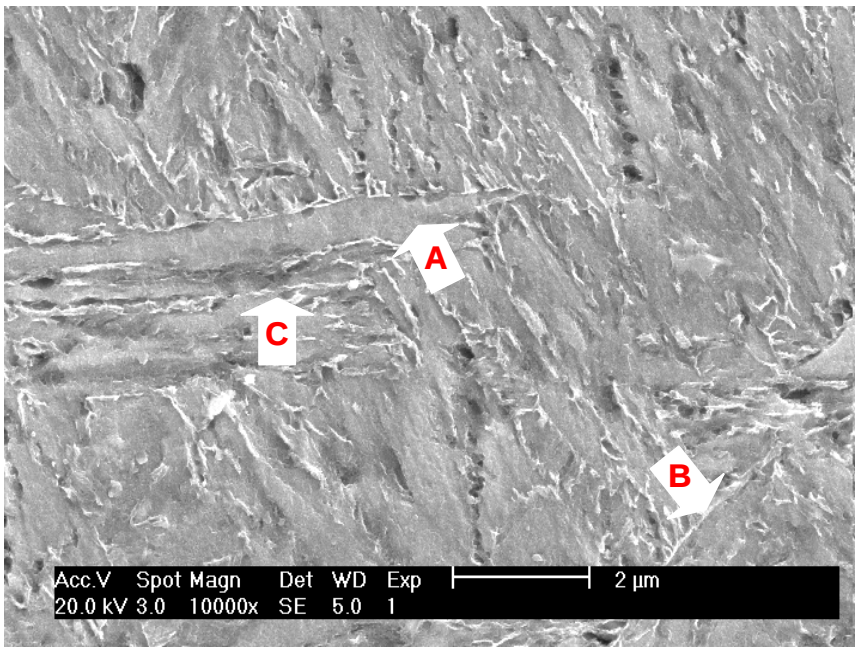

Figure 147. *SEM* micrographs for AerMet®100 high strength steel presumably showing: A) martensite lath, B) reverted austenite at martensite lath boundaries, and C) reverted austenite at prior austenite grain boundaries.

Concerning measuring the amount of reverted austenite with *XRD*, no austenite peaks were found as **Figure 148** is showing. R. Ayer. *et al*.[41] has reported less than 1vol.% of reverted austenite for AerMet®100 steels quenched and tempered at 482°C, which was the same condition used in the present project. It is clear, that these small percentages of reverted austenite are far below the detection limit of the *XRD* technique carried out using a Co-K_α radiation source. [165, 166]

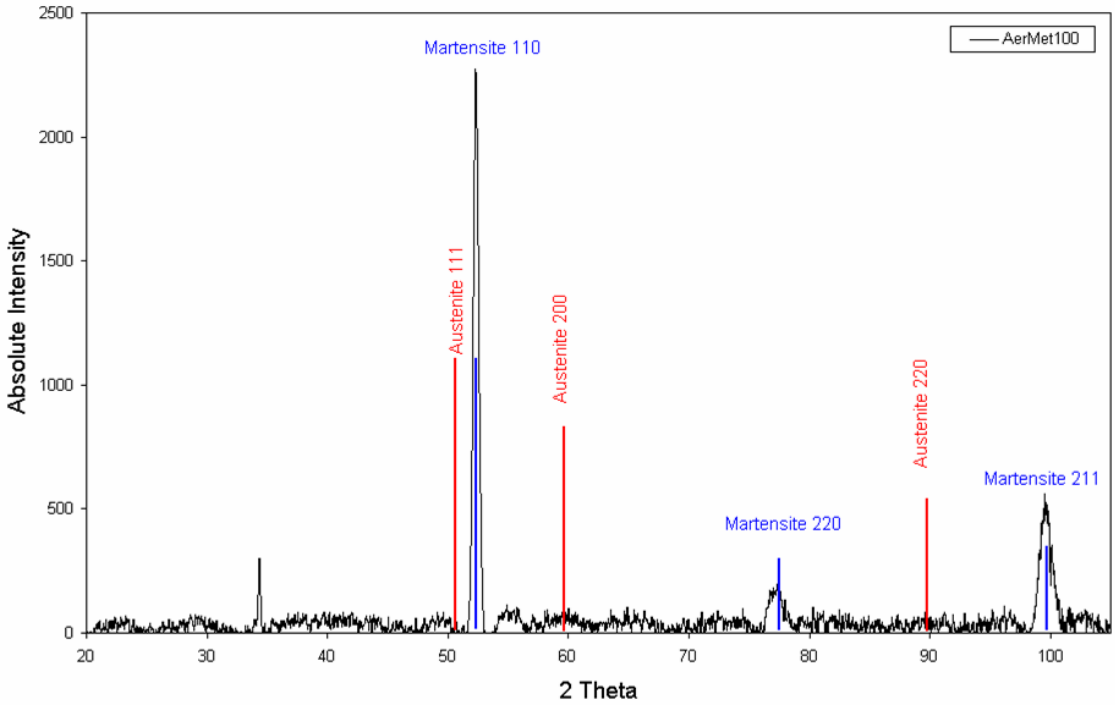

Figure 148. X-Ray diffraction pattern for AerMet®100 steel showing the corresponding angles for austenite (red) and martensite (blue) phases, using a Co-K_α radiation source.

It has been proposed that AerMet®100 is susceptible to a limited extent of brittle intergranular fracture due to hydrogen embrittlement in acid and near-neutral chloride solutions with cathodic polarizations, and certainly much less than less-clean ultrahigh strength steels like AISI-4340 and 300M, in which elements like Si and Mn are added. It has been argued that the mechanism of intergranular fracture due to hydrogen embrittlement of at least moderate-strength steels (800MPa<σ_{YS}<1400Mpa) and tempered martensite microstructures is likely to involve a reduction of boundary cohesion due to segregation of hydrogen and impurities such as S, P, Si, and Mn.[49,146,147] This statement has been corroborated through the previously discussed fractographic analyses performed on cadmium plated 300M and AerMet®100 specimens.

In contrast to the conventional low alloyed 300M steel, the alternative AerMet®100 has been associated with a trap rich-microstructure. Extensive reversible hydrogen trapping is likely to occur in three or more distinct trap states: coherent M_2C carbides, dissolved Ni, and precipitated

austenite. Whereas, extensive irreversible traps occur at high mis-orientated interfaces such as incoherent metal carbides and martensite lath structures. Substantial hydrogen is retained at these high energy trap states. Therefore, it has been suggested that hydrogen diffusivity of AerMet®100 is greatly reduced due to both types of trapping.[100, 146]

Hydrogen trapping critically affects the resistance of AerMet®100 to hydrogen embrittlement due to three major characteristics. First, the low hydrogen diffusivity results in lower rates of hydrogen direct embrittlement and re-embrittlement in trapping-rich steels. Where hydrogen diffusion at the crack tip region plays an important step in the hydrogen induced crack. Secondly, strong reversible and irreversible hydrogen traps containing hydrogen might define a brittle-crack path and decrease the resistance to hydrogen embrittlement. Third, the quantity of hydrogen available to diffuse to brittle fracture sites depends on the strength and distribution of hydrogen traps in the alloy.[146]

An interesting and different approach had been taken into account by Pound *et al*.[38,174] in order to rank the susceptibility of a group of high strength steels to hydrogen embrittlement. He established a relationship between a rate constant for hydrogen irreversible trapping (*K*) and the intrinsic susceptibility to hydrogen embrittlement observed in mechanical tests. The magnitude *K* depends upon the irreversible trapping capacity of the material, lattice diffusion and trapping density, thus it is considered to be an index of the alloys intrinsic susceptibility to *HE*.

He indicated that the threshold stress intensity factor to produce stress corrosion cracking, K_{ISCC}, in 3.5% NaCl solutions is inversely proportional to *K*, as **Figure 149** shows for different high strength steels. Among this group, AerMet®100 steel is associated with the lowest *K* and therefore is considered to be the less susceptible to hydrogen induced fracture than AISI-4340. This effect was attributed mainly to a large population of M_2C particles at high tempering temperatures.[38, 174]

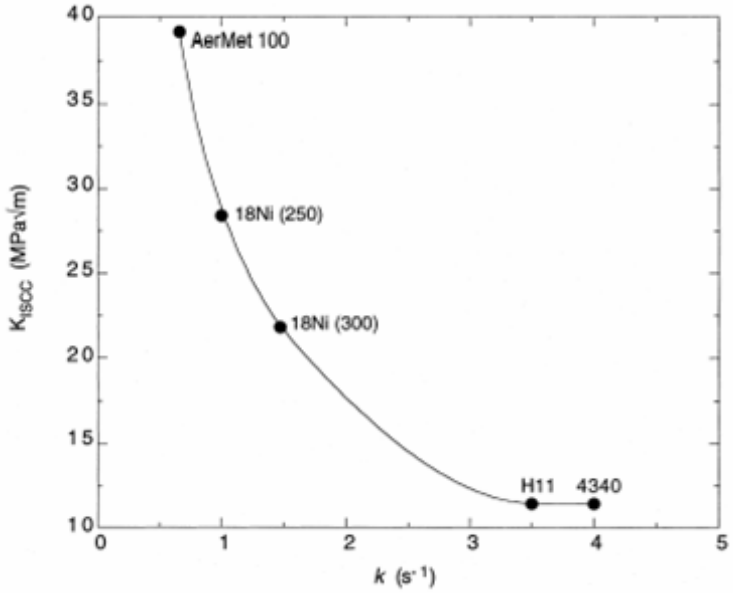

Figure 149. Variation of K_{ISCC} values with K for high strength steels.[38]

Hydrogen occluded in a large population of low binding-energy reversible traps like finely distributed M_2C particles, dislocations and low mis-orientated martensite interfaces has a high possibility of being released at room temperature. Consequently, a large population of weak traps might provided a reservoir of mobile hydrogen in AerMet®100 steel.[100,146] Subsequently, it has been proposed that embrittlement of rich-trap high strength steels such as AerMet®100 might takes place as **Figure 150** describes.

In the presence of stress, occluded hydrogen among interstitial sites and reversible and irreversible traps, provided by embrittlement or re-embrittlement processes or initially dissolved within the material, drains from these states to martensite interfaces and cleavage-fracture sites within the fracture process zone. In the picture, hydrogen trapped at M_2C, solute zones and other metallic carbides, M_xC_y, migrates to the martensite lath interfaces at the fracture process zone to induce preferentially transgranular fracture.[146]

On the other hand, it is feasible to think that levels of load (within the elastic regime) or even the presence of residual stresses produced by

manufacturing process like heat treatments or machining, might affect hydrogen transport characteristics of the high strength steels and therefore their susceptibilities to hydrogen embrittlement and re-embrittlement. Therefore, an assessment on how these factors might affect the hydrogen internal concentration and diffusivity of the steels is presented and discussed in the following sections.

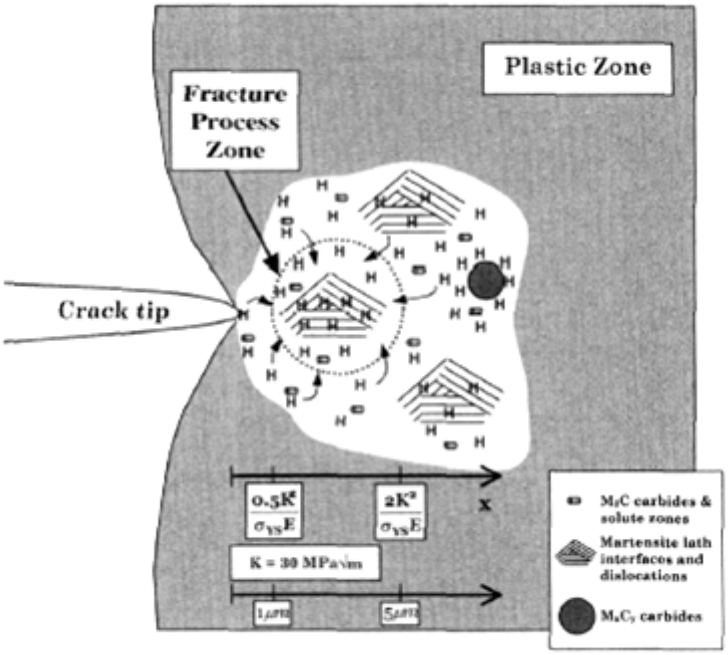

Figure 150. The hypothesized scenario for internal hydrogen embrittlement of ultra high-strength steel such as AerMet®100, containing hydrogen trapped at a variety of microstructural sites and subjected to high crack-tip stresses. [146]

13.7. Effect of Residual Stresses on Hydrogen Diffusion

Shot peening is normally applied to high strength steels used for structural aerospace applications to increase the fatigue resistance of the component. For example, E. U. Lee *et al*[175] has reported that shot peening extends the fatigue life of AerMet®100 steel by 100% with the induced residual compressive stress. For similar reasons, it has been suggested that residual stress fields induced by such treatments might be beneficial to the *SCC* and *HE* resistance of structural materials.[176, 177] In this particular area, the effect of the residual stresses on the hydrogen transport characteristics and the susceptibility to hydrogen embrittlement has been widely debated.[176, 180]

The role of shot-peening on the hydrogen embrittlement is primarily dependent on the material and the hydrogen environment.[176, 180] For example, it has been suggested that the effect of shot peening on the hydrogen embrittlement susceptibility of unstable 304 stainless steels in H_2S environments is entirely detrimental. This effect has been associated to the formation of α' martensite phase in the cold-work layer. On the contrary, it has been proposed that shot peening treatments reduce the hydrogen embrittlement susceptibility of low carbon steels.

This phenomenon is thought to be a consequence of the more homogeneous distribution of hydrogen in the cold-worked superficial layer and the beneficial role of compressive stress on the crack initiation.[178] In other cases the results are less clear and it appears that residual stresses induced by cold drawing processes applied on the surface of pre-stressed concrete steel wires have little effect on hydrogen embrittlement susceptibility.[179]

In views of this differing behaviour it was proposed that the effect of residual stress on the hydrogen embrittlement behaviour of 300M steel should be assessed. It is known that residual stresses produced in engineering components during fabrication and heat treatment may affect

their subsequent behaviour. Regarding 300M high strength steel, it was found that the shot peening treatment slightly affected the hydrogen transport characteristics of the alloy. A comparison of the hydrogen permeation transient obtained for the steel membrane before and after the shot peening treatment is graphically depicted in **Figure 151**.

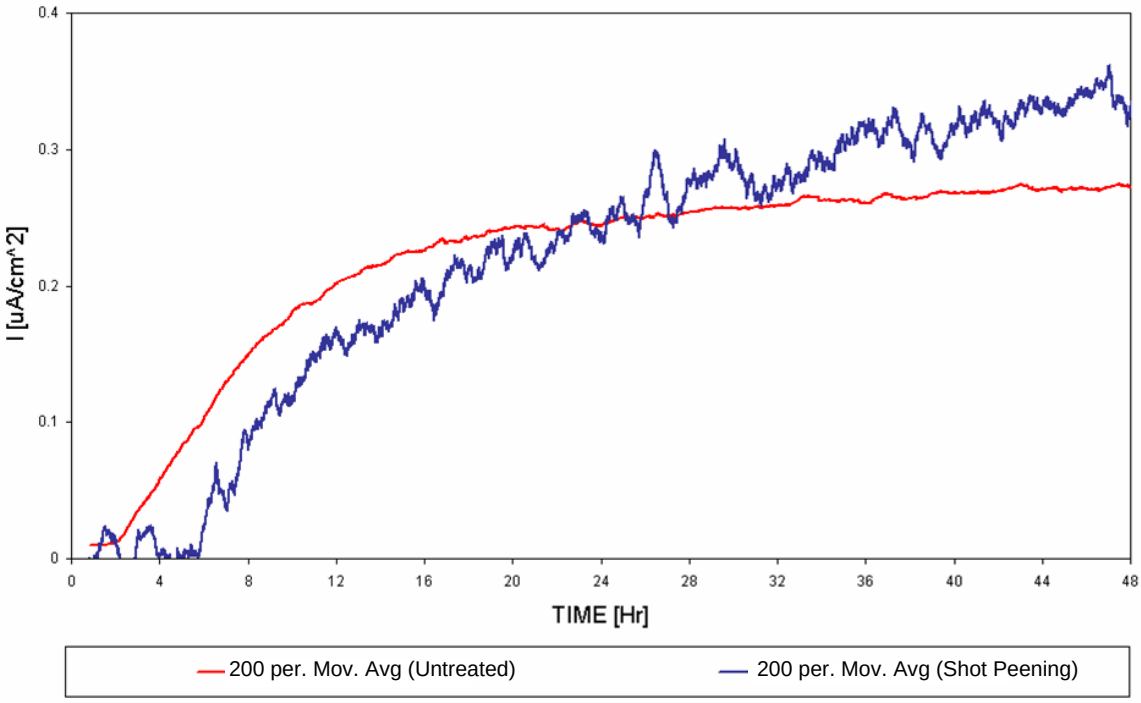

Figure 151. Hydrogen permeation transients for the 300M steel membrane before and after the shot peening.

First, it can be noticed that the mean breakthrough time increased from 1.90 hours, for the untreated membrane to 4.33 hours for the shot peened condition. It is thought that compressive residual stresses produced on the surface of the 300M steel membrane increase the dislocation density and therefore introduced more reversible hydrogen traps within the material. Consequently, more time was needed to fill these new traps, delaying the breakthrough time in the permeation transients.

This finding was in good agreement with those previously reported by other researchers. Toribio *et al*[176, 177] noted that diffusion-based numerical models developed to predict the life of cylindrical metallic

structural elements suffering from hydrogen embrittlement in the presence of residual stresses, showed that tensile residual stresses enhance hydrogen permeation and hence tend to decrease the life of the structural elements, whereas compressive residual stresses delayed hydrogen ingress, and therefore extend the life of the material. Similarly, M. Elices *et al*.[180] has shown an improvement in the hydrogen embrittlement performance when high compressive stresses were produced in high strength steels with *UTS* up to 1700MPa.

The mean hydrogen diffusion coefficient for the untreated and shot peened 300M steel membrane slightly decreased from 7.31×10^{-8} to 3.60×10^{-8} $cm^2 s^{-1}$, respectively. However, there was a noticeable difference between the values obtained from the t_b and t_{Lag} methods. This finding was due to the transient continuing to show a steady rise instead of reaching a steady state value, which made it more difficult to assess t_{Lag}. The t_b method is thought to be more reliable.

The validity of this finding was corroborated after performing the hydrogen permeation transients three times for each condition. Statistical analyses using student *t*-tests revealed with a 95% level of confidence that the two conditions tested belong to different statistical populations. The practical implications of these experimental results might suggest that hydrogen would required a longer time to penetrate the shot peened 300M steel component than that for the untreated steel. However, regardless of the surface condition it may be that a sufficient concentration to cause embrittlement will eventually be reached.

The second observation that can be made from **Figure 151** is that the steady-state hydrogen permeation current, I_∞, significantly increased after the shot peening treatment. In this particular example, it was found that the mean I_∞ value increased from 0.26 to 0.31 $\mu A.cm^2$. It has been considered that this difference might occur due to an increase in the hydrogen charging area of the steel membrane after the shot peening treatment. Nevertheless, a possible reduction in the hydrogen evolution

(as bubbles) due to an improvement in the surface roughness of the membrane might be considered.

By substituting I_∞ values and the corresponding hydrogen diffusion coefficients in equation [XXXXII], it is possible to estimate the hydrogen solubility of the 300M steel membrane in terms of the hydrogen concentration. It was found that the internal hydrogen concentration, C_o, just below the membrane surface increased after the shot peening treatment. The mean C_o values for the untreated and the shot peened 300M membrane were 3.81×10^{-6} and 9.14×10^{-6} mol.cm^{-3}, respectively. In addition, the corresponding student *t*-test analysis revealed with a 95% of confidence that this difference was significantly high and the two groups did not belong to the same statistical population.

Considering that an increase in dislocation density produces more reversible hydrogen traps within the alloy, it is expected to find such increases in the hydrogen solubility after the surface treatment. Similarly, it has been suggested elsewhere that increases in hydrogen solubility in cold worked specimens, usually also observed in hydrogen embrittlement studies, can be understood in terms of a density dislocations increased by the cold work.[181] However, in contrast with the results obtained for the 300M steel membrane, the same authors reported that the hydrogen diffusion coefficient of low alloy carbon membranes remained unaffected by the shot peening. Instead, they noted a drop in the steady state hydrogen permeation current after shot peening treatment. [181]

In contrast to these results for 300M, E. U. Lee *et al*.[175] showed that shot peening does not affect the susceptibility of AerMet®100 steel to stress corrosion cracking in *SSRT* tests. Two possible reasons are thought to explain this situation: 1) The high density of reversible and irreversible hydrogen traps present in AerMet®100 steels[100, 146] might hide the effect of any change induced by plastic deformation produced by shot peening treatments, or indeed 2) from a practical point of view, the reported reduction in hydrogen diffusivity and increase in hydrogen solubility might

only represent a limited beneficial role on the hydrogen embrittlement susceptibility of 300M steels.

All the foregoing discussion considers the time delay in hydrogen uptake that results from introducing compressive stresses into the surface. There is a second and perhaps more important effect in terms of the local stress acting at microstructural flaws in the material at which cracks will nucleate when sufficient hydrogen concentration is reached. The introduction of compressive residual stresses will lower the tensile component of stress at these flaws such that a crack may no longer develop. This argument is similar to that for the beneficial effect of compressive residual stresses in controlling fatigue.

13.8. Effect of Elastic Stresses on Hydrogen Diffusion

The effect of elastic stress on the low alloy 300M and GifloM2000 as well as the CSS-42L^{TM} martensitic stainless steel was evaluated using tensile specimens with rectangular cross sections. Results showed that the application of elastic stresses at 0%, 25% and 50% of the yield strength with simultaneous galvanostatic hydrogen charging did not affect the hydrogen diffusion coefficients of the three alloys. These results were corroborated using student *t*-test statistical analyses and further details are discussed below.

13.8.1. 300M Steel

It was found that the mean hydrogen diffusion coefficient of 300M steel specimens at 0%*YS* was lower than that reported from the previous hydrogen permeation measurements for 300M membranes. Those values were $3.76\pm1.53\text{x}10^{-8}$ and $1.02\pm0.04\text{x}10^{-7}$ cm^2s^{-1}, for the tensile specimens and the 300M membrane, respectively. 300M tensile specimens used to assess the effect of elastic stresses on hydrogen diffusivity were taken from a second batch of material. Therefore, it is feasible to attribute this difference in hydrogen transport characteristic to slight variations in the

heat treatments applied to the first and second batch of material, which might display small differences in the mechanical properties.

To prove this speculation, comparisons of the mechanical properties were performed in terms of *UTS* and *YS* values. Indeed, it was found that despite receiving the same heat treatment, the ductility of the second batch was slightly superior to that for the first batch. The ultimate tensile strengths were 1938 and 2250MPa for the first and second batch, respectively. In the same order, their yield strengths were found to be 2000 and 1700 MPa, as is shown in **Figure 152**. In this graph the stress-strain plots of the most representative specimens for each batch are displayed.

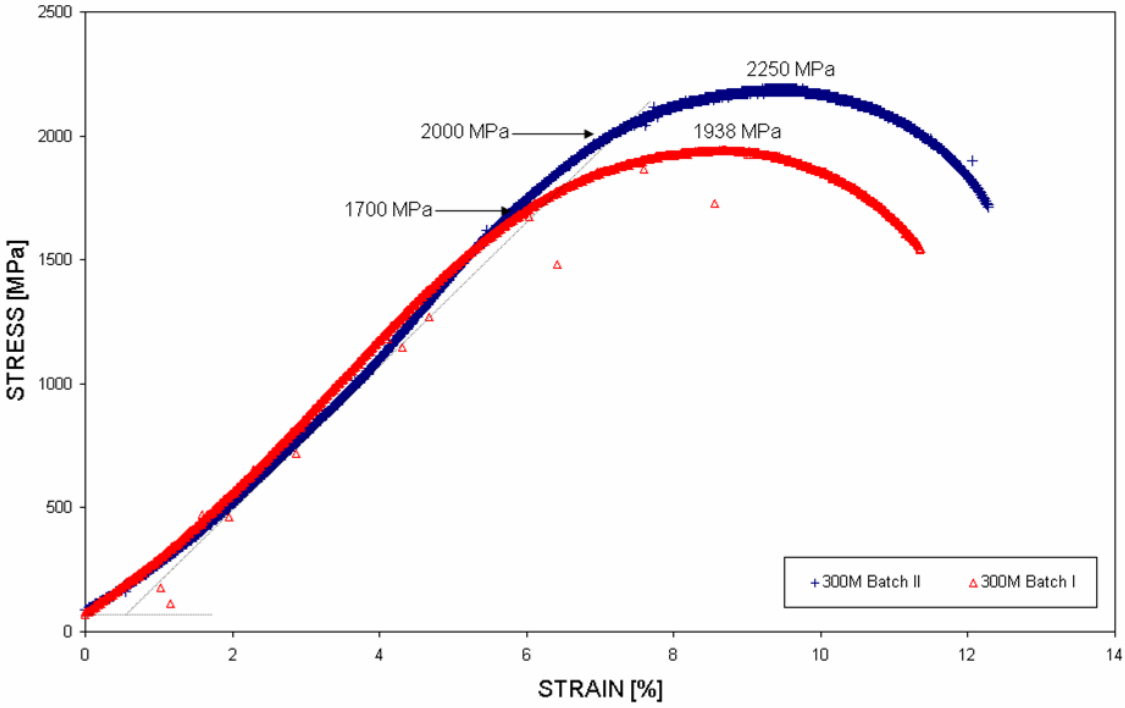

Figure 152. Comparison of mechanical properties of the first and second batch of 300M specimens.

By comparing the mean hydrogen diffusivity of 300M specimens at the three stress levels taken into consideration, there was no noticeable change on the hydrogen transport characteristics. Moreover, there was some variability in the results, particularly in the group tested at zero stress level, which is thought to be associated with the high sensitivity of the galvanostatic charging method in response to the hydrogen diffusivities of the four different tensile specimens used during the test.

Furthermore, it has been considered that slight temperature fluctuations during the hydrogen charging periods may have contributed to those results as tests were performed outside the temperature control room used for permeation experiments.

However, results from the three groups are in agreement with previous work on different iron-based alloys, including AISI-4340 high strength steels, where no changes in hydrogen diffusion coefficients upon the application of stress were recorded.[160, 181-185] Bockris *et al*,[181] studied Armco iron and AISI-4340 high strength steel in the elastic range. He found that permeation of hydrogen increases by tensile stress and decreases by compressive stress with the diffusion coefficient being unaffected by the applied stress.

It has been found that applied stress increases the hydrogen permeation rates but does not influence the magnitude of the diffusion coefficient.[160, 181-185] Moreover, the reversibility effect of stresses on the permeability of AISI-4340 steels membranes has been described in **Figure 153**.

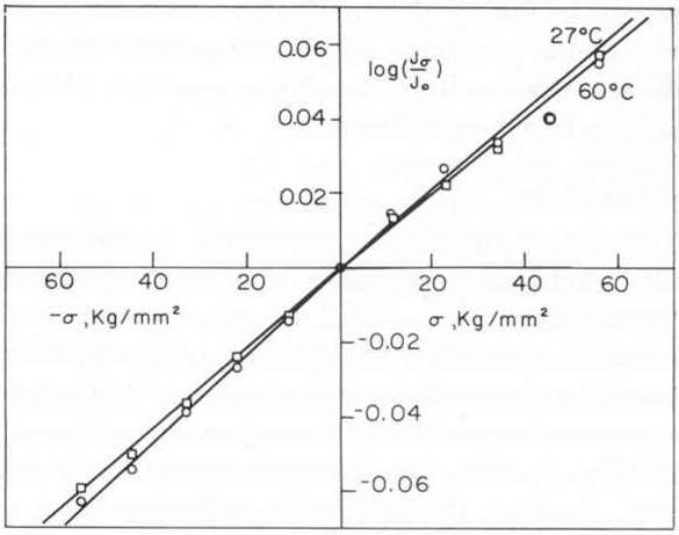

Figure 153. Hydrogen permeability-stress relationship for AISI-4340 steels at different temperatures.[181]

It can be seen in the previous figure that by applying compressive stresses the permeation current linearly decreased. By increasing

permeations rates, J_∞, and keeping constant the hydrogen diffusion coefficients, D, the hydrogen concentration in the steel surface (i.e. solubility), C_o, should increased with the applied stress, as previously shown by the equation [XLII]. Hence, it is expected that stress affects parameters directly related to hydrogen solubility such as hydrogen concentrations, C_o, and hence increases its chemical potential.[181] The concentration of solute hydrogen at constant chemical potential is related to the stress by:

$$\frac{V_H}{3RT} = \frac{\partial Ln\left(C_\sigma / C_o\right)}{\partial_\sigma} \qquad [\text{XLVII}]$$

Where C_σ and C_o is the concentration of hydrogen with and without stress, V_H is the partial molar volume of hydrogen in the metal, R the gas constant, 8.311 Joul.cm/mol, T the temperature in Kelvin and σ is the tensile stress. The partial molar volume of AISI-4340 steel had been established at approximately $2.6x10^{-6}$ m^3/mol.[181]

However, such small concentration changes upon the application of tensile stresses, (i.e. C_σ / C_o = 1.047 for α-iron under $\Delta\sigma$=+12 $Kgmm^{-1}$), were not possible to detect using the galvanostatic hydrogen charging method used. However, as hydrogen embrittlement of steels takes place when the hydrogen concentrations reaches a critical value at the most significant microstructural flaw, any small increase in the hydrogen content might have an important effect.

13.8.2. GifloM2000 Steel

The mean hydrogen diffusion coefficient of the low alloyed GifloM2000 high strength steel was found to be $4.40\pm0.37x10^{-8}$ cm^2s^{-1}. This value is similar to that for 300M steel, suggesting that the hydrogen transport characteristics of GifloM2000 are equivalent to that for the second batch of 300M steel. Nevertheless, unexpected failure occurred when GifloM2000 steel specimens were galvanostatically charged with hydrogen under 50% of the yield strength. These specimens showed one transverse

crack propagated at the point where the specimen failed. Failure points were repeatedly found to occur at the end of the gauge length; hence it is thought that the presence of residual stresses at this region might contribute to the sudden failure of the specimens. Nevertheless, further analyses have to be done in order to corroborate this assumption.

Additional microstructural examination carried out on GifloM2000 revealed the presence of relatively large metallic inclusions randomly distributed within the martensitic matrix, probably due to segregation, as is shown in **Figure 154(A)**. What is more, a large population of microvoids was also found in the microstructure. **Figure 154(B)** shows an angular metallic inclusion with length of approximately 5 μm and compositions rich in Ti, Nb and Zr.

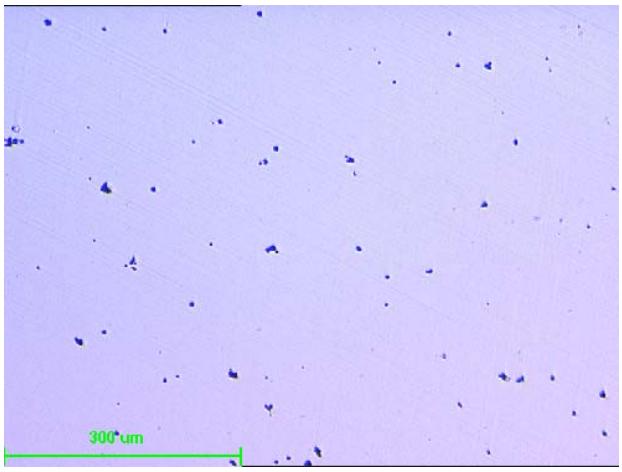

(A)

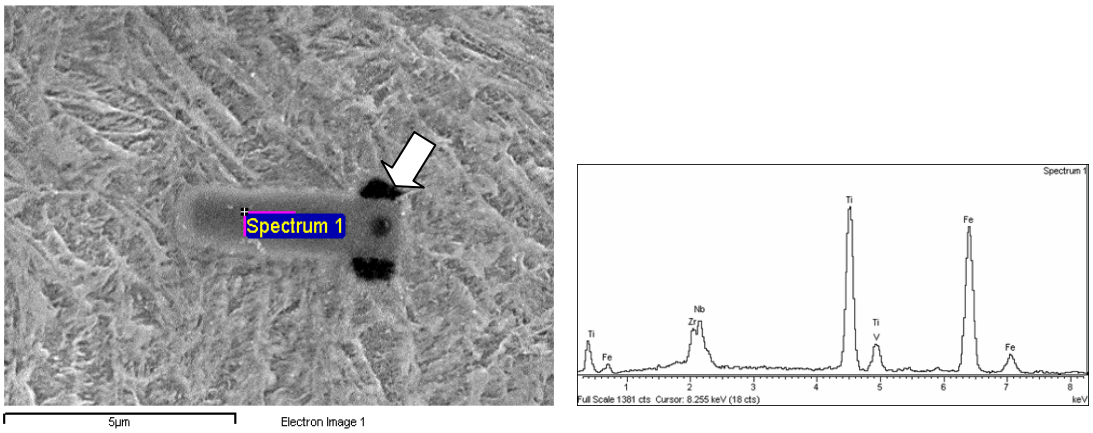

(B)

Figure 154. A) Micrograph showing large population of inclusions, and B) *SEM* micrographs showing a Ti-Nb-Zr-rich metallic inclusion found in the martensitic matrix of GifloM2000 steel. Arrow indicates microvoids at the inclusion interface.

The nominal composition of GifloM2000 alloy does not show significant content of these elements but further analyses might corroborate their presence. It has been estimated that the presence of microvoids and relatively large inclusions might promotes the hydrogen embrittlement of these steels producing a delayed fracture problem. This suggestion has been previously proposed and demonstrated for AISI-4340 high strength steels, where microvoids formed at interfaces of MnS inclusions were directly related to hydrogen embrittlement of this steel.[104]

Further fractographic analyses on *SSRT* GifloM2000 specimens revealed a high population of relatively large voids nucleated at regions where metallic inclusions were located in the fracture surface, as is shown in **Figure 155**. The elemental analysis of some of the inclusions also shows Ti and Al-Zr-Ca-rich compositions, **Figures 156** and **157**. Moreover, by comparing these findings with the conventional 300M high strength steel, it was considered that the latter has a much cleaner microstructure than GifloM2000.

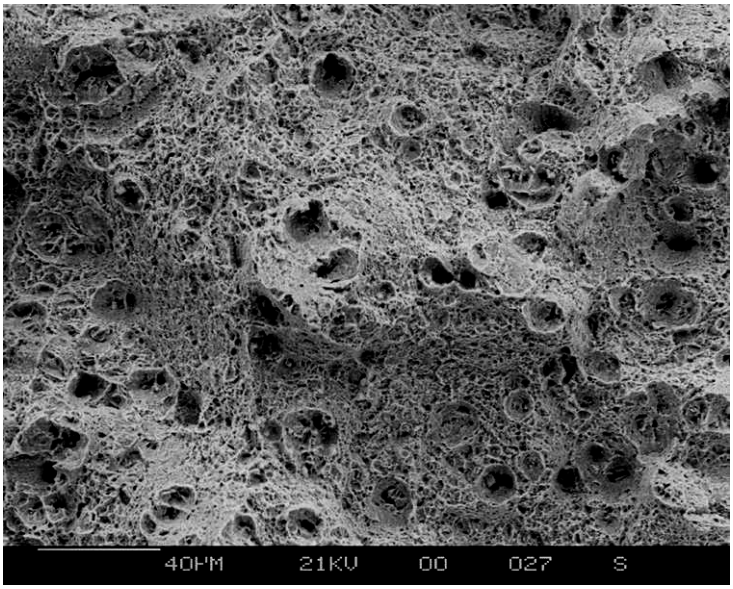

Figure 155. *SEM* micrographs showing a high population of relatively large voids nucleated at regions where metallic inclusions were present.

Therefore, there is a concern about the increased risk of hydrogen induced failure at such large microstructural flaws presented in the alternative GifloM2000 steel. This assumption has been supported by the *SSRT* tests in which the alternative GifloM2000 steel displayed slightly higher hydrogen re-embrittlement susceptibilities than the conventional 300M steel under equivalent hydrogen charging conditions.

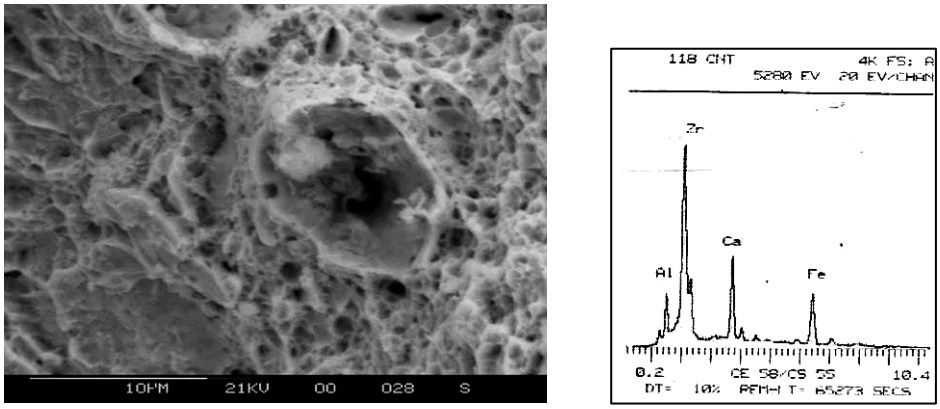

Figure 156. *SEM* micrographs showing a Al-Zr-Ca-rich inclusion within the fracture surface of *SSRT* GifloM2000 specimens.

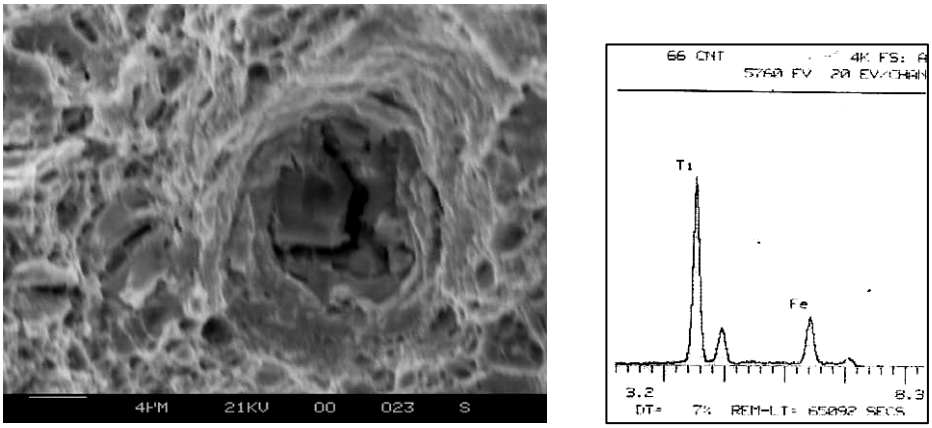

Figure 157. *SEM* micrographs showing a Ti-rich inclusion with angular shape within the fracture surface of *SSRT* GifloM2000 specimens.

13.8.3. CSS-42L™ Stainless Steel

Finally, the effect of elastic stresses on the hydrogen diffusivity of CSS-42L™ martensitic stainless steels was studied. First, the mean hydrogen diffusivity for CSS-42L™ at 0%YS was $2.95\pm1.8\times10^{-7}$ cm^2s^{-1}. This value is higher than those for 300M, GifloM2000 and AerMet®100 steels, therefore it is feasible to suggest that hydrogen diffuses and migrates to regions of stress triaxiality faster than in the rest of the high strength steels. The susceptibility to hydrogen induced failure of the CSS-42L™ martensitic stainless steel is likely to be slightly higher than the *low alloy* high strength steels. Nevertheless, results from the *SSRT* corresponding to the SermeTel®1140/962 coated and corroded 300M and CSS-42L™ steels showed that the susceptibility of both steels to hydrogen re-embrittlement were equivalent.

M. D. Danford,[184, 185] studied the uptake and desorption of hydrogen by A-286 and 303 stainless steels in the elastic range, using a potentiostatic charging technique. He found that the apparent hydrogen concentration, C_o, the mean hydrogen concentration, C, as well as the hydrogen distribution uniformity all increased up to a stress level of 50% of the yield strength and decreased for higher stress levels. Hydrogen diffusion coefficients were relatively unaffected by stress while the percent of trapped hydrogen appeared to decrease with increasing stress for A-286 steels. Whereas, a high percentage of hydrogen trapped was found in the 303 stainless steel probably due to numerous sulphur-rich phases.

On the other hand, during the application of stress levels 25% of the yield strength and simultaneous hydrogen galvanostatic charging, several transverse cracks were found along the gauge length of the tensile specimens. These cracks seemed to preferentially follow an intergranular crack path along prior austenite grain boundaries, as is shown in **Figure 158**.

Transverse cracks might be induced by the simultaneous effect of longitudinal residual stress and diffusible hydrogen.[186] This cracking phenomenon reinforces the finding that CSS-42L™ stainless steel specimens are particularly susceptible to delayed fracture due to hydrogen embrittlement, as was previously shown during the *SSRT* for SermeTel®1140/962 coated and corroded CSS-42L™ specimens in 3.5% NaCl solutions.

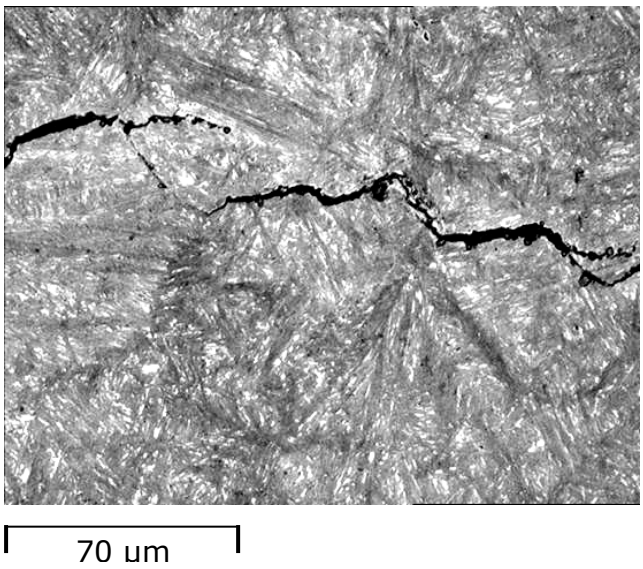

Figure 158. Intergranular cracking paths following prior austenite grain boundaries found on CSS-42L™ stainless steels after two consecutive hydrogen charging periods of 8 hours with no stress applied.

In addition to the high diffusion rate, the hydrogen solubility of CSS-42L™ stainless steel is expected to be higher than that for the 300M and GifloM2000 low alloy steels due to higher concentrations of Cr and Ni. It has been accepted that hydrogen solubility of steels increases with addition of those alloying elements suspected to act as atomic hydrogen traps such as Nb, Mn, Ti, Cr, V and Ni. The effect of some of these elements on the hydrogen solubility of iron is shown in **Figure 159**.[187]

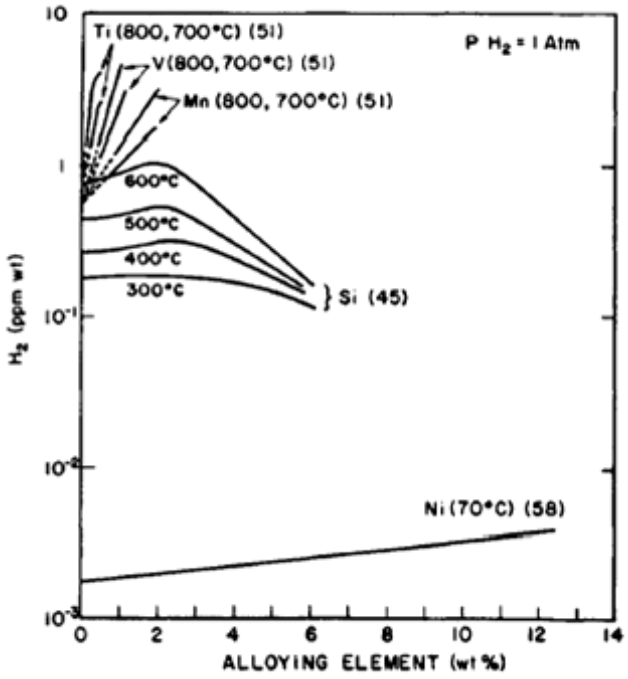

Figure 159. Solubility of hydrogen in solid iron for different temperatures and different alloy content.[187]

14. Sacrificial Coatings

Barrier properties of the electroplated cadmium, Zinc-14%Nickel and aluminium based SermeTel®1140/962 sacrificial coatings are discussed individually in this section and a comparison between them is finally presented.

14.1. Cadmium Coating

During the potassium permanganate, *$KMnO_4$*, porosity test the manganese ions, *Mn^{2+}*, formed a dark brown or black manganese oxide, *MnO*, where the steel substrate was exposed. This deposition took place following reaction [11]:

$$MnO_4^- + (5/2)\ Fe_{(s)} + 8\ H^+ \rightarrow \mathbf{Mn^{2+}_{(s)}}\downarrow + (5/2)\ Fe^{2+}_{(aq)} + 4H_2O_{(l)} \qquad [11]$$

Alternatively, during the cooper sulphate or *Preece* test the exposed regions of the steel substrate where revealed by the deposition of bright copper deposits resulting from reaction [12]:

$$Fe_{(s)} + Cu^{2+}{}_{(aq)} \rightarrow Fe^{2+}{}_{(aq)} + \mathbf{Cu_{(s)}}\downarrow \qquad [12]$$

However, during this last test a secondary redox reaction occurred between the cadmium and copper ions, Cu^{2+}, producing a progressive partial dissolution of the coating. Therefore, the results displayed after longer periods of immersion, i.e. 8 minutes, represented an advanced stage in the corrosion of the cadmium sacrificial coating.

$$Cd_{(s)} + Cu^{2+}{}_{(aq)} \rightarrow Cd^{2+}{}_{(aq)} + \mathbf{Cu_{(s)}}\downarrow \qquad [13]$$

From both porosity tests it was revealed that the steel substrate was freely expose to the reagent solutions preferentially in some of the crater like irregularities or *through-thickness* pores in the cadmium coating.

These irregularities represented potential regions for the development of localised galvanic cells between the sacrificial cadmium coating and the steel substrate, which eventually led to hydrogen uptake by the steel due to partial dissolution of the coating.

Nevertheless, a wide variety of discontinuities are thought to exist on an electroplated sacrificial coating, some of which are graphically depicted in **Figure 160**. These defects represents sites at which hydrogen re-embrittlement of the steel substrate might take place.[188, 189]

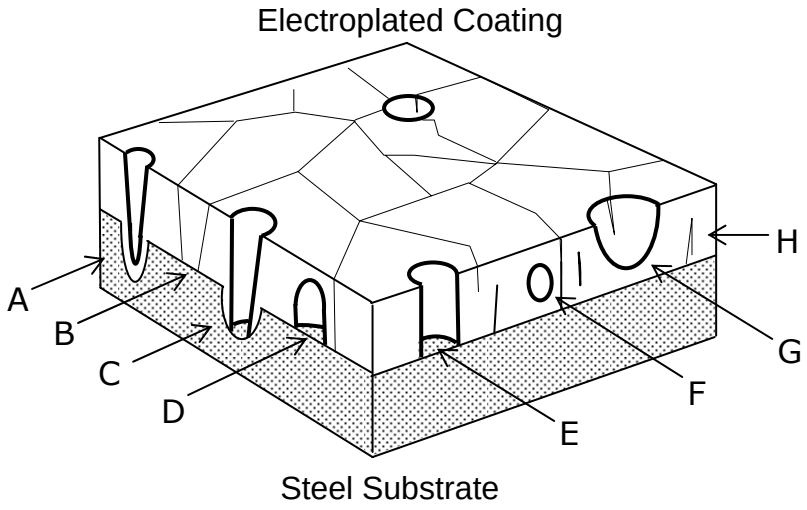

Figure 160. 3-D Representation of different types of pores and cracks: A) notched substrate pore, B) through-thickness cracks, C) open U-notched substrate pore, D) masked or bridged pores, E) through-thickness pore, F) enclosed pore, G) dead end pore, H) closed cracks.[188, 189]

During the initial stages of exposure to any corrosive environment it is thought that open discontinuities such as *through-thickness* cracks, *through-thickness* pores and open *U-notched* pores represent the regions where hydrogen re-embrittlement occurred. Thereafter, following a progressive dissolution of the coating the rest of the discontinuities might also expose the steel substrate to the electrolyte.

Surface roughness of the substrate has a noticeable influence on the porosity of the final coating.[128, 188] Small irregularities on the substrate surface appear to act as hydrogen bubble nucleation sites, which later

formed small pores or '*holidays*' in the coating.[12] Surface roughness could be a result of acid pickling, abrasive cleaning processes or even surface treatments to improve fatigue resistance like shot peening.[188]

In addition, further metallographic examination on the cross section of the cadmium coating, showed in **Figure 41**, revealed good barrier properties with the presence of *closed* pores. Although there were some large discontinuities that might have exposed the steel substrate after some corrosion had occurred. Moreover, following 1200 hours immersion in quiescent 3.5% NaCl solutions, crater like discontinuities started to be noticeable on the surface layer as is shown in **Figure 161**.

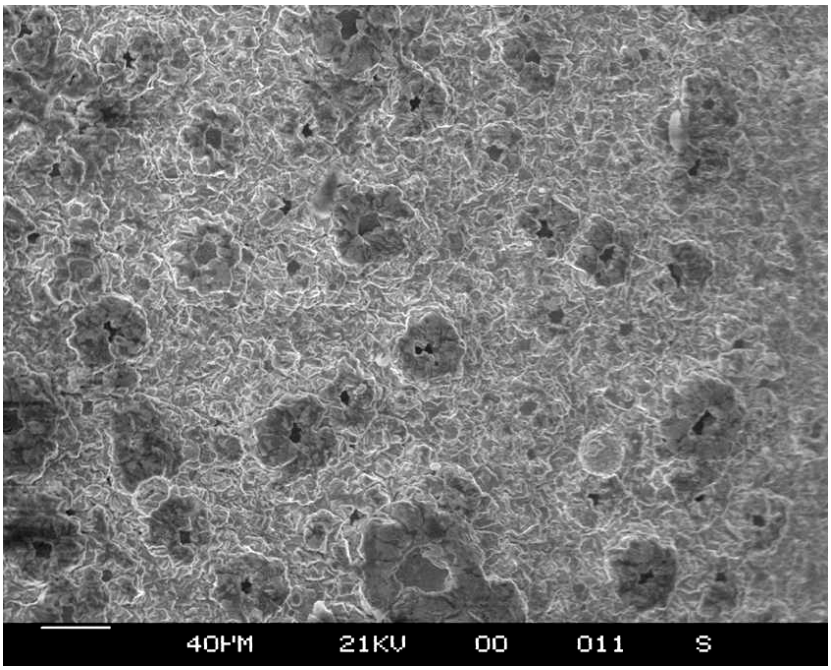

Figure 161. Crater like discontinuities in a cadmium coated specimen after 1200 hours immersion in quiescent 3.5% NaCl solutions.

In addition, the presence of white corrosion products spread all over the surface after the immersion period is thought to be related to the formation of relatively adherent cadmium hydroxide or hydride products with small particle volume, such as $Cd(OH)_2$ or CdH respectively. The stability of these chemical species was evidenced in the *Pourbaix* diagram for cadmium in aqueous solutions depicted in **Figure 162**.

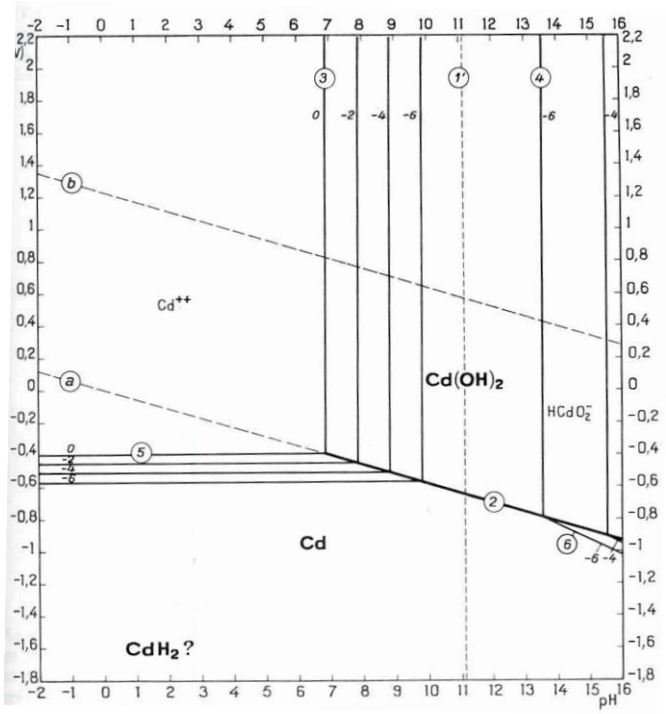

Figure 162. Pourbaix diagram for the cadmium-water system.[46]

Regarding the open circuit potential results, displayed in **Figure 111**, attention is drawn to the excellent sacrificial properties of the cadmium coating which displayed a constant sacrificial behaviour after long immersion periods.

14.2. Zinc-14%Nickel Coating

Results from the potassium permanganate, $KMnO_4$, and copper sulphate, $CuSO_4$, porosity tests displayed in **Figures 102** to **105**, have revealed that the steel substrate was exposed in some of the *through-thickness* pores found in the sacrificial Zinc-14%Nickel coating.

The observation that most of the manganese oxide black spots were found on the bottom of these *crater-like* indentations implied that only *passer-by* or *open U-notched* pores were revealed using the potassium permanganate test. Whereas, solid copper deposits precipitated from

reaction [14] during the *Preece* test, were not completed adhered and therefore were easily removed from the surface after each immersion. Therefore, not only *through-thickness* pores were revealed in the Preece test as the coating dissolution also occurred following this reaction.

$$Zn_{(s)} + Cu^{2+}{}_{(aq)} \rightarrow Zn^{2+}{}_{(aq)} + \mathbf{Cu_{(s)}} \downarrow \qquad [14]$$

The cross-section of the electroplated Zinc-14%Nickel coating also revealed that *open* pores in the coating, possibly due to *holidays* formation, exposed the steel substrate to corrosion environments. Formation of *holidays* can be suppressed by reducing surface roughness prior to the electroplating process. Moreover, during electroplating additions of wetting agents or surfactants such as sodium laural sulphate minimise the build up of hydrogen bubbles on the substrate surface that could lead to the formation of *holidays* in the electrodeposit.[128]

In addition, an extensive crack network appears to be the characteristic feature of the partial dissolution of this coating, after 1200 hours immersion in 3.5% NaCl solutions (**Figure 163**). Again, in some of these *through-thickness* cracks the steel substrate was directly exposed to the corrosive environment causing hydrogen re-embrittlement. This corrosion behaviour of the Zinc-14%Nickel coating was corroborate by the results shown in **Figure 106**, from the electrographic test and has been reported by other researches.[60, 62, 64, 190, 191]

The open circuit potential measurements for the sacrificial Zinc-14%nickel coating in a quiescent 3.5% NaCl solution, shown in **Figure 112**, revealed an ennoblement effect of this coating where the corrosion potential became more noble with time. This ennoblement process has been related to the slow and preferential dissolution of zinc from the coating surface as corrosion proceeds.[12, 15] This selective dissolution would result in an increase in nickel surface concentration and therefore a more noble potential is displayed.

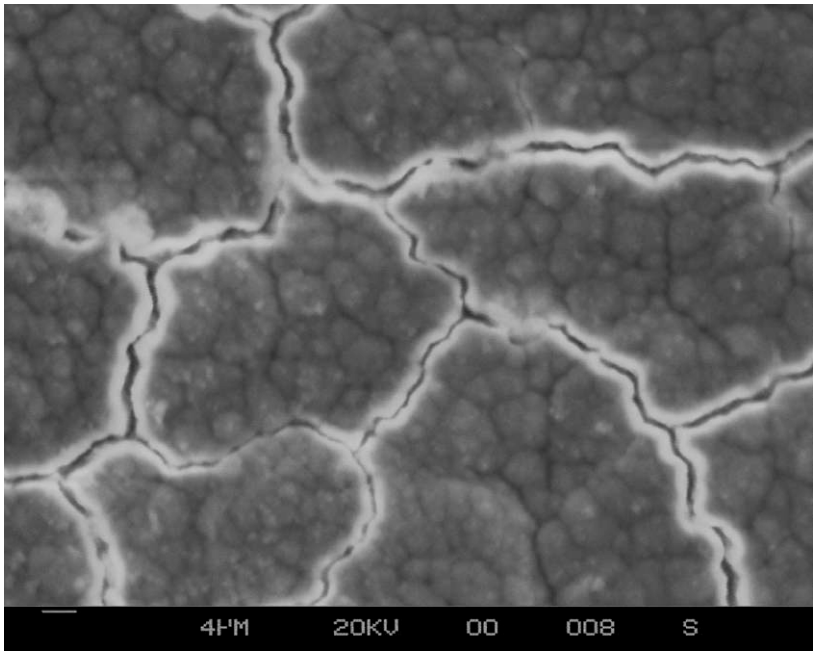

Figure 163. Crack network in a Zinc-14%Nickel coated specimen after 1200 hours immersion in quiescent 3.5% NaCl solutions.

Figure 164 shows the variations of open-circuit potential with immersion time for different zinc-nickel alloy compositions.[12, 15] In this Figure, the trends displayed for unpassivated Zn-14%Ni could be compared to the performance of the Zn-14%Ni coating studied in this project. It was clear that the ennoblement occurred more slowly on the passivated coating.

Furthermore, the initial abrupt change of potential to a more noble value in a relatively short period of time suffered by the Zinc-Nickel coating is attributed to more rapid corrosion of the coating following the breakdown of the chromium oxide passivation layer previously deposited on the coating. This phenomenon has been confirmed by the dissolution of the Cr_2O_3 colour fringes pattern characteristic from the passivation layer after 150 hours immersion.

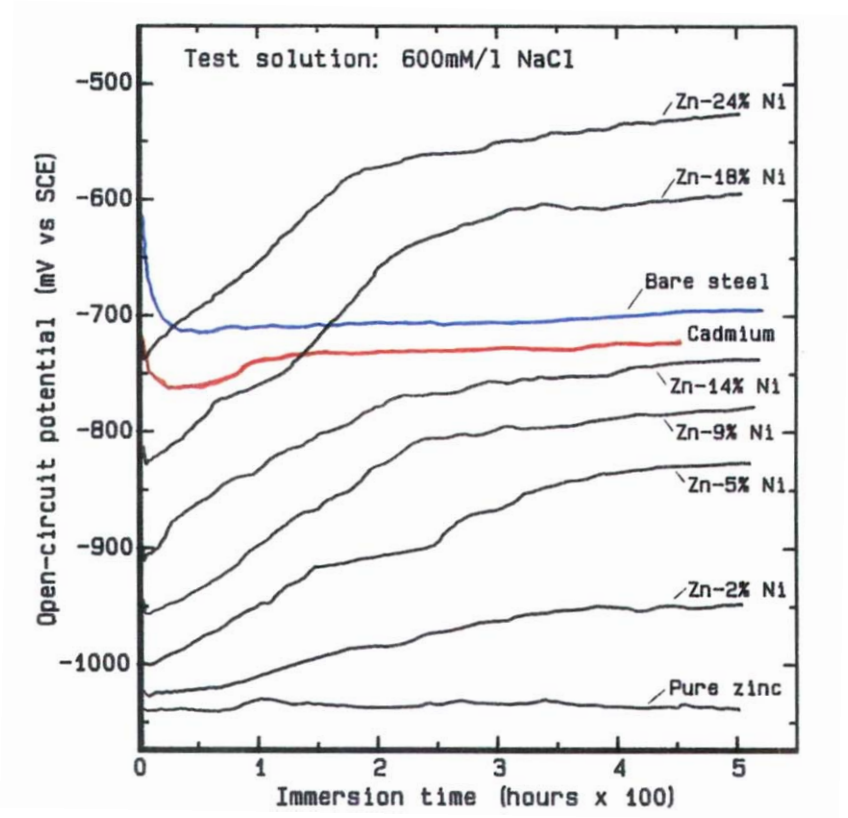

Figure 164. Variations of open-circuit potentials with time for bare steel, unpassivated electrodeposited detached zinc-nickel alloys and cadmium coatings on steel in quiescent 600mM/l NaCl solution.[12, 15]

14.3. SermeTel®1140/962 Coating

The presence of a fluorocarbon modified topcoat layer over the sacrificial aluminium coating provides a very effective physical barrier to the potassium permanganate solution and therefore any other corrosive environment. This topcoat layer seals the porosity network within the binder and the aluminium particles.[68, 69]

However, once the topcoat degrades it is feasible for an electrolyte to penetrate and reach the steel substrate due to the porous nature of the coating itself. The breakdown of the polymer topcoat, after 1200 hours immersion in quiescent 3.5%NaCl solutions, can be appreciated in **Figure 165**. In addition, **Figures 110** previously showed the presence of a high

population of *closed* and *bridged* pores in the cross section of the SermeTel®1140/962 coating, forming a randomly distributed network.

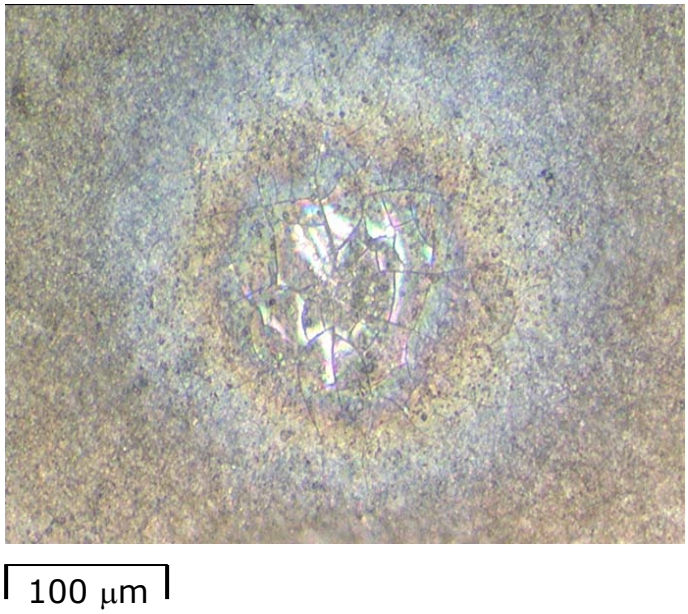

Figure 165. Polymer topcoat breakdown in the SermeTel®1140/962 coated specimen after 1200 hours immersion in quiescent 3.5% NaCl solutions.

The open circuit potential of SermeTel®1140/962, after 1200 hours immersion in quiescent 3.5% NaCl solutions, became close to the free corrosion potential of the bare steel of approximately -640 mV(SCE). This finding posed some concerns about the sacrificial behaviour of this coating under direct exposure to corrosive environments for long periods of time.

14.4. Comparison of the Sacrificial Coatings

Barrier properties of the coating materials depend directly on their physical characteristics such as porosity and surface morphology. By comparing the three sacrificial coatings, it has been possible to assign the best barrier properties to the SermeTel®1140/962 aluminium based coating mainly due to the addition of a polymeric topcoat system.

The electroplated cadmium coating is constituted by relatively small grains randomly distributed, forming an irregular coating surface. This morphology can be considered favourable to hydrogen uptake by the steel substrate during re-embrittlement. However, it is known that some degree of porosity is needed to allow hydrogen to diffuse out from the steel during the baking process following the electro-deposition.

Regarding the electroplated Zinc-14%Nickel coating, a highly uniform and compact grain structure has been shown, this observation suggests a coating with better barrier properties than the electrodeposited cadmium. Nevertheless, for both coatings, grain boundaries, micro-cracks and porosity are features that might lead to re-embrittlement. Specifically, *through-thickness* pores for the cadmium and *through-thickness* cracks for the Zinc-14%Nickel coating. Whereas, the SermeTel®1140/962 coating has uniform barrier properties with no superficial discontinuities. However, some degree of internal porosity was evident.

It has been demonstrated that the three sacrificial coatings showed in some degree flaws and discontinuities that eventually produce delayed failure problems during service. All these characteristics are conveniently summarized in **Figure 166**, where Focussed Ion Beam, *FIB*, images for cadmium, Zinc-14%Nickel and SermeTel®1140/962 coatings were obtained by milling a crater 10-20 μm in depth on their surfaces.

(A)

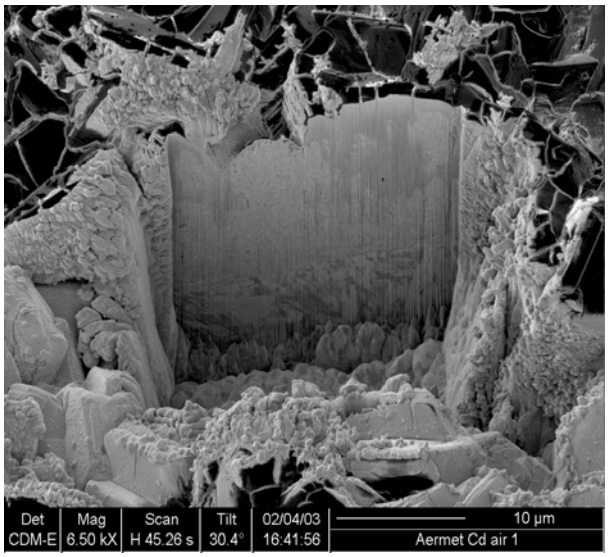

(B)

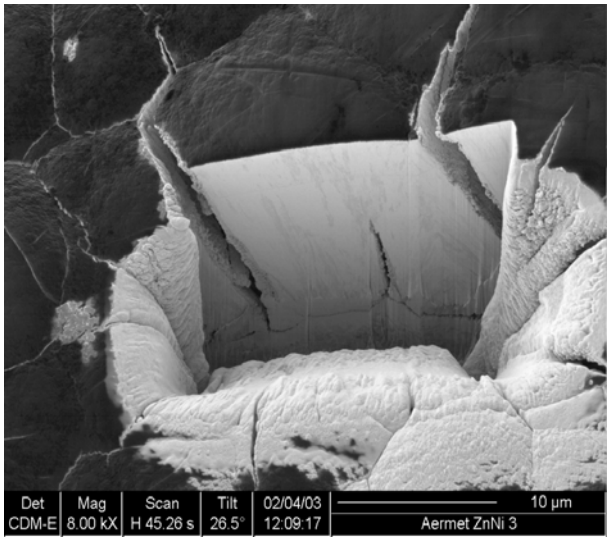

(C)

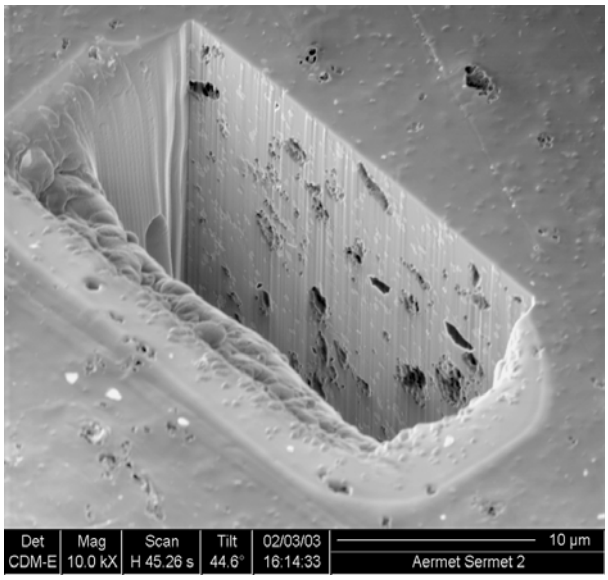

Figure 166. Focussed ion beam images for A) Cadmium, B) Zinc-14%Nickel and C) SermeTel®1140/962 coatings.

15. General Discussion

It has been shown that the direct hydrogen embrittlement produced during manufacturing processes such as electroplating of both cadmium and Zinc-Nickel metallic coatings, was effectively eliminated after a baking process. In relation to this finding, standard manufacturing procedures have been commercially used for decades to eliminate the occluded hydrogen from the steel microstructure. Likewise, the sprayed aluminium based SermeTel®1140/962 did not need to be baked as its deposition process lacked hydrogen uptake by the substrate. Therefore, it was considered that the re-embrittlement phenomena embodied a process with more technological relevance since its deleterious effect takes place during service of the high strength steel structural component.

In terms of re-embrittlement, it was shown that the electroplated Zinc-Nickel produced the most severe deleterious damage of the mechanical properties of the steels. Whereas, SermeTel®1140/962 appeared to be the best coating to replace cadmium from the two alternative materials considered in this project. However, it still produced re-embrittlement of 300M and CSS-42L™ steels, but not in AerMet®100.

During the previous section it was shown that the barrier properties of the sacrificial coatings played an important role on the extent and distribution of re-embrittlement suffered by the steels due to direct exposure of the sacrificial coating to 3.5%NaCl solutions. Also, it was discussed that as the sacrificial coatings were more electronegative, more hydrogen was generated and taken up by the steel substrate. In this particular matter, a convenient comparison is presented between the re-embrittlement levels of the conventional 300M and the alternative AerMet®100 steel, and the open circuit potentials of the three sacrificial coatings taken into consideration. **Figure 167** graphically depicts this comparison.

It is clear that, the more active the cathodic potential of the sacrificial coating the higher the susceptibility of 300M steel to prematurely fail due

to hydrogen re-embrittlement. This trend was not so clear for the AerMet®100 specimens as the mean *EI* value for the cadmium and SermeTel®1140/962 coated, cured and corroded conditions were negative. Nonetheless, again at much more negative potentials, the embrittlement index hopped up to 0.34.

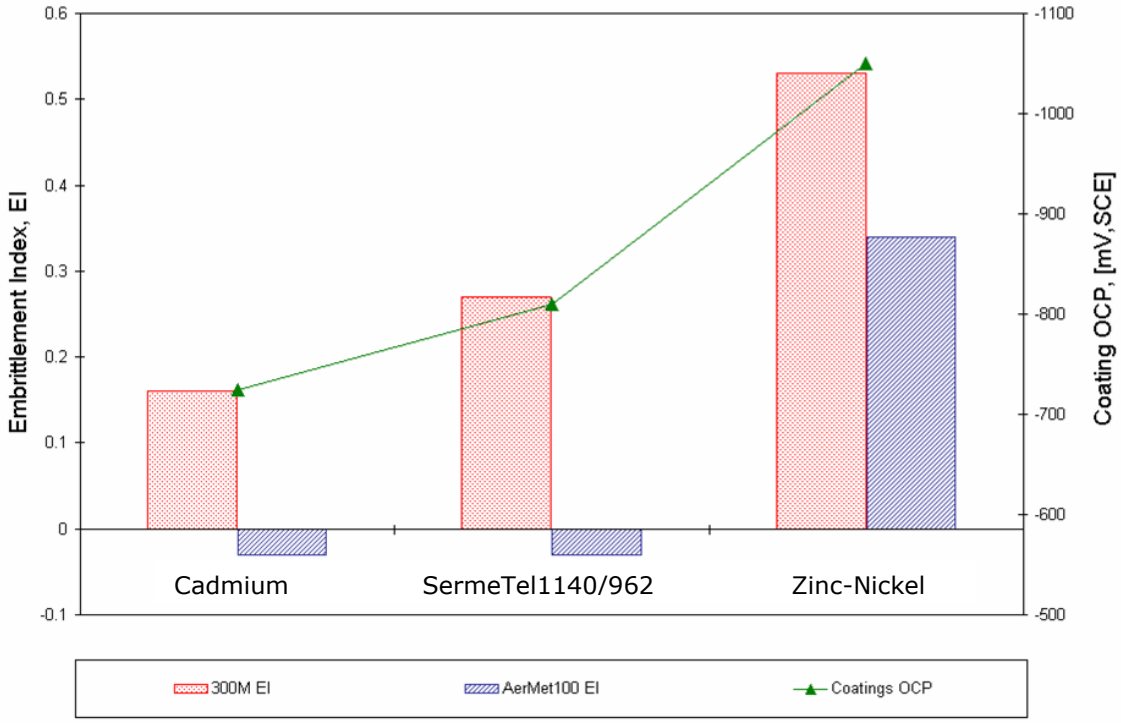

Figure 167. Comparison of hydrogen re-embrittlement susceptibilities of 300M and AerMet®100 steels coated with cadmium, Zinc-Nickel and SermeTel®1140/962, and the open circuit potentials of the sacrificial coatings.

Nevertheless, questions were raised when the new alternative AerMet®100 steel showed such low hydrogen embrittlement susceptibilities in comparison with the conventional 300M and a second alternative material represented by the CSS-42L™ martensitic stainless steel, under exactly the same hydrogen charging conditions. These charging conditions corresponded to the re-embrittlement test performed when the sacrificial SermeTel®1140/962 coating became corroded in 3.5% NaCl solutions.

Therefore a comparison was done between the susceptibilities to hydrogen re-embrittlement of the three alloys and their corresponding hydrogen

transport characteristics obtained from the galvanostatic hydrogen charging technique. **Figure 168** graphically represents this analysis. Allowing for given some scatter between the 300M and CSS-42L™ steels, it is clear that the susceptibility to become embrittled by occluded hydrogen remarkably decreases as the hydrogen diffusion coefficient decreases for AerMet®100.

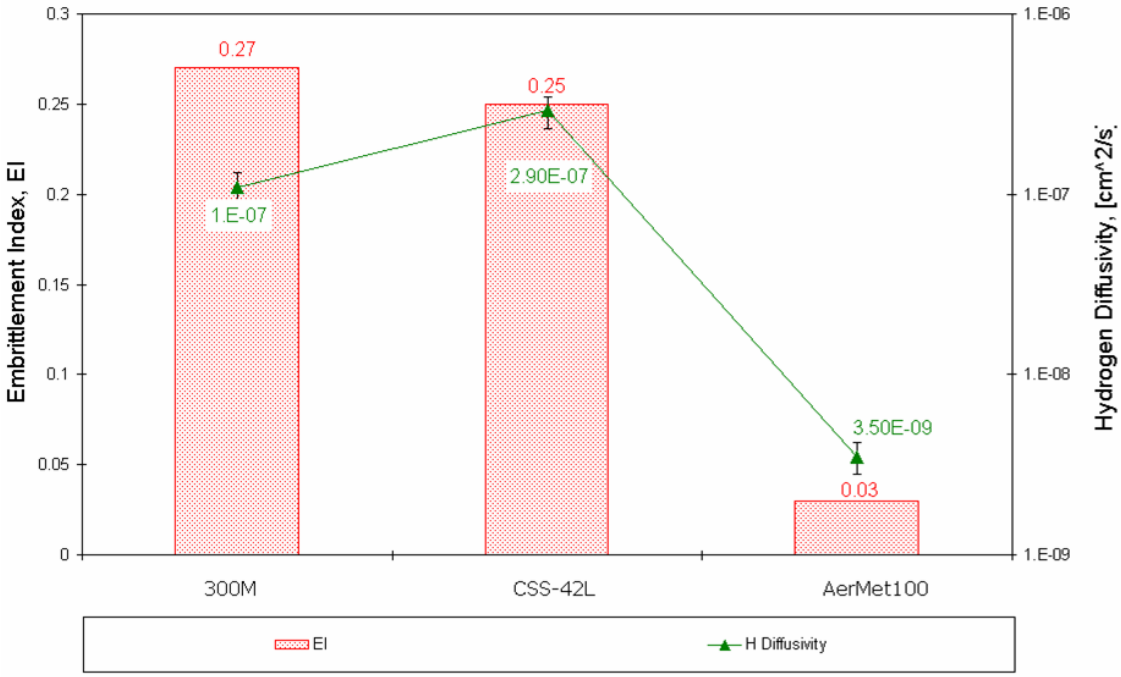

Figure 168. Comparison of hydrogen re-embrittlement susceptibilities of 300M, CSS-42L™ and AerMet®100 high strength steels when SermeTel®1140/962 coating became corroded in 3.5% NaCl solutions, and the hydrogen diffusion coefficients of the alloys.

It was suggested that the hydrogen transport characteristics of the steels played a key factor in determine how fast the hydrogen diffuses to regions of high triaxiality to reach the critical localised hydrogen concentration required to produce loss of ductility in the material. It is thought that the faster the atomic hydrogen moves within the lattice the faster the critical hydrogen concentration should be reached, increasing the tendency to produce hydrogen embrittlement. It had been proposed that the

susceptibility of AerMet®100 to hydrogen induced cracking increases as the diffusible and total hydrogen concentration increases.[100, 146]

It was also demonstrated that the hydrogen lattice concentration (C_o) increases due to increasing cathodic potentials, and presumably also the coverage of trap sites in equilibrium within the lattice increases. It has been suggested that a dynamic equilibrium might exists between the reversibly trapped hydrogen population and the hydrogen within interstitial lattice sites. Subsequently, the interaction between diffusing hydrogen and lower binding energy reversible traps, like those associated with the AerMet®100 microstructure, slows down the diffusion coefficient.[146]

At this point, by using the same electrochemical technique it has been possible to show that the hydrogen diffusivity of the high strength steels evaluated in this project are ranked in the order: CSS-42L™> 300M ≥ GifloM2000 >> AerMet®100 with the lowest coefficient. It was show that in this technique the higher the hydrogen diffusivity the less noticeable became the initial parabolic segment of the potential, *E*, vs. time respond. **Figure 169** graphically represents the galvanostatic charging response of the four high strength steels under equivalent hydrogen charging conditions.

As expected, the higher the hydrogen diffusivity the shorter the initial parabolic segment of the transient. Therefore, it can be easily noticeable that CSS-42L™ displays the shorter parabolic period followed by 300M and GifloM2000. On the contrary, AerMet®100 displays the longest and much deeper parabolic segment which depends mainly upon *D* values. This high alloy high strength steel was described to be highly affected by a high trap density which contributed to its lower hydrogen diffusion.

As important technological implications it is feasible to consider that the lower the hydrogen diffusivity of the high strength steel, the less hydrogen should penetrate the material due to direct embrittlement or re-embrittlement. Atomic hydrogen can be produced by direct embrittlement

during manufacturing processes such as electroplating, or re-embrittlement during service at any breach in the sacrificial coating. In relation with the previous statement, it has been suggested the susceptibility to hydrogen induced fracture of the high strength steels taken into consideration in this project are ranked in the order: CSS-42L™ > GifloM2000 > 300M > AerMet®100 being the less susceptible.

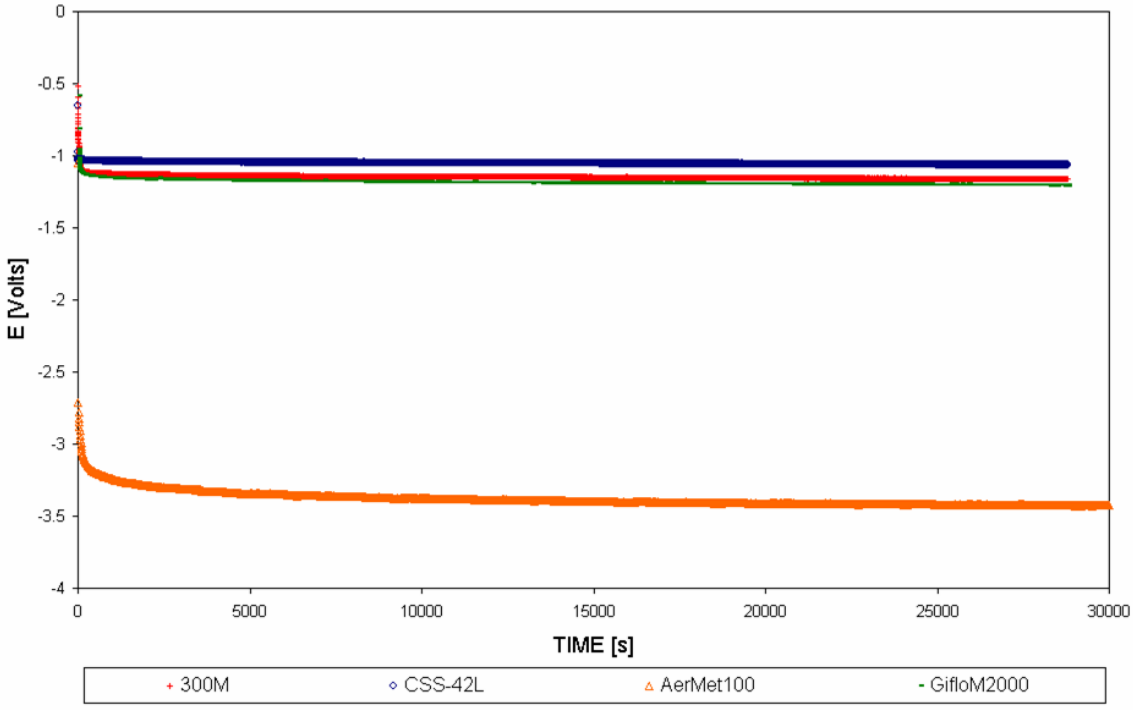

Figure 169. Comparison of the potential vs. time response for 300M, GifloM2000, CSS-42L™ and AerMet®100 high strength steels under similar hydrogen galvanostatic charging.

Finally, the effect of elastic stress did not appear to have an important effect on the hydrogen diffusivity and embrittlement susceptibility of the high strength steel. Nonetheless, the presence of compressive residual stresses induced by shot peening slows down the hydrogen uptake of at least the low alloy 300M steel, decreasing to some extent its susceptibility to *HE*. In addition, a subsequent increase in the hydrogen solubility is thought to be related with the high dislocation density produced by the plastic deformation induced by the surface treatment.

CONCLUSIONS

- Cadmium electroplating produced severe direct hydrogen embrittlement to the conventional 300M high strength steel. In contrast, no direct embrittlement was suffered by the alternative high alloy AerMet®100 steel. In the same order, their corresponding embrittlement indices, *EI*, were 0.54 and 0.05, respectively.

- Fractographic analysis performed on cadmium plated 300M specimens showed a high percentage (16-23%) of inter-granular and trans-granular brittle fracture regions. These results were consistent with the high *EI* mean value of 0.54 found for these specimens, whereas only a small proportion of brittle cleavage fracture regions (3-6%) were found for cadmium plated AerMet®100 specimens. These results were directly related to a low mean *EI* index of 0.05.

- Both 300M and AerMet®100 steels were successfully de-embrittled by baking for 24 hours at 200°C after cadmium electroplating. These findings corroborated the effectiveness of this post-plating treatment in recovering the original mechanical properties of the steels after the electroplating of cadmium. *EI* for cadmium plated and baked 300M and AerMet®100 specimens remained very low at 0.04 and 0.03, respectively.

- 300M steel displayed a significantly high susceptibility to hydrogen re-embrittlement when the cadmium sacrificial coating became corroded in 3.5%NaCl solutions. The mean embrittlement index for this condition was 0.16. Moreover, a similar re-embrittlement level of 0.18, was found for the alternative low alloy GifloM2000 steel. Nevertheless, the high alloy AerMet®100 steel did not suffer from hydrogen re-embrittlement during corrosion of the cadmium coating.

- It was shown that a thin layer of nickel that had been applied before the cadmium acted as a barrier to hydrogen uptake by the GifloM2000 steel. This alloy displayed no susceptibility to hydrogen re-embrittlement, (*EI*=-0.05), when the cadmium coating, applied after the *'nickel strike'* process, was corroding in 3.5% NaCl solutions. It appears that a thin nickel layer beneath the sacrificial coating would provide a promising method for controlling both direct hydrogen embrittlement and hydrogen re-embrittlement. Alternatively, the second group of cadmium plated, baked and corroded GifloM2000, which did not received a nickel strike treatment, showed to be susceptible to hydrogen re-embrittlement, displaying *EI* of 0.19.

- Considering an alternative Zinc-Nickel sacrificial coating as a replacement for cadmium, it was shown that the electroplating process caused severe direct embrittlement to the low alloy 300M steel. AerMet®100 steel did not appear to suffer delayed failure problems due to occluded hydrogen introduced during the electroplating of the Zinc-Nickel. In this respect, *EI* for Zinc-Nickel plated 300M and AerMet®100 specimens were 0.46 and -0.03, respectively.

- Baking treatments for 24 hours at 200°C following the Zinc-Nickel electroplating led to a complete recovery of the mechanical properties for the conventional 300M steel. AerMet®100 specimens were shown to be unaffected by the baking process.

- Substantial hydrogen re-embrittlement of 300M steel was produced by the corrosion of the alternative Zinc-Nickel sacrificial coating. The mean embrittlement index reported for this condition was 0.53, a value similar to that produced by the conventional cadmium coating. Likewise, AerMet®100 steel displayed a significant susceptibility to hydrogen re-embrittlement with *EI*=0.34, but it was still slightly lower than that for 300M steel. Considering both

alloys, these results showed higher re-embrittlement susceptibilities than those produced by cadmium.

- The second alternative sacrificial coating, SermeTel®1140/962, proved to have an advantage over the electroplated cadmium and the Zinc-Nickel based on the lack of direct embrittlement produce by its deposition process. Both alloys, 300M and AerMet®100 were shown to be not susceptible to direct hydrogen embrittlement after the spraying of the aluminium based sacrificial coating. Moreover, equivalent results were reported for SermeTel®1140/962 coated CSS-42L™ stainless steel specimens.

- Curing at a temperature higher than the tempering temperature led to a small increase in ductility for SermeTel®1140/962 coated 300M specimens. A similar situation was not found for AerMet®100 specimens.

- Hydrogen re-embrittlement produced by the corrosion of the aluminium based SermeTel®1140/962 coating was considerably high for 300M and the alternative CSS-42L™ stainless steel. Their corresponding *EI* were 0.27 and 0.25, respectively. In contrast, AerMet®100 proved to be not susceptible to re-embrittlement under the same condition.

- CSS-42L™ martensitic stainless steels showed relatively high susceptibilities to hydrogen re-embrittlement, (*EI*=0.25), but slightly lower than 300M steels, when a SermeTel®1140/962 sacrificial coating was corroded in 3.5% NaCl solutions. On the contrary, uncoated CSS-42L™ specimens directly exposed to corrosive environments displayed much less susceptibility to hydrogen embrittlement, (*EI*= 0.03). This result suggests that CSS-42L™ stainless steel had better embrittlement resistance in the uncoated condition.

- The levels of re-embrittlement susceptibilities displayed by the high strength steels due to the corrosion of the three sacrificial coatings were associated to two main factors: 1) the electro-negativity and 2) the barrier properties of the coating. The electrochemical activity of the coatings increased in the order SermeTel®1140/962 < Cadmium < Zinc-Nickel coating. In relation to this finding, permeation measurements showed that the hydrogen-uptake increased in an exponential rate as the potential was lowered from -0.90 to -1.15 V (SCE). Secondly, chemical porosity test showed that hydrogen re-embrittlement was likely to occur during corrosion of the sacrificial cadmium and Zinc-Nickel coatings within *crater-like* and *through-thickness* cracks, respectively. Whereas, the steel substrate only became exposed to corrosive environments once the polymer topcoat layer of the SermeTel®1140/962 was degraded.

- The measured permeation transient for 300M was shown to be in good agreement with a theoretical lattice diffusion model. The hydrogen diffusion coefficient for 300M was $1.02 \times 10^{-7} cm^2/s$. However, the hydrogen permeation method was not useful to measure hydrogen diffusivity of AerMet®100 membranes. Therefore, the alternative galvanostatic charging technique was used, and it was revealed that the hydrogen diffusion coefficients for the alternative AerMet®100 was two orders of magnitude lower than 300M. These values corresponded to approximately 3.5×10^{-9} cm^2/s. These differences in hydrogen diffusion coefficients appeared to be an important factor in the low hydrogen embrittlement and re-embrittlement susceptibilities of AerMet®100.

- The effect of compressive residual stresses induced by shot penning on 300M steels was an increase in the hydrogen solubility and a decrease in the hydrogen diffusion. From a practical point of view, it was considered that shot peening will not necessarily eliminate the hydrogen embrittlement problem in 300M. Although hydrogen transport may be affected, failure could still occur eventually. The

beneficial effects appear to be limited largely to the introduction of compressive stresses which oppose the tensile stresses in the component.

- The hydrogen transport characteristic in terms of diffusion coefficients for 300M steel was not affected by the application of tensile elastic stresses up to 50% yield strength. Instead, it was suggested that applied tensile stresses should increase the solubility of hydrogen in the steel.

- Hydrogen diffusion measurements showed that the low alloy GifloM2000 steel had similar hydrogen transport characteristics to the second batch of 300M specimens, with coefficients of $3.8x10^{-8}$ and $4.4x10^{-8}$ cm^2/s, respectively. Whereas, CSS-42L™ martensitic stainless steel displayed hydrogen diffusion coefficients of $3.0\ x10^{-7}$ cm^2/s, which was the highest value for the high strength steels studied.

- The hydrogen transport characteristics in terms of hydrogen diffusivity appeared to indicate the different extents of hydrogen embrittlement or re-embrittlement displayed by the high strength steels. In relation to this finding, the hydrogen diffusion coefficients of the four different steels were ranked as follows: CSS-42L™ > 300M ≥ GifloM2000 > AerMet®100 with the lowest.

- AerMet®100 has shown less susceptibility to hydrogen embrittlement and re-embrittlement in all conditions tested, therefore this high alloy steel was considered to be an exceptional replacement material for the conventional 300M steel. On the other hand, GifloM2000 and CSS-42L™ steels were not considered suitable replacement materials mainly due to their unexpected failure during simultaneous hydrogen charging and the application of elastics stresses equivalent to 0% and 50% of their yield strength, respectively.

- The alternative aluminium based SermeTel®1140/962 sacrificial coating was considered to be a suitable replacement to the conventional cadmium sacrificial coating if the structural steels used as substrate was AerMet®100. Mechanical tests showed that AerMet®100 did not suffer from either direct hydrogen embrittlement or re-embrittlement when it was coated with the SermeTel®1140/962. Otherwise, the used of this sacrificial coating might produce considerable high re-embrittlement of the conventional 300M and the alternative CSS-42L™ stainless steel.

FUTURE WORK

- The beneficial effects of applying a thin nickel layer beneath a sacrificial coating requires further investigation. If it can be shown that this controls hydrogen re-embrittlement in all circumstances then it would have important practical applications.

- CSS-42L™ steel displayed low hydrogen embrittlement susceptibility when tested in the uncoated condition. However, this alloy showed to be highly susceptible to the simultaneous application of hydrogen charging and elastic stresses. Similar characteristics were found for GifloM2000. Therefore, it is recommended to carry out further work on these effects in order to consider both alternative alloys for aerospace applications.

- The effect of residual stresses on hydrogen embrittlement has not been widely studied yet. They could provide benefits in controlling the problem. Compressive stresses have been shown in this project to delay hydrogen uptake and transport within the material. However, the more important effects on stress distribution within the material and the possible suppression of crack initiation at microstructural flaws remain to be investigated.

APPENDICES

1. Table including student *t*-test tabular values.

PERCENTAGE POINTS OF THE T DISTRIBUTION

Tail Probabilities									
One Tail		0.10	0.05	0.025	0.01	0.005	0.001	0.0005	
Two Tails		0.20	0.10	0.05	0.02	0.01	0.002	0.001	
D	1	3.078	6.314	12.71	31.82	63.66	318.3	637	1
E	2	1.886	2.920	4.303	6.965	9.925	22.330	31.6	2
G	3	1.638	2.353	3.182	4.541	5.841	10.210	12.92	3
R	4	1.533	2.132	2.776	3.747	4.604	7.173	8.610	4
E	5	1.476	2.015	2.571	3.365	4.032	5.893	6.869	5
E	6	1.440	1.943	2.447	3.143	3.707	5.208	5.959	6
S	7	1.415	1.895	2.365	2.998	3.499	4.785	5.408	7
	8	1.397	1.860	2.306	2.896	3.355	4.501	5.041	8
O	9	1.383	1.833	2.262	2.821	3.250	4.297	4.781	9
F	10	1.372	1.812	2.228	2.764	3.169	4.144	4.587	10
	11	1.363	1.796	2.201	2.718	3.106	4.025	4.437	11
F	12	1.356	1.782	2.179	2.681	3.055	3.930	4.318	12
R	13	1.350	1.771	2.160	2.650	3.012	3.852	4.221	13
E	14	1.345	1.761	2.145	2.624	2.977	3.787	4.140	14
E	15	1.341	1.753	2.131	2.602	2.947	3.733	4.073	15
D	16	1.337	1.746	2.120	2.583	2.921	3.686	4.015	16
O	17	1.333	1.740	2.110	2.567	2.898	3.646	3.965	17
M	18	1.330	1.734	2.101	2.552	2.878	3.610	3.922	18
	19	1.328	1.729	2.093	2.539	2.861	3.579	3.883	19
	20	1.325	1.725	2.086	2.528	2.845	3.552	3.850	20
	21	1.323	1.721	2.080	2.518	2.831	3.527	3.819	21
	22	1.321	1.717	2.074	2.508	2.819	3.505	3.792	22
	23	1.319	1.714	2.069	2.500	2.807	3.485	3.768	23
	24	1.318	1.711	2.064	2.492	2.797	3.467	3.745	24
	25	1.316	1.708	2.060	2.485	2.787	3.450	3.725	25
	26	1.315	1.706	2.056	2.479	2.779	3.435	3.707	26
	27	1.314	1.703	2.052	2.473	2.771	3.421	3.690	27
	28	1.313	1.701	2.048	2.467	2.763	3.408	3.674	28
	29	1.311	1.699	2.045	2.462	2.756	3.396	3.659	29
	30	1.310	1.697	2.042	2.457	2.750	3.385	3.646	30
	32	1.309	1.694	2.037	2.449	2.738	3.365	3.622	32
	34	1.307	1.691	2.032	2.441	2.728	3.348	3.601	34
	36	1.306	1.688	2.028	2.434	2.719	3.333	3.582	36
	38	1.304	1.686	2.024	2.429	2.712	3.319	3.566	38
	40	1.303	1.684	2.021	2.423	2.704	3.307	3.551	40
	42	1.302	1.682	2.018	2.418	2.698	3.296	3.538	42
	44	1.301	1.680	2.015	2.414	2.692	3.286	3.526	44
	46	1.300	1.679	2.013	2.410	2.687	3.277	3.515	46
	48	1.299	1.677	2.011	2.407	2.682	3.269	3.505	48
	50	1.299	1.676	2.009	2.403	2.678	3.261	3.496	50
	55	1.297	1.673	2.004	2.396	2.668	3.245	3.476	55
	60	1.296	1.671	2.000	2.390	2.660	3.232	3.460	60
	65	1.295	1.669	1.997	2.385	2.654	3.220	3.447	65
	70	1.294	1.667	1.994	2.381	2.648	3.211	3.435	70
	80	1.292	1.664	1.990	2.374	2.639	3.195	3.416	80
	100	1.290	1.660	1.984	2.364	2.626	3.174	3.390	100
	150	1.287	1.655	1.976	2.351	2.609	3.145	3.357	150
	200	1.286	1.653	1.972	2.345	2.601	3.131	3.340	200
Two Tails		0.20	0.10	0.05	0.02	0.01	0.002	0.001	
One Tail		0.10	0.05	0.025	0.01	0.005	0.001	0.0005	
Tail Probabilities									

* This table was calculated by APL software. The format of the table is adapted form a table constructed by Drake Bradley, Department of Physiology, Bates College, Lewiston-Ashburn, Maine, U.S.

Table 27. Tabular values for the student t-test distribution.

2. Table with the complete *SSRT* data recorded for the project.

Airbus SSRTs for Ultra-High Strength Steels														
					Preload 50Kg		Strain Rate 9.70E-07							
Specimen	**File**		**Diameter**	**Area**	**Max Load (kN)**		**UTS(MPa)**		**TTF (hrs)**	**Mean TTF**	**EI**	**EI mean**	**ln (Ps)**	
300M														
300M		**Uncoated**												**TTF (hrs)**
MISC/1215/37/8	300Mair1		2.735	5.87553		thread failed			#19.68					
MISC/1215/37/18	300Mair2		2.73	5.854067	12.98		2217.262		29.3				-0.223	29.3
MISC/1215/37/25	300Mair3		2.74	5.897032	13.27		2250.285		32.36				-0.916	32.36
MISC/1215/37/36	300Mair4		2.715	5.789913	13.8		2383.456		32.1				-0.511	32.1
MISC/1215/37/31	300Mair5		2.73	5.854067	13.03		2225.803	2269.201	32.52	**31.57**			-1.609	32.52
300M		**Cd plated/unbaked**												
MISC/1215/37/16	300Mcad1		2.735	5.87553	10.15		1727.504		14.34		0.545771		-0.511	14.34
MISC/1215/37/1	300Mcad2		2.73	5.854067	10.01		1709.922		15.26		0.51663		-1.609	15.26
MISC/1215/37	300Mcad3		2.72	5.811258	9.15		1574.53		13.97		0.557491		-0.223	13.97
MISC/1215/37	300Mcad4		2.74	5.897032	8.96		1519.408		14.27	**14.46**	0.547989	**0.54197**	-0.916	14.27
300M		**Cd plated/baked**												
MISC/1215/37/2	300Mcadb1		2.745	5.918574	13.22		2233.646		32.01		-0.01394		-1.609	32.01
MISC/1215/37/14	300Mcadb2		2.725	5.832643	13.6		2331.705		29.65		0.060817		-0.511	29.65
MISC/1215/37/16	300Mcadb3		2.73	5.854067	13.36		2282.174		30.9		0.021223		-0.916	30.9
MISC/1215/37/35	300Mcadb4		2.725	5.832643	13.41		2299.129		28.24	**30.2**	0.10548	**0.043396**	-0.223	28.24
300M		**Cd plated/baked/corroded**												
MISC/1215/37/17	300Mcadbc1		2.73	5.854067	13.51		2307.797		26.22		0.169465		-0.511	26.22
MISC/1215/37/32	300Mcadbc2		2.73	5.854067	13.75		2348.795		25.18		0.202407		-0.223	25.18
MISC/1215/37/34	300Mcadbc3		2.73	5.854067	13.36		2282.174		26.51		0.160279		-0.916	26.51
MISC/1215/37/37	300Mcadbc4		2.73	5.854067	13.89		2372.71		28.45	**26.59**	0.098828	**0.157745**	-1.609	28.45
300M		**Sermet plated/baked**												
MISC/1286/37/15	300Mser1		2.896	6.587634	13.56		2058.402		35.16		-0.11372		-1.609	35.16
MISC/1286/37/3	300Mser2		2.879	6.51052	13.42		2061.279		33.58		-0.06367		-0.511	33.58
MISC/1286/37/30	300Mser3		2.848	6.371069	13.795		2165.257		33.75		-0.06905		-0.916	33.75
MISC/1286/37/28	300Mser4		2.854	6.397942	13.94		2178.826	2115.941	32.78	**33.8175**	-0.03833	**-0.07119**	-0.223	32.78
300M		**Sermet plated/baked/corroded**												
MISC/1215/37/23	300Mserc1		2.883	6.528624	13.22		2024.929		23.98		0.240418		-1.609	23.98
MISC/1215/37/33	300Mserc2		2.861	6.429365	13.45		2091.964		23.6		0.252455		-0.916	23.6
MISC/1215/37/12	300Mserc3		2.887	6.546753	13.51		2063.619		22.04		0.301869		-0.223	22.04
MISC/1215/37/38	300Mserc4		2.886	6.542218	13.56		2072.692		22.96	**23.145**	0.272727	**0.266867**	-0.511	22.96
300M		**Zinc-Nickel Plated/Unbaked**												
MISC/1215/37/21	300MZnNiair1		2.79	6.114216	10.3		1684.599		15.75		0.501109		-0.223	15.75
MISC/1215/37/24	300MZnNiair2		2.765	6.005133	11.26		1875.063		16.08		0.490656		-0.916	16.08
MISC/1215/37/22	300MZnNiair3		2.755	5.961775	12.6		2113.465		21.73		0.311688		-1.609	21.73
MISC/1215/37/13	300MZnNiair4		2.75	5.940155	9.68		1629.587		15.01	**17.1425**	0.524549	**0.457**	-0.223	15.01
300M		**Zinc-Nickel Plated/baked**												
MISC/1215/37/29	300MZnNibaked1		2.78	6.070465	13.75		2265.065		30.75		0.025974		-0.223	30.75
MISC/1215/37/26	300MZnNibaked2		2.75	5.940155	13.36		2249.1		31.16		0.012987		-0.511	31.16
MISC/1215/37/05	300MZnNibaked3		2.74	5.897032	13.22		2241.806		31.5		0.002217		-0.916	31.5
MISC/1215/37/19	300MZnNibaked4		2.78	6.070465	13.56		2233.766		32.33	**31.435**	-0.02407	**0.004276**	-1.609	32.33
300M		**Zinc-Nickel Plated/Baked/Corrode**												
MISC/1215/37/9	300MZnNiBCorr1		2.721	5.815532	12		2063.44		19.44		0.384226		-1.609	19.44
MISC/1215/37/11	300MZnNiBCorr2		2.76	5.983434	9.44		1577.689		13.69		0.56636		-0.916	13.69
MISC/1215/37/7	300MZnNiBCorr3		2.748	5.931518	8.67		1461.683		13.18		0.582515		-0.223	13.18
MISC/1215/37/20	300MZnNiBCorr4		2.738	5.888426	8.86		1504.646		13.36	**14.9175**	0.576813	**0.527479**	-0.511	13.36
AerMet100 Steel														
Aermet 100		**Uncoated**												
MISC/1286/2/25	Airmetair1		2.69	5.683776	12.45		2190.445		29.59				-0.223	29.59
MISC/1286/2/29	Airmetair2		2.725	5.832643	12.21		2093.391		34.08				-0.916	34.08
MISC/1286/2/30	Airmetair3		2.72	5.811258	12.65		2176.809		34.6				-1.609	34.6
MISC/1286/2/35	Aermetair5		2.71	5.811258	12.12		2176.809		33.27	**32.885**			-0.511	33.27
Aermet 100		**Cd plated/unbaked**												
MISC/1286/2/12	Airmetcad1		2.75	5.940155	12.65		2129.574		30.56		0.070701		-0.511	30.56
MISC/1286/2/	Airmetcad2		2.715	5.789913	12.21		2108.84		31.44		0.043941		-0.916	31.44
MISC/1286/2/	Airmetcad3		2.75	5.940155	12.26		2063.919		32.59		0.008971		-1.609	32.59
MISC/1286/2/	Airmetcad4		2.72	5.811258	12.12		2085.607		29.8	**31.0975**	0.093812	**0.054356**	-0.223	29.8
Aermet 100		**Cd plated/baked**												
MISC/1286/2/38	Aermetcadb1		2.725	5.832643	12.79		2192.831		30.38		0.076175		-0.223	30.38
MISC/1286/2/11	Aermetcadb2		2.76	5.983434	12.41		2074.06		32.96		-0.00228		-0.916	32.96
MISC/1286/2/13	Aermetcadb3		2.735	5.87553	11.98		2038.965		31.31		0.047894		-0.511	31.31
MISC/1286/2/6	Aermetcadb4		2.73	5.854067	12.6		2152.35		33.45	**32.025**	-0.01718	**0.026152**	-1.609	33.45
Aermet 100		**Cd plated/baked/corroded**												
Aermet18	Aermetcadbc1		2.68	5.641596	12.4		2197.96		33.9		-0.03087		-0.916	33.9
Aermet34	Aermetcadbc2		2.76	5.983434	12.31		2057.347		33.72		-0.02539		-0.223	33.72
Aermet4	Aermetcadbc3		2.74	5.897032	12.74		2160.409		33.76		-0.02661		-0.511	33.76
Aermet32	Aermetcadbc4		2.72	5.811258	12.84		2209.504		33.91	**33.8225**	-0.03117	**-0.02851**	-1.609	33.91
Aermet 100		**Sermet plated/baked**												
MISC/1286/2/16	Aermetser1		2.848	6.371069	12.74		1999.664		34.06		-0.03573		-1.609	34.06
MISC/1286/2/28	Aermetser2		2.861	6.429365	12.6		1959.758		33.9		-0.03087		-0.916	33.9
MISC/1286/2/33	Aermetser3		2.818	6.237554	12.69		2034.451		32.95		-0.00198		-0.223	32.95
MISC/1286/2/10	Aermetser4		2.835	6.313039	12.4		1964.189	1989.516	33.16	**33.5175**	-0.00836	**-0.01923**	-0.511	33.16
Aermet 100		**Sermet plated/baked/corroded**												
MISC/1286/2/7	Aermetserc1		2.854	6.397942	12.5		1953.753		34.66		-0.05398		-0.916	34.66
MISC/1286/2/26	Aermetserc2		2.834	6.308586	12.69		2011.544		35.92		-0.09229		-1.609	35.92
MISC/1286/2/3	Aermetserc3		2.909	6.64691	12.74		1916.68		33.41		-0.01596		-0.511	33.41
MISC/1286/2/31	Aermetserc4		2.814	6.219859	11.83		1901.972		31.67	**33.915**	0.036947	**-0.03132**	-0.223	31.67
Aermet 100		**Zinc-Nickel Plated/Unbaked**												
MISC/1286/2/13	AermetZnNiair1		2.76	5.983434	12.5		2089.101		33.97		-0.03299		-0.511	33.97
MISC/1286/2/1	AermetZnNiair2		2.737	5.884126	12.26		2083.572		34.67		-0.06428		-0.916	34.67
MISC/1286/2/??	AermetZnNiair3		2.81	6.202189	12.55		2023.479		32.08		0.024479		-0.223	32.08
MISC/1286/2/??	AermetZnNiair4		2.79	6.114216	12.5		2044.416		35.02	**33.935**	-0.06492	**-0.03193**	-1.609	35.02
Aermet 100		**Zinc-Nickel Plated/baked**												
MISC/1286/2/37	AermetZnNibaked1		2.78	6.070465	12.84		2115.159		37.07		-0.12726		-1.609	37.07
MISC/1286/2/27	AermetZnNibaked2		2.76	5.983434	12.69		2120.856		35.33		-0.07435		-0.916	35.33
MISC/1286/2/9	AermetZnNibaked3		2.75	5.940155	12.31		2072.337		34.57		-0.05124		-0.511	34.57
MISC/1286/2/4	AermetZnNibaked4		2.76	5.983434	12.36		2065.703		33.67	**35.16**	-0.02387	**-0.06918**	-0.223	33.67
Aermet 100		**Zinc-Nickel Plated/Baked/Corrode**												
MISC/1286/2/16	AermetZnNiBCorr1		2.66	5.557707	11.02		1982.832		22.05		0.329482		-1.609	22.05
MISC/1286/2/23	AermetZnNiBCorr2		2.724	5.828363	12.31		2112.085		21.5		0.346206		-0.511	21.5
MISC/1286/2/2	AermetZnNiBCorr3		2.723	5.824084	12.5		2146.26		21.49		0.346511		-0.223	21.49
MISC/1286/2/14	AermetZnNiBCorr4		2.741	5.901337	12.31		2085.968		21.53	**21.6425**	0.345294	**0.341873**	-0.916	21.53

Table 28. Complete Excel Spread sheet for the *SSRT* data.

Airbus SSRTs for Ultra-High Strength Steels				Preload 50Kg	Strain Rate 9.70E-07						
Specimen	**File**	**Diameter**	**Area**	**Max Load (kN)**	**UTS(MPa)**	**TTF (hrs)**	**Mean TTF**	**El**	**El mean**	**ln (Ps)**	
CSS42L Unplated											
No.20	CSS42L Air1	2.77		6.026296	11.93	1979.657		40.15		0	-1.609
No.8	CSS42L Air2	2.78		6.069885	11.93	1965.441		38.98		0	-0.916
No.11	CSS42L Air3	2.76		5.982863	12.02	2009.072		37.64		0	-0.223
No.17	CSS42L Air4	2.75		5.939588	12.26	2064.116		38.86		0	-0.511
					12.035	**2004.571**		**38.9075**	1.025975		
CSS42L Corroded											
No.13	CSS42L NaCl 1	2.78		6.069885	12.12	1996.743		37.16		0.044914	-0.511
No.18	CSS42L NaCl 2	2.76		5.982863	12.26	2049.186		38.22		0.01767	-0.916
No.7	CSS42L NaCl 3	2.74		5.896469	12.2	2069.036		39.06		-0.00392	-1.609
No.22	CSS42L NaCl 4	2.74		5.896469	11.64	1974.063		36.8		0.054167	-0.223
					12.055	**2022.257**		**37.81**	1.028462	**0.028208**	
CSS42L Sermet Coated											
No.??	CSS42LSermet1	2.87		6.469261	12.12	1873.475		38.03		0.022553	-0.405
No.??	CSS42LSermet2	2.88		6.514422	12.45	1911.144		39.71		-0.02063	-1.099
					12.285	**1892.31**		**38.87**	1.187939	**0.000964**	
CSS42L Sermet Coated / Corroded											
No.??	CSSSermetNaCL1	2.86		6.424258	11.31	1760.515		27.24		0.299878	-0.693
No.??	CSSSermetNaCL2	2.83		6.29019	9.63	1530.955		20.14		0.482362	-0.288
No.??	CSSSermetNaCL3	2.87		6.469261	12.36	1910.574		39.77		-0.02217	-1.386
					11.1	**1734.015**		**29.05**	9.939381	**0.253357**	
CSS42L Sermet Coated / Corroded (Different Strain Rate)											
No.??	CSSSermetNaCL1	2.86		6.424258	11.31	1760.515		27.24		0.302611	-0.693
No.??	CSSSermetNaCL2	2.83		6.29019	9.63	1530.955		20.14		0.484383	-0.288
No.??	CSSSermetNaCL3	2.87		6.469261	12.36	1910.574		39.77		-0.01818	-1.386
					11.1	**1734.015**		**29.05**	9.939381	**0.256272**	
Giflo2000 Unplated											
No.15	GifloAirNo.15	2.77		6.026871	11.93	1979.468		31.5		0	-0.511
No.10	GifloAirNo.10	2.76		5.983434	12.31	2057.347		31.64		0	-0.916
No.21	GifloAirNo.21	2.75		5.940155	11.88	1999.948		30.67		0	-0.223
No.6	GifloAirNo.10	2.75		5.940155	12.26	2063.919		32.15		0	-1.609
					12.095	**2025.171**		**31.49**	0.613895		
Giflo2000 Cd Plated/Baked/Nickel Strike											
No.?	GifloCdBaked1	2.79		6.114216	12.31	2013.341		31.59		-0.00318	-0.288
No.?	GifloCdBaked2	2.81		6.202189	12.02	1938.025		32.32		-0.02636	-1.386
No.?	GifloCdBaked3	2.81		6.202189	12.31	1984.783		31.7		-0.00667	-0.693
					12.21333	**1978.716**		**31.87**	0.393573	**-0.01207**	
GifloM2000 Cd Plated/Baked/ Corroded/Nikel Strike											
No.?	Giflo220305	2.82		6.246411	12.31	1970.732		33.22		-0.05494	-0.511
No.?	Giflo250305	2.78		6.070465	12.26	2019.615		30.88		0.019371	-0.223
No.?	Giflo270305	2.79		6.114216	12.22	1998.621		33.7		-0.07018	-0.916
No.?	Giflo290305	2.8		6.158124	12.2	1981.123		33.8		-0.07336	-1.609
					12.2475	**1992.522**		**32.9**	1.370255	**-0.04478**	
GifloM2000 Cd Plated/Baked/ Corroded/											
No.1	GifloCdBCorr1	2.77		6.026871	12.02	1994.401		27.92		0.113369	-1.609
No.2	GifloCdBCorr2	2.79		6.114216	12.22	1998.621		27.39		0.1302	-0.916
No.3	GifloCdBCorr3	2.79		6.114216	11.31	1849.787		22.51		0.28517	-0.223
No.4	GifloCdBCorr4	2.8		6.158124	12.07	1960.012		24.56		0.22007	-0.511
					11.905	**1950.706**		**25.595**	2.530883	**0.187202**	

Table 28. Complete Excel Spread sheet for the *SSRT* data. (Continuation)

3. Galvanostatic data obtained for 300M steel under different levels of elastic stress.

Test	Area [cm^2]	Current [Amp]	$\partial E/\partial t$ [$V.s^{-1}$]	$\partial E/\partial t^{1/2}$ [$V.s^{-1/2}$]	$\lvert E_t - E_o \rvert$ [V]	D_a [$cm^2.s^{-1}$]	D_b [$cm^2.s^{-1}$]
0%YS							
1	1.44	0.001	$7x10^{-7}$	$9x10^{-4}$	0.055	$7.9x10^{-9}$	$4.3x10^{-8}$
2	1.44	0.001	$1x10^{-6}$	$9x10^{-4}$	0.055	$1.2x10^{-8}$	$6.8x10^{-8}$
3	1.44	0.001	$8x10^{-7}$	$1.6x10^{-3}$	0.051	$3.2x10^{-9}$	$5.2x10^{-8}$
4	1.44	0.001	$2x10^{-6}$	$1.8x10^{-4}$	0.066	$1.6x10^{-8}$	$1.0x10^{-7}$
25%YS							
1	1.44	0.001	$9x10^{-7}$	$8x10^{-4}$	0.052	$1.7x10^{-8}$	$5.8x10^{-8}$
2	1.44	0.001	$1x10^{-6}$	$7x10^{-4}$	0.040	$2.6x10^{-8}$	$8.4x10^{-8}$
3	1.44	0.001	$1x10^{-6}$	$1.1x10^{-3}$	0.059	$1.1x10^{-8}$	$5.7x10^{-8}$
4	1.44	0.001	$1x10^{-6}$	$1x10^{-3}$	0.056	$1.0x10^{-8}$	$5.9x10^{-8}$
50%YS							
1	1.44	0.001	$9x10^{-7}$	$9x10^{-4}$	0.064	$1.3x10^{-8}$	$4.7x10^{-8}$
2	1.44	0.001	$9x10^{-7}$	$8x10^{-4}$	0.069	$1.6x10^{-8}$	$4.4x10^{-8}$
3	1.44	0.001	$9x10^{-7}$	$9x10^{-3}$	0.034	$1.3x10^{-8}$	$5.3x10^{-8}$
4	1.44	0.001	$7x10^{-7}$	$5x10^{-4}$	0.031	$2.5x10^{-8}$	$7.6x10^{-8}$

Table 29. Galvanostatic data for 300M specimens under 0%, 25% and 50%*YS* of elastic stress.

4. Galvanostatic data obtained for GifloM2000 steel under 0%*YS* of elastic stress.

Test	Area [cm^2]	Current [Amp]	$\partial E/\partial t$ [$V.s^{-1}$]	$\partial E/\partial t^{1/2}$ [$V.s^{-1/2}$]	$\lvert E_t - E_o \rvert$ [V]	D_a [$cm^2.s^{-1}$]	D_b [$cm^2.s^{-1}$]
1	1.44	0.001	$2x10^{-6}$	$6x10^{-4}$	0.047	$7.8x10^{-8}$	$1.6x10^{-8}$
2	1.44	0.001	$7x10^{-7}$	$5x10^{-4}$	0.034	$6.8x10^{-8}$	$2.5x10^{-8}$
3	1.44	0.001	$1x10^{-6}$	$1x10^{-3}$	0.051	$6.5x10^{-8}$	$1.3x10^{-8}$
4	1.44	0.001	$1x10^{-6}$	$9x10^{-4}$	0.047	$7.1x10^{-8}$	$1.6x10^{-8}$

Table 30. Galvanostatic data for GifloM2000 specimens under 0%YS of elastic stress.

5. Galvanostatic data obtained for CSS-42L™ steel under 0%*YS* of elastic stress.

Test	Area [cm^2]	Current [Amp]	$\partial E/\partial t$ [$V.s^{-1}$]	$\partial E/\partial t^{1/2}$ [$V.s^{-1/2}$]	$\lvert E_t - E_o \rvert$ [V]	D_a [$cm^2.s^{-1}$]	D_b [$cm^2.s^{-1}$]
1	1.44	0.001	$8x10^{-7}$	$2x10^{-4}$	0.013	$2.0x10^{-7}$	$2.1x10^{-7}$
2	1.44	0.001	$7x10^{-7}$	$1x10^{-4}$	0.005	$6.2x10^{-7}$	$5.2x10^{-7}$
3	1.44	0.001	$5x10^{-7}$	$2x10^{-4}$	0.005	$8.2x10^{-8}$	$3.3x10^{-7}$
4	1.44	0.001	$9x10^{-7}$	$3x10^{-4}$	0.011	$1.2x10^{-7}$	$2.8x10^{-7}$

Table 31. Galvanostatic data for CSS-42L™ specimens under 0%*YS* of elastic stress.

REFERENCES

1. D. Wiser, 'The 4 horsemen of landing gear apocalypse', U.S. Air Force Flying Safety Magazine, Vol. 60, No.68, 7-11, August 2004.

2. Australian Transport Safety Bureau, *ATSB*, Aviation Safety, Technical Analysis Reports, 'Analysis of Main Landing Gear Pin/Lug Joint Failures, Boeing 737'. (*www.atsb.gov.au*)

3. A. Wrigley, 'The material low-down on takeoff and touchdowns – aircraft landing gear materials – Aerospace Metals, American Metal Market, May, 1994.

4. Timken Latrobe Company, 'Data Sheet: Lescalloy® 300M VAR-ARC®', U.S, 1988. (*www.timken.com*)

5. Timken Latrobe Company, 'Data Sheet: Lescalloy® 4340 VAR-ARC®', U.S, 1988. (*www.timken.com*)

6. L. L. Sherir, 'Corrosion 1, Metal / Environment Reactions', Newnes-Butterworths, London, Second Edition, 8:3-8:73, 1976.

7. H. Uhlig, 'Corrosion Handbook', Second Edition, John Wiley & Sons, U.S, 191-231, 2000.

8. G. M. Ugiansky, J. Payer, 'Stress Corrosion Cracking, the Low Strain Rate Technique', ASTM, U.S, 320-332, 1977.

9. British Standard BS1706:1990, 'Method for Specifying Electroplating Coatings of Zinc and Cadmium on Iron and Steel, 1990.

10. R. Baboian, 'Corrosion Tests and Standards, Applications and Interpretations', ASTM, U.S, 513-524, 1995.

11. L. L. Sherir, 'Corrosion 2, Corrosion Control', Newnes-Butterworths, London, Second Edition, 14:17-14:86, 1976.

12. K. Baldwin, 'The Corrosion of Zinc-Nickel Alloys', PhD Thesis, Cranfield University, 1992.

13. E. J. Baier, 'Cadmium Overexposure in the Aircraft Repair Industry', OSHA Hazard Information Bulletins, February 21, 1989. (*www.osha.com*)

14. European Commission DG ENV. E3, 'Heavy Metal in Waste, Final Report', COWI A.S, Denmark, February 2002.

15. K.R. Baldwin, M.J. Robinson, C.J. Smith, 'Corrosion Rate Measurements of Electrodeposited Zinc-Nickel Alloy Coatings', Corrosion Science, Vol.36, No.7, 1115-31, 1994.

16. D. A. Wright, N. Gage, *et al*, 'Verification of the Development of Low Hydrogen Embrittling Zinc-Nickel Electroplate by Slow Strain Rate Testing', Metal Finishing, 40-45, April 1995.

17. Sermatech® International Inc., 'Sermetel® Dense Pack Coatings, Replacements for Cadmium Plating', U.S. (*www.sermatech.com*)

18. G. Chalaftris, 'Evaluation of Aluminium-Based Coatings for Cadmium Replacement', PhD Thesis, Cranfield University, 2003.

19. Timken Latrobe Company, 'Alloy Data: AerMet®100 Alloy', U.S, 2003. (*www.timken.com*)

20. M. L. Schmidt, 'AerMet®100 alloy for Landing Gear Applications – A Summary of Forging Studies', Emerging Technologies in Aircraft Landing Gears, A. T. John, P. C. Ulrich, Progress in Technology Series PT-66, SAE International, 59-77, 1997.

21. Giflo Steels Company, 'High-Strength, Wear Resistant, Low alloyed Structural Steels Resistant to Atmospheric Corrosion, Giflo F-Steel Grades ', Hungary. (*www.giflo-steels.com*)

22. Timken Latrobe Company, 'Data Sheet: CSS-42L™ VIM-VAR Stainless Steel', U.S. (*www.timken.com*)

23. R. W. K. Honeycombe, 'Steels, Microstructures and Properties', Metallurgy and Materials Science Series, Edward Arnold, 12-27/76-105/186-210, 1981.

24. 'IT Diagrams, Isothermal Transformation of Austenite in a Wide Variety of Steels', United State Steel, 3rd Edition, U.S., 20-21-103, 1963.

25. C. H. Yoo, H. M. Lee *et. al*, 'M_2C Precipitates in Isothermal Tempering of High Co-Ni Secondary Hardening Steel', Metallurgical and Materials Transactions A, Vol. 37A, 3466-3472, 1996.

26. H. I. Burrier, C. M. Tomasello *et al*, 'Development of CSS-42L™, a High Performance Carburizing Stainless Steel for High Temperature Aerospace Applications', Bearing Steels: Into the 21st Century, ASTM STP 1327, 374-390, 1998.

27. P. M. Novonty, T. J. McCaffrey, 'An Advanced Alloy for Landing Gear and Aircraft Structural Applications - AerMet®100 Alloy', Emerging Technologies in Aircraft Landing Gears, A. T. John, P. C. Ulrich, Progress in Technology Series PT-66, SAE International, 79-85, 1997.

28. J. W. Morris, Z. Guo *et al*, 'The Limits of Strength and Toughness in Steel', ISIJ International, Vol. 41, No. 6, 599-611, 2001.

29. Z. Guo, K. Sato *et al*, 'Ultra-fine Grain Size Trough Thermal Treatment of Lath Martensitic Steels', Ultra-fine Grain Materials, R. S. Mirshra, S. L. Semiatin *et al*, TMS, 2000.

30. Y. Tomita, T. Okawa, 'Effect of Modified Heat Treatment on Mechanical Properties of 300M Steel', Materials Science and Technology, Vol. 11, No. 6, 245-251, 1995.

31. 'Military Handbook - MIL-HDBK-5H: Metallic Materials and Elements for Aerospace Vehicle Structures', U.S. Department of Defence, 2:2-2:242, 2003. (Knovel Interactive Edition, *www.Knovel.com*)

32. Y. Tomita, 'Fracture Toughness of Ultra High Strength Low Alloy Steels', Materials Science and Technology, Vol. 7, No. 6, 481-489, 1991.

33. J. L. Youngblood, M. Raghavan, 'Correlation of Microstructure with Mechanical Properties of 300M Steel', Metallurgical Transactions A, Vol. 8A, 1439-1448, 1977.

34. G. Krauss, 'Martensite in Steel: Strength and Structure', Materials Science and Engineering A, 273-275, 40-57, 1999.

35. R. Padmanabhan, W. E. Wood, 'Microstructural Analysis of a Multistage Heat-Treated Ultra-High Strength Low Alloy Steel', Materials Science and Engineering, No.66, 125-143, 1984.

36. D. A. Porter, K. E. Easterling, 'Phase Transformation in Metals and Alloys', CRS Press, 2ND Edition, London, 410-427, 1992.

37. T. Gladman, 'The Physical Metallurgy of Microalloyed Steels', The Institute of Materials', Institute of Materials,1st Edition, London, 81-136, 1997.

38. B. G. Pound, 'Hydrogen Trapping in High Strength Steels', Acta Materials', Vol.46, No.16, 5733-5743, 1998.

39. K. E. Thelning, 'Steel and its Heat Treatments', Butterworths, 2nd Edition, London, 14-24 / 284-305, 1984.

40. C. H. Yoo, H. M. Lee, 'M_2C Precipitates in Isothermal Tempering of High Co-Ni Secondary Hardening Steel', Metallurgical and Materials Transactions A, Vol.27A, 3466-3472, 1996.

41. R. Ayer, P. M. Machmeier, 'Transmission Electron Microscopy Examination of Hardening and Toughening Phenomena in AerMet100', Metallurgical Transactions A, Vol.24A, 1943-1955, 1993.

42. H. Smith, D. R. F. West, 'The reversion of Martensite to Austenite in certain Stainless Steels', Journal of Materials Science, Vol.8, 1413-1420, 1973.

43. X. Li, Z. Yin, 'Reverted Austenite during Aging of in 18Ni-(350) Maraging Steels', Materials Letter, Vol.24, 239-242, 1995.

44. Y. Tomota, Y. Morioka *et al*, 'Epsilon Martensite to Austenite Reversion and Related Phenomena in Fe-24Mn and Fe-24Mn-6Si Alloys', Acta Metallurgica, Vol.46, No.4, 1419-1416,1998.

45. D. H. Ping, M. Ohnuma *et al*, 'Microstructural Evolution in 13Cr-8Ni-2.5Mo-2Al Martensitic Precipitation-hardened Stainless Steel', Materials Science and Engineering A, *Article in Pre*ss, 2005.

46. J. L. Maloney, C. M. Tomasello *et al*, 'Case Carburized Stainless Steel Alloy for High Temperature Applications', U. S. Patent No.5,424,028, 1995.

47. M. Pourbaix, 'Atlas of Electrochemical Equilibria in Aqueous Solutions', NACE, Second English Edition, Houston, 1974.

48. M. Pourbaix, 'Thermodynamics of Dilute Aqueous Solutions', E. Arnolds, London, 1949.

49. E.U. Lee, 'Corrosion Behaviour of Landing Gear Steels', Naval Air Warfare Center, Aircraft Division Warminster, Report No. NAWCADWAR-94001-60, Warminster, P.A, U.S, 1993.

50. M. A. Ragen, D. L. Anthony *et al*, 'A Comparison of the Mechanical and Physical Properties of Contemporary and New Alloys for Aerospace Bearing', Symposium on Bearing Steel Technology, ASM Special Technical Publication 1419, U.S., 362-374, 2001.

51. D. Talbot, J. Talbot, 'Corrosion Science and Technology', CRC Press, Electronic Edition (*www.crcpress.com*), 1998.

52. W. J. Dini, 'Electrodeposition, the Material Science of Coatings and Substrates', WestWood, U.S, 249-278, 1993.

53. W. Blum, G. B. Hogaboom, 'Principles of Electroplating and Electroforming', McGraw-Hill, 3rd Edition, 200-220/307-335, U.S., 1949.

54. L. Marder, A. M. Bernardes *et. al*, 'Cadmium Electroplating Waste Water Treatment using a Laboratory Scale Electro-dialysis System', Separation and Purification Technology, Vol. 37, 247-255, 2004.

55. H. Morrow, 'Cadmium Electroplating', Metal Finishing, Vol. 100, No. 1, 199-203, 2002.

56. F. A. Lowenheim, 'Electroplating', McGraw-Hill, 1st Edition, U.S., 167-188, 1978.

57. ASM International handbook committee, 'Alloys Phase Diagrams', Baker Hugh, Vol. 3, 1992.

58. D. E. Hall, 'Electroplating of Zinc-Nickel Alloy Coatings', Plating and Surface Finishing, No.70, No.11, 59-65, 1983.

59. Z. Wu, *et al*, ' Electrochemical studies of Zinc-Nickel Codeposition in Chlorine Baths', Surface & Coatings Technology, No.85, 170-174, 1996.

60. M. S. Heydarzadeh, M. Jalali, 'Study of the Corrosion Properties of Zinc-Nickel Alloy Electrodeposits Before and After Chromating', Journal of Material Processing Tech., Article in Press, 2003.

61. E. Beltowska-Lehman, *et. al*, 'Electrodeposition of Zn-Ni Protective Coatings form Sulphate-Acetate Baths', Surfaces and Coating Technologies, No. 151-152, 444-448, 2002.

62. C. Muller, M. Sarret *et. al*, 'Some Peculiarities in the Deposition of Zinc-Nickel Alloys', Electrochimica Acta, No.36, 2811-2817, 2001.

63. A. B. Velichenko, J. Portillo, *et. al*, 'Nature of Anode Passivation in Zn-Ni Electroplating Baths', Electrochimica Acta, No.46, 407-414, 2000.

64. M. Gavrila, J. P. Millet *et. al*, 'Corrosion behaviour of Zinc-Nickel Coatings, electrodeposited on Steel', Surface & Coatings Technology, No.123, 164-172, 2000.

65. M. J. Carr, 'An Investigation of Hydrogen Embrittlement of High Strength Steels due to Zinc/Nickel Alloy Electroplating', PhD Thesis, Cranfield University, 1995.

66. E. M. K. Hiller, M. J. Robinson, 'Hydrogen Embrittlement of High Strength Steel Electroplated with Zinc-Cobalt Alloys', Corrosion Science, Vol. 46, 715-727, 2003.

67. British Standard BS 6338:1982 / ISO 4520:1981, 'Specification for Chromate Conversion Coatings on Electroplated Zinc and Cadmium Coatings', 1989.

68. M. F. Mosser, B. G. McMordie, 'Evaluation of Aluminium/Ceramic Coating on Fasteners to Eliminate Galvanic Corrosion', *SAE* Technical Paper Series, No.860112, 47-58, U.S, 1986.

69. M. F. Mosser, 'Metallic-Ceramic Coating as Replacements for Cadmium Plating, *SAE* Technical Paper Series, No.900968, 1-6, U.S, 1990.

70. Z. Szklarska-Smialowska, 'Various Forms of Localized Corrosion Common Features and Differences', Stress Corrosion Cracking and Hydrogen Embrittlement of Iron Base Alloys, Editors R.W. Staehle,

J. Hochmann, R.D. Mc.Cright and J.E. Slater, Proc. Conf. Unieux-Firminy, NACE-5, 30-36, 1973.

71. N. Eliaz, A. Shachar *et. al*, 'Characteristics of Hydrogen embrittlement, stress corrosion cracking and Tempered Martensite Embrittlement in High-Strength Steels', Engineering Failure Analysis, No.9, 167-184, 2002.

72. R.D. Mc.Cright, 'Effect of Environmental Species and Metallurgical Structure on the Hydrogen Entry into Steel', Stress Corrosion Cracking and Hydrogen Embrittlement of Iron Base Alloys, Editors R.W. Staehle, J. Hochmann, R.D. Mc.Cright and J.E. Slater, Conf. Proc. Unieux-Firminy, 12-16 June 1973, NACE-5, 306-325, 1977.

73. J. O'M. Bockris, J. McBreen, L. Nanis, 'The Hydrogen Evolution Kinetics and Hydrogen Entry into α-Iron', Journal Electrochemical Society, Vol. 112, No.10,1025-1031, 1965.

74. M. A. V. Devanathan & Z. Stachurski, 'The Mechanism of Hydrogen Evolution on Iron in Acid Solutions by Determination of Permeation Rates', Journal of the Electrochemical Society, Vol. 111, No. 5, 615-623, 1964.

75. R. N. Iyer, H. W. Pickering, 'Analysis of Hydrogen Evolution and Entry into Metals for the Discharged-Recombination Process', Journal of the Electrochemical Society, Vol. 136, No. 9, 2463-2470, 1989.

76. W. W. Gerberich, 'Effect of Hydrogen on High-Strength and Martensitic Steels', Hydrogen in Metals, Proc. Int. Conf. on the Effect of Hydrogen on Materials Properties and Selection and Structural Design, I. M. Bernstein, A.W. Thompson, American Society for Metals, 115-147, 1974.

77. C. A. Zapffe, C. E. Sims, 'Hydrogen Embrittlement, Internal Stress and Defects in Steel', Trans. AIME, Vol.145, 225-261, 1941.

78. A. R. Troiano, 'The Role of Hydrogen and other Interstitials in the Mechanical Behaviour of Metals', Trans. ASM, Vol. 54, 1960.

79. N. J. Petch, P. Stables, 'Delayed Fracture of Metals under Static Load', Nature, Vol.169, 1952.

80. D. G. Westlake, 'A Generalised Model for Hydrogen Embrittlement', Trans. ASM, Vol.62, 1000-1006, 1969.

81. R. Thompson, 'Brittle Fracture in a Ductile Material with Application to Hydrogen Embrittlement, Journal of Material Science, Vol. 13, 128-142, 1978.

82. C. D. Beachem, 'A New Model for Hydrogen-Assisted Cracking (Hydrogen Embrittlement)', Metallurgical Transactions, Vol.3, 437-451, 1972.

83. R. A. Oriani, 'A Decohesion Theory for Hydrogen-Induced Crack Propagation', Stress Corrosion Cracking and Hydrogen Embrittlement of Iron Base Alloys, Editors R.W. Staehle, J. Hochmann, R.D. Mc.Cright and J.E. Slater, Conf. Proc. Unieux-Firminy, 12-16 June 1973, NACE-5, 351-358, 1977.

84. H. H. Johnson, 'Fundamental Aspects of Stress Corrosion Cracking', NACE, 439, 1969.

85. T. D. Lee, T. Goldenberg, 'Effect of Hydrogen on Fracture of U-Notch Bend Specimens of Spheroidized AISI-1095 Steel', Metallurgical Transactions A, Vol. 10A, 199-208, 1979.

86. J. P. Hirth, 'Effects of Hydrogen on the Properties of Iron and Steels', Metallurgical Transaction A, Vol. 11A, 861-890, 1980.

87. E. N. Pugh, 'A Post Conference Evaluation of our Understanding of the Failure Mechanisms', Stress Corrosion Cracking and Hydrogen Embrittlement of Iron Base Alloys, Editors R.W. Staehle, J. Hochmann, R.D. Mc.Cright and J.E. Slater, Conf. Proc. Unieux-Firminy, 12-16 June 1973, NACE-5, 37-51, 1977.

88. H. H. Uhlig, 'Stress Sorption Cracking and the Critical Potential', Stress Corrosion Cracking and Hydrogen Embrittlement of Iron Base Alloys, Editors R.W. Staehle, J. Hochmann, R.D. Mc.Cright and J.E. Slater, Conf. Proc. Unieux-Firminy, 12-16 June 1973, NACE-5, 174-179, 1977.

89. J.O'M Bockris, M. A. Genshaw *et al*, 'Electro-Permeation of Hydrogen into Metals', Electrochim. Acta, Vol. 15, 47-60, 1970.

90. J. J. Gilman, 'The Role of Surface Hydrides in Stress Corrosion Cracking', Stress Corrosion Cracking and Hydrogen Embrittlement of Iron Base Alloys, Editors R.W. Staehle, J. Hochmann, R.D. Mc.Cright and J.E. Slater, Conf. Proc. Unieux-Firminy, 12-16 June 1973, NACE-5, 326-331, 1977.

91. R. Speiser, 'Hydrogen in Metals', Stress Corrosion Cracking and Hydrogen Embrittlement of Iron Base Alloys, Editors R.W. Staehle, J. Hochmann, R.D. Mc.Cright and J.E. Slater, Conf. Proc. Unieux-Firminy, 12-16 June 1973, NACE-5, 226-243, 1977.

92. J. P. Hirth, 'SCC and HE from the Viewpoint of the Defect Solid State', Stress Corrosion Cracking and Hydrogen Embrittlement of Iron Base Alloys, Editors R.W. Staehle, J. Hochmann, R.D. Mc.Cright and J.E. Slater, Conf. Proc. Unieux-Firminy, 12-16 June 1973, NACE-5, 1-10, 1977.

93. J. P. Hirth, B. Carnahan, 'Hydrogen Adsorption at Dislocations and Cracks in Fe', Acta Metallurgica, Vol.26, 1795-803, 1978.

94. C. D. Beachem, 'Electron Fractographic Support for a New Model for Hydrogen-Assisted Cracking', Stress Corrosion Cracking and Hydrogen Embrittlement of Iron Base Alloys, Editors R.W. Staehle, J. Hochmann, R.D. Mc.Cright and J.E. Slater, Conf. Proc. Unieux-Firminy, 12-16 June 1973, NACE-5, 376-381, 1977.

95. I. M. Robertson, 'The Effect of Hydrogen on Dislocation Dynamics', Engineering Fracture Mechanics, Vol.64, 649-673, 1999.

96. A. R. Troiano, 'General Keynote Lecture', Hydrogen in Metals, Proc. Int. Conf. on the Effect of Hydrogen on Materials Properties and Selection and Structural Design, I. M. Bernstein, A.W. Thompson, American Society for Metals, 3-15, 1974.

97. H. M. Alfons K, A. D. Bakker, 'Hydrogen Trapping Models in Steel', Metallurgical & Materials Transaction B, Vol.31B, 1475-1482, 2000.

98. M. Nagumo, 'Hydrogen Related Failure of Steels – a New Aspect', Materials Science and Technology, Vol. 20, No. 8, 940-950, 2004.

99. R. Padmanabhan, W. E. Wood, 'Stress Corrosion Cracking Behaviour of 300M Steel under Different Heat Treated Conditions', Corrosion-NACE, Vol41, No. 12, 688-699, 1985.

100. R.L.S. Thomas, D. Li, *et al*, 'Trap-Governed Hydrogen Diffusivity and Uptake Capacity in Ultrahigh-Strength AerMet®100 Steel', Metallurgical and Materials Transactions, Vol. 33 A, 1991-2004, 2002

101. R. McKibben, *et. al*, 'A Potentiostatic Double-Step Method for Measuring Hydrogen Atom Diffusion and Trapping in Metal Electrodes-I. Theory', Acta Metallurgical, Vol.35, No.1, 253-262, 1987.

102. A. Turnbull, *et. al*, 'Analysis of Hydrogen Diffusion and Trapping in a 13% Chromium Martensitic Stainless Steel', Acta Metallurgical, Vol.37, No.7, 2039-2046, 1989.

103. R. A. Oriani, 'The Diffusion and Trapping of Hydrogen in Steel', Acta Metallurgica, Vol. 18, 147-157, 1970.

104. J. L. Lee, J. Young L., 'Hydrogen Trapping in AISI-4340 Steel', Metal Science, Vol. 17, 426-432, 1983.

105. A. J. Kumnick, H. H. Johnson, 'Hydrogen Transport Through Annealed and Deformed Armco Fe', Metallurgical Transactions, Vol. 5, 1199-1206, 1974.

106. M. I. Luppo, J. Ovejero-Garcia., 'The Influence of Microstructure on the Trapping and Diffusion of Hydrogen in a Low Carbon Steel', Corrosion Sceince, Vol. 32, 1125-1136, 1991.

107. D. Li, R. P. Gangloff *et al*, 'Hydrogen Trap States in Ultrahigh-Strength AerMet100', Metallurgical and Materials Transactions A, Vol.35A, 849-863, 2004.

108. G. Hong, J. Lee, 'The Interaction of Hydrogen with Dislocations in Iron', Acta Metallurgica, Vol.32, No. 10, 1581-1589, 1984.

109. J. K. Tien, A. W. Thompson *et al*, 'Hydrogen Transport by Dislocations', Metallurgical Transactions, Vol. 7A, 821-827, 1976.

110. A. McNabb, P. K. Foster, 'A New Analysis of the Diffusion of Hydrogen in Iron and Ferritic Steels', Transactions AIME, Vol.227, 618-627, 1963.

111. I. M. Bernstein, A. W. Thompson, 'Effect of Metallurgical Variables on Environmental Fracture of Steels', International Metals Review, Vol.212, 269-287, 1976.

112. G. P. Tiwari, A. Bose *et al*, 'A Study of Internal Hydrogen Embrittlement of Steels', Material Science and Engineering A, Vol.286, 269-281, 2000.

113. J. Crank, 'The Mathematics of Diffusion', Oxford University Press, 71-74, 1975.

114. M. A. V. Devanathan & Z. Stachurski, 'The Mechanism of Hydrogen Evolution on Iron in Acid Solutions by Determination of Permeation Rates', Journal of the Electrochemical Society, Vol. 111, No. 5, 615-623, 1964.

115. M. D. Archer, N. C. Grant, 'Achievable Boundary Conditions in Potentiostaic and Galvanostatic Hydrogen Permeation Through Palladium and Nickel Foils', Proceedings Royal Society London, Vol. A395, 165-183, 1984.

116. N. Boes, H. Zuchner, 'Electrochemical Methods for Studying Diffusion, Permeation and Solubility of Hydrogen in Metals', Journal of Less Common Metals, Vol.49, 223-240, 1976.

117. C. J. Wen Ho, C. B. A. Boukamp, 'Use of Electrochemical Methods to Determine Chemical-Diffusion Coefficients in Alloys: Application to LiAl', International Metals Reviews, No.5, 253-668, 1981.

118. P. A. Sundaram, D. K. Marble, 'Hydrogen Diffusivity in AerMet100® at Room Temperature under Galvanostatic Charging Conditions', Journal of Alloys & Compounds, Vol.360, No.1-2, 90-97, 2003.

119. P. A. Sundaram, E. Wessel, *et al*, 'Determination of the Diffusion Coefficient of Hydrogen in Gamma Titanium Aluminides During Electrolytic Charging', Acta Materialia, No.48, 1005-1019, 2000.

120. A. J. Bard, R. L. Faulkner, 'Electrochemical Methods, Fundamental & Applications', John Willey & Sons, U.S, 249-264, 1980.

121. British Standard BS EN ISO 7539-1:1995, 'Corrosion of Metals and Alloys-Stress Corrosion Testing', Part 1: General Guidance on Testing Procedures, 1995.

122. G. E. Dieter, 'Mechanical Metallurgy', SI Metric Edition, London, 348-362, 1988.

123. British Standard BS EN ISO 7539-7:1995, 'Corrosion of Metals and Alloys-Stress Corrosion Testing, Part 7: Slow Strain Rate Testing, 1995.

124. N. R. Parkins, 'Development of Strain-Rate Testing and its Implications', Stress Corrosion Cracking – The Slow Strain Rate Technique. Editors G.M. Ugiansky and J. H. Payer, ASTM STP 665, 5-25, 1979.

125. G. J. Theus, J. R. Cels, 'The Slow Strain Rate Technique: Application to Caustic Stress Corrosion Cracking Studies', Stress Corrosion Cracking – The Slow Strain Rate Technique. Editors G.M. Ugiansky and J. H. Payer, ASTM STP 665, 81-96, 1979.

126. J. H. Payer, W. E. Berry *et al*, 'Application of Slow Strain-Rate Technique to Stress Corrosion Cracking of Pipelines Steel', Stress Corrosion Cracking – The Slow Strain Rate Technique. Editors G.M. Ugiansky and J. H. Payer, ASTM STP 665, 222-236, 1979.

127. Dictionary of Materials Science, Sixth Edition, McGraw-Hill, U.S, 265, 2003.

128. E. M. K. Hiller, 'The Effect of Zinc-Cobalt Electroplating on the Hydrogen Embrittlement of High Strength Steel', PhD Thesis, Cranfield University, 2001.

129. C. D. Kim, B. E. Wilde, 'A Review of the Constant Strain-Rate Stress Corrosion Cracking Test', Stress Corrosion Cracking-The Slow Strain Rate Technique, Editors G. M. Ugiansky and J. H. Payer, ASTM STP 665, 97-112, 1979.

130. J. R. Scully, H. Dogan *et al*, 'Controlling Hydrogen Embrittlement in Ultra-High Strength Steels', Corrosion/2004, New Orleans, L.A., U.S., 2004.

131. W. J. Pollock, 'Assessment of the Degree of Hydrogen Embrittlement Produced in High Strength 4340 Steel by Plating and Baking Processes using Slow Strain Rate Testing', Hydrogen

Embrittlement: Prevention and Control, ASTM STP 962, 68-60, 1988.

132. G. Chalaftris, M. J. Robinson, 'Evaluation of Aluminium Coatings for Cadmium Replacement', 42nd Corrosion Science Symposium, Swansea, U.K., 11-13, 2001.

133. W. Weibull, 'A Statistical Distribution Function of Wide Applicability', Journal of Applied Mechanics, Vol.18, 293-297, 1951.

134. W. W. Hines, D. C. Montgomery, 'Probability and Statistics in Engineering and Management Science', 164-167, 1980.

135. T. Yokobori, 'Strength Fracture and Fatigue of Materials', Ed. P. Noordhoff, Groningen, 22-28, 1965.

136. M. J. Robinson, R. M. Sharp, 'The effect of post-exposure Heat Treatment on the Hydrogen Embrittlement of High Strength Steel', Corrosion-NACE, Vol. 41, No.10, 582-586, 1985.

137. K. Massavetas, 'Experiment Design and Mathematical Treatment of Experimental Data – Error Theory', Athens, 1990.

138. ASTM Standard E-975-00, 'Standard Practice for X-Ray Determination of Retained Austenite in Steel with Near Random Crystallographic Orientation', 2000.

139. R. L Miller, 'A Rapid X-Ray Method for the Determination of Retained Austenite', Transactions of the ASM, Vol.57, 892-899, 1964.

140. British Standard BS EN ISO 10308:1997, 'Metallic Coatings-Review of Porosity Tests', 1997.

141. A. Kutzelnigg, 'Testing Metallic Coatings-Translation series number 4', Robert Draper LTD, U.K, 79-102, 1963.

142. ASTM Standard A-239-89, 'Standard Test method for Locating the Thinnest Spot in a Zinc (Galvanized) Coating on Iron or Steel articles by the Preece test (Copper Sulphate Dip)', 1989.

143. R. M. Pelloux, J. A. Van Den Avyle, 'Testing and Diagnosis of Hydrogen Susceptibility', Hydrogen in Metals, Proceedings International Conference, Editors I. M. Bernstein and R. G. Dermott, 547-558, 1973.

144. H. Gupta, M. Zhang *et al*, 'Barkhausen Effect in Ground Steels', Acta Materilia, Vol. 45, No. 5, 1917-1921, 1997.

145. T. D. Lee, T. Goldenberg *et al*, 'Effect of Hydrogen on Fracture of U-Notch Bend Specimens of Quenched and Tempered AISI-4340 Steel', Metallurgical Transactions A, Vol. 10A, 439-448, 1979.

146. R.L.S. Thomas, J. R. Scully, *et al*, 'Internal Hydrogen Embrittlement of Ultrahigh-Strength AerMet®100 Steel', Metallurgical and Materials Transactions A, Vol. 34 A, No.2, 327-344, 2003.

147. E.U. Lee, H. Sanders *et al*, 'Stress Corrosion Cracking of High Strength Steels', Naval Air Warfare Centre, Aircraft Division, Patuxent River, Maryland, Technical Report, U.S, 1999.

148. Molycorp Inc., 'Cerium: A Guide to its Role and Chemical Technology', 21, USA, 1992. (*www.molycorp.com/cerium_book.pdf*)

149. G. B. Olson, 'In Innovations in Ultrahigh Strength Steel Technology, 34th Sagamore Army Materials Research Conference, G. B. Olson, M. Azrin and E. S. Wright, Eds., United States Army Laboratory Command, Watertown, M. A., 549-593, 1987.

150. Ministry of Defence (MOD)-Defence Standard 03-36 Issue 1, 'Guidance to the Use of Cadmium Alternatives in the Protective Coating of Defence Equipment', January 2005.

151. K. R. Baldwin, C. J. E. Smith and M. Robinson, 'A Study into the Electrodeposition Mechanism of Zinc-Nickel Alloys from an Acid-Sulphate Bath', Trans. I. M. F., Vol. 72(2), 79-88, 1994.

152. K. A. Lucas, M. J. Robinson, 'The Influence of Lattice Hydrogen Content on the Hydrogen Assisted Cracking of High Strength Steels', Corrosion Science, Vol.26, No.9, 705-717, 1986.

153. M. J. Robinson, P. J. Kilgallon, 'Hydrogen Embrittlement of Cathodically Protected High-Strength, Low-Alloy Steels Exposed to Sulphate-Reducing Bacteria', Corrosion, Vol.50, No.8, 626-635, 1994.

154. P. Surrey, 'Detection of Heat Treatment Effects on Environmentally Induced Degradation of a Martensitic Stainless Steel and Nickel-Based Alloy by the Slow Strain Rate Method', M. Ugiansky, J. Payer, 'Stress Corrosion Cracking, the Low Strain Rate Technique', ASTM, U.S, 320-332, 1977.

155. E. Tolls, 'Deposizione di Zinco su Acciaio con Alto Carico di Rotura, senza Infragilimento de Idrogeno', AIFM Galvano Tecnica e Nuove Finiture, Vol.10, No.5, 282-284, 2000.

156. T. M. Harris, 'Hydrogen Diffusion and Trapping in Electroplated Nickel', PhD Thesis, Massachusetts Institute of Technology, 1989.

157. R. H. Song, S. Pyun, 'Hydrogen Permeation Through a Bilayer of Fe/Electrodeposited Ni', J. Electrochemical Soc., Vol.134, No.4, 1051-1056, 1990.

158. M. A. V. Devanathan & Z. Stachurski, 'The Mechanism of Hydrogen Evolution on Iron in Acid Solutions by Determination of Permeation Rates', Journal of the Electrochemical Society, Vol. 111, No. 5, 615-623, 1964.

159. D. A Jones, 'Principles and Prevention of Corrosion', Mac Millan International, U.S, 98, 1992.

160. W. Beck, J. O' M. Bockris, *et al*, 'Hydrogen Permeation in Metals as a Function of Stress, Temperature and Dissolved Hydrogen Concentrations', Proceeding of Royal Society, Vol. 290 A, 220-235, 1966.

161. R. P. Gangloff *et al*, 'Diffusion Control of Hydrogen Environment Embrittlement in High Strength Alloys', International Conference on Hydrogen Effects on Materials Behaviour and Corrosion Deformation Interactions; Moran, WY, US, 477-498, 2003.

162. M. J. Robinson, P. J. Kilgallon, 'A Review of the Effect of Microstructure on the Hydrogen Embrittlement of High Strength Steels', Final Report, Agreement No.MaTSU/8932/3706, Cranfield University, 1999.

163. R. O. Ritchie, M. H. Castro *et al*, 'The Effect of Silicon Additions and Retained Austenite on Stress Corrosion Cracking in Ultra High Strength Steels', Metallurgical Transactions A, Vol. 9A, 35-40, 1978.

164. G. Thomas, 'Retained Austenite and Tempered Martensite Embrittlement', Metallurgical Transactions A, Vol.9A, 439-450, 1978.

165. ASTM Designation E 975-00, 'Standard Practice for X-Ray Determination of Retained Austenite in Steel with Near Random Crystallographic Orientation[1]', 2000.

166. R. L. Miller, 'A Rapid X-Ray Determination of Retained Austenite', Transactions of the ASM, Vol.57, 892-899, 1964.

167. K. J. Bimal, S. M. Nirmalendu, 'Microstructural Evolution During Tempering of a Multiphase Steel Containing Retained Austenite', Materials Science & Engineering A, A263, 42-55, 1999.

168. B. D. Cullity, 'Elements of X-Ray Diffraction', Addison-Wesley Inc, Second Edition, 397-417, 1978.

169. A. Zielinski, P. Domzalicki, 'Hydrogen Degradation of High Strength Low-alloyed Steels', Journal of Material Processing Technology, Vol.133, No.1-2, 230-235, 2003.

170. T. Zakroczymski, 'An Electrochemical Method for Hydrogen Determination in Steel', Corrosion-NACE, Vol.38. No.4, 218-223, 1982.

171. P. Kumar, R. Balasubramaniam, 'Determination of Hydrogen Diffusivity in Austenitic Stainless Steels by Subscale Microhardness Profiling', Journal of Alloys and Compounds, 225, 130-134, 1997.

172. W. Weppner, R. A. Huggins, 'Determination of the Kinetic Parameters of Mixed-Conducting Electrodes and Application to the System Li_3Sb', J. Electrochemical. Soc., Vol.124, No. 10, 1569-1578, 1977.

173. L. B. Anderson, D. J. Macero, 'Generalized Chronopotentiometric Potential-Time Equations and their Application to Quasi-Reversible Processes', Analytical Chemistry, Vol. 37, No. 3, 322-326, 1965.

174. B. G. Pound, 'The Application of a Diffusion/Trapping Model for Hydrogen Ingress in High-Strength Alloys', Corrosion, Vol. 45, No.1, 18-25, 1989.

175. E.U. Lee, D. R. Tenney *et. al*, 'Surface Treatment Effects on AerMet100: Part 1. Shot Peening Effect on Corrosion and Fatigue of AerMet100 Steel', Naval Air Warfare Centre, Aircraft Division, Patuxent River, Maryland, Technical Report No.NAWCADPAX-95-126-TR, U.S, 1996.

176. J. Toribio, 'Numerical Modelling of Hydrogen Embrittlement of Cylindrical Bars with Residual Stress Fields', Journal of Strain Analysis for Engineering Design, Vol. 35, No. 3, 189-203, 2000.

177. J. Toribio, 'Residual Stress Effects in Stress-Corrosion Cracking', Journal of Materials Engineering and Performance, Vol. 7, No. 2, 173-182, 1998.

178. A. M. Brass, G. Anteri *et al*, 'Role of Shot-Peening on Hydrogen Embrittlement of a Low-Carbon Steel and a 304 Stainless Steel', Journal of Materials Science, Vol. 26, No. 16, 4517-4526, 1991.

179. Y. S. Kim, D. Jeong *et al*, 'Effect of Residual stress on the Hydrogen Embrittlement of PC Steel Wire', RIST Journal of R&D, Vol.16, No.1, 95-102, 2002.

180. M. Elices, G. Maeder *et al*, 'Effect of Surface Residual Stress on Hydrogen Embrittlement of Prestressing Steels', Br. Corrosion Journal, Vol. 18, No.2, 80-81,1983.

181. J. O'M. Bockris, W. Beck *et al*, 'The Effect of Stress on the Chemical Potential of Hydrogen in Iron and Steel', Acta Metallurgica, Vol. 19, 1209-1217, 1971.

182. J.O'M. Bockris, P. K. Subramanyan, 'A Thermodynamic Analysis of Hydrogen in Metals in the Presence of an Applied Stress Field', Acta Metallurgica, Vol. 19, 1205-1208, 1971

183. L. Nanis, T. K. Namboodhiri, 'Analysis of the Permeation Technique for the study of Hydrogen Entry into Iron-Base Alloys', Stress Corrosion Cracking and Hydrogen Embrittlement of Iron Base Alloys, Editors R.W. Staehle, J. Hochmann, R.D. Mc.Cright and J.E. Slater, Conf. Proc. Unieux-Firminy, 12-16 June 1973, NACE-5, 432-444, 1977.

184. M. D. Danford, 'The Effect of Tensile Stress on Hydrogen Diffusion in Metal Alloys', NASA Report TM-108386, 1992.

185. M. D. Danford, 'The Effect of Stress on Hydrogen Uptake and Desorption by A-286', NASA Report TM-103537, 1991.

186. E. Takahashi, 'Relations Between Occurrence of Transverse Cracks and Parameters of Residual Stress and Diffusible Hydrogen Concentrations: Prevention of Transverse Cracks in Heavy section Butt', J. Japanese Welding Society, Vol. 48, No. 10, 865-872, 1979.

187. R. A. Oriani, J. P. Hirth *et al*, 'Hydrogen Degradation of Ferrous Alloys', Noyes Publications, 1985.

188. W. J. Dini, 'Electrodeposition, the Material Science of Coatings and Substrates', WestWood, U.S, 249-278, 1993.

189. H. A. Ponte, A. M. Maul, 'Porosity Determination of Nickel Coatings on Copper by Anodic Voltametry', Journal of Applied Electrochemistry, Vol. 32, 641-646, 2002.

190. N. M. Martyak, *et al*, 'Surface Structures of Zinc Chromate Coatings', Metal Finishing, 20-27, 1996.

191. N. M. Martyak, 'Internal Stresses in Zinc-Chromate Coatings', Surface & Coating Technology, Vol. 88, 139-146, 1996.